CERN-THESIS-2020-328
16/10/2020

Search for Pair Production of Bottom-Squarks in Final States with Hadronically Decaying Tau-leptons, b-jets and missing transverse momentum with the ATLAS Detector at the Large Hadron Collider

Nikolai Fomin

Dissertation for the degree of Philosophiae Doctor (PhD)

Department of Physics and Technology
University of Bergen

June 2020

Scientific environment

The work on this thesis has been a part of the "Norwegian High Energy Particle Physics research with the ATLAS detector at the Large Hadron Collider" (Project Number 255182/F50) project funded by the Norwegian Research Council. Among other things it has supported my ATLAS membership and has organised ATLAS software tutorials.

Acknowledgements

I would like to thank my supervisors Anna Lipniacka, Bjarne Stugu and Martin Bertrand dit Latour for the guidance, help and support during the years spent working on the PhD project. Your contribution is invaluable and I am truly privileged to have worked with you.

I am grateful to Alexander Mann for the help with RECAST and writing. I would also like to thank Rosa Simoniello, Calum Macdonald, Laura Jeanty, Federico Meloni, Priscilla Pani, Christopher Lester, Sahal Yacoob for the insight and knowledge provided, for the time spent reviewing the project and for the fantastic feedback.

My deep gratitude goes to all members of the Bergen SUSY, Higgs, Taus, DM group and the ATLAS bb+MET and multi-b group. Thank you for your comments, questions and suggestions.

Last but not least I would like to thank my family for the support and patience.

Abstract

In this thesis a search for beyond the Standard Model physics, in particular for bottom-squark pairs in events with missing transverse momentum, b-tagged jets and hadronically decaying tau leptons is documented. The dataset used is recorded by the ATLAS detector from the proton-proton collisions at 13 TeV centre-of-mass energy at the Large Hadron Collider during the 2015-2018 period. The full dataset corresponds to an integrated luminosity of 139 fb^{-1}. No significant excess was observed, the results are compatible with the predictions of the Standard Model. Exclusion limits on bottom-squark mass are set at the 95% confidence level. Model-independent upper limits are set on the cross sections of new physics.

Contents

Chapter 1

Introduction

High energy particle physics studies elementary particles - the smallest building blocks of matter - and interactions between them. The cornerstone of particle physics is the Standard Model, a highly successful theory describing all observed elementary particles and the three fundamental forces affecting them. The theory in it's current form has been formulated in the 70s and since then has been tested and validated numerous times by various experiments. The final particle predicted by the Standard Model - the Higgs boson - has been observed by the Large Hadron Collider (LHC) experiments in 2012 during the Run 1. With the LHC increasing the energy and luminosity of the particle beams during the Run 2 data taking, a new era of precision measurements and searches for physics beyond the Standard Model has begun.

Despite it's successes the Standard Model is not able to answer every question about the universe and everything. It doesn't describe gravity in the same framework as the other fundamental forces. It also has no candidates for the particles that could constitute Dark Matter. This leads us to believe that there is more new physics to discover beyond the Standard Model. Many theories have been proposed for what is there with perhaps the most prominent one being supersymmetry.

Searches for physics beyond the Standard Model are in general performed in two different ways. One can try to precisely measure an existing process that is sensitive to the possible contributions from new physics and compare the result to the Standard Model prediction. Alternatively one can try to search for the new physics in the form of new particles or phenomena directly. In this thesis a direct search for pair-production of bottom squarks motivated by the supersymmetry predictions is described. The search is performed on the proton-proton collision at $\sqrt{13}$ TeV centre-of-mass energy data gathered by the ATLAS detector at the LHC during the Run 2 in 2015-2018.

The thesis is structured as follows: Chapters 2 - 4 give a short introduction to the theoretical framework of the Standard Model, the LHC and the ATLAS experiments and to some other concepts relevant for the thesis. Chapter 5 describes the datasets used. Chapters 6 - 9 describe the search for physics beyond the Standard Model itself, from the initial design to the final implementation. Finally chapters 10 and 11 describe the results of the search and the interpretations as well as present the conclusions.

1.1 Development of the Thesis

Initially the thesis was aimed at searches involving Z boson, jets and missing transverse momentum. A conference note [1] by the ATLAS experiment based on the first 3.2 fb^{-1} of data gathered during 2015 has observed an excess with a significance of 2.2 standard deviations. The study used final states with Z boson decaying to electrons and muons, the idea was to contribute to the study with the $Z \to \tau\tau$ channel. While the expected yields would be lower than for electrons or muons, the channel would still provide additional statistical power and could be considered an independent check of the result. However after the early 2016 dataset with 14.7 fb^{-1} of data has been examined [2] the disagreement with the data was no longer there for the muon and electron channels. After some discussion with the conveners of the SUSY working group at ATLAS it was decided to abandon the project.

The next target the thesis set was the titular pair-production of bottom squarks searches with final states including b-jets, missing transverse momentum and hadronically decaying tau leptons. Initially the model with the lightest supersymmetric particle (LSP) mass of 60 GeV has been considered, but that has been excluded by the search utilising signatures with multiple b-jets [3] first. The presented study then regeared to target almost massless LSPs where the multiple b-jets signature isn't effective.

At the moment of submission of the theses the search is complete. The first draft of the paper has been submitted to the Editorial Board at ATLAS. The aim is to have the results public in time for the ICHEP 2020 conference that starts at the end of July.

Parallel to the presented analysis I have contributed to a search for squarks and gluinos with hadronically decaying tau leptons in the final states [4]. The contribution consisted of trigger studies and Monte Carlo studies. While not directly related to the titular search the experience and intuition gained have proved to be extremely useful.

Chapter 2

Theory

In this chapter a brief overview of the Standard Model of particle physics (SM) is given. Furthermore the limitations and open questions of the SM are discussed and the basic ideas of Supersymmetry (SUSY) are introduced. The discussion is based on a variety of books and lectures, see [5] and [6]. Here and in the following a typical particle physics convention is used where the speed of light c and the reduced Planck constant $\hbar$ are set to be equal to 1. One of the consequences is that the units of mass, momentum and energy all become eV. It is impossible to give justice to the SM and SUSY in a single short chapter, this section aims to give a brief overview of important ideas of the theories.

2.1 Basic Principles

There are two basic theories that describe the world at the microscopic level - quantum mechanics and special relativity. Quantum Field Theory (QFT) is a theoretical framework that combines the two theories in a consistent way. The fundamental objects of QFT are quantum fields. The excitations of the fields correspond to the elementary particles.

The particles are classified as bosons (with spin $s = n \in Z$) and fermions ($s = n + \frac{1}{2}, n \in Z$) that have fundamentally different properties. All elementary matter particles like electrons, quarks or neutrinos are fermions. Pauli exclusion principle states that two identical fermions cannot occupy the same quantum state. Bosons (such as photons and Z bosons) have no such limitations which can be observed in e.g. Bose-Einstein condensates.

The basic tool of QFT is the concept of symmetry. Symmetry is defined (rather generally) as mappings of the physical states of a system that leaves the dynamics invariant [7]. What is meant by "dynamics" and "invariant" is dependent on the framework, but the overall idea is clear - symmetry is a feature of the system to stay invariant (whatever that means in the context) under a given transformation. Symmetries relevant in particle physics can be generally classified in two types:

- Spacetime symmetries - symmetries corresponding to transformations of the space-time itself. A typical example would be translation symmetry: $\vec{r} \rightarrow \vec{r} + \vec{a}$. More general examples include Lorentz transformations, Poincare transformations and general coordinate transformations.

- Internal symmetries - corresponding to transformations of fields of the theory: $\Phi^a(x) \rightarrow \Lambda^a_b \Phi^b x$.

Why are symmetries so important? Noether's theorem [8] states that each differentiable symmetry implies a conserved quantity. In the context of particle physics and QFT it means that we can identify particles with the conserved quantities (quantum numbers such as spin, charge, mass) based on the behaviour of the corresponding fields under the transformations. This allows for classification and labelling of all the various particles that are experimentally observed.

Symmetries also determine the interactions between particles through the gauge principle. The main idea is that promoting global (coordinate-independent) symmetries to local (coordinate-dependent) symmetries has to be coupled with introduction of gauge fields (bosons). They provide interaction terms between particles with gauge fields acting as mediators. Finally, the concept of (spontaneous) symmetry breaking is important in particle physics. This particular topic will be explained later in the chapter when discussing the Higgs boson and SUSY breaking.

2.2 Standard Model of Particle Physics

The Standard Models of particle physics is a quantum field theory that describes all known elementary particles and their interactions via three of the four fundamental forces - electromagnetic, the weak and the strong interaction. Gravity, the fourth fundamental force, can only be described at the classical level which is a valid approximation at energies below the Planck scale ($M_{pl} \approx 10^{19}$). The SM has been built gradually over decades before reaching its modern form in 1970s, see [9] for a more detailed history of the SM. From a theoretical point of view the SM is a renormalisable gauge theory based on the internal symmetry $SU(3)_C \times SU(2)_L \times U(1)_Y$.

Particle Content

As mentioned in the previous section the elementary particles of the SM are divided into fermions that have half-integer spin and bosons with whole number spins. The fermions are up-type quarks, down-type quarks, charged leptons and neutrinos and the corresponding antiparticles. There are three families of fermions that have same quantum numbers except for mass which makes for a total of 12 fermionic particles and 12 antiparticles. Antiparticles are not treated separately as they mostly behave like their counterparts. In the SM all fermions are matter particles, they are the fundamental building blocks of matter as we know it.

In the SM bosons can have spin $= 1$ (called vector bosons) and spin $= 0$ (scalar bosons, only example being Higgs boson). If one tried to introduce a graviton, a theoretical particle associated with the gravitational force, it would have to have spin $= 2$ (tensor boson), but it is usually not considered a part of the SM proper (and hasn't been experimentally observed). Vector bosons include photons (mediators of electromagnetic force), $W^{\pm}$-bosons and Z-boson associated with the weak interaction and eight types of gluons, carriers of the strong force. The particle content of the SM is summarised in Figure 2.1.

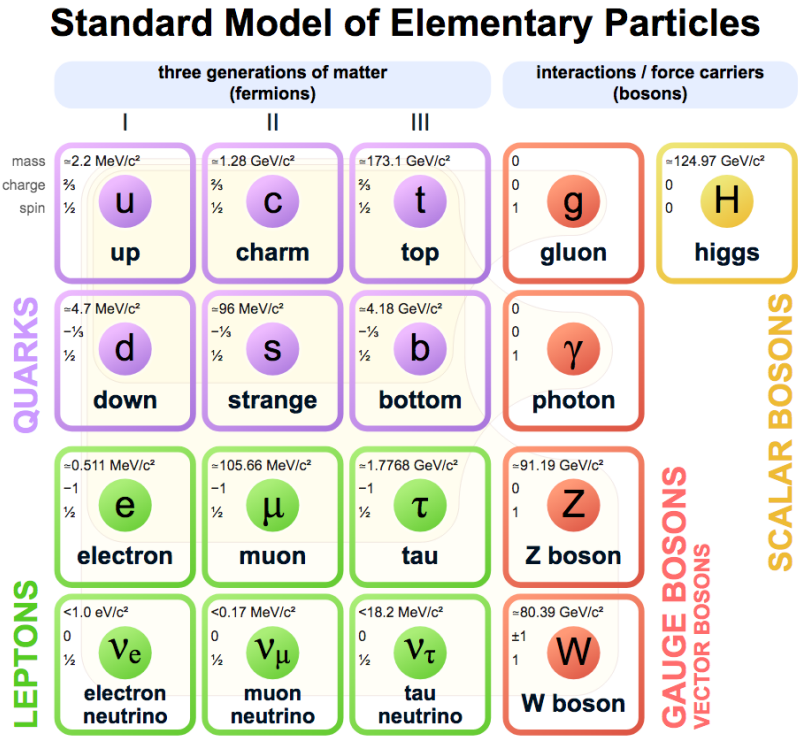

(a) Table of particles of Standard Model [10]. The mass measurements are the latest available as of 2019.

Figure 2.1

Quantum Electrodynamics and Gauge Principle

Quantum electrodynamics (QED) is the QFT version of electrodynamics. It is an important stone in the foundation of the SM. Here the basic ideas on which the more complex theories are built are introduced.

Let us start with the Lagrangian density of a Dirac field (it is common to refer to the Lagrangian density as just "Lagrangian") that can be obtained from the Dirac equation:

$$\mathcal{L}_D = \bar{\psi}(i\gamma^\mu \partial_\mu - m)\psi$$

where ψ is the Dirac spinor. The system is invariant under a global symmetry transformation $\psi \to e^{i\theta}\psi$. Now we want to make the symmetry local, i.e. θ should be a function of coordinates $\theta(x)$. This causes the system to no longer be invariant since:

$$\partial_\mu \psi \to \partial_\mu (e^{i\theta(x)}\psi) = e^{i\theta(x)}\partial_\mu \psi + i\partial_\mu \theta(x) e^{i\theta(x)}\psi$$

The solution is to introduce the covariant derivative D_μ such that $\bar{\theta} D_\mu \theta \to \bar{\theta} D_\mu \theta$. This is done by introducing a gauge field A_μ such that:

$$\begin{aligned} D_\mu \psi = (\partial_\mu + iqA_\mu)\psi \to & e^{i\theta(x)}\partial_\mu \psi + i\partial_\mu \theta(x) e^{i\theta(x)}\psi + iq(A_\mu + \delta A_\mu)e^{i\theta(x)}\psi = \\ & = e^{i\theta(x)} D_\mu \psi + i\partial_\mu \theta(x) e^{i\theta(x)}\psi + iq\delta A_\mu e^{i\theta(x)}\psi \end{aligned} \tag{2.1}$$

where q is the charge under the relevant transformation. If we now require that the system is invariant under the transformation we get:

$$A_\mu \to A_\mu + \delta A_\mu = A_\mu - \frac{1}{q}\partial_\mu \theta(x).$$

Now we identify q with the electric charge and A_μ with the covariant four-potential of the electromagnetic field. This simple example demonstrates application of the gauge principle - when attempting to localise a global symmetry we had to introduce an additional gauge field A_μ to keep the system invariant under the transformation. This leads to a term of the form $\bar{\psi} A_\mu \psi$ being added to the Lagrangian that describes (in the context of QED) interactions of photons and electrons. To complete the QED Lagrangian we add the kinetic term of the photon $-\frac{1}{4}F_{\mu\nu}F^{\mu\nu}$, $F_{\mu\nu} = \partial_\mu A_\nu - \partial_\nu A_\mu$ (notice that it is invariant under the gauge transformation):

$$\mathcal{L}_D = \bar{\psi}(i\gamma^\mu D_\mu - m)\psi - \frac{1}{4}F_{\mu\nu}F^{\mu\nu}$$

Generally speaking we can also add a photon mass term $\frac{1}{2}m' A_\mu A^\mu$ to the Lagrangian. However the only way for this term to be invariant under the gauge transformation is if $m' = 0$ so the photon has to be massless.

Quantum Chromodynamics and the Strong Interaction

Quantum Chromodynamics (QCD) is the theory of the strong interaction. Similar to how the QED deals with particles with electric charge the QCD describes interaction of particles charged under "colour". There are three different colour charges typically referred to as red, blue and green by analogy to usual basic colours. The two types of fundamental particles that have colour charge and can participate in the strong interaction are quarks and gluons. The QCD is a non-abelian gauge theory defined by the $\mathrm{SU}(3)_C$ group where "C" stands for "colour".

The concept of colour charges has been first suggested due to studies of omega baryon Ω^- (consisting of three strange quarks, sss) and delta baryon Δ^{++} (three up quarks, uuu). These baryons are made up of three identical quarks with parallel spins which (since quarks are fermions) violates the Pauli exclusion principle. The solution was to introduce an additional quantum number, colour. The theory of QCD has been extensively developed in 1970s. In 1979 PETRA observed first experimental evidence of the existence of gluons in three-jet events [11] and the 4 LEP experiments at CERN have later confirmed most of the QCD predictions.

The QCD has two interesting features that set it apart from other interactions - asymptotic freedom and confinement. Asymptotic freedom implies that the strength of the interaction (it's coupling strength) decreases as the energy scale increases. The result of colour confinement is that quarks and gluons are not observed directly as they cannot be isolated (as long as hadronic matter is stable). Instead, if one tries to separate two quarks, at some point it becomes energetically favourable for another quark-antiquark pair to be created. This process is called hadronisation and is the primary reason for the creation of jets.

The QCD Lagrangian is

$$\mathcal{L}_{QCD} = \bar{\psi}_i^f (i(\gamma^\mu D_\mu)_{ij} - m^f \delta_{ij})\psi_j^f - \frac{1}{4}G_{\mu\nu}^a G_a^{\mu\nu}$$

where $D_\mu = \partial_\mu - \frac{i}{2}gA_\mu^\alpha \lambda_\alpha$ is the covariant derivative, A_μ^α are eight gauge fields that correspond to gluons and λ_α are Gell-Mann matrices. $G_{\mu\nu}^a$ is the gluon field strength:

$$G_a^{\mu\nu} = (\partial^\mu A^\nu - \partial^\nu A^\mu + g_s f_{abc} A_b^\mu A_c^\nu)$$

with f_{abc} being the structure constant of SU(3). An interesting consequence is that unlike QED in the QCD gluons carry the colour charge so gluon-gluon vertices are possible. One exotic prediction of the QCD is existence of glueballs - composite particles that consist of only gluons.

The Electroweak Interaction

One could try to describe the weak interaction similar to the QCD. An issue that arises is that such theories predict massless bosons. Experimentally we know that the $W^{\pm}$ and Z boson are massive. A mechanism to explain this difference is needed. The Glashow-Salam-Weinberg electroweak theory unifies the weak and the electromagnetic interactions. The general idea is that the two interactions behave differently at lower energies, but above the electroweak scale (that will be discussed in the following sections) they can be described as effects of one force related to the $SU(2)_L \times U(1)$ gauge symmetry. A mechanism suggested by Higgs et al. [12], [13], [14] predicts existence of the Higgs field that breaks the SU(2) symmetry without disturbing the gauge invariance which leads to a massive spin 0 particle, the Higgs boson. It has remained the last undiscovered particle of the SM until 2012 when its discovery has been announced by the the ATLAS and CMS experiments at the LHC further validating the Standard Model [15, 16].

The weak interaction is defined by the non-abelian $SU(2)_L$ gauge group. It differs from the QCD and the QED in that it is a chiral theory - particles with different chirality have different properties. Left-chiral fermions are grouped in doublets that transform under SU(2) and right-chiral fermions are singlets that do not transform under SU(2), e.g:

$$\Psi^L = \begin{pmatrix} \psi_e^L \\ \psi_{\nu_e}^L \end{pmatrix} \rightarrow \Psi'^L = e^{ig\tau_j\omega_j(x)/2}\Psi^L;\ \psi_e^R \rightarrow \psi_e'^R = \psi_e^R;\ \psi_{\nu_e}^R \rightarrow \psi_{\nu_e}'^R = \psi_{\nu_e}^R;$$

where g is the weak coupling constant and τ_i are the Pauli matrices.

The electroweak Lagrangian can be divided in multiple parts:

$$\mathcal{L}_{EW} = \mathcal{L}_{gauge} + \mathcal{L}_{fermion} + \mathcal{L}_{Higgs} + \mathcal{L}_{Yukawa}.$$

The gauge term is

$$\mathcal{L}_{gauge} = -\frac{1}{4}W_{\mu\nu}^i W^{\mu\nu i} - \frac{1}{4}B_{\mu\nu}B^{\mu\nu}$$

where $W_{\mu\nu}^i = \partial_\mu W_\nu^i - \partial_\nu W_\mu^i - g\varepsilon^{ijk}W_\mu^j W_\nu^k$ and $B_{\mu\nu} = \partial_\mu B_\nu - \partial_\nu B_\mu$ are the field strength tensors for SU(2) and U(1) respectively. This term includes the gauge bosons kinetic energy terms and describes the self-interactions of $W_{\mu\nu}$ gauge bosons. The abelian U(1) gauge bosons $B_{\mu\nu}$ have no self-interactions.

The fermion part of the Standard Model is

$$\mathcal{L}_{fermion} = \Sigma_j^3 \left(\bar{q}'_{jL} i\not{\partial} q'_{jL} + \bar{l}'_{jL} i\not{\partial} l'_{jL} + \bar{u}'_{jR} i\not{\partial} u'_{jR} + \bar{d}'_{jR} i\not{\partial} d'_{jR} + \bar{e}'_{jR} i\not{\partial} e'_{jR} + \bar{\nu}'_{jR} i\not{\partial} \nu'_{jR} + h.c.\right)$$

where $q'_{jL} = \begin{pmatrix} u'_i \\ d'_i \end{pmatrix}_L$ represents the left-handed doublets of quarks, $l'_{jL} = \begin{pmatrix} e'_i \\ \nu'_i \end{pmatrix}_L$ are the left-handed doublets of leptons, q'_{jR}, d'_{jR} are the right-handed quark singlets and e'_{jR}, ν'_{jR} are

the right-handed lepton singlets. This term describes the interactions of fermions with gauge bosons.

The Higgs part of the Lagrangian is given by

$$\mathcal{L}_{Higgs} = (D^{\mu}H)^{\dagger}(D_{\mu}H) - V(H)$$

where $H = \binom{h^+}{h^0}$ is a complex Higgs scalar and $V(H) = -\mu^2 H^{\dagger}H + \lambda(H^{\dagger}H)^2$ is the Higgs potential. This term describes the Higgs interactions with the gauge bosons and the Higgs self-interactions.

The Yukawa Lagrangian is given by:

$$\mathcal{L}_{Yukawa} = -\Sigma_{i,j}\left(\bar{q}'_{iL}g^{(d)}_{ij}\phi d'_{jR} + \bar{q}'_{iL}g^{(u)}_{ij}\widetilde{\phi}u'_{jR} + \bar{l}'_{iL}g^{(e)}_{ij}\phi e'_{jR} + \bar{l}'_{iL}g^{(\nu)}_{ij}\widetilde{\phi}\nu'_{jR}\right) - h.c.$$

where $g^{(u)}, g^{(d)}, g^{(e)}, g^{(\nu)}$ are 3×3 matrices that describe the so called Yukawa couplings between the single Higgs doublet ϕ and the fermions.

Higgs Mechanism and Spontaneous Symmetry Breaking

The classical example of the spontaneous symmetry breaking is the so-called "Mexican hat" potential of a scalar ϕ, $V = -a|\phi|^2 + |\phi|^4$, see Figure 2.2. If the minimum of the potential is at the vacuum expectation value of the scalar $<\phi>= 0$ then the vacuum state is symmetric. In the "Mexican hat" potential case the ground state is not at $<\phi>= 0$, there is in fact an infinite number of ground states. The symmetry of the potential is then lost. An analogy would be a ball being placed at the top of the potential. As long as the ball is carefully balanced at the top the system is symmetric. However if the ball falls down until stopping in the trench (or ground state) the symmetry has been spontaneously broken. Looking at the previous section we see that the Higgs potential has exactly the same form as discussed here.

Select the constants μ^2 and λ to be positive in the Higgs potential:

$$V(H) = -\mu^2 H^{\dagger}H + \lambda(H^{\dagger}H)^2.$$

Then the minimum of the potential is at $\langle H^{\dagger}H\rangle = \nu^2$ with vacuum expectation value (VEV) $\nu = \frac{\mu}{\sqrt{2\lambda}}$. The Higgs doublet can be transformed under SU(2) to set $h^+ = 0$ and make $h^0 = \nu$ real. Now the masses of the SM bosons can be obtained from the Higgs VEV.

Define $h'_0 = h_0 - \nu$ such that $\langle h'_0\rangle = 0$. Then in the kinetic Higgs term we can write:

$$D_{\mu}H = D_{\mu}\begin{pmatrix} h^+ \\ h'_0 + \nu \end{pmatrix} = D_{\mu}\begin{pmatrix} h^+ \\ h'_0 \end{pmatrix} + D_{\mu}\begin{pmatrix} 0 \\ \nu \end{pmatrix}$$

and the second term written explicitly is:

$$D_{\mu}\begin{pmatrix} 0 \\ \nu \end{pmatrix} = \frac{i\nu}{2}\begin{pmatrix} gW_{1\mu} - igW_{2\mu} \\ -gW_{3\mu} + g'B_{\mu} \end{pmatrix}.$$

Computing $(D^{\mu}H)^{\dagger}(D_{\mu}H)$ and writing out terms that have two gauge field strength tensors we get:

$$\mathcal{L}_{gaugemass} = \frac{\nu^2}{4}g^2(W_1^2 + W_2^2) + \frac{\nu^2}{4}(gW_3 - g'B)^2.$$

We identify $W_\mu^\pm = \frac{1}{\sqrt{2}}(W_{1\mu} \pm iW_{2\mu})$ so that the first term of $\mathcal{L}_{gaugemass}$ is

$$\frac{v^2}{4}g^2(W_1^2 + W_2^2) = \frac{v^2}{4}g^2(W_{1\mu} + iW_{2\mu})(W_1^\mu - iW_2^\mu) = \frac{v^2}{4}g^2 W^{+\mu}W_\mu^-.$$

This looks like a mass term now, define $m_w^2 = \frac{vg}{2}$ and we get $m_w^2 W^{+\mu}W_\mu^-$. To get the mass term for the neutral massive boson (that we identify with the Z-boson) define:

$$\frac{1}{2}m_Z^2 Z_\mu Z^\mu = \frac{v^2}{4}(gW_3 - g'B)^2$$

This way we get $Z_\mu = \frac{1}{\sqrt{g^2+g'^2}}(gW_{3\mu} - g'B_\mu)$ and $m_Z^2 = \frac{v^2}{2}(g^2+g'^2)$. A field orthogonal to Z_μ is massless (as the mass term is lacking in the Lagrangian) so it can be identified with the massless photon:

$$A_\mu = \frac{1}{\sqrt{g^2+g'^2}}(gW_{3\mu} + g'B_\mu).$$

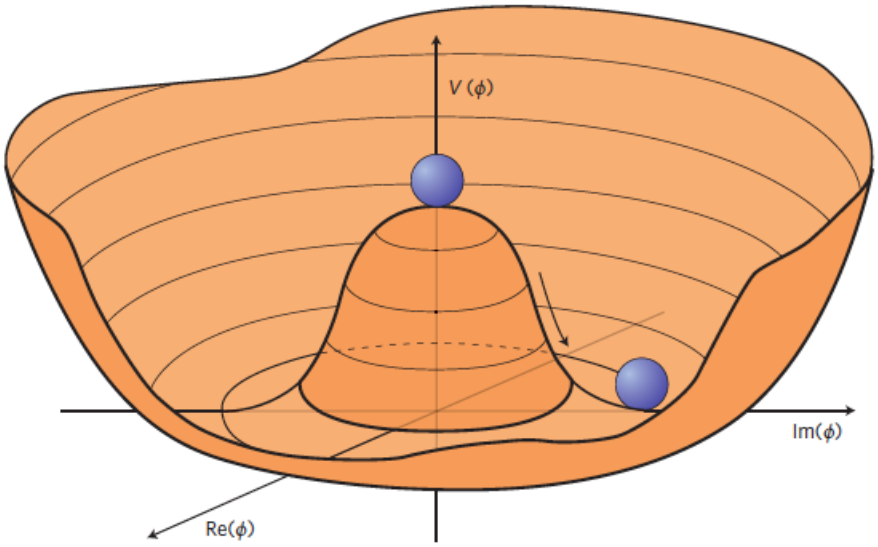

(a) "Mexican hat" potential that leads to spontaneous symmetry breaking. [17]

Figure 2.2

The Weinberg mixing angle θ_W is defined through $\tan\theta_W = \frac{g'}{g}$. It follows that

$$\cos\theta_W = \frac{g}{\sqrt{g'^2+g^2}};\ \sin\theta_W = \frac{g'}{\sqrt{g'^2+g^2}};$$

$$W_{3\mu} = \cos\theta_W Z_\mu + \sin\theta_W A_\mu;$$

$$B_\mu = \cos\theta_W A_\mu - \sin\theta_W Z_\mu.$$

The constant g' describes the strength with which particles couple to B_μ, so the strength of coupling to the photon field A_μ is $g'\cos\theta_W$.

Limitations of the Standard Model

The Standard Model is, overall, a very successful theory. It has been tested and verified by numerous experiments in the last 50 years. However there are many open questions that the SM cannot (or doesn't attempt to) answer. In this section an overview of the limitations of the SM is given to motivate the need for physics beyond the Standard Model (BSM).

- The SM describes the interactions of three fundamental forces at the quantum level. However gravity is not included in the discussion and is only treated classically. This is a valid approach at the relatively low energies that we have access to now, but at the Planck scale ($M_{pl} \approx 10^{19}$ GeV) the quantum effects of gravity are expected to be dominating and the predictions of the SM are no longer valid. There is also a discussion to be had on the possibility to treat general relativity as a quantum field in the framework of quantum field theories, but it is far outside of the scope of this simple overview.

- The SM relies on 19 parameters that are determined experimentally. The theoretical understanding of why there are exactly 19 and what their origin is is lacking. The local gauge symmetry $G_{SM} = SU(3)_C \otimes SU(2)_L \otimes U(1)$ defines many properties of the SM, but the understanding of why looks like it does is lacking.

- The strong CP problem. Processes that only involve the strong interactions seem to preserve CP-symmetry. There are a priori no reasons why that should be the case. Possible solutions to this problem involve introducing a new elementary particle - axion.

- The hierarchy problem. There are two energy scales in the SM that are very far apart. The electroweak scale is of the order of $M_{ew} \approx 10^2$ GeV while the Planck scale is $M_{pl} \approx 10^{19}$ GeV. The fact that the difference between the two scales is large is, by itself, not an issue. More concerning is the fact that the Higgs potential is sensitive to the introduction of new physics to the SM. Such additions would require excessive fine-tuning to keep the Higgs boson mass consistent with the experimentally observed one.

- In the same vein the cosmological constant problem exists. From the QFT we know that vacuum has energy. This energy gravitates and should enter the general relativity field equations as the cosmological constant. However the experimental limits on the cosmological constant and the perturbative computations from QFT give two very different values, varying by $60 - 120$ orders of magnitude depending on choice of parameters. What's worse, the perturbative calculations of the vacuum energy are very sensitive to new physics, they are radiatively instable.

- Dark matter candidates. Experimental results predict that a significant part of the universe consists of the dark matter. However none of the SM particles are good dark matter candidates.

- Neutrino mass terms. Originally the SM predicted massless neutrinos. Neutrino oscillation experiments have shown that neutrinos have mass. The SM has been

modified with neutrino mass terms, but the fundamental understanding is still lacking.

- Baryon asymmetry problem. There is an observed imbalance of matter and anti-matter in the Universe which the SM cannot account for.

All of the above suggests that the SM should be treated as an effective model that is only correct at (relatively) low energies. There are several ways to try and extend and generalise the SM to a more fundamental theory. One could try to add new particles and/or interactions ad hoc. Such approaches lack any physical motivation, but they can fix some of the above-mentioned problems. A more traditional approach is to consider more general symmetries of the theory, be it internal or spacetime symmetries. Attempting to generalise the internal symmetries of the SM generally leads to Grand Unified Theories (GUTs) which suggest that the observed $SU(3)_C \otimes SU(2)_L \otimes U(1)$ symmetries of the SM are a result of an even larger symmetry group.

There are two ways to fiddle with the spacetime symmetry. First one could try to add additional spacetime dimensions so that the symmetries Poincare symmetries can be enhanced. This is generally known as Kaluza-Klein theory. In these scenarios the additional dimensions are in some way "hidden" from current experiments. Alternatively one can try to introduce a symmetry under exchange of fermions and bosons, the supersymmetry. This approach solves the naturalness issue, can be combined with the GUT theories and provides dark matter candidates. The basic ideas of the supersymmetric theories are introduced in the next section.

2.3 Supersymmetry

One of the most popular and well-regarded branches of the BSM physics is Supersymmetry (SUSY). Experimentally speaking SUSY is interesting as it predicts new physics at the scale of few TeV. Such energies are achievable at the LHC and SUSY searches have been one of the main motivations (behind the searches for the Higgs boson) for the LHC design and construction. This section gives an overview of the main ideas behind the SUSY models as well as summarising some of the predictions. The discussion is based mainly on the SUSY primer [18] and lecture notes [19] and is limited to the Minimal Supersymmetric Standard Model (MSSM), the minimal possible extension of the SM to be consistent with the basic premises of SUSY.

The Hierarchy Problem

As mentioned in the previous section the Higgs vacuum expectation value resulting from the potential of the Lagrangian is $v^2 = \frac{\mu^2}{2\lambda}$. Experimentally Higgs VEV has been calculated (using the relationship with the reduced Fermi constant $G_F = \frac{1}{\sqrt{2}v^2}$) to be around 246 GeV. This value is often referred to as the electroweak scale, the typical energy of electroweak processes. The corresponding μ^2 value is $\approx 10^4 \text{GeV}^2$. The basic premise of the hierarchy problem is that $-\mu^2$ receives quantum loop corrections $\Delta\mu^2$ from particles that couple to the Higgs boson. The corrections are of the order of $\approx \frac{1}{16\pi^2}M^2$ for a loop containing a fermion of a mass M. Even if the hypothetical

particle doesn't couple to the Higgs boson directly indirect loop effects can be large. Another thing to keep in mind is that, e.g. Planck mass M_P^2 is 30 orders of magnitude larger than the electroweak scale. The μ^2 parameter is therefore naively expected to be of the order of scale of new physics, be it Grand Unified Theories, String Theories, Planck Scale etc.

It should be noted that the hierarchy problem is not a problem with the consistency of the model - it is in principle possible to introduce cancellation terms for each and every potential high-mass particles. The issue is with the "naturalness" of such approach. The cancellation terms cannot be justified physically and they would need excessive fine-tuning. However it is possible to introduce a symmetry that would "protect" the μ^2 by automatically cancelling the loop contributions $\Delta\mu^2$. Such a symmetry has to relate fermions and bosons because of the relative "$-$" sign in the loop contributions from the two. This symmetry is SUSY. Alternative approaches to solving the Hierarchy problem include composite Higgs theories and large extra dimensions theories.

SUSY Algebra and No-Go Theorem

In 1967 Coleman and Mandula proved that the most general Lie group symmetry that a QFT can have is Poincare $\otimes$ internal symmetries [20]. This is the so called no-go theorem. To get around it and get a supersymmetric Poincare algebra the concept of graded algebra was introduced in 1975 [21]. A graded Lie algebra is a vector space L that is a direct sum of two vector spaces L_0 and L_1 with a binary operation $\cdot$ such that $x_i \cdot x_j \in L_{(i+j)\mathrm{mod}2}$, $x_i \in L_i$ (grading) and $x_i \cdot x_j = -(-1)^{ij} x_j \cdot x_i$.

Generally speaking a supersymmetry operator Q transforms bosons into fermions and fermions into bosons, $Q|\text{fermion}\rangle = |\text{ boson }\rangle$ and $Q|\text{boson}\rangle = |\text{ fermion }\rangle$. Particles of SUSY are grouped into supermultiplets that correspond to the irreducible representations of the theory. Supersymmetry generators commute with the generators of the gauge transformations so the members of the supermultiplets have the same electric charge, weak isospin and colour degrees of freedom.

An important property of supermultiplets is that the number of fermionic and bosonic degrees of freedom has to be equal. The simplest way to construct a supermultiplet is to take a Weyl fermion ($n_F = 2$) and match it with a complex scalar field ($n_B = 2$). These multiplets are called chiral or scalar supermultiplets. Another option is to start with a spin-1 vector boson with two helicity states ($n_B = 2$). The superpartner is then a spin-1/2 Weyl fermion, $n_F = 2$. That makes gauge supermultiplets.

Minimal Particle Content of SUSY

The fundamental particles of the SM belong to either gauge or chiral supermultiplets. Quarks and leptons of the SM fit into the chiral multiplets, their superpartners are named by adding an "s" to the beginning - squarks, sleptons, sfermions etc. The convention is to mark superpartners by the tilde sign ˜. Since left-handed and right-handed quarks and leptons of the SM have different gauge transformations they have to have different superpartners. For example the superpartners of the left-handed and right-handed parts of the muon field are $\tilde{\mu_L}$ and $\tilde{\mu_R}$. Notice that smuons are spin-0 particles here, the "L" and "R" subscripts refer to the handedness of the superpartners. Right-handed neutrinos that are singlets under $SU(3)_C \otimes SU(2)_L \otimes U(1)_Y$ are traditionally

omitted from the discussion of the minimal SUSY.

Spin-1 bosons of the SM belong to the gauge supermultiplets. Their superpartners are spin-1/2 fermions usually referred to as gauginos collectively. There is a colour-octet of spin-1/2 gluinos corresponding to the eight gluons. The three winos and a bino are superpartners of W^+, W^-, W^0, B^0.

The only SM particle left is Higgs boson. As it is a spin-0 boson it belongs to a chiral supermultiplet. The problem is, however, that one Higgs supermultiplet isn't enough to build a successful SUSY theory. In the SM one relies on $H^C = -i(H^\dagger \sigma_2)^T$ to give masses to the up-type quarks. In SUSY however a superpartner of this construct would mix left- and right-handed states. Therefore a second Higgs supermultiplet is needed in a minimal SUSY theory. The convention is to use H_u and H_d that have weak hypercharge ± 1:

$$H_u = \begin{pmatrix} H_u^+ \\ H_u^0 \end{pmatrix}; \quad H_d = \begin{pmatrix} H_d^0 \\ H_d^- \end{pmatrix}.$$

The SM Higgs is a linear combination of H_u^0 and H_d^0. The superpartners of Higgs doublets are fermionic, spin-1/2 higgsinos. This concludes the list of particle needed to construct a minimal working version of SUSY. The particle content is summarised in Tables 2.1 and 2.2.

Table 2.1: SUSY particle content, chiral multiplets

Supermultiplet	spin 0	spin 1/2
Squarks, quarks (3 families	$(\tilde{u_L}, \tilde{d_L})$ $\tilde{u}_R^*$ $\tilde{d}_R^*$	(u_L, d_L) $u_R^\dagger$ $d_R^\dagger$
Sleptons,leptons (3 families)	$(\tilde{\nu}, \tilde{e_L})$ $\tilde{e}_R^*$	(ν, e_L) $e_R^\dagger$
Higgs sector	$(H_u^+ \; H_u^0)$ $(H_d^0 \; H_d^-)$	$(\tilde{H_u^+} \; \tilde{H_u^0})$ $(\tilde{H_d^0} \; \tilde{H_d^-})$

Table 2.2: SUSY particle content, gauge multiplets

Supermultiplet	spin 1/2	spin 1
gluinos,gluons	$\tilde{g}$	g
winos, W-bosons	$\tilde{W^\pm}$, $\tilde{W^0}$	$W^\pm$, W^0
binos, B-boson	$\tilde{B^0}$	B^0

After the electroweak symmetry breaking higgsinos, winos and binos can mix as long as they have the same $U(1)$ charges. $\tilde{H_d^0}$, $\tilde{H_u^0}$, $\tilde{B^0}$ and $\tilde{W^0}$ form four mass eigenstates called neutralinos and denoted as $\tilde{\chi}_i^0$ (or $\tilde{N}_i$ in some references). Similarly the charged higgsinos and $\tilde{W^\pm}$ mix and form charginos with charges ± 1. They are typically denoted as $\tilde{\chi}_i^\pm$ or $\tilde{C}_i^\pm$, $i = 1, 2$.

SUSY Breaking

The most straightforward prediction of SUSY as defined previously would be that the masses of the superpartners are equal to their SM counterparts. Since no SUSY particles have been discovered yet the conclusion that the supersymmetry (if it exists) has to be broken somehow causing the masses of the superpartners to differ. One can try to break the SUSY by requiring that the VEV of the SUSY potential doesn't vanish in the vacuum state. There are two types of mechanisms that could be used to do that in the MSSM - Fayet-Iliopoulos supersymmetry breaking (also known as D-term SUSY breaking) and O'Raifeartaigh (F-term) supersymmetry breaking. Unfortunately neither of the models leads to a satisfactory result.

For Fayet-Iliopoulous in non-abelian theories only $U(1)$ symmetries can drive the spontaneous symmetry breaking. However in the Standard Model (and MSSM) the only such symmetry is $U(1)_Y$ breaking of which leads to breaking of colour or electromagnetism, but not SUSY. If another $U(1)$ gauge symmetry exists it can be broken in that way, but this falls outside the scope of MSSM. The O'Raifeartaigh SUSY breaking mechanism generally predicts a mass spectrum with at least some superpartners lighter than the known Standard Model particles. Since no such particles have been observed the direct breaking of SUSY is not possible in the MSSM.

The convention is to break the SUSY explicitly in the MSSM, that is to ignore the exact mechanism and to just parametrise our ignorance of the exact process of the symmetry breaking by adding terms to the Lagrangian that break the symmetry. One can show that by selecting "soft" terms (i.e. of positive mass-dimension) to break the symmetry the main features of SUSY are preserved.

There are several theories that propose different mechanisms for the SUSY breaking. The general idea is that the breaking occurs in a "hidden sector" of particles that have (almost) no coupling to the "visible sector" of the MSSM. The two sectors however still communicate through some flavour-blind interaction or "messenger sector". In more involved theories the visible and hidden sectors are not fully decoupled, but coupled by higher dimension operators constrained by the Planck scale. However the two main SUSY breaking theories have clear mediator mechanisms. They are gravity-mediated and gauge-mediated SUSY breaking.

The gravity-mediated SUSY breaking suggests that the interactions between the hidden and visible sectors are carried by gravity. Such models are also sometimes known as Planck-scale supersymmetry breaking since gravity becomes relevant around Planck scale. An important subclass of such models is mSUGRA, or minimal Super Gravity, models. mSUGRA models can be parametrised by 4 parameters and fixing a sign, large improvement from > 100 parameters of pure MSSM.

The second type of models describing SUSY breaking are gauge-mediating SUSY breaking or GMSB. In this case normal electroweak and QCD gauge interactions are mediating the SUSY breaking. Some new chiral multiplet that couples to the symmetry breaking terms and is charged under the $SU(3)_C \times SU(2)_L \times U(1)_Y$ acts as the messenger sector providing connection to the MSSM sector. In this case the soft terms that are used to explicitly break the MSSM are coming from loop diagrams involving the messenger particles.

Another interesting possibility is auxiliary fields of supergravity getting a VEV. This effect is always present, but suppressed by loop factors. If for some reason the

tree-level contributions to SUSY breaking are also suppressed these anomaly mediated SUSY breaking can become the dominant contribution.

Simplified Models

Various SUSY models can predict various signatures that can be observed in detector in a proton-proton collision. The issue is that the same signature (if observed) can be attributed to many different models. Furthermore the SUSY models have a large amount of free parameters and the relationship of the parameters to the signature is not straightforward. If a deviation from the Standard Model is observed it is not clear what kind of model describes it best, if no excess is observed what models are then excluded? The simplified model approach [22, 23] suggests simplifying the models used as the baseline for searches. Such models are based on the existing SUSY models, but the number of free parameters is greatly reduced, typically keeping only 2-3 sparticles and only the dominant decay channels. In this kind of a model the few free parameters remaining (e.g. masses of the sparticles) will have a clear effect on the observables and are therefore the ones that should be studied in the first place.

The simplified model approach is just a framework in which an analysis can be performed. Any simplified model result can be reinterpreted in the context of the full SUSY models (or any other extension of the SM). However in practice simplified models are a good stepping stone to perform general searches that are not heavily dependent on a specific model phenomenology and that can serve as a baseline for more complicated theories if an excess is observed.

R-parity

An important concept in the MSSM is the R-parity. The baryon and lepton numbers are not conserved in the supersymmetric theories, to enforce the conservation (that we know is correct from, e.g. stability of protons) an additional symmetry is postulated. It is typically defined as $P_R = (-1)^{3B+L+2s}$ where B is the baryon number, L is the lepton number and s and the spin. All SM particles have the R-parity of $+1$ and superpartners have R-parity of -1. A consequence of postulating the R-parity conservation is that sparticles are expected to be produced in pairs at colliders such as the LHC. Furthermore, the produced sparticles will decay in cascades to the lightest supersymmetric particles (LSP) which is stable. At colliders this will result in events with missing transverse momentum as the LSPs will be escaping the detector.

2.4 Model Analysed in this Thesis

One of the common results in various SUSY theories is that the lightest sbottom ($\tilde{b}_1$) and stop ($\tilde{t}_1$) squarks can have masses significantly lower than other squarks. If the masses are sufficiently low they could be produced in collisions at colliders. In some scenarios final states with the SM Higgs boson are preferred. The thesis focuses on searches of sbottom decaying via $\tilde{b}_1 \to b\tilde{\chi}_2^0 \to bh\tilde{\chi}_1^0$ where $\tilde{\chi}_i^0$ are neutralinos with $\tilde{\chi}_1^0$ being the lightest one. The search is interpreted in the framework of simplified models following earlier searches at ATLAS [3].

This analysis targets a simplified model of sbottom pair production where $BR(\tilde{b} \to b\tilde{\chi}_2^0) = 100\%$, and $BR(\tilde{\chi}_2^0 \to \tilde{\chi}_1^0 h) = 100\%$. The simplified model, illustrated in Figure 2.3, is representative of MSSM scenarios where $\tilde{\chi}_2^0$ is a wino-higgsino mixture and the $\tilde{\chi}_1^0$ LSP is bino-like. It is further assumed that h is a Standard-Model-like Higgs boson with $BR(h \to b\bar{b}) = 57.7\%$ and $BR(h \to \tau^+\tau^-) = 6.32\%$.

The free parameters of the model are $m_{\tilde{b}}$ and $m_{\tilde{\chi}_2^0}$ with $\Delta m(\tilde{\chi}_2^0, \tilde{\chi}_1^0)$ fixed to 130 GeV; in this configuration, the Higgs boson is produced on-shell, but gets no extra boost from the mass difference between $\tilde{\chi}_2^0$ and $\tilde{\chi}_1^0$.

The previous searches [3, 24] are able to probe a large region of the parameter space, as shown in Figure 2.3, but have limited sensitivity in the region $m_{\tilde{\chi}_1^0} \simeq 0$ (i.e. $m_{\tilde{\chi}_2^0} \simeq$ 130 GeV). In this thesis a search focusing on final states with hadronically decaying tau leptons that is sensitive in the $m_{\tilde{\chi}_1^0} \simeq 0$ region is presented.

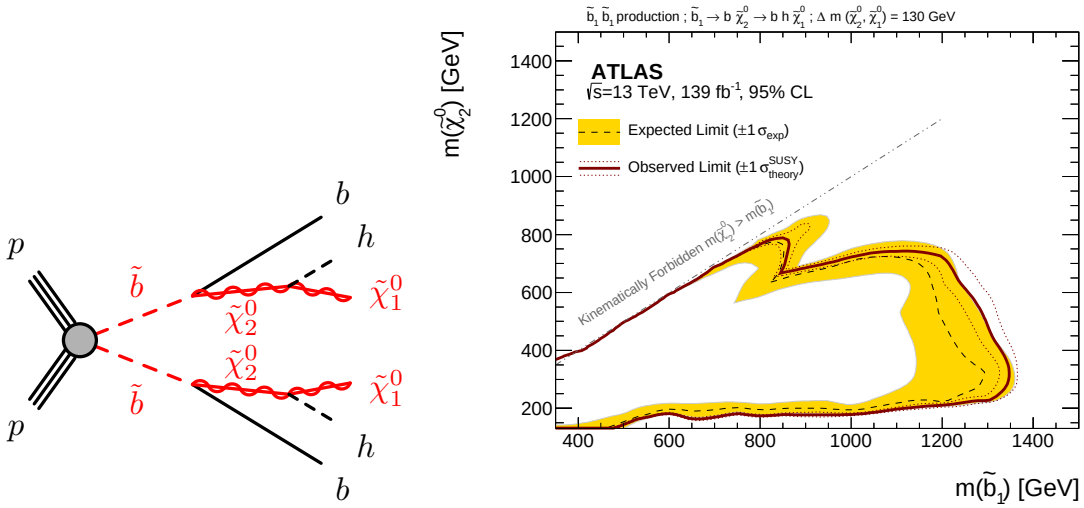

(a) (b)

Figure 2.3: (a) Simplified model of sbottom pair production, and (b) Run-2 limits obtained by the previous searches [3].

Chapter 3

Detector

The data used for the analysis is collected by the the ATLAS (A Toroidal LHC ApparatuS) experiment at the Large Hadron Collider (LHC), built and operated by the European Organization for Nuclear Research (CERN). This chapter describes the design, basic functionality and principles of ATLAS and LHC. The discussion is primarily based on the overview of the ATLAS detector and it's expected performance [25] as well as on the technical reports of the individual components of the detector.

3.1 CERN

CERN is a European research organisation founded in 1954 operating a particle physics laboratory located northwest of Geneva. The laboratory itself is often referred by the same name. CERN is home to many various particle physics experiments the largest of which is the LHC.

3.2 LHC

The LHC is, at the moment of writing, worlds largest and most powerful particle accelerator and collider [26]. It is built in a 26.7 km tunnel that was previously used for the Large Electron-Positron Collider (LEP) machine. The tunnel is situated 50 m to 175 m below the ground and consists of eight straight (545 m long) and eight arced (2.45 km long) sections forming an approximately circular shape. Additionally two 2.5 km tunnels connect the LHC to the accelerators at CERN serving as injectors. The tunnel's diameter reaches 3.7 m and houses 2 particle rings surrounded by magnets used to control and steer the particle beams inside the rings. Due to the space limitations it is almost impossible to treat the rings separately and instead a "two-in-one" approach is used. LHC uses twin-bore magnets that consists of two sets of coils and beam channels in the same mechanical and cooling structure, also see Figure 3.1. The disadvantage of such design is the reduced flexibility of the overall setup with the particle rings being magnetically coupled.

The final design consists of 1232 main dipole magnets bending the beams and 392 main quadrupole magnets focusing the beams with a number of auxiliary insertion quadrupoles magnets [28]. The main dipoles are providing the central field of 8.33 T operating at the nominal 11600 A current while the main quadrupoles reach 7.5 T.

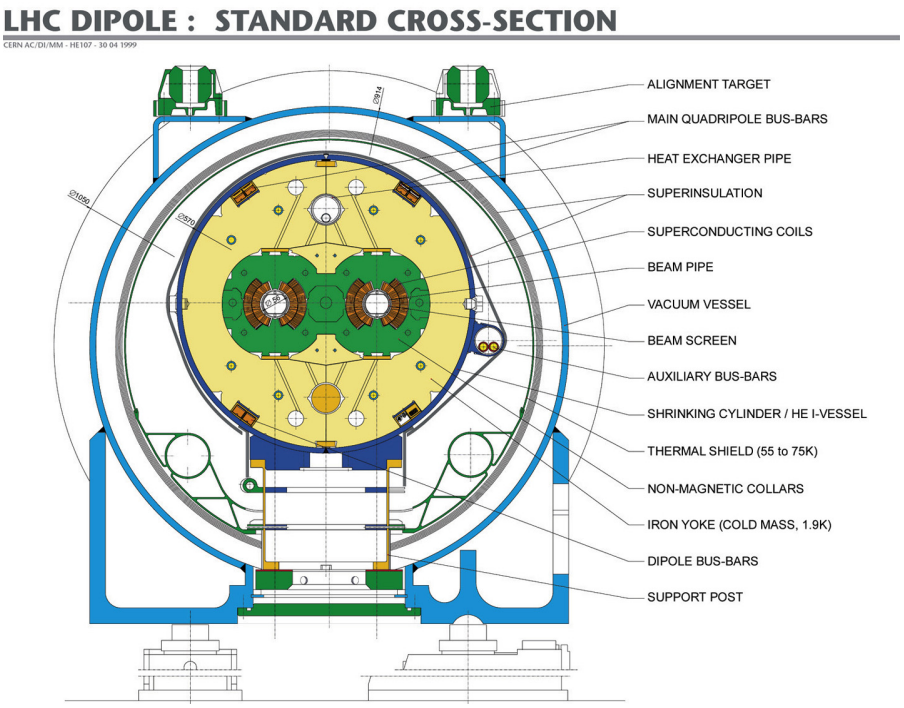

(a) Cross section of the LHC dipole. [27]

Figure 3.1

In order to reach such field strengths LHC relies on superconducting magnets. The magnet system is submerged in superfluid Helium to cool it down to 1.9 K.

In a particle-particle collider the two particle beams intersect at Interaction Points (IP). By design LHC has eight potential IPs in the straight segments of the tunnel. Four of them are used by the four main LHC experiments - ATLAS [25], CMS [29], ALICE [30] and LHCb [31], at the other four IPs the beam crossing is suppressed to prevent beam disruptions. The two beams are sharing common pipes of 126-140 m length at the IPs.

The LHC is primarily designed to collide two beams of protons with centre-of-mass energies up to 14 TeV with the target peak luminosity 10^{34} cm^{-2} s^{-1}. The beams are not continuous with protons grouped in bunches with up to 2808 bunches per proton beam. The nominal bunch spacing is 25 ns (or, equivalently, around 7.5 m). Alternatively LHC can accelerate and collide heavier objects like lead nuclei in which case the target luminosity is 10^{27}cm^{-2} s^{-1}.

The LHC has seen the first particle collision in 2009 and the first data-taking period began in 2010 with the centre-of-mass proton beam energy of 7 TeV. Later the beam energy has been raised to 4 TeV per beam. The first data-taking period (also known as Run 1) concluded late 2012 and the LHC was shut down for 2 years of upgrades. In early 2015 the second data-taking period (Run 2) started, this time with 13 TeV centre-of-mass energy. The data-taking was concluded in December 2018. The third data-taking period (Run 3) is planned to start at the beginning of 2021 and will last until the end of 2024 reaching the 14 TeV centre-of-mass beam energy. After another upgrade LHC is supposed to enter a new regime, High-Luminosity LHC.

One of the challenges of the LHC is production and acceleration of a large number of high intensity proton bunches at specific intervals. The whole accelerator complex is

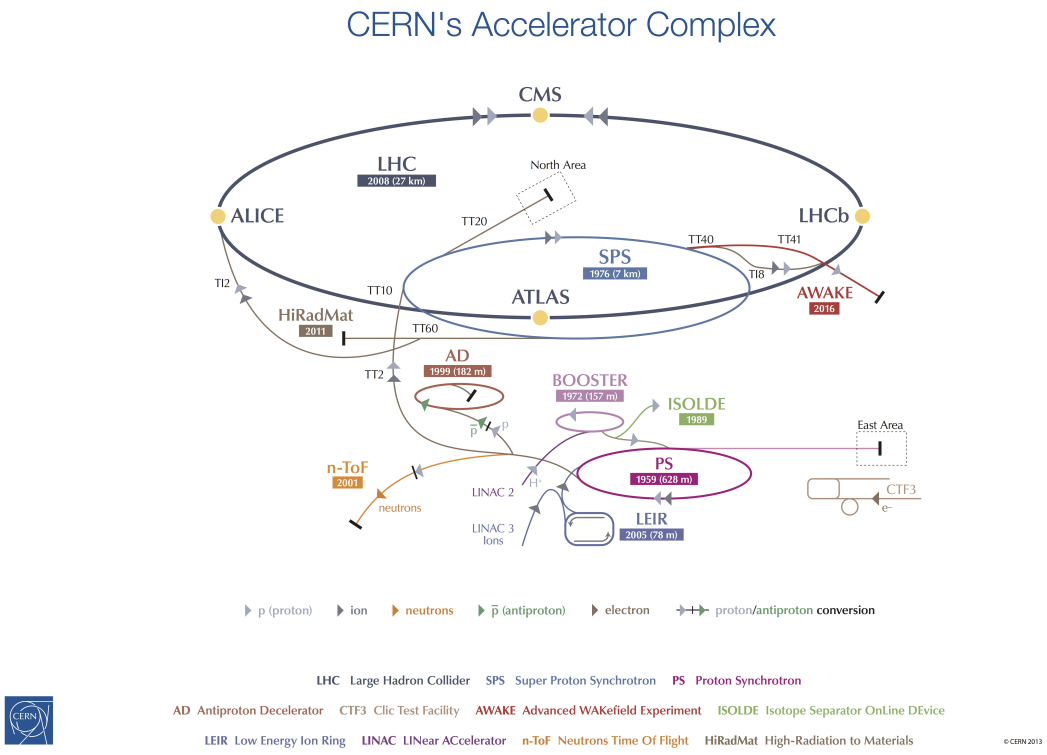

(a) The structure of CERN's accelerator complex. [32]

Figure 3.2

illustrated in Figure 3.2. The LHC itself is only the last step of a chain of accelerators know collectively as the accelerator complex. The protons are produced by stripping away electrons from the hydrogen gas with an electric field. They are then sent to a linear accelerator, Linac2 that accelerates the protons to 50 MeV. The next step is Proton Synchrotron Booster (PSB) that further accelerates protons to the energy of 1.4 GeV. Next the protons are injected in the Proton Synchrotron (PS) where the bunches with the desired bunch spacing (25 ns) is achieved and the proton bunches are accelerated to 25 GeV. Finally the protons are sent to the Super Proton Synchrotron (SPS) that further accelerates them and shapes the beam to be injected in the LHC proper. After that the two LHC rings are filled with protons that reach the nominal 6.5 TeV energy after approximately 20 minutes. Alternatively Linac3 and Low Energy Ion Ring (LEIR) are used to accelerate lead ions that then follow through the same stages as the protons.

An important concept to mention when talking about LHC and data-taking is pile-up. Every time two proton bunches collide at LHC there is on average more than just one proton-proton interactions occurring. To a good approximation the collision of two proton bunches is instantaneous so the detector observes the result of several collisions at the same time. This is known as pile-up. The number of interactions per crossing is denoted μ while the time averaged pile-up (usually called mean) is $< \mu >$. Figure 3.3 summarises the observed pile-up during 2015-2018 data-taking.

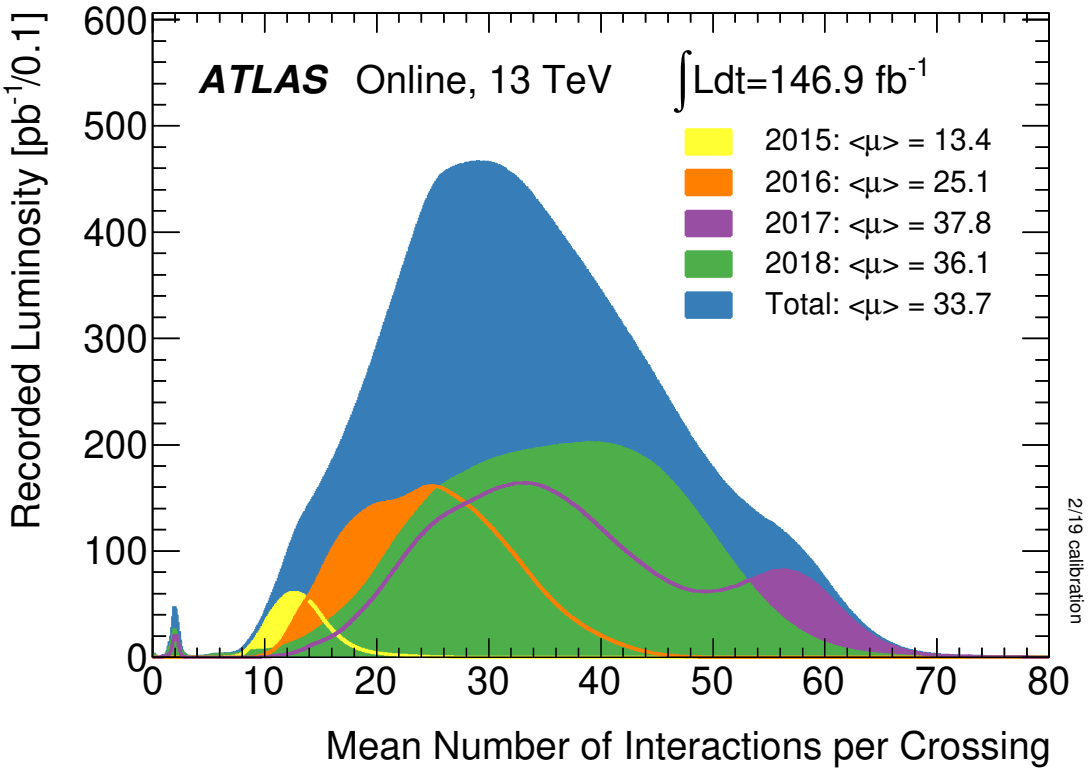

(a) Mean number of interactions per crossing for the full Run 2 dataset. [33]

Figure 3.3

3.3 ATLAS Detector

ATLAS is a general-purpose particle detector at the LHC. It is shaped like a cylinder to have as close to the full 4π coverage of the particles produced as possible. The ATLAS detector has the length of 46 m, 25 m in height and weights over 7000 tonnes. It is situated in a cavern 100 m below the ground around one of the LHC's IPs. The detector itself consists of several concentric layers with the beam pipe in the middle, see Figure 3.4. The four major subsystems of ATLAS are:

- Inner Detector
- Calorimeters
- Magnet System
- Muon Detectors

3.3.1 Coordinates

The coordinate system used at the ATLAS experiment (and many other particle detectors) have the nominal interaction point as the origin of the coordinate system. The z-axis is aligned with the beam pipe while the x-y plane (also called the transverse plane in the context of ATLAS) is perpendicular to the beam. The positive x-direction

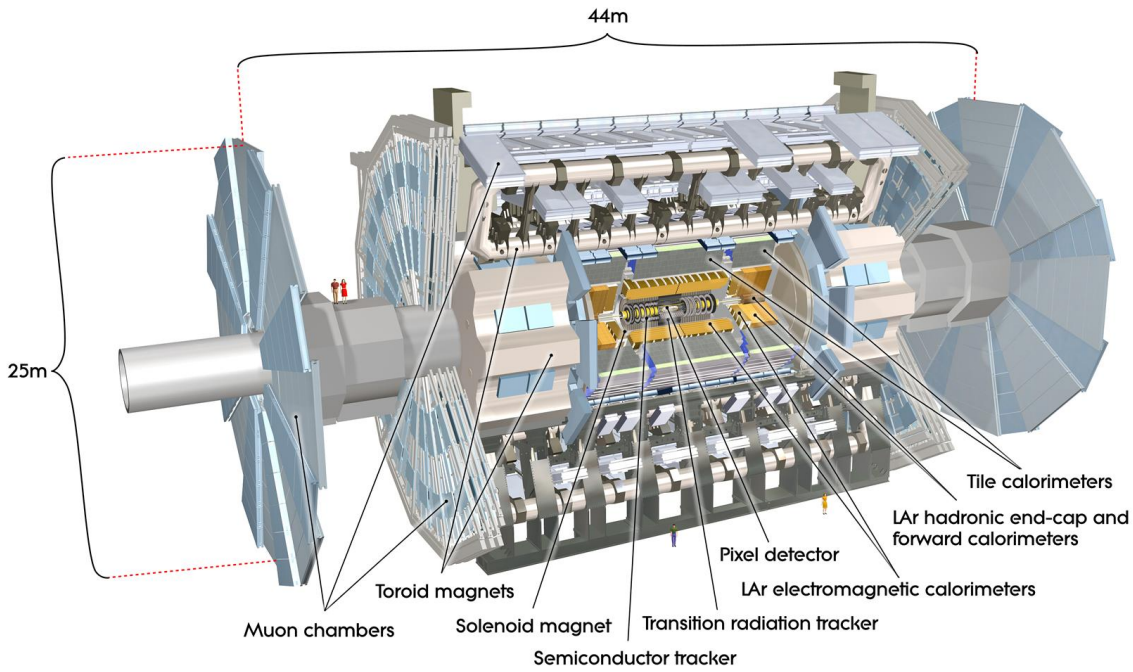

(a) The main subsystems of the ATLAS detector. [34]

Figure 3.4

is defined to be towards the centre of the LHC ring parallel to the surface and the positive y-direction is defined to be upwards. The positive-z side is called side A and the negative-z side is side C.

In the context of a particle detector the momentum vector (p_x, p_y, p_z) of the particles is usually more interesting. Considering the cylindrical shape of the detector a variation of cylindrical coordinates is used. The three variables describing a particle in the detector are amplitude of the transverse momentum $\mathbf{p_T} = (p_x, p_y)$, the azimuthal angle ϕ measured in the plane transverse to the beam and pseudorapidity $\eta = -\ln\tan(\theta/2)$ where θ is the polar angle measured from the beam axis. For massive objects rapidity $y = -\frac{1}{2}\ln[(E+p_z)/(E-p_z)]$ is used instead.

3.3.2 Inner Detector

Closest to the beam pipe is the Inner Detector (ID). It's purpose is to accurately measure trajectories of charged particles (to track them) leading to accurate measurements of the momentum and primary and secondary vertices. The ID is designed to provide coverage for charged tracks with pseudorapidity $|\eta| < 2.5$ with p_T as low as 0.5 GeV. Additionally the ID serves to provide electron identification in the range of $|\eta| < 2.0$. Last, but not least, it is designed to perform at the high luminosity and high pile-up expected at LHC. The ID consists of three different independent detectors that act complimentary to each other - the Pixel Detector (PD), the Semi-Conductor Tracker (SCT) and the Transition Radiation Tracker (TRT), see Figures 3.5 and 3.6. Surrounding the ID is the 2T central solenoid magnet that will be further described in Section 3.3.5.

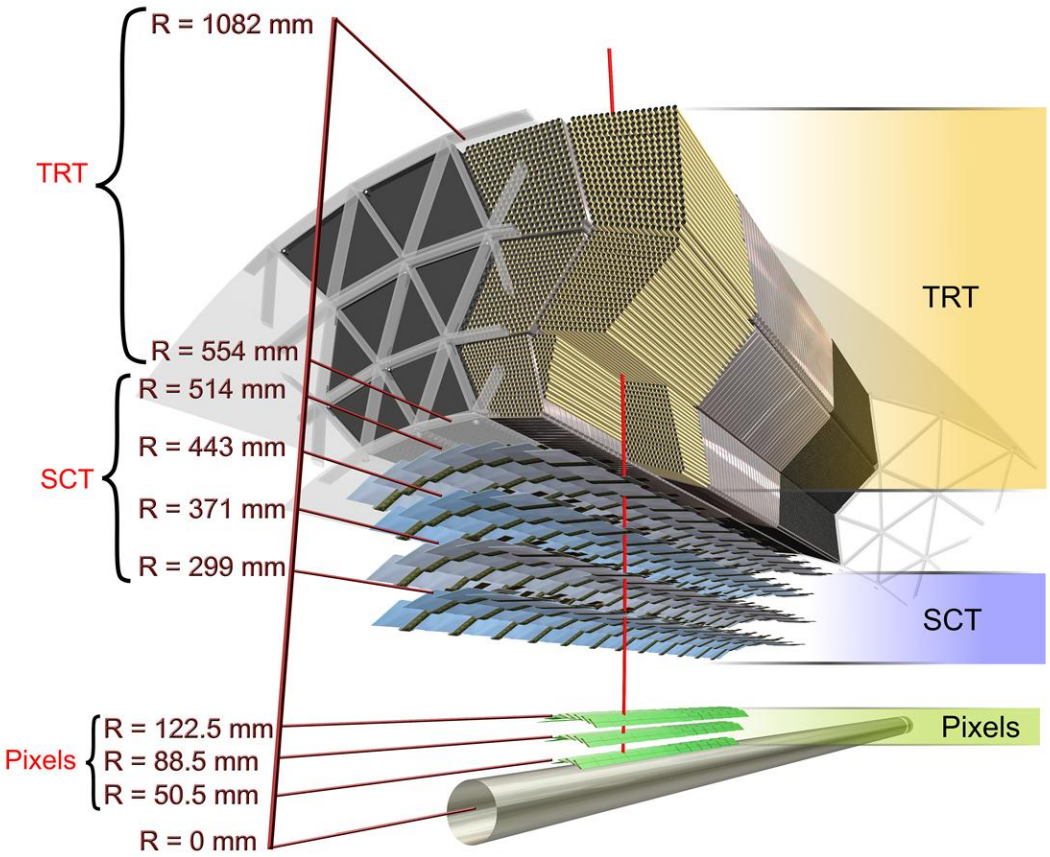

(a) Cross section of the Inner Detector at the ATLAS experiment. [35]

Figure 3.5

Pixel Detector Closest to the beam pipe lies the Pixel Detector (PD). It consists of 3 layers of pixel modules with three discs on each end, 1744 sensors in total. Each sensor (19×63 mm^2, 250μm thick) contains 47232 pixels with 46080 readout channels. The modules in the layers are arranged in staves, with 13 modules per stave while in the end-cap disks they are arranged in sectors with 6 modules in each. The staves are placed parallel to the beam and are slightly overlapping and rotated in the ϕ plane to provide full azimuthal coverage. The layers are made of 22, 38 and 52 staves respectively. The sectors in the wheels are arranged like petals with 8 sectors per wheel. In total that amounts to more than 80 million pixels. The PD achieves hit spatial resolution of 10μm in the $\phi - r$ plane and 115μm in the z plane.

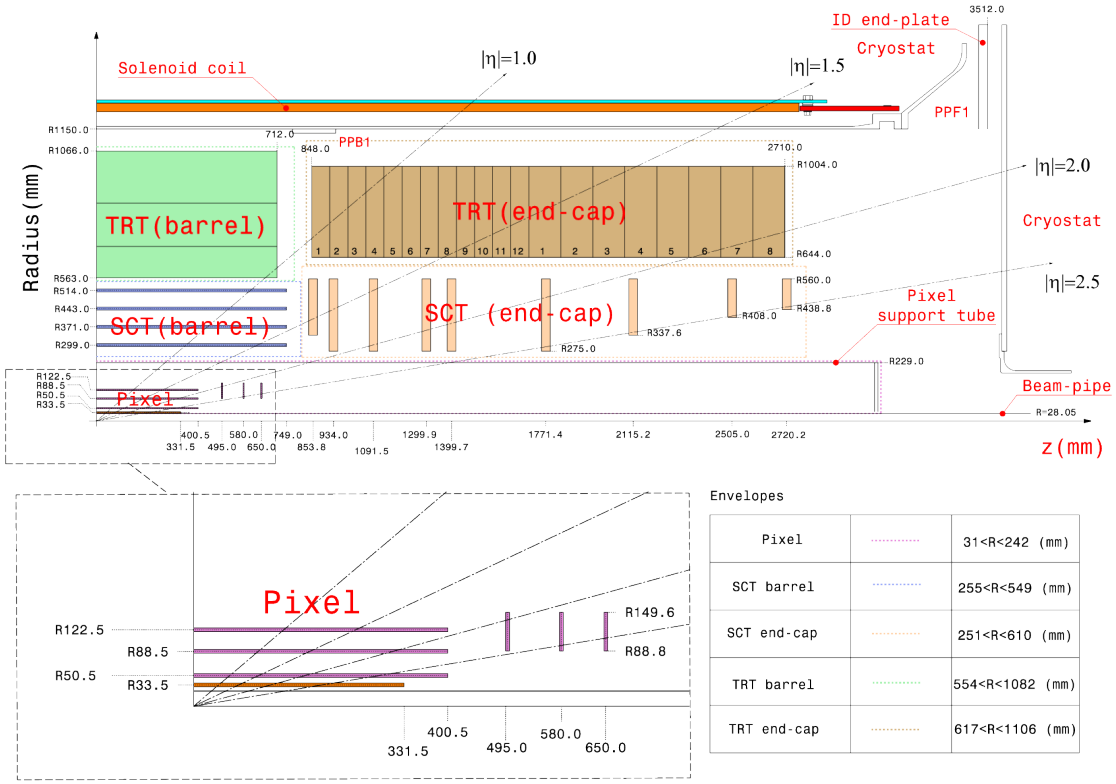

(a) Side view diagram of the Inner Detector at the ATLAS experiment. [36]

Figure 3.6

During the shutdown after Run 1 (2013-2014) another layer was added to the PD, the Insertable B-Layer (IBL) [37]. It is the innermost layer (3.3 cm radius) that was designed to help with high-precision tracking during the higher energy and high-radiation Run 2. To fit the IBL in the original beam pipe has been replaced by a smaller one. The technology used for the IBL has been upgraded too - it was the first large scale application of 3D pixel sensors alongside usual planar sensors. Due to the proximity to the beam and higher expected radiation new readout chips were developed, FE-I4 that are more robust to radiation damage. The IBL consists of 14 staves, slightly overlapping to ensure full coverage. The hit spatial resolution of IBL is measured to be 10μm in the transverse, $\phi - r$, plane and 66.5μm in the longitudinal, z, plane [38].

Semi-Conductor Tracker Surrounding the PD is the Semi-Conductor Tracker [39]. It consists of 4 concentric barrels and two endcaps with 9 disks in each. Unlike the PD the SCT uses long silicon strips instead of pixels. This allows to reduce the required number of output channels and to cover a larger area at reasonable costs. The sensors have dimensions of 6.4×6.3 cm^2 and are 285μm thick. In the SCT the sensors are arranged in modules in the barrels with two sensors connected together to form a 12.8 cm strip with two more sensors glued back-to-back at an angle of 40 mrad. In total there are 4088 modules used, 2112 in the four barrels and 988 modules per endcap. This design provides eight strip measurement for most particles originating at the IP. Similarly to the PD case the modules in the barrels are slightly overlapping and rotated to provide full azimuthal coverage. The endcap disks are made of up to three rings of trapezoidal sensors with the inner ring consisting of two sensors and the middle and outer rings of four sensors each. The SCT provides the resolution of 17μm in the $\phi - r$ plane and 580μm in the z plane.

Transition Radiation Tracker The outer part of the ID is the Transition Radiation Detector. It consists of polyimide drift straw tubes, 4 mm in diameter, with a 0.03 mm gold-plated tungsten wire in the middle. The tubes are filled with a xenon-based mixture of gases. The tubes are 144 cm long in the barrel and 37 cm in the end-caps. The barrel consists of 73 layers of tubes and the end-caps have 160 layers each. The charged particles (with $|\eta| < 2.0$) are expected to fire at least 36 straws with the exception of the barrel-end-cap zone ($0.8 < |\eta| < 1.0$) where the particle is expected to pass at least 22 straws. The TRT provides resolution of approximately 130 μm.

The TRT electronics have two adjustable discrimination thresholds. There are used for particle identification, in particular to separate pions from electrons [40]. The idea is that the transition radiation is proportional to the Lorentz factor γ so there is a difference in the transition radiation produced by electrons and pions of the same momentum. A threshold is selected and the fraction of high threshold hits to low threshold hits is used to discriminate electrons from pions.

3.3.3 Calorimeters

After the ID and the central solenoid magnet the next layer of ATLAS is composed of calorimeters. Their purpose is to absorb (most of) the particles coming from the collisions at the IP while accurately measuring the energy deposited. First the particles pass through the electromagnetic calorimeter that stops most of photons and electrons, then through the hadronic calorimeter that absorbs hadrons. The only particles that are expected to go through the calorimeters are neutrinos and sufficiently high energy muons.

The ATLAS calorimeter system is composed of two different types of calorimeters - the Liquid Argon (LAr) Calorimeter and the Tile Hadronic Calorimeter. The LAr includes the electromagnetic calorimeter in the barrel, the electromagnetic and hadronic calorimeters in the end-caps and the forward calorimeter designed to capture particles at large η. The tile calorimeter is used as the hadronic calorimeter in the barrel. The calorimeters allow a coverage of $|\eta| < 4.9$ and full a ϕ coverage. The overall structure of the calorimeters is presented in Figure 3.7.

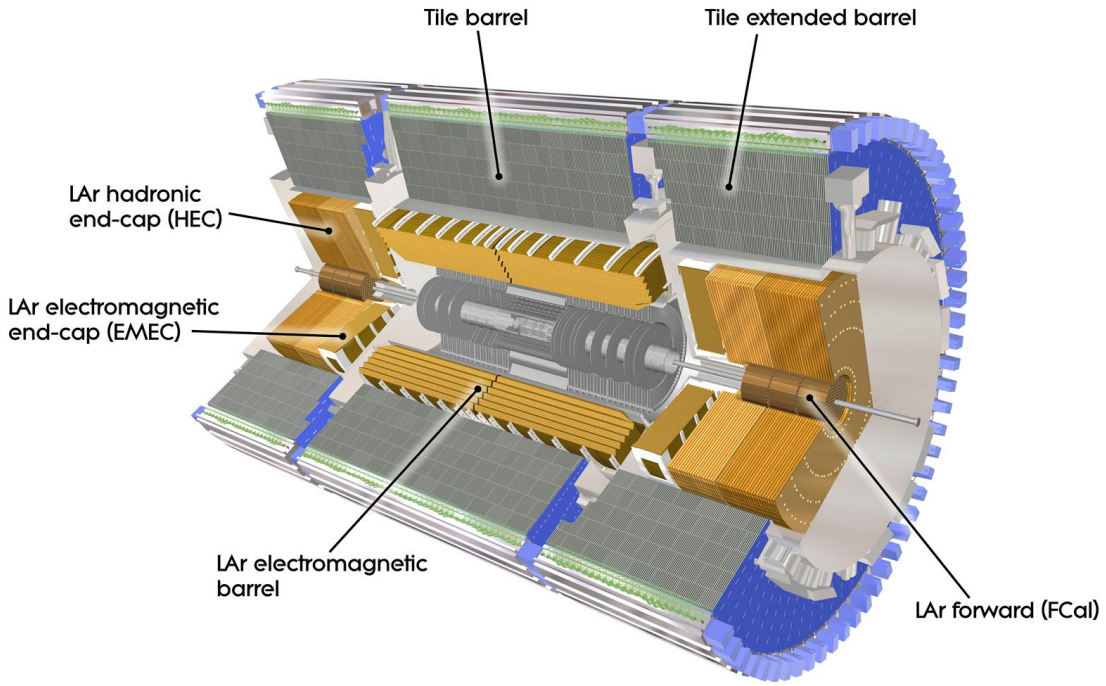

(a) The calorimeter system consisting of the Liquid Argon Calorimeter and the Tile Hadronic Calorimeter at the ATLAS experiment. [41]

Figure 3.7

Electromagnetic Calorimeters The EM calorimeter consists of the barrel (covering $|\eta| < 1.475$) and two end-cap components. Each of the end-cap calorimeters is further divided - outer ring covering the region $1.375 < |\eta| < 2.5$ and the inner ring covering the $2.5 < |\eta| < 3.2$ region. Finally the Forward Calorimeter provides the coverage in the $3.1 < |\eta| < 4.9$ region. The EM calorimeters are sampling calorimeters using liquid argon as the active detector medium with lead absorbers. Additionally the calorimeter is complimented by a liquid argon presampler detector that provides a measurement of the energy lost before reaching the calorimeter. Both the barrel and the end-cap calorimeters consist of three layers.

Hadronic Calorimeters The ATLAS hadronic calorimeters consist of the tile calorimeter at the barrel, the liquid-argon hadronic calorimeters at the end-caps and liquid-argon forward calorimeter. The tile calorimeter uses scintillator as the active medium and steel as the absorber. It is built around the EM calorimeter and has the coverage of $|\eta| < 1.7$. It is made of 64 modules each covering 5.625° in azimuth. The end-cap calorimeters use liquid argon as the active medium with copper serving as the absorber. It provides the coverage in the $1.5 < |\eta| < 3.2$ region. Finally the forward calorimeter uses liquid argon as the active medium with two modules using tungsten as the absorber and the third module using copper. It provides the coverage over $3.1 < |\eta| < 4.9$ region.

3.3.4 Muon Detectors

The Muon Spectrometer is the outer part of ATLAS. The calorimeters (see Section 3.3.3) are designed to stop photons, electrons and hadrons coming from the collisions at the centre of the detector. The only particles that escape it are neutrinos (that are not detectable by ATLAS) and muons. The muon spectrometer is designed to detect and accurately measure the momentum of charged particles that escape the barrel with the coverage of $|\eta| < 2.7$. Additionally the muon system was designed with the ability to trigger on muon tracks (in the $|\eta| < 2.4$ region) in mind. The ATLAS muon system consists of the following elements - Thin Gap Chambers (TGC), Resistive Plate Chambers (RPC), Monitored Drift Tubes (MDT) and Cathode Strip Chambers (CSC).

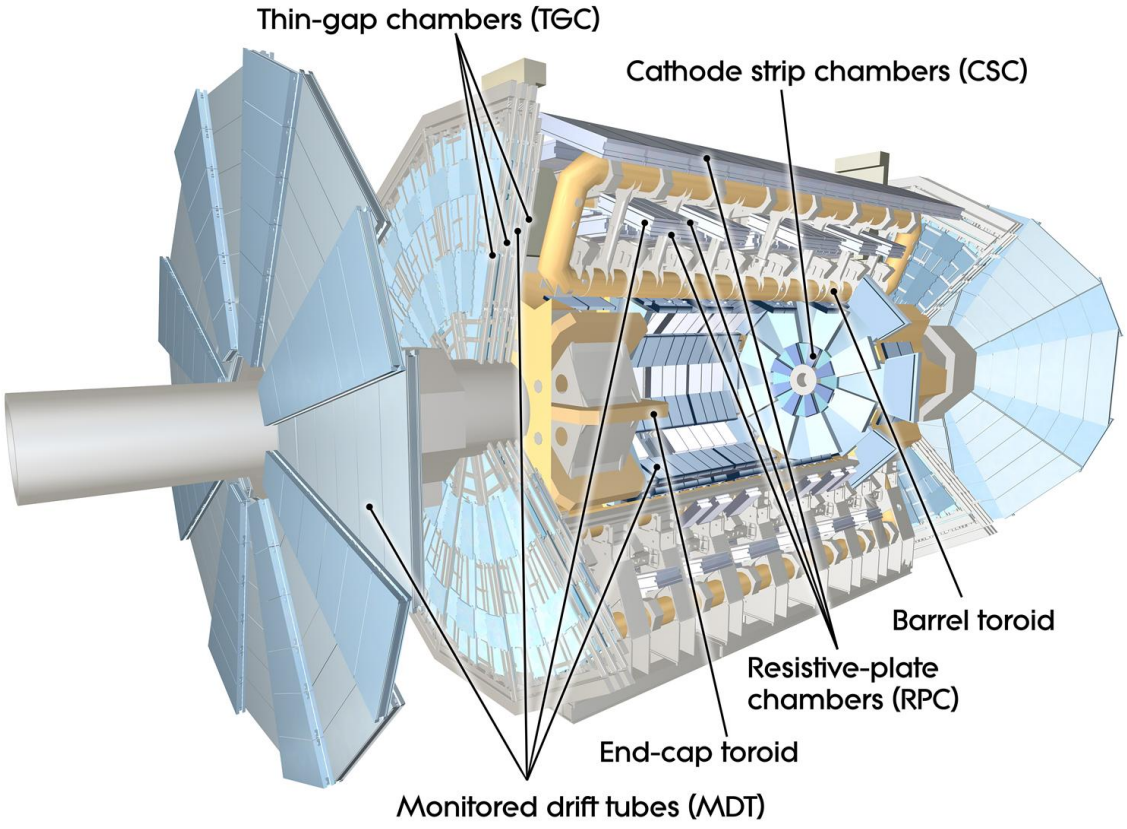

(a) Muon system at the ATLAS experimenent. [42]

Figure 3.8

The muon detectors are arranged in three cylinders surrounding the beam pipe with radii of roughly 5m, 7.5m and 10m. Each layer consists of eight large and eight small chambers. At the end-caps the detectors are arranged in 4 wheels located approximately 7.4m, 10.8m, 14m and 21.5m from the IP. The majority of the momentum measurements are performed by the MDT chambers. They provide the coverage in the range of $|\eta| < 2.7$ everywhere except the innermost end-cap wheel where the expected muon rates are exceeding the MDT counting rate. Therefore the $2 < |\eta| < 2.7$ region of the end-caps closest to the IP are covered by the CSC instead.

The MDTs chambers are made of three to eight layers of drift tubes (29.97 mm diameter, $0.85 - 6.5$m long) filled with argon-based gas mixture at three bar. At the

middle of the tubes are 50μm tungsten-rhenium wires. The MDT provides a resolution of 35μm. The CSCs on the other hand are multi-wire chambers. They are arranged in two disks consisting of eight large and eight small chambers, each chamber containing 4 CSC planes. The advantages of using CSCs are good two-track resolutions and low electron drift times resulting in low timing resolution. The resolution of CSC heavily depends on the signal-to-noise ratio, with RMS value of 40μm. There are, in total, 1171 MDT chambers with 354240 tubes and 32 CSC chambers with 31000 output channels. MDTs and CSCs together are responsible for the precision tracking performed by the MS.

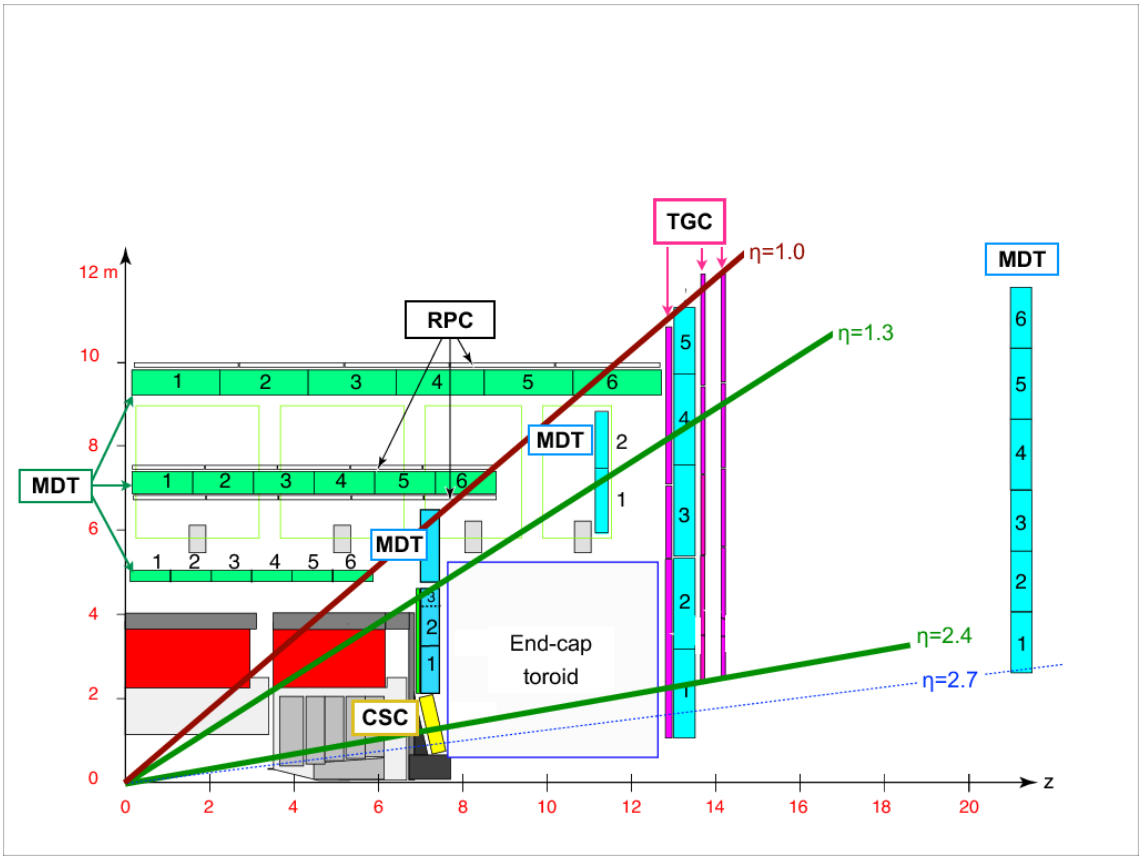

(a) Side view diagram of the muon system at the ATLAS experiment. [43]

Figure 3.9

Besides the tracking the MS is responsible for triggering on muon tracks. In the barrel ($|\eta| < 1.05$) the RPCs are used and in the end-caps ($1.05 < |\eta| < 2.4$) Thin Gap Chambers are employed. The main requirements of the muon trigger system are ability to trigger on muon p_T thresholds, providing bunch-crossing identification and measuring muon coordinates in the direction orthogonal to that measured by the tracking system. Due to the expected difference in the muon p_T in the barrel and the end-cap regions the latter require higher granularity. Another issue is higher radiation at the end-caps (expected factor of 10). The RPCs in the barrel are used due to having good time resolution, rate capability and relatively simple structure. There are three layers of RPCs in the barrel, two sandwiching the middle MDT layer and the third outside of the outermost MDT layer. The TGCs operate similarly to the multi-wire chambers and provide sufficient time resolution and high rate capability. They are arranged in four

planes in each end-cap, with the first being in front of the innermost tracking layer and the other three surrounding the second MDT wheel.

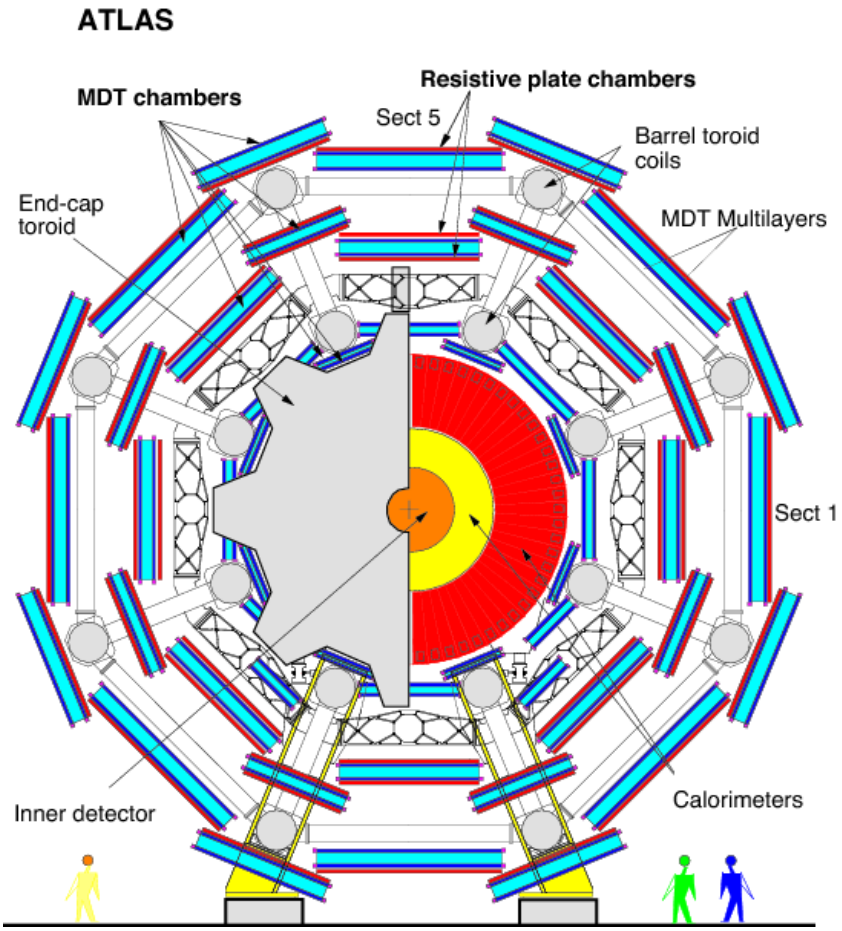

(a) Cross section diagram of the whole ATLAS detector including the muon system. [44]

Figure 3.10

It is important to mention that while the tracking and the trigger systems are described separately they are both essential and inseparable parts of the MS. MDT and trigger chambers hits are matched together to provide accurate tracking information about the muons.

3.3.5 Magnet System

A typical way to measure the transverse momentum of charged particles (travelling at velocities close to speed of light) is to bend their trajectories with a constant magnetic field and to measure the curvature. There are four large superconducting magnets employed by the ATLAS that bends trajectories of the particles passing through various parts of the detector. The innermost part of the magnet system is the Central Solenoid Magnet (CSM). It surrounds the Inner Detector and provides a 2T axial field. The diameter of the solenoid is 2.56 m and the axial length is 5.8m. An important challenge to solve was the optimisation of the LAr calorimeter which resulted, among other things, in the magnet sharing the vacuum vessel with the calorimeter.

Aside from the solenoid magnet the ATLAS has three toroid magnet systems - one in the barrel and two at the end-caps. The barrel magnet system is in total 25.3 and the inner and outer diameters of 9.4 m and 20.1 m and consists of eight coils. It produces toroidal magnetic field up to 4 T. Two more toroids provide magnetic fields up to 4 T at the end-caps to optimise the bending power for the trajectories of muons. They are 5 m long with the inner and outer diameters of 1.65 m and 10.7 m with eight coils each.

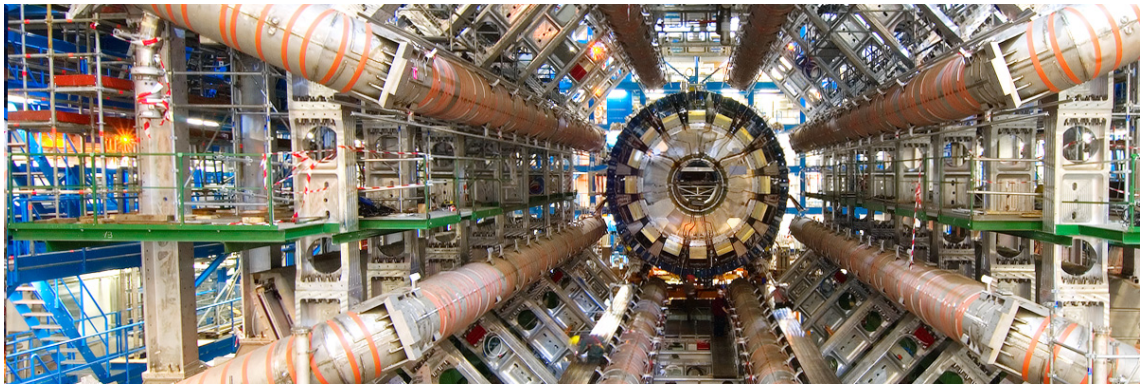

(a) The magnet system at the ATLAS detector. [45]

Figure 3.11

3.3.6 Data Taking and Trigger Systems

As described in Section 3.2 ATLAS is designed to observe a collision of two proton bunches every 25 ns. Furthermore the expected number of interactions per bunch-crossing is significantly larger than one. During Run 2 the average pile-up rate was around 40. This results in approximately 1.6×10^9 proton-proton collisions per second. Storing and processing such incredibly large amounts of information is impossible due to technical limitations. However not every proton-proton collision is interesting from physics point of view. The trigger system is designed to provide instantaneous decision on whether the observed event is worth reconstructing and storing or if it should be discarded.

The ATLAS trigger system is divided in two stages - the hardware-based Level-1 triggers (L1) and the software-based High-Level Trigger (HLT) which is essentially a CPU farm. The L1 triggers select event based on the very coarse on-the-fly computations of the missing and total transverse energies as well as observations of the high transverse-momentum muons, electrons, photons, jets and hadronically decaying taus. The L1 trigger system is expected to make the decision in less than 2.5 μs so only a very limited amount of information can be used (e.g. the transverse momentum of muons is not used in the computation of the transverse energies as that information isn't available in time). Additionally the L1 triggers define Regions of Interest (RoI), the η and ϕ coordinates of the regions of the detector where the interesting features have been observed.

A feature of the L1 triggers is the possibility to pre-scale meaning that only 1 out of x events that otherwise pass the selection are recorded. This is useful for sampling commonly occurring processes without completely killing the available bandwidth. All the triggers are gathered in a so-called trigger menu. Understanding what type of events

are interesting and what typical signatures they produce is an important part of the analysis design. The L1 trigger system reduces the rate of events to at most 100 kHz before sending the events to the HLT.

After an event passed the L1 selection the HLT system takes over. If needed the HLT can perform reconstruction of the whole event (with the various sub-detectors readout available on demand), but usually it is limited to the RoI identified by the L1 [46]. The HLT can also perform more nuanced selection like b-tagging of jets. HLT selects around 1000 events per second that are fully recorded and sent to the data storage. An example of HLT trigger rates in a fill taken in September 2018 with peak luminosity of $L = 2 \times 10^{34}\text{cm}^{-2}\ \text{s}^{-1}$ is shown in Figure 3.12. The increase in rates are due to change of prescales used for optimisation of bandwidth, dips are caused by dead-time and spikes by detector noise.

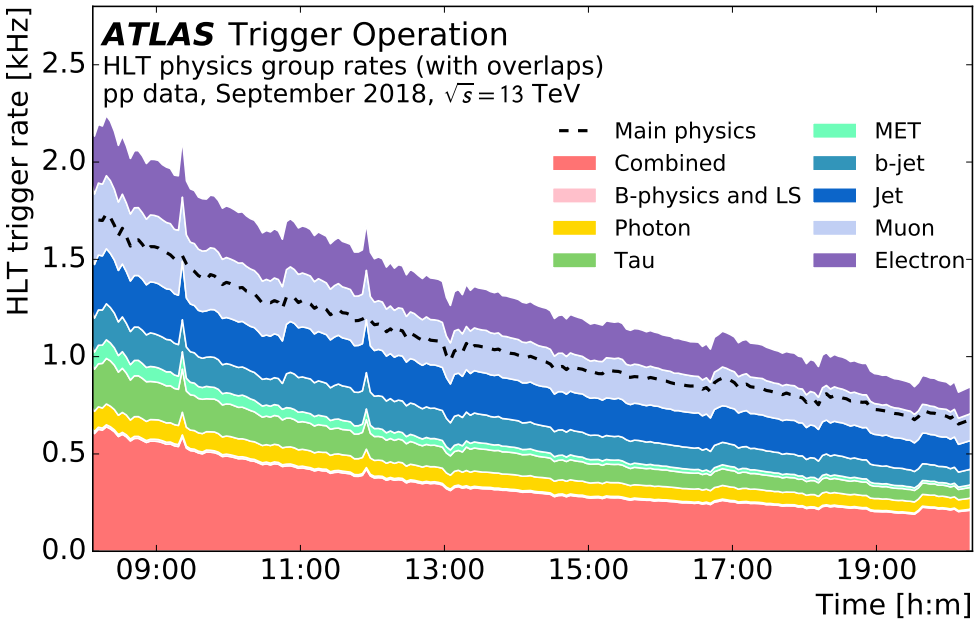

(a) Example of trigger rates at the ATLAS detector in September 2018. [47]

Figure 3.12

3.3.7 Real and Simulated Data

An important aspect of the ATLAS experiment is (Monte Carlo) simulated data. These are events that have not been recorded by the ATLAS detector, but are predicted using theoretical models. The simulation process is complex and involves several steps:

- Event generation where proton-proton collisions and subsequent decays of various particles are emulated. This step is discussed further in Section 4.3.
- Detector simulation where the response of the ATLAS detector to the various particles created during event generation is estimated. The entire ATLAS detector is emulated using Geant4 [48] software and the interaction of every particle in the event with the detector is simulated. Computationally this is the "heaviest" step.

- The next step is digitisation where the detector response from GEANT4 is converted into a format similar to what the real detector output looks like.
- Finally the simulated events pass the same reconstruction procedure as the real data events.

The simulated events are not expected to describe the real data perfectly, both due to the limitations of theoretical descriptions and the simulation itself. However they are still an incredibly important tool for many ATLAS analyses including this one. For further discussion on the simulated data used in the analysis see Chapter 5.

Chapter 4

Tools and Concepts

In this section a handful of useful formulas, ideas and concepts not directly related to the SM and BSM physics are gathered. They are mostly concerned with statistics and tools like Monte-Carlo generators as well as some typical terms and variables used in experimental particle physics.

4.1 Important Kinematic Variables

In this section some kinematic variables that are used by the analysis are defined.

- the scalar sum of the transverse momenta of all tau leptons, muons and jets in the event,
  $H_{\mathrm{T}} = \sum_i p_{\mathrm{T}}^{\tau_i} + \sum_j p_{\mathrm{T}}^{\mu_j} + \sum_k p_{\mathrm{T}}^{\mathrm{jet}_k}$

- the magnitude of the missing transverse momentum $|-\mathbf{p_T}| = E_{\mathrm{T}}^{\mathrm{miss}}$. Additionally the analysis makes use of $E_{\mathrm{T}}^{\mathrm{miss}}$ computed with muons treated as invisible. This is done since the $E_{\mathrm{T}}^{\mathrm{miss}}$ triggers do not have access to any muon information.

- the transverse mass of the tau lepton, defined as:

$$m_{\mathrm{T}}^{\tau} = \sqrt{2 p_{\mathrm{T}}^{\tau} E_{\mathrm{T}}^{\mathrm{miss}} (1 - \cos\Delta\phi(\tau, p_{\mathrm{T}}^{\mathrm{miss}}))} \tag{4.1}$$

  This value is computed per tau. In the case when more than one tau is present in the event, the variable is computed separately for each tau

- the m_{T2} variable, also called stransverse mass, computed (using an algorithm provided by [49]) as:

$$m_{\mathrm{T2}} = \sqrt{\min_{\mathbf{p}_{\mathrm{T}}^{a} + \mathbf{p}_{\mathrm{T}}^{b} = \mathbf{p}_{\mathrm{T}}^{miss}} \left(\max \left[m_{\mathrm{T}}^2(\tau_1, \mathbf{p}_{\mathrm{T}}^{a}), m_{\mathrm{T}}^2(\tau_2, \mathbf{p}_{\mathrm{T}}^{b}) \right] \right)}, \tag{4.2}$$

  where (a, b) refers to two invisible particles that are assumed to be produced with transverse momentum vectors $\mathbf{p}_{\mathrm{T}}^{a,b}$; (τ_1, τ_2) refers to two visible particles and m_{T} is the transverse mass

- $\min_{\Theta}$, the minimal angle between $\tau_{1,2}$ and b-jet$_{1,2}$. Note that only angles between a tau lepton and a b-jet are considered, not e.g. the angle between two taus

- the minimum $\Delta\phi$ between $E_{\mathrm{T}}^{\mathrm{miss}}$and the 2 leading jets, $\Delta\phi(\mathrm{jet}_{1,2}, E_{\mathrm{T}}^{\mathrm{miss}})$
- ΔR is used to define various objects in the analysis (e.g. jets use $\Delta R = 0.4$ in the clustering algorithm). It is defined simply as:

$$\Delta R = \sqrt{(\Delta\phi)^2 + (\Delta\eta)^2}$$

When referring to an object as "tau" in the context of the analysis a hadronically decaying tau lepton is meant. Objects like jets, b-jets, τ leptons and others are ordered by p_{T}, from largest to lowest. Whenever a "leading" or "second" jet/b-jet/τ is mentioned, it is used in this sense.

4.2 Important Concepts

In this section short write ups on several concepts from particle and generator physics are gathered.

Acceptance and Efficiency Acceptance A is a measure of how the geometry of a detector affects whether a particle is observed or not. The efficiency ε describes how good the detector is at detecting various objects passing through the detector. Depending on the context efficiency can refer to purely detector based efficiency or can include the efficiency of the algorithms used for reconstruction and identification too. In general the acceptance times efficiency should satisfy:

$$N_{obs} = N_{occurred} \times A\varepsilon$$

that is the number of events observed by the detector is equal to the number of events that actually happened times the limitations of the geometry of the detector times the efficiency of the detector. In practice the difference between the two becomes smeared especially when the dimensions of the objects get involved.

Luminosity and Integrated Luminosity Luminosity L is a measure of how many events pass through some area in a unit of time, $[L] = m^{-2}s^{-1}$. When combined with the cross-section θ, the probability that a process will take place in the collision, it can describe the number of events per time unit:

$$L\sigma = \frac{dN}{dt}$$

Integrating the luminosity over time (e.g. over the measurement period on a detector) gives the integrated luminosity L_{int}. As long as one knows the cross-section for a specific process the total expected number of such processes happening can be calculated as:

$$N_{occurred} = L_{int} \times \sigma$$

Scaling this number by acceptance and efficiency $A\varepsilon$ leads to the total number of events available to an analysis.

Stransverse Mass The stransverse mass m_{T2} [50, 51] is used by the analysis as one of the main discriminators. The formal definition is given in Section 4.1, but it is not a self-explanatory one. The m_{T2} can be computed events with two invisible particles that decay semi-invisibly into observed particles (e.g. $\tilde{\chi}_2^0 \to \tilde{\chi}_1^0 h$). As inputs m_{T2} uses the $E_{\mathrm{T}}^{\mathrm{miss}}$ vector, the vectors of the visible parts of the two decays and the predicted masses of the invisible particles. Very loosely described the variable attempts to divide the $E_{\mathrm{T}}^{\mathrm{miss}}$ vector into two parts and assign them to the two decay chains in the most optimal way.

$E_{\mathrm{T}}^{\mathrm{miss}}$ Significance Assume that an event with no invisible particles produced. The true $E_{\mathrm{T}}^{\mathrm{miss}}$ of such an event is 0. However the p_{T} of each object in the event is measured within the detector resolution. The resolution effects propagate to the $E_{\mathrm{T}}^{\mathrm{miss}}$ calculation. Typically even in an event with no invisible particles $E_{\mathrm{T}}^{\mathrm{miss}}$ will have some non-zero value due to that. Computing the fraction of $E_{\mathrm{T}}^{\mathrm{miss}}$ and the resolution allows to separate events with no invisible particles (ratio ≤ 1) and events with invisible particles (ratio > 1). A simple approximation for the resolution is $\sqrt{\sum E_{\mathrm{T}}}$ so that the $E_{\mathrm{T}}^{\mathrm{miss}}$ significance is:

$$E_{\mathrm{T}}^{\mathrm{miss}}\ \mathrm{sig} = \frac{E_{\mathrm{T}}^{\mathrm{miss}}}{\sqrt{\sum E_{\mathrm{T}}}}$$

For the analysis a proper object-based method of computing $E_{\mathrm{T}}^{\mathrm{miss}}$ significance is used where the resolution of every object entering the $E_{\mathrm{T}}^{\mathrm{miss}}$ calculation is considered separately.

Impact Parameter In the context of ATLAS the transverse impact parameter of a track d_0 is defined as the transverse distance of closest approach from the track to the primary interaction vertex. The longitudinal impact parameter z_0 is defined as the z value of the point of the track used to define d_0. These variables are used for reconstruction of charged particles, in particular electrons and muons.

4.3 Monte Carlo Generators

Monte Carlo generators [52, 53] are software equivalents of particle colliders. They emulate collision of two particles and the subsequent decays of the daughter particles. High energy hadron-hadron collisions are complex events that are hard (if at all possible) to describe analytically. Monte Carlo event generators offer a framework that divides the description into smaller steps, some of which can be solved from the first principles while others need to be tuned to measurements. Modularity is another great feature of event generators - improvements of one of the steps do not (usually) require changes of the whole setup.

Monte Carlo generators are not perfect. The description of various physics processes vary in precision and in implementation. There isn't one definitive answer on how to model everything. There is also a purely practical problem – running Monte Carlo generators takes a lot of time and machine power, there are limitations to how precise one can be. Nevertheless Monte Carlo generated events are extremely important for many particle physics analysis (including this one). The main reason for it is that

generators are extremely helpful in understanding the expected background and signal. This is especially important for proton-proton collisions that can be pretty "noisy" compared to much more controlled electron-positron collisions.

Particle-particle collisions and decays are probabilistic in nature, in case the of proton-proton collisions the energies and momenta of the initial parton are also not known. Furthermore, even if a theoretical understanding of the process is present it is not quite clear how that translates to what the detector observes and records. Monte Carlo generated events (usually coupled with detector simulation toolkits like Geant4) allow for a much more practical approach where the observed data and the Monte Carlo simulated events go through the same reconstruction algorithms and end up in the same format so that they are directly comparable. This is especially important in the case of new physics searches. Such analyses typically look for signatures that "shouldn't exist" in the SM.

Due to the probabilistic nature of the theory the decision of whether a certain phenomena observed is consistent with the prediction can only be statistical in nature. Monte Carlo generated events not only allow us to estimate what the background should look like (there are data-driven techniques to do the same thing, even if MC usually provides more statistical power), but also to understand how exactly we expect the new physics to manifest. In this way Monte Carlo generators serve as a link between theoretical and experimental physics.

A quick summary of the steps that a Monte Carlo generator typically goes through:

- Two partons are selected for the collision and are collided. This is usually done using Parton Distribution Functions (PDF). Strictly speaking most of the processes occurring at this stage are not interesting and are usually filtered out very early on.
- Colliding partons carry colour and electromagnetic charges. Collisions and scattering of particles carrying charges leads to brehmsstrahlung and it's equivalent in QCD in case of colour charges. Emissions related to the incoming partons are called Initial-State Radiation (ISR).
- Similarly to the previous point there are emissions associated with the outgoing particles, the so called Final-State Radiation (FSR).
- Both ISR and FSR can be modelled by so called parton showers.
- At some point the assumption of asymptotic freedom starts to break down. The confinement fields that hold partons together break up due to production of quark-antiquark pairs. This process is called hadronisation.
- After the initially colour-neutral protons collide they can be left in coloured states. The secondary interactions of the proton remains give rise to the underlying event. The phenomenon of more than one pair of partons interacting in a single collision is called multiple interactions.
- Finally some of the particles produced in the collisions can be very unstable and short-lived so they need to be decayed further. Others are long-lived enough to be visible in the detector. At this point the generator framework and the detector-simulation framework have to be matched.

4.3.1 Matrix Element

Generally speaking knowing the Lagrangian of the theory is enough to derive the corresponding Feynman rules and to construct and calculate the matrix elements (ME). Integrating the ME (or, rather, the differential cross section calculated with the matrix element) over the phase space leads to the total cross section:

$$\sigma_{tot}(pp \to X) = \Sigma_{i,j} \int dx_1 dx_2 d\hat{t} \rho(x_1, Q^2) \rho(x_2, Q^2) \frac{d\hat{\sigma}_{ij}}{d\hat{t}}$$

where $\rho(x_i, Q^2)$ are parton distribution functions that are determined experimentally, $\hat{t} = (p_1 - p_3)^2$ is one of the Mandelstam variables and $d\hat{\sigma}_{ij}$ is the differential cross section that can be expressed in terms of the ME. The issue is that in QCD the $\hat{\sigma_{ij}}$ part is divergent when integrated over all angles, specifically in the collinear limit. This is an universal feature of QCD. Additionally most cross sections diverge in the soft gluon limit too. In these regions the matrix element is no longer a suitable approach.

4.3.2 Parton Showers

A typical QCD process is $q \to qg$ or $g \to gg$. The cross section diverges if the gluon energy goes to 0 or if the gluon is collinear with the quark. The issue is that QCD events become cascades of large numbers of soft gluons. Computing such processes with the matrix element would require many loops and high-order calculations. Parton showers offer a solution.

In case of collinear gluons and quarks one should notice that the cross section can be described universally by DGLAP equations [54]. Such descriptions allow for combining multiple subsequent emissions in one step. The particles need not be exactly collinear for this approximation to work, the angles just have to be sufficiently smaller than the hard process angles. In addition an infrared cutoff (order of 1 GeV usually) is used to constrain the divergencies after which the hadronisation algorithms take over.

The second important feature of parton showers are Sudakov form factor. The idea is relatively simple - Sudakov form factors represent the probability of emitting no (resolvable) radiation. It is similar to radioactive decay, but instead of time the key variable is the scale of the hard process. The basic DGLAP equation has a form of:

$$dP_{a\to bc} = \frac{\alpha_s}{2\pi} \frac{dQ^2}{Q^2} P_{a\to bc}(z) dz$$

It is multiplied by the Sudakov form factor to ensure the total probability for a parton to branch is at most 1:

$$dP_{a\to bc} = \frac{\alpha_s}{2\pi} \frac{dQ^2}{Q^2} P_{a\to bc}(z) dz \ \exp(-\Sigma_{b,c} \int_{Q^2}^{Q^2_{max}} \frac{dQ^2}{Q^2} \int P_{a\to bc}(z) dz)$$

Sudakov form factor is an approximation to the complete virtual corrections from loops. Starting with some $q\bar{q}$ the quarks are evolved from the initial scale Q^2_{max} until they branch. Then each of the two daughter particles resulting from the branching are taken and the procedure is repeated. Initial state radiation is generally treated in the same way, but here the evolution is going in the other way, backward evolution.

Matrix elements are great for the cases where the jets are well separated. Parton showers on the other hand only offer approximate results, but are better for describing the structure of jets. They are also universal, there is no model dependence. Ideally one would like to combine the two techniques together in the most meaningful way to make use of the strong sides. It is not possible to do so perfectly, but there are methods that can be very useful depending on the application. Merging algorithms aim to provide a transition from ME to PS in the whole space phase. The typical example is when a process is calculated at the leading order (LO) and at the next-to-leading-order (NLO) with emission of an additional gluon. Merging is typically used for resonance decays. Vetoed parton showers is an extension of the ideas of merging algorithms to cases with several different orders. Finally MC@NLO algorithms aim to include both real and virtual contributions correctly. Neither of the algorithms are strictly speaking superior to each other, but suited for different tasks and processes.

4.3.3 The Les Houches Accord

As mentioned before, the Monte Carlo generators offer a modular framework that supports "plug and play" of various software components. An important part of making that work is common language and conventions used. The Les Houches Accord [55] specifies a common event file format. The Les Houches Accord Parton Density Functions [56] is a library of various PDF sets provided in a common framework. In SUSY it is usual to start from a few parameters at a certain energy scale that are then expanded to the full set of theory parameters by a spectrum calculator. The SUSY Les Houches Accord [57] specify the format of the output of such calculators that can be passed on to the other software.

HepMC [58] is a C++ format for Monte Carlo event records, i.e. the output of the generator. These event records are also referred to as "MC truth" since these are true numbers produced by the generators, not the smeared reconstructed and digitised objects used for analysis.

4.4 Statistical Methods

The discussion in this section is based on the "Asimov Paper", [59].

What exactly does "searching for new physics" mean? In the context of particle physics one starts with a model describing a predicted, but yet unobserved process. In the simplest case just the number of events observed is counted and then some statistical tests are performed to see whether the number of events are consistent with the theoretical prediction or not. In this section a somewhat more formal description of the searches is given and the statistical methods used by the analysis are described.

There are two main types of tests to perform - discovery (testing whether the observed signal is consistent with the expected, already known, background) and limit setting (testing how likely a specific model is with the observed results). For the case of discovery the null hypothesis H_0 is that the observed data is described by the already known processes (background) and the alternative hypothesis H_1 is that the data is described by the background-plus-signal model (that is predicted by some theory). For the limit setting the situation is reversed and the null hypothesis is background-plus-signal

tested against the alternative hypothesis of background only. A typical way to quantify the results is by using p-values, the probabilities of observing results at least as extreme as observed if the null hypothesis is correct. The measure of "extremeness" can be a simple count of events, shapes of some distributions, ratios etc. The null hypothesis is rejected if the p value is sufficiently low (that is if the probability that the observed result comes from a statistical fluctuation of the null hypothesis is low enough).

In particle physics the convention is not to use the p-values directly, but to compute the significance Z defined as

$$Z = \Phi^{-1}(1-p)$$

where p is the p-value and Φ is the probit function (or quantile function of the Gaussian, the inverse of the cumulative function). The interpretation of significance is the upper-tail probability starting from Z standard deviations away from the mean is equal to p. Figure 4.1 illustrates the relationship between p-value and significance for a one-tailed p-value. In particle physics for the discovery tests to reject the background-only null hypothesis the significance Z should be equal to at least 5σ. $Z = 5$ corresponds to the p-value of 2.87×10^{-7}. It should be noted that usually there is a range of similar hypothesis that are being tested (as is the case with this analysis) and each one is treated separately.

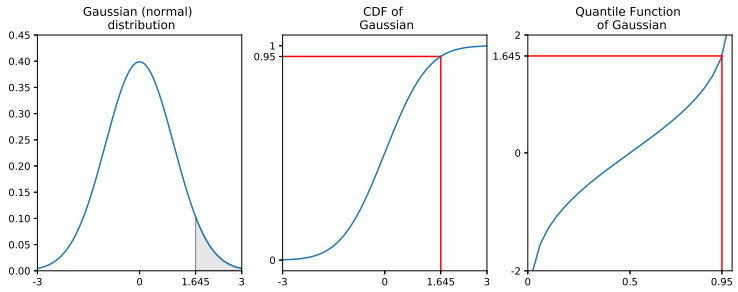

(a) Relations between p-values and significance Z. A p-value of 0.05 corresponds to the area under the curve of the Gaussian for $x > 1.645 (\times\sigma)$ (one-tailed). This can be read from the cumulative distribution function (CDF) of the Gaussian. The quantile function is the inverse of the CDF. The significance is defined as $Z = \Phi^{-1}(1-p)$, in this case $p = 0.05$ so the corresponding significance is 1.645σ.

Figure 4.1

Given the number of expected background and signal events (according to some model) in some region, how does one determine the median significance (also referred to as expected significance)? What significance value is enough to reject the H_0 hypothesis? Given the predicted background contribution b, the predicted signal contribution s and number of observed events n, the likelihood function is dependent on s:

$$L(s) = \frac{(s+b)^n}{n!} \exp^{-(s+b)}$$

and log-likelihood is:

$$\ln L(s) = n \ln(s+b) - (s+b) - \ln n!$$

The estimator for s is $\hat{s} = n - b$. The likelihood ratio for testing $s = 0$ hypothesis is then:

$$\Lambda(0:\hat{s}) = (-2) \ln \frac{L(0)}{L(\hat{s})} = 2\left(n \ln \frac{n}{b} + b - n\right)$$

From Wilks' theorem [60]:

$$Z_0 \approx \sqrt{\Lambda(0:\hat{s})} = \sqrt{2\left(n\ln\frac{n}{b}+b-n\right)}$$

assuming $n > b$. To get the median Z_0 let $n = s+b$, i.e. the assumption of Asimov dataset:

$$\text{median } Z_0 = \sqrt{2((s+b)\ln(1+\frac{s}{b})-s} \tag{4.3}$$

The median significance calculated in this way (Asimov significance) is a good approximation for a wide range of s and b. The formula can be modified to include b with the variance θ_b^2:

$$Z_A = \left[2\left((s+b)\ln[\frac{(s+b)(b+\sigma_b^2)}{b^2+(s+b)\sigma_b^2}]-\frac{b^2}{\sigma_b^2}\ln[1+\frac{s\sigma_b^2}{b^2+b\sigma_b^2}]\right)\right]^{\frac{1}{2}}$$

Suppose we observe an experimental result consistent with no signal. Perhaps there is even a downward fluctuation in the background. In this case we can possibly reject the background-only hypothesis at 95% confidence level. This is, statistically speaking, a valid result. What does it mean physically though? The interpretation is less about the existence of the signal and more about the probability of observing a similar or stronger result during repeated experiments. Needless to say that it is the existence of the signal that is the interesting part! An approach commonly used at LHC and LEP (and in this thesis in particular) to deal with the ambiguity of the results is the CL_s technique [61]. The idea is to normalise the signal+background hypothesis to just background hypothesis:

$$CL_s = CL_{s+b}/CL_b$$

The CL_s is not a confidence interval (in the strict frequentist sense), but it is effectively treated as one. A signal hypothesis is considered excluded at confidence level n if $1 - CL_s \leq n$. The CL_s method is sometimes called ad hoc as it includes desirable properties of frequentist and Bayesian paradigms without following either one precisely.

4.5 Statistical Framework

The statistical analysis of the data is performed within the HistFitter software framework [62]. In this section the key concepts are explained and the basic workflow is described while the practical implementation is described in depth in Chapter 8.

Signal Region: A part of searching for something is knowing where to search. The typical approach is to define a region of the phase space where the effect of the new physics is expected to be noticeable. Such a region is called a signal region (SR). Signal regions are often defined using a set of requirements on kinematic variables (also called "cuts"), but other possibilities exist, such as using the score of machine learning algorithms. Likewise, the "noticeability" of the new physics can range from simply a higher number of events observed than expected to difference in shapes of

certain kinematic variables. The concept of signal (and control and validation) regions is built-in in the HistFitter framework allowing for a statistically rigorous treatment.

It is important to mention that, following the ATLAS policies, the data in signal regions is "blinded". That means that before the definitions of the regions themselves, the background descriptions, the statistical methods that are going to be used and systematic uncertainties present are understood and developed the data in the signal region is not used and only "unblinded" when all other parts of analysis are complete. When designing a signal region one goes through tens (if not hundreds!) of distributions of various kinematic variables further binned in multiple bins, attempting to find how signal differs from background. Each such bin can be considered a measurement. The probability of observing a statistical fluctuation (with, say, $p < 0.01$) in data are much larger when you essentially perform thousands of counting experiments! This is called "look-elsewhere" effect. Blinding the signal regions helps to avoid the bias.

Control Region: Another part of the analysis is understanding and modelling of the expected SM background. A crucial concept related to background modelling is that of control regions (CR). Control regions are to background what signal regions are to signal, selections that enhance the presence of the background processes (and have little to no signal contribution). In the most basic case there is one single bin control region per dominant background process, but more complex techniques can be used, e.g. using the shape information of some kinematic variable. Once the selection is done one can compare the prediction from the Monte-Carlo simulations to the real data yields in the control regions and correct the Monte-Carlo predictions for the differences. These corrections are then propagated to the signal regions, estimating the background processes in a "semi-data-driven" way. The more in-detail description of how the control regions are designed for the current analysis and what backgrounds are corrected for is presented in Chapter 8.

Validation Region: Control regions are designed to have as little signal contamination as possible. This usually means that the kinematic selections between the signal and control regions differ rather significantly. A natural question to ask is whether the corrections derived in the control regions are actually viable in the signal regions that are located in a different part of the phase space. To check the validity of the modelling of backgrounds validation regions (VR) are used. They are typically defined "between" the control and the signal regions such that the extrapolation over kinematic variables can be checked. The design of validation regions for the analysis is presented in Chapter 8.

Probability Density Functions (PDFs) are used to model the data in the various regions. Parameters of these PDFs are changed when the comparison of the data to the Monte-Carlo predictions is made, during the fit procedure (hence the name, HistFitter). The regions are designed to be statistically independent and are described by separate PDFs which can all be used in a simultaneous fit. The model built by the HistFitter depends on three types of input - number of MC (expected) and data (observed) events in regions of interest and the errors of the MC predictions (due to statistical and systematic uncertainties).

The likelihood function L that is maximised during the fit is constructed from Poisson distributions of yields in control and signal regions and special distributions describing systematic uncertainties (Gaussians for independent nuisance parameters). It can be schematically written as:

$$\begin{aligned} L(\vec{n}, \overrightarrow{\theta^0} | \mu_{sig}, \vec{b}, \vec{\theta}) =& P_{SR} \times P_{CR} \times C_{syst} = \\ =& P(n_S | \lambda_S(\mu_{sig}, \vec{b}, \vec{\theta})) \times \prod_{i \in \mathrm{CR}} P(n_i | \lambda_i(\mu_{sig}, \vec{b}, \vec{\theta})) \times C_{syst}(\overrightarrow{\theta^0}, \vec{\theta})) \end{aligned} \tag{4.4}$$

where P_{CR} and P_{SR} are Poission distributions of event counts in the corresponding CRs and SR and the probability density function C_{syst} represents systematic uncertainties. $C_{syst}(\overrightarrow{\theta^0}, \vec{\theta})$ depends on central values $\overrightarrow{\theta^0}$ as well as on the nuisance parameters $\vec{\theta}$ themselves. n_S and n_i are number of observed events, λ_S and λ_i are Poisson expectations that are functions of signal strength μ_{sig}, background predictions $\vec{b}$ and the nuisance parameters $\vec{\theta}$. $\mu_{sig} = 0$ corresponds to the no-signal model and $\mu_{sig} = 1$ is the nominal signal expectation. The C_{syst} term is, in the case of independent nuisance parameters, just a product of Gaussian probability distributions G describing systematic uncertainties:

$$C_{syst}(\overrightarrow{\theta^0}, \vec{\theta}) = \prod_{sinS} G(\theta_s^0 - \theta_s)$$

where S represents the set of all systematics. The central values θ_s^0 are expected to be 0 for independent nuisance parameters, but that can change if some correlation is present.

There are three common fitting procedures (or strategies) - background-only, model-dependent and model-independent. All three have been used by the analysis and are described in more details further.

4.5.1 Background-only Fit

Background-only fit is the simplest fitting strategy. The purpose is to derive correction factors for the dominant backgrounds in the CRs and consequently to estimate the background contributions to the VRs and SRs. No assumptions about the signal model are made, it is assumed that the CRs are free from signal contamination and only background (and data) samples are used for the fit. The predicted number of events (from Monte-Carlo) are normalised to the observed number of events (i.e. data). The fit is performed only using the yields in CRs, but the PDF variables are shared across all regions so that the corrections to MC are propagated to the VRs and SRs. The CRs can both be single-bin and multi-bin.

The background-only fit is independent of the predicted and observed yields in the SRs and VRs. Therefore it can be used to validate the modelling (or suggest that reoptimisation of CRs is required) by comparing the predicted and observed yields in the VRs. Another advantage of the background-only fit is that it provides unbiased predictions of the backgrounds in the SRs that can be easily used for any hypothesis testing for various signal models.

Related to the background-only fit are the transfer factors (TFs) that are used to extrapolate measurements in CRs to the background predictions in the SRs. TFs are

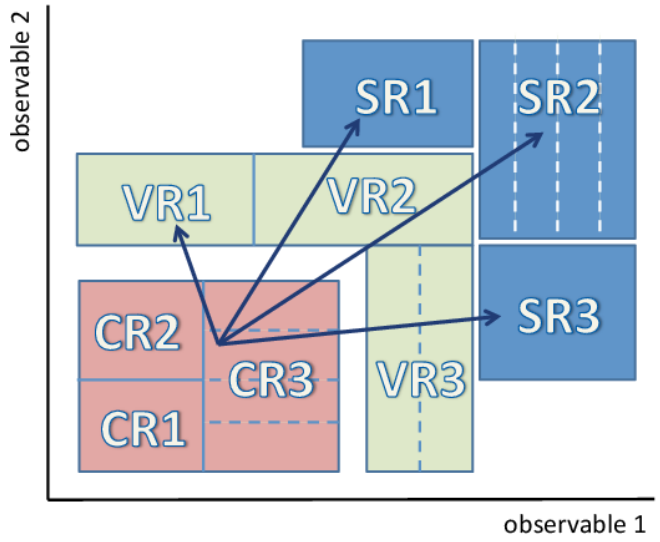

(a) Illustration of a typical analysis workflow with HistFitter. [62]

Figure 4.2

defined as ratios of expected contributions in CRs and SRs per background. The predicted background in the SR is:

$$n(SR, pred) = n(CR, obs) \times \left[\frac{n(SR, MC)}{n(CR, MC)}\right] = \omega \times n(SR, MC)$$

where the ratio in the parentheses is the TF and the ω term is called normalisation factor (NF).

4.5.2 Exclusion Fit

Model-dependent signal fit (also known as exclusion fit) is run under the assumption of a specific signal model. All CRs and SRs are used in the fit (as long as they are statistically independent). The contributions from the signal model studied are also included in the CRs and SRs. If no significant excess is observed (compared to the background-only hypothesis) exclusion limits are set on the model. If an excess is observed a scan in signal strength μ_{sig} is performed to determine the one most compatible with the excess. Similar to the background-only fit both the CRs and SRs can be single-bin or multi-bin. Since the fit is model-dependent it is performed for each of the models studied, the result being presented as the exclusion contour.

4.5.3 Discovery Fit

Model-independent signal fit or discovery fit is the third fit strategy implemented in the HistFitter framework. It uses all CRs and one single-bin SR. Unlike the exclusion fit no assumptions are made on the signal model, the limits are set on the number of events

beyond the expected backgrounds in the SR. This produces a robust result that can be used to evaluate whether any model (that predicts any yields in the SR) is excluded or not by the measurement.
To summarise the Monte-Carlo predictions are fitted to data in control regions and the corrections are extrapolated over some kinematic variables to validation regions and further to signal regions. This is schematically shown in Figure 4.2. All regions are statistically independent.

Chapter 5

Data and MC Samples Used

In this chapter the data and the Monte-Carlo simulations used by the analysis are described. Various procedures applied on the datasets are documented. Additionally the physical objects (such as jets) used by the analysis are defined.

5.1 Data Format

The analysis is based on the data recorded by the ATLAS detector during Run 2. The full dataset is extremely large due to both the number of events and the amount of information about each event recorded. Using the full dataset requires a lot of processing power and is heavily discouraged. Therefore the data is sliced in smaller sub-samples (called derivations) based on the needs of various analysis groups. Both the number of events and the information about each event stored are heavily reduced in derivations making them much easier to process and work with. The Monte-Carlo simulations are treated in the same way to make them directly comparable and to reduce the size. The analysis presented makes use of three derivations - SUSY3, SUSY5 and SUSY11.

The main format is SUSY3, designed for SUSY searches with taus. It requires the presence of one hadronically decaying tau lepton with $p_{\mathrm{T}} > 15$ GeV and that events fire a logical OR of a range of $E_{\mathrm{T}}^{\mathrm{miss}}$, jet+$E_{\mathrm{T}}^{\mathrm{miss}}$, tau, electron and muon triggers. SUSY5 is based on light leptons, it requires that the event fires a $E_{\mathrm{T}}^{\mathrm{miss}}$ or a lepton trigger, has an electron or a muon and 1 jet with $p_{\mathrm{T}} > 200$ GeV or 2 jets with $p_{\mathrm{T}} > 25$ GeV. The SUSY11 selection is based on a logical OR of single-jet triggers.

5.2 Collision Data

The analysis is using proton-proton collision data at $\sqrt{s} = 13$ TeV recorded by the ATLAS detector in the period of 2015-2018. Centrally produced GoodRunLists (GRLs) are applied to reject events recorded during unacceptable beam or detector conditions and to ensure that only well reconstructed physics objects are used. In addition to the standard GRL a specific GRL for b-jet triggers is used by the analysis.

5.3 Monte-Carlo Samples for SM Backgrounds

The Monte-Carlo (MC) samples are used for the background estimations of most processes. The analysis makes use of MC samples produced with SHERPA [63], MADGRAPH [64] and POWHEGBOX [65] generators. MADGRAPH and POWHEGBOX samples use PYTHIA8 [66] for showering. For most of the events, the detector is fully simulated using Geant4 [48]. Some exceptions have been simulated using the simplified AtlFast II (AFII) approach instead where the calorimeter is simulated using FastCaloSim [67]. The full ATLAS simulation chain is described in [68]. The MC samples are divided in 3 campaigns designed to match 2015-2016, 2017 and 2018 data-taking conditions, trigger menus and pile-up profiles. They are called mc16a, mc16d and mc16e correspondingly.

The Monte-Carlo samples are not inclusive, each background process is modelled independently and normalised by the integrated luminosity of the corresponding data-taking period. The full list of Monte-Carlo samples used for the analysis includes approximately 1000 entries. A short summary of the processes modelled is listed in the following.

Pair production of top quarks or $t\bar{t}$ is expected to be the largest background for the analysis. A pair of top-antitop quarks is produced and subsequently decayed through the electroweak interaction into real, on-shell W bosons and down type quarks, predominantly bottom. Depending on the decays of the W bosons the $t\bar{t}$ decays are classified as fully hadronic, semi-leptonic and fully-leptonic, the latter two being most important for the analysis. Production modes of $t\bar{t}$ at the LHC are summarised in Figures 5.1a-5.1c and a typical semi-leptonic $t\bar{t}$ decay tree is shown in Figure 5.2.

The $t\bar{t}$ Monte-Carlo is generated in three samples, all hadronic, single lepton and dilepton. The majority of the $t\bar{t}$ events have a relatively low H_{T} and $E_{\mathrm{T}}^{\mathrm{miss}}$ values (compared to the needs of typical SUSY analysis) so that statistical extensions are produced in bins of $E_{\mathrm{T}}^{\mathrm{miss}}$ and H_{T}. All the samples are normalised to the expected integrated luminosity and merged into one inclusive $t\bar{t}$ sample.

Nominal (as in used for the analysis itself) $t\bar{t}$ samples are produced with POWHEGBOX generator used to calculate the matrix element and PYTHIA8 for parton shower. Two alternative $t\bar{t}$ samples are produced to calculate systematic uncertainties related to generators, by replacing either POWHEGBOX or PYTHIA8 with different software. The generator combinations used are MADGRAPH5_aMC@NLO to compute the matrix element while keeping the PYTHIA8 for showering and POWHEGBOX with HERWIG7 used for showering.

Single top quark production Similar to the $t\bar{t}$ production the single top quark production results in final states resembling the signatures the analysis is looking for. While not as dominant as $t\bar{t}$ it is still expected to be a significant contribution to the background. There are three main modes in which single top quarks are produced at the LHC - s-channel, t-channel and Wt associated production, summarised in Figures 5.3a-5.3b.

Similar to the $t\bar{t}$ case the single top samples are produced as an inclusive sample (one per channel) and statistical extensions binned in H_{T} and $E_{\mathrm{T}}^{\mathrm{miss}}$. The nominal single top samples are produced using POWHEGBOX+PYTHIA8. MAD-

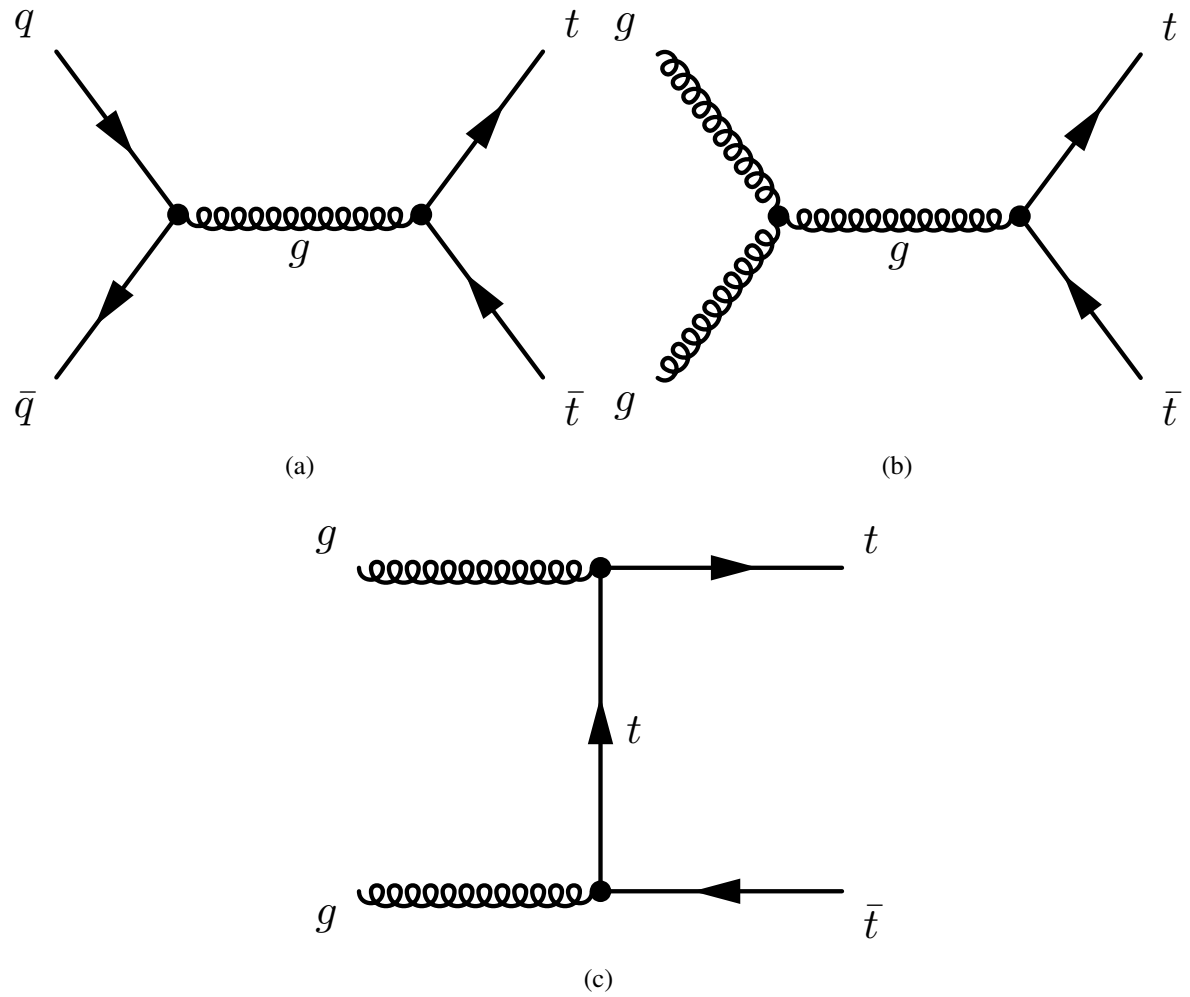

Figure 5.1: Feynman diagrams of $t\bar{t}$ production.

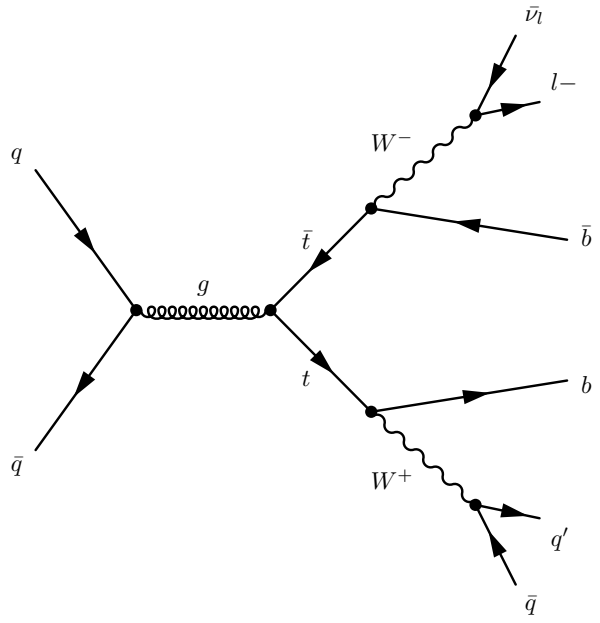

Figure 5.2: An example of semi-leptonic decay of $t\bar{t}$.

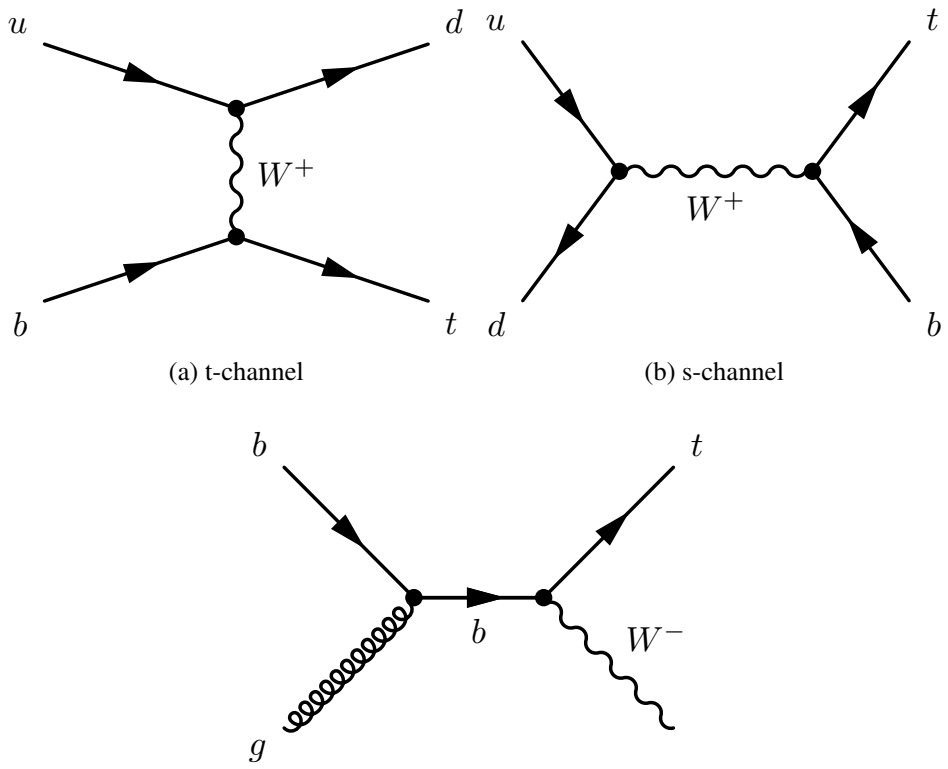

(a) t-channel

(b) s-channel

(c) Wt associated production

Figure 5.3: Feynman diagrams of single top production.

GRAPH5_aMC@NLO+PYTHIA8 and POWHEGBOX+HERWIG are used for systematic uncertainties, same as for the $t\bar{t}$ case. An additional systematic uncertainty is considered for the Wt channel where the nominal diagram removal (DR) scheme used for distinguishing it from the $t\bar{t}$ production is compared to an alternative approach, the diagram subtraction (DS) scheme. Therefore an additional Wt channel sample is produced with POWHEGBOX+PYTHIA8, but using the DS scheme.

Top quark pair production in association with W, Z or Higgs bosons or ttW, ttZ, ttH and more generally ttX for short are a family of processes that can create final states similar to those the analysis is searching for. Examples of typical production modes of ttW and ttZ are shown in Figures 5.4a - 5.4d. The yields are expected to be rather low, but can become significant in the signal region, specifically ttZ and ttH. An important distinction from $t\bar{t}$ is that the taus are expected to come from the decay of the resonance and not from top decays resulting in slightly different topologies and kinematic properties.

The ttX samples are produced with MADGRAPH5_aMC@NLO+PYTHIA8.

Z/W boson and jets production or V+jets are a large family of events that are characterised by production of a vector boson and jets (originating from either gluons or light quarks). Typical production modes are similar to these of ttX and are shown in Figures 5.5a - 5.5b. The Monte-Carlo production is divided based on the decay modes of the boson, e.g. $Z \to \nu\nu$ and there are further binned in H_{T}. The samples are also separated in those with b-jets filtered and vetoed. These processes are not expected to contribute to the

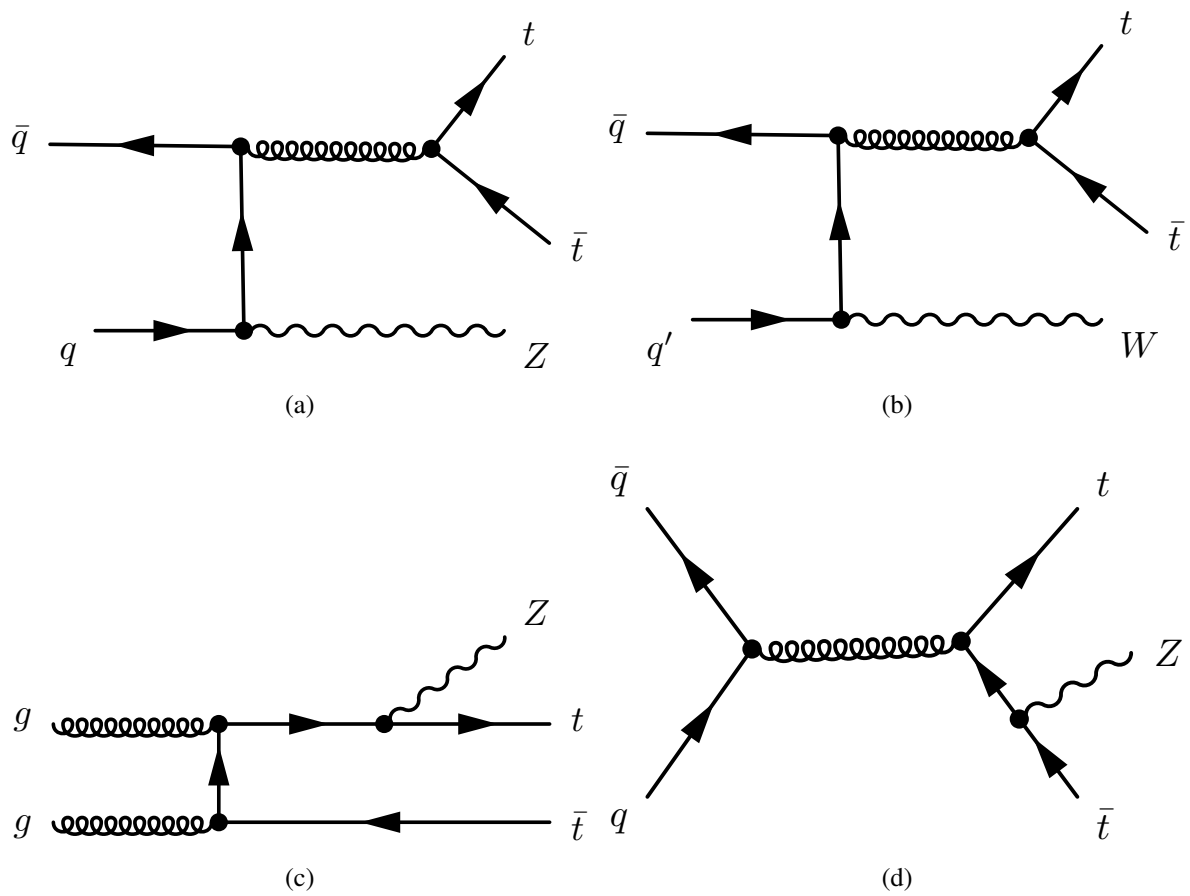

Figure 5.4: Feynman diagrams of typical ttW and ttZ production modes.

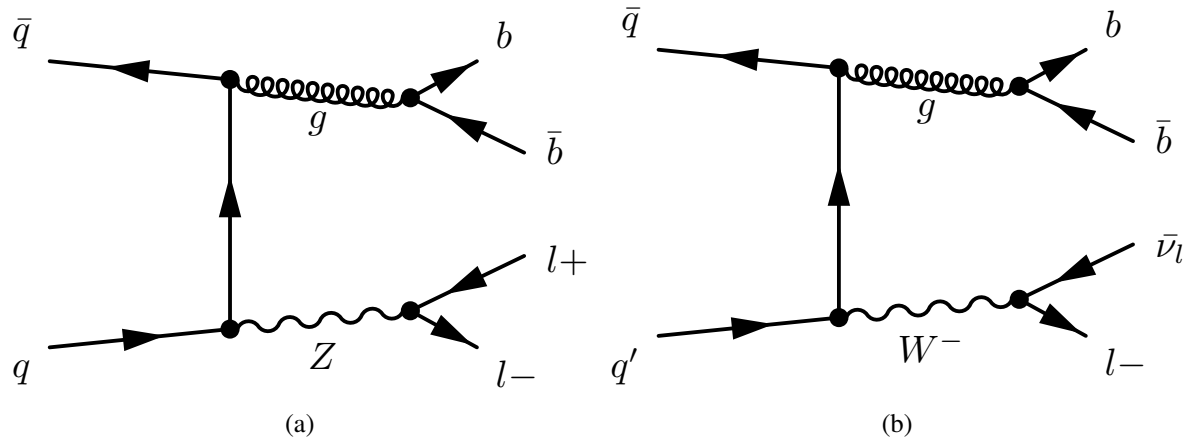

Figure 5.5: Feynman diagrams of typical V+jets production modes.

signal regions with the exception of $Z \to \tau\tau$ with associated jets production, but can be significant in various control regions. The samples are produced using SHERPA 2.2.1. For generator related systematic uncertainties alternative $Z \to \mu\mu$ and $Z \to \tau\tau$ samples are produced using the MADGRAPH generator.

Diboson and triboson production are events with two or more vector bosons produced. The samples are divided based on the boson content (e.g. WZ and ZZ) and number of leptons (e.g. WWZ with 4 leptons and 2 neutrinos). The samples are generated using SHERPA 2.2.2 (different version from what was used for V+jets). Some typical production modes are shown in Figures 5.6a - 5.6c. These samples are not expected to contribute heavily to the analysis phase space.

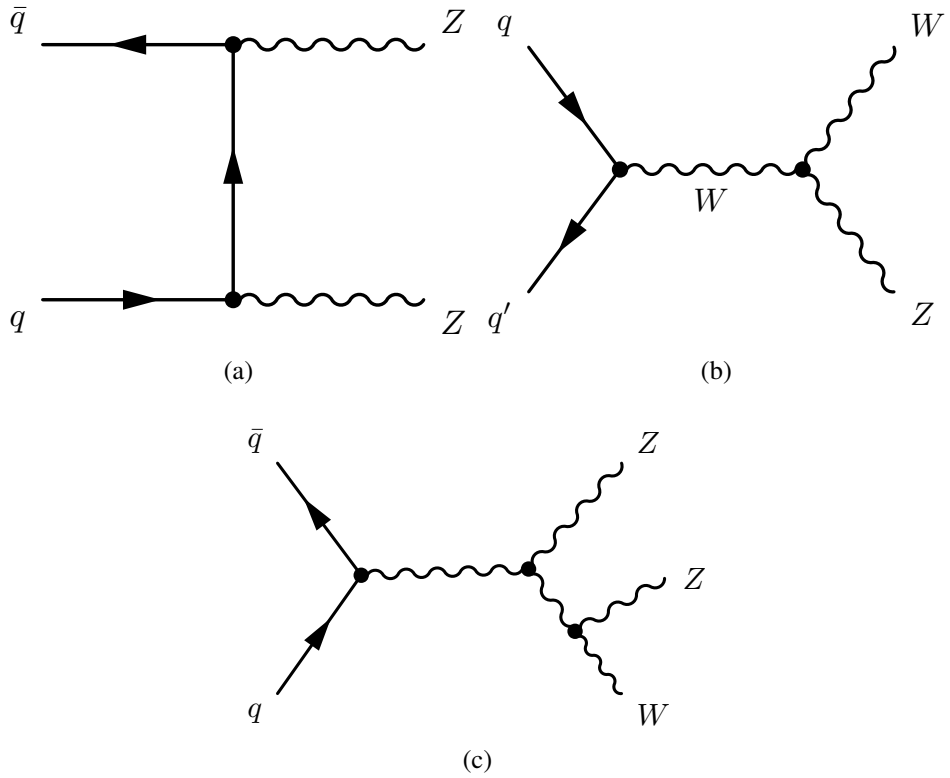

Figure 5.6: Feynman diagrams of some diboson and triboson production modes.

5.4 Monte-Carlo Samples for SUSY Signal

The analysis targets a simplified model of sbottom pair production with

$$\tilde{b}_1 \to b\tilde{\chi}_2^0 \to bh\tilde{\chi}_1^0.$$

Other decay modes of $\tilde{b}_1$ and $\tilde{\chi}_2^0$ are suppressed. $\tilde{\chi}_1^0$ is considered to be the lightest supersymmetric particle and to be stable. Furthermore the analysis is focused on the $\Delta m(\tilde{\chi}_2^0, \tilde{\chi}_1^0) = 130$ GeV mass separation that forces the Higgs boson to be produced on-shell. The final states of interest include two hadronically decaying tau leptons coming

from the Higgs boson decay $h \to \tau\tau$. The natural $E_{\mathrm{T}}^{\mathrm{miss}}$ from the hadronically decaying tau leptons allows us to probe lower $E_{\mathrm{T}}^{\mathrm{miss}}$ regions.

The signal samples have been generated with MADGRAPH5_aMC@NLO v2.2.3.p4 [64] with showering using PYTHIA8 v8.210. AFII technique is used for reconstruction. The analysis uses SUSY3 as the main derivation, but due to the $h \to \tau\tau$ branching ratio being relatively low requiring even 1 hadronically decaying tau (like SUSY3 does) would reject approximately 85% of all signal events. The steps that require the most processing power (and take the longest time) are reconstruction and digitisation of the events so the usual approach is to apply a filter at the generator level.

To achieve the needed statistical power without requiring hundreds of thousands of events per signal point, the following 2 filters are applied to the samples:

- the leading jet p_{T} (not necessary a b-jet) is required to be larger than 100 GeV at the generator level;
- presence of at least one hadronically decaying tau lepton with $p_{\mathrm{T}} > 12$ GeV at the generator level;
  - in the low $m_{\tilde{b}}$ region of the parameter space this requirement is increased to at least two hadronically decaying tau leptons with $p_{\mathrm{T}} > 12$ GeV each at the generator level.

The baseline analysis selections include the requirement of leading jet $p_{\mathrm{T}} > 140$ GeV and tau $p_{\mathrm{T}} > 25$ GeV so the first two filters do not affect the further analysis. The signal region requires 2 taus, but some control and validation regions require exactly 1 or 0 taus. This is not a problem in general, however it makes estimation of signal contamination in those regions harder.

Various signal models are considered by the analysis. They are differing by $m_{\tilde{b}}$ and $m_{\tilde{\chi}_2^0}$ masses in intervals of 50 GeV forming a grid in the parameter space. Initially the analysis only considered and was optimised for the $m_{\tilde{\chi}_2^0} = 131$ and $m_{\tilde{\chi}_2^0} = 180$ points as shown in Figure 5.7a. After the design of the analysis has been finalised it became apparent that it is sensitive to points beyond what has been considered so far. An extension of the signal grid has been produced to match the reach of the analysis, see Figure 5.7b.

Some tests concerning the quality of the signal Monte-Carlo samples are gathered in Appendix E.

5.5 Object Description

It is (somewhat) straightforward to describe what a jet or a muon is from the theory point of view. Things get a little more complicated when dealing with a real detector with finite resolution. Various algorithms exist that e.g. combine tracks into jets of different sizes. A b-jet tagger assigns each jet a value describing how likely it is for this jet to be a b-jet (and how likely it is that a "not bjet" object will be tagged as a b-jet), it is up to the needs of the analysis to select what jets to consider as b-jets based on that. Similar considerations apply to identification and reconstruction of taus, electrons, muons. Generally several recommended working points (WPs) exist for objects with

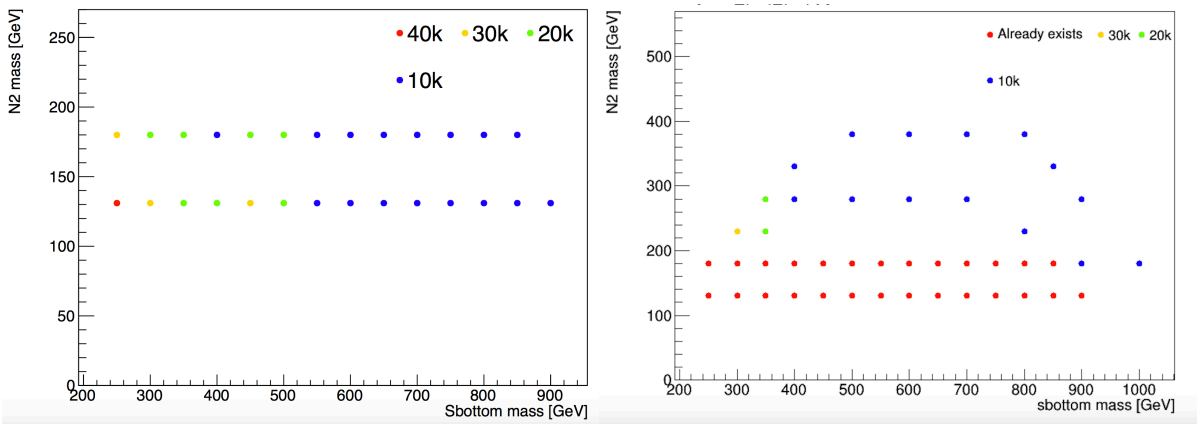

(a) (b)

Figure 5.7: Grid points corresponding to different $m_{\tilde{b}}$ and $m_{\tilde{\chi}_2^0}$ masses used in the analysis. The colours represent the number of raw Monte-Carlo events produced per data-taking period (mc16a/d/e). (a) shows the initial models considered by the analysis (b) shows the extension of the signal grid.

given efficiency and rejection rates (type 1 and 2 errors). In this section the definitions of various objects used by the analysis are summarised.

Primary Vertex: tracks from the Inner Detector with $p_{\mathrm{T}} > 500$ MeV are combined into interaction vertices [69], locations where some particle activity is happening. If more than one vertex candidate is available the one with the largest Σp_{T}^2 of the associated tracks is defined as the primary vertex.

Jet: jets are reconstructed with an anti-k_t clustering algorithm [70] using distance parameter R=0.4. Collections of massless positive-energy topological clusters [71] built from calorimeter cells containing energy above noise threshold measured at the electromagnetic scale are used as input. Global Sequential Calibration (GSC) [72] and Jet Energy Scale (JES) [73] calibration are applied to jets. Jets are required to have $p_{\mathrm{T}} > 20$ GeV and $|\eta| < 2.8$. Jets originating from pileup are suppressed using a jet-vertex-tagger (JVT) [74], this cut is only applied to jets with $p_{\mathrm{T}} < 120$ GeV. The surviving candidates are used by the analysis.

B-jet: baseline jets are assigned a score by the MV2c10 tagger [75, 76], a multivariate algorithm using tracks, primary vertex and jets information as the input. Several working points are defined by applying different cuts on the score. The analysis is using a 77% efficiency working point meaning that the true b-jets are correctly identified 77% of the time. This corresponds to a cut of 0.64 on the score. The expected rejection rates are 5 for jets originating from charm quarks, 15 for hadronically decaying taus and 110 for light flavour jets [76]. Jets that pass the b-tagging selection are called signal b-jets.

$E_{\mathrm{T}}^{\mathrm{miss}}$: $E_{\mathrm{T}}^{\mathrm{miss}}$ is defined to be the magnitude of the missing transverse momentum vector $p_{\mathrm{T}}^{\mathrm{miss}} = -\mathbf{p_T}$ [77]. It is calculated as a negative vector sum of transverse momenta of

electrons, muons, taus, jets and photons. The tracks not associated to any reconstructed object with $p_{\mathrm{T}} > 500$ MeV form the soft term that also enters the calculation.

Electron: electron candidates are reconstructed from energy deposits in the EM calorimeter that are matched to an Inner Detector track [78]. Candidates that pass the "loose" ID criteria [79], pass the $|z_0 \sin\Theta| < 0.5$ mm selection on the longitudinal impact parameter and have $p_{\mathrm{T}} > 10$ GeV and $|\eta| < 2.47$ are called baseline electrons.

Muon: muon candidates are reconstructed from the Inner Detector tracks that are matched to the Muon Spectrometer in the region $|\eta| < 2.7$ [80]. Candidates that have $p_{\mathrm{T}} > 10$ GeV, $|\eta| < 2.7$, satisfy a "medium" identification requirement and pass the $|z_0 \sin\Theta| < 0.5$ mm selection are called baseline muons. Baseline muons that survive the overlap procedure (as described further in the section), have $p_{\mathrm{T}} > 25$ GeV and the "loose" isolation criteria and satisfy $\frac{|d_0|}{\sigma(d_0)} < 3$ requirement on the transverse impact parameter are selected for the analysis and are called signal muons.

(Hadronically Decaying) Tau Lepton: tau candidates are reconstructed [81] from anti-k_t seed jets with $\Delta R = 0.4$, similar to what is described in the jets reconstruction section. The seed jets are built from topological clusters calibrated with a hadronic weighing scale [82]. The tau candidates are built around jet axis from tracks and clusters within $\Delta R = 0.2$. Tau candidates are required to have $p_{\mathrm{T}} > 20$ GeV $|\eta| < 2.5$ and to have either 1 or 3 charged tracks with a charge sum of ± 1. Candidates reconstructed in the transition region $1.37 < |\eta| < 1.52$ are rejected. The tau energy is calibrated using a boosted regression tree [83]. A recurrent neural network (RNN) algorithm [84] is used to suppress jet background and select tau leptons. The "loose" working point is used, corresponding to an efficiency of 85% for taus with one track (also called one-prong taus) and 75% for taus with three tracks (three-prong). The electron-tau likelihood rejection is applied to differentiate taus from electrons.

5.5.1 Overlap Removal

After the reconstruction of objects is complete an overlap removal procedure is applied. The purpose is to remove ambiguous objects that have been reconstructed by multiple different algorithms, e.g. if an object is identified both as an electron and a tau. Only one of the "interpretations" is kept so that variables like $E_{\mathrm{T}}^{\mathrm{miss}}$ and H_{T} are consistent. For the purposes of the analysis electrons, muons, taus and jets participate in the overlap removal, no specific treatment is applied to b-jets and presence of photons is ignored (as the analysis doesn't use any photon information).

The overlap removal is performed sequentially. First the electrons that share the same track are cleaned with only one remaining. The next step is to discard taus that overlap ($\Delta R < 0.2$) with an electron or a muon. In the next step electrons and muons that share the inner-detector track are resolved. If a muon candidate is only tagged in the calorimeter without the corresponding Muon Spectrometer tracks it is removed, otherwise the electron is removed. If a jet and a light lepton overlap with $\Delta R < 0.2$ the jet is removed, otherwise ($0.2 < \Delta R < 0.4$) the light lepton is removed. Finally if

Table 5.1: Overview of the successive steps in the overlap removal algorithm. Only surviving objects participate in subsequent steps.

	Object discarded	Object kept	Matching condition
1.	electron	electron	shared track, $p_{T1} < p_{T2}$
2.	loose tau	electron	$\Delta R < 0.2$
3.	loose tau	muon	$\Delta R < 0.2$
4.	calo-tagged muon	electron	shared inner-detector track
5.	electron	muon	shared inner-detector track
6.	jet	electron	$\Delta R < 0.2$
7.	electron	jet	$\Delta R < 0.4$
8.	jet	muon	nTracks < 3 and (ghost-associated or $\Delta R < 0.2$)
9.	muon	jet	$\Delta R < 0.4$
10.	jet	tau	$\Delta R < 0.2$

a tau and a jet overlap with $\Delta R < 0.2$ the jet is removed. The process is summarised sequentially in Table 5.1.

5.6 Preselection

In parallel with the calibration of the events and the overlap removal some "cleaning" selections are applied to the datasets to ensure that only properly reconstructed events are used. Some of them are crucial, e.g. the $E_{\mathrm{T}}^{\mathrm{miss}}$ calculator crashes when attempting to compute $E_{\mathrm{T}}^{\mathrm{miss}}$ for an event without a primary vertex, so such events have to be filtered out first. Others serve to improve the data/MC agreement in specific parts of the phase space or simply to reduce the size of the dataset and the processing power needed. All of these selections are referred collectively to as preselection. The preselection is performed within a framework developed at the University of Bergen and adapted to the needs of the analysis presented. The various components of the preselection procedure are listed below:

- The event is in a luminosity block included in the Good Run List. As the analysis is relying on b-jet triggers, the b-jet specific Good Run Lists are also used.
- The LAr, Tile, SCT and Core EventInfo flags show no data quality/integrity issue.
- The event has a primary vertex with at least two tracks.
- No cosmic muon candidate (with $|z_0^{\mathrm{PV}}| > 1$ mm or $|d_0^{\mathrm{PV}}| > 0.2$ mm) is present after overlap removal.
- The event does not contain a badly-reconstructed muon, defined as a baseline muon found before overlap removal with large curvature error, $\frac{\sigma(q/p)}{|q/p|} > 0.2$.
- All jets in the event are required to pass the "loose" selection criteria based as described in [85] that selects jets with efficiency of 99.5%.

- The leading jet is additionally required to pass the "tight" selection criteria [85] which suppresses the beam background.
- At least one tau or one muon candidate is required.
- The event has either $E_{\mathrm{T}}^{\mathrm{miss}}$or $E_{\mathrm{T}}^{\mathrm{miss}}$computed without muons of at least 100 GeV. This selection is slightly relaxed for SUSY5 to also include events with two muons with invariant mass close to that of a Z boson.
- A typical issue with the Tile Calorimeter encountered during the data-gathering runs is tiles tripping or being unpowered. Such defects are considered minor and the events are not vetoed centrally. Instead the list of inactive and faulty tiles and the corresponding run numbers are provided and the analyses are asked to check whether the effect is significant on an individual basis. If an object (a jet or a tau lepton) is close in ϕ to $p_{\mathrm{T}}^{\mathrm{miss}}$ it is possible that the missing momentum is coming from the detector not measuring it properly and not from an invisible particle. If the jet or the tau closest to the $p_{\mathrm{T}}^{\mathrm{miss}}$ in ϕ hit one of the problematic modules (both geometrically and during the runs when they were misbehaving) the event is vetoed.

It should be mentioned that for all CRs, VRs and SRs used an additional set of selections is applied. These selections are not used to veto events from the dataset since they are still useful for studies of triggers and multijet backgrounds. However when describing control, validation and signal regions it is assumed that these selections are applied as well (unless specifically stated otherwise). The additional selection criteria are:

- The event fires one of the triggers used for the analysis (the triggers used will be discussed in section 6).
- The trigger plateau requirements are fulfilled (depending on the trigger fired, once again see section 6).
- Multijet background with $E_{\mathrm{T}}^{\mathrm{miss}}$ due to jet energy mismeasurements is suppressed by requiring that the ϕ angle between the two leading jets and the $E_{\mathrm{T}}^{\mathrm{miss}}$is larger than 0.5, $\Delta\phi(\mathrm{jet}_{1,2}, E_{\mathrm{T}}^{\mathrm{miss}}) > 0.5$. This is further discussed in Section 8.5.

Chapter 6

Trigger Studies

Only events that fire one of the triggers are recorded and processed by the ATLAS detector. Selecting and understanding what triggers to use are the first steps of the event selection. In this section the triggers used by the analysis are described. The selection of the triggers is motivated, measurements of the trigger efficiency and trigger specific scale factors are described. A quick discussion of possible alternative triggers is also included.

6.1 Basic Trigger Ideas

The ATLAS trigger system consists of two main parts - L1 and HLT, described in more details in Section 3.3.6. The HLT triggers only have to process events that have fired a L1 trigger already, it is said that an HLT trigger is seeded by a L1 trigger. What is referred to as a "trigger" is the logical AND of a L1 and an HLT triggers. The events selected by the trigger system are recorded and precise reconstruction and calibration procedures are performed "offline".

The L1 trigger momentum and energy reconstruction is rather imprecise and can differ significantly from the offline reconstruction. If the L1 trigger selects events with the leading jet $p_{\mathrm{T}} > 50$ GeV (at the L1 level) the trigger efficiency as a function of jet p_{T} is a sharp step. The p_{T} of the same object after offline reconstruction can be anywhere between 25 and 75 GeV causing the trigger efficiency to have a turn-on, see Figure 6.1. A selection on the offline objects (such as jet p_{T}, $E_{\mathrm{T}}^{\mathrm{miss}}$ etc) matched to the trigger-level objects is placed to select events for which the trigger is at full efficiency (trigger plateau). In our example of L1 trigger requiring a leading jet $p_{\mathrm{T}} > 50$ GeV we would select events with an offline jet with $p_{\mathrm{T}} > 75$ GeV that is matched to the L1 jet firing the trigger.

The trigger selection should ultimately serve to improve the sensitivity in the signal region. I describe the triggers before the signal region optimisation for better structure and readability, but they do depend on each other. As such I refer to Tables 7.2 and 7.4 that describe unoptimised and fully optimised signal region selections when the effects of some plateau cuts on the signal region need to be evaluated without really explaining why these are used yet. The more involved discussion on how and why these variables are selected to define the signal region are available in Section 7

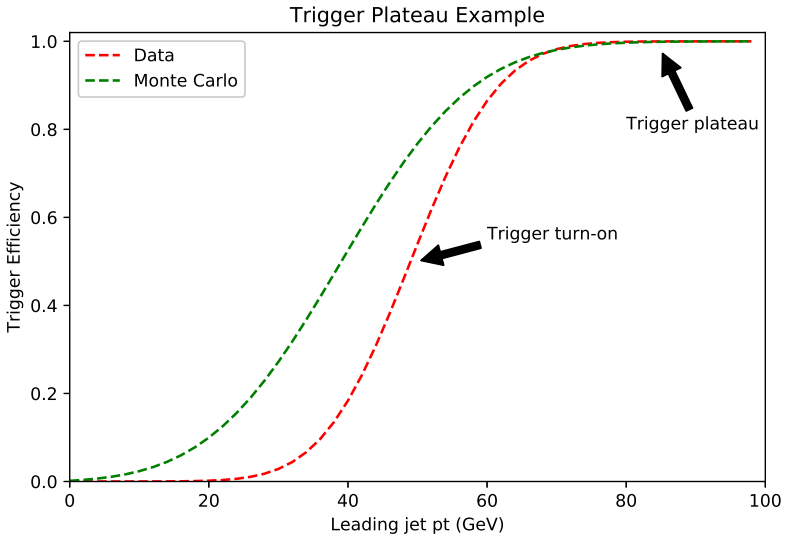

Figure 6.1: An example of trigger efficiency as a function of leading jet p_{T}. The efficiency curves are just used as an example and are not based on any real datasets.

6.2 Trigger Selection

The signatures of interest for the analysis includes b-jets, hadronically decaying tau-leptons and $E_{\mathrm{T}}^{\mathrm{miss}}$ (coming from the $\tilde{\chi}_1^0$ that are stable and invisible to the detector). The triggers used should be based on some of these variables to enhance the selection. A common choice for SUSY searches is to use the lowest unprescaled $E_{\mathrm{T}}^{\mathrm{miss}}$ triggers (i.e. $E_{\mathrm{T}}^{\mathrm{miss}}$ triggers that record every event that fires them). However by themselves they do not provide enough sensitivity in the low $\tilde{\chi}_1^0$ mass region of the $\Delta m(\tilde{\chi}_2^0, \tilde{\chi}_1^0) = 130$ GeV grid.

Triggers based on combination of $E_{\mathrm{T}}^{\mathrm{miss}}$ and b-jets allow for looser cuts on offline $E_{\mathrm{T}}^{\mathrm{miss}}$ than pure $E_{\mathrm{T}}^{\mathrm{miss}}$ triggers. However the efficiency of b-jet based triggers depends on b-tagging that differs between triggers and offline reconstruction. This leads to combined b-jet and $E_{\mathrm{T}}^{\mathrm{miss}}$ triggers missing some events that could be of interest. The lowest unprescaled $E_{\mathrm{T}}^{\mathrm{miss}}$ triggers are used to recover these "lost" events in higher $E_{\mathrm{T}}^{\mathrm{miss}}$ regions of the phase space. In case an event fires both triggers it is treated as if it only fired the $E_{\mathrm{T}}^{\mathrm{miss}}$ trigger.

Figure 6.2a illustrates $E_{\mathrm{T}}^{\mathrm{miss}}$ distributions of backgrounds and benchmark signal points in the unoptimised signal region while the $E_{\mathrm{T}}^{\mathrm{miss}}$ in the fully optimised signal region is shown in Figure 6.2b. These plots suggest that increasing the $E_{\mathrm{T}}^{\mathrm{miss}}$ cut is never beneficial for the significance so that using b-jet + $E_{\mathrm{T}}^{\mathrm{miss}}$ triggers to access lower $E_{\mathrm{T}}^{\mathrm{miss}}$ regions is a good idea.

The trigger menu evolves during the data-taking periods so what triggers are available is also period-dependent. Availability of b-jet + $E_{\mathrm{T}}^{\mathrm{miss}}$ and $E_{\mathrm{T}}^{\mathrm{miss}}$ triggers are summarised in Tables 6.1 and 6.2. $E_{\mathrm{T}}^{\mathrm{miss}}$ triggers are available for the whole Run 2, b-jet + $E_{\mathrm{T}}^{\mathrm{miss}}$ triggers are available during 2016-2018, but many periods during 2016 are vetoed by the b-jet specific GoodRunList (due to the data-MC agreement of the trigger efficiency being off).

What does "b-jet + $E_{\mathrm{T}}^{\mathrm{miss}}$" trigger actually mean? Looking at the Table 6.1, the trig-

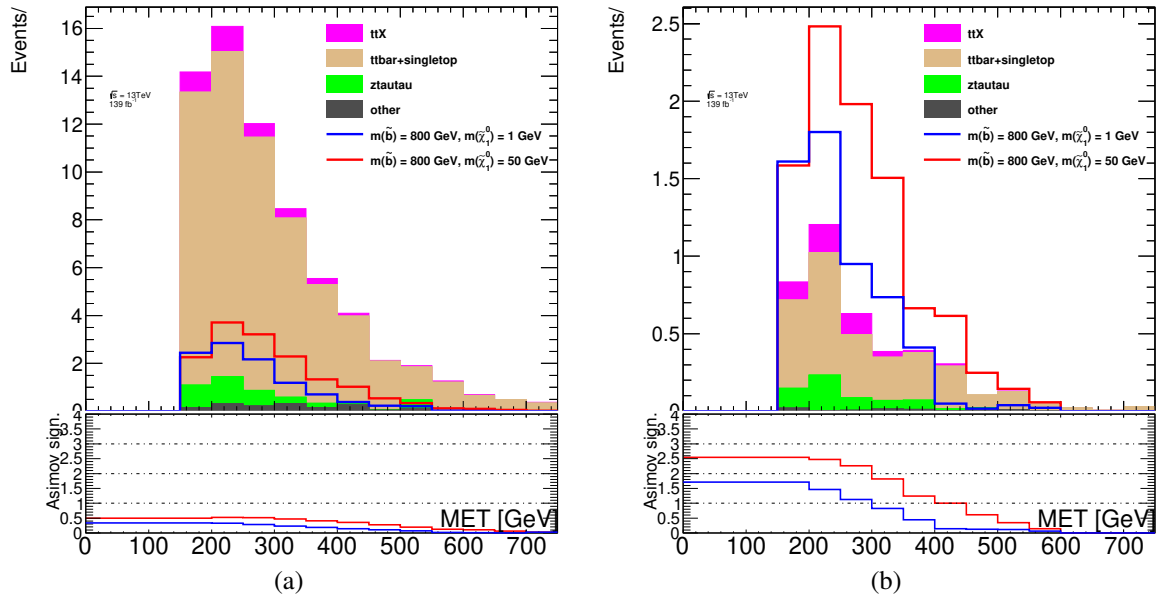

Figure 6.2: (a) Distribution of $E_{\mathrm{T}}^{\mathrm{miss}}$ in SM background and benchmark signal points in the unoptimised SR (see Table 7.2), (b) distribution of $E_{\mathrm{T}}^{\mathrm{miss}}$ in SM background and benchmark signal points in the fully optimised SR (see Table 7.4). The upper panels show distributions of the expected SM yields with the signal yields overlaid. The lower panels show the significance of the signal-plus-background model as described in Section 4.4 with 40% uncertainty on the background events assumed. All yields are scaled to the 139fb^{-1} integrated luminosity.

Table 6.1: A list of combined $E_{\mathrm{T}}^{\mathrm{miss}}$ and b-jet triggers used for the low $\tilde{\chi}_1^0$ region of the $\Delta m(\tilde{\chi}_2^0, \tilde{\chi}_1^0) = 130$ GeV grid. The lowest unprescaled trigger during each data-taking period is shown.

Data Period	Trigger	Luminosity pb^{-1}
Data 2015	not available	
Data 2016	`HLT_j80_bmv2c2060_split_xe60_L12J50_XE40`	24555.6
Data 2017	`HLT_j80_bmv2c1050_split_xe60_L12J50_XE40`	43650.0
Data 2018	`HLT_j80_bmv2c1050_split_xe60_L12J50_XE40`	58450.1

ger for the 2017 data is `HLT_j80_bmv2c1050_split_xe60_L12J50_XE40`. The "HLT" and "L1" parts describe the HLT and L1 parts of the trigger. The L1 trigger is `2J50_XE40` meaning that it requires events with (at least) two jets with $p_{\mathrm{T}} > 50$ GeV and $E_{\mathrm{T}}^{\mathrm{miss}} > 40$ GeV at the L1 level. The HLT part of the trigger is `j80_bmv2c1050_split_xe60` meaning (at least) one "split" jet with $p_{\mathrm{T}} > 80$ GeV that satisfies the b-tagging requirements of the `mv2c10` tagger at the 50% efficiency working point. Additionally $E_{\mathrm{T}}^{\mathrm{miss}} > 60$ GeV is required at the HLT level. It should be noted that despite the HLT part of the trigger requiring only one b-jet, the L1 part does require at least two jets which should be reflected in the trigger plateau selection. Another point that needs to be mentioned is that L1 $E_{\mathrm{T}}^{\mathrm{miss}}$ triggers are notoriously hard to model so that $40-50$ GeV $E_{\mathrm{T}}^{\mathrm{miss}}$ at L1 can result in 200 GeV or more offline $E_{\mathrm{T}}^{\mathrm{miss}}$ needed to reach the plateau.

Table 6.2: A list of lowest unprescaled $E_{\mathrm{T}}^{\mathrm{miss}}$ triggers used for the low $\tilde{\chi}_1^0$ region of the $\Delta m(\tilde{\chi}_2^0, \tilde{\chi}_1^0) = 130$ GeV grid used for the analysis.

Data Period	Period	Trigger
Data 2015	276262-284484	`HLT_xe70_mht`
Data 2016	296939-302872	`HLT_xe90_mht_L1XE50`
Data 2016	302919-303892	`HLT_xe100_mht_L1XE50`
Data 2016	303943-311481	`HLT_xe110_mht_L1XE50`
Data 2017	325713-331975	`HLT_xe110_pufit_L1XE55`
Data 2017	332303-340453	`HLT_xe110_pufit_L1XE50`
Data 2018	348885-350013	`HLT_xe110_pufit_xe70_L1XE50`
Data 2018	350067-364292	`HLT_xe110_pufit_xe65_L1XE50`

6.3 Muon Triggers

The analysis also uses unprescaled single-muon triggers, namely `HLT_mu50` and `HLT_mu26_ivarmedium`. They are used to select events for some of the control regions and to measure the trigger efficiency of $E_{\mathrm{T}}^{\mathrm{miss}}$ and b-jet + $E_{\mathrm{T}}^{\mathrm{miss}}$ triggers, as described in Section 6.4. Single muon triggers are well studied and the trigger plateau recommendations and scale factors are provided centrally [86]. In the analysis whenever the single muon triggers are used the muons are required to be matched, that is the muon as reconstructed by the trigger and by the offline reconstruction should be the same object. The matching is done by comparing the p_{T} vectors of the objects by requiring some minimal separation in ΔR. The offline muon p_{T} cut is set at > 30GeV to select events on the trigger plateau. The scale factors provided by the muon trigger group are applied to improve the data/MC agreement.

6.4 Trigger Efficiency Measurements

After selecting the triggers the corresponding offline plateau cuts need to be defined. For this we need to know the trigger efficiency.

The trigger efficiency is defined as the ratio of the number of events that fire the trigger to the baseline number of events before the trigger is fired. The question is how to select the initial, baseline events to measure the efficiency against. The data events recorded have to have fired some trigger already, preferably one looser than the one being tested to avoid any bias. Another option is to select events that fire triggers based on different objects, like muon-based triggers. The background that is expected to be the largest in most CRs and in the SR is $t\bar{t}$. It is expected to produce muons in the final state so the unprescaled single-muon triggers can be used to measure the trigger efficiency.

First a subset of events is selected by applying $\Delta\phi(\mathrm{jet}_{1,2}, E_{\mathrm{T}}^{\mathrm{miss}}) > 0.5$ cuts that suppress the multijet (QCD) background contribution and requiring the presence of at least 1 muon, 1 tau and 2 b-jets (as the analysis uses at least 2 b-jets in all CRs and SR that use b-jet + $E_{\mathrm{T}}^{\mathrm{miss}}$ triggers). Note that due to the differences in the offline and trigger-level b-tagging the efficiency of b-jet + $E_{\mathrm{T}}^{\mathrm{miss}}$ triggers depends on number of b-jets in an

event as there are more objects that could pass the selection criteria. All CRs and SRs require at least 3 jets so this cut is applied too. Additionally these events are required to fire either `HLT_mu50` or `HLT_mu26_ivarmedium`, one of the two unprescaled single-muon triggers. The trigger efficiency is defined as the ratio of the number of events that pass the initial selection and fire the b-jet + $E_{\mathrm{T}}^{\mathrm{miss}}$ triggers over the number of events that just pass the initial selection. All the additional cuts discussed in this chapter, e.g. b-jet p_{T} cuts, are applied on top of the initial (or baseline) selection.

6.5 Trigger Plateau

The b-jet + $E_{\mathrm{T}}^{\mathrm{miss}}$ triggers require a 80 GeV p_{T} HLT-level b-jet. The minimal offline cuts needed to account for that are found to be $p_{\mathrm{T}} \geq 100$ GeV for the b-jet. Such a cut is obviously excessive for the $E_{\mathrm{T}}^{\mathrm{miss}}$ triggers. However the signal in the signal region tends to have high leading b-jet p_{T}. Events in the unoptimised signal region (see Table 7.2) that would have fired the $E_{\mathrm{T}}^{\mathrm{miss}}$ triggers were selected and the b-jet p_{T} measured, see Figure 6.3. To keep the definition of the trigger plateau consistent between the triggers the leading b-jet $p_{\mathrm{T}}>$ 100 GeV cut is kept for $E_{\mathrm{T}}^{\mathrm{miss}}$ triggers. It is only relaxed when a need to access a region without any b-jets arises.

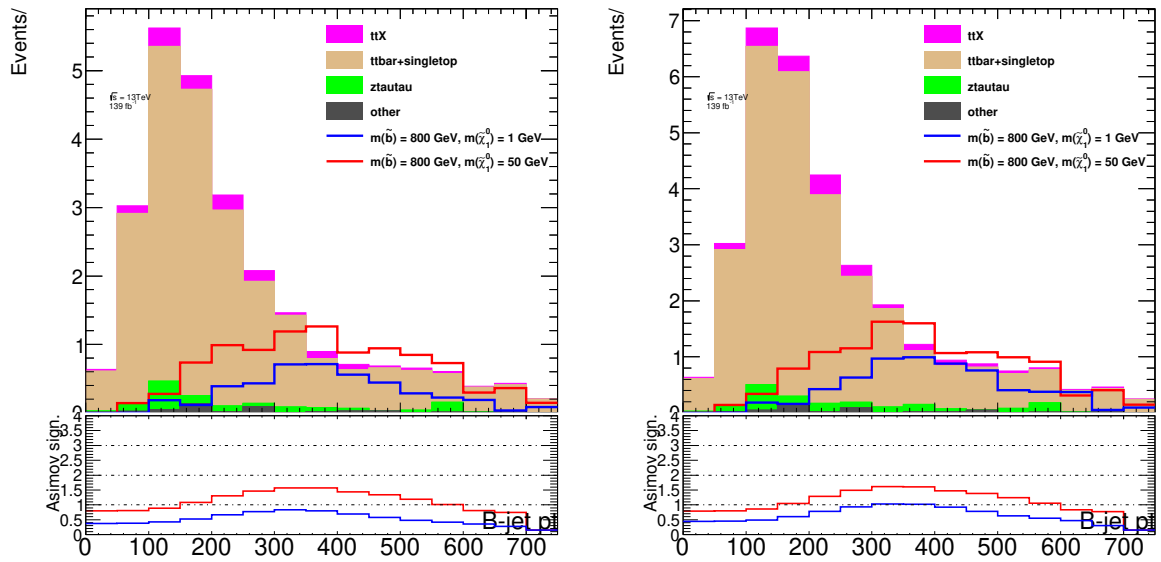

(a) (b)

Figure 6.3: Leading b-jet p_{T} in the unoptimised signal region (see Table 7.2) with ditau mass cuts applied. (a) shows the selection that includes only the events that would fire one of the lowest unprescaled $E_{\mathrm{T}}^{\mathrm{miss}}$ triggers and pass all plateau cuts with the exception of b-jet p_{T} cuts. (b) shows the selection with the combined b-jet + $E_{\mathrm{T}}^{\mathrm{miss}}$ and $E_{\mathrm{T}}^{\mathrm{miss}}$ triggers where the b-jet p_{T} cuts are relaxed for $E_{\mathrm{T}}^{\mathrm{miss}}$ triggers. The upper panels show distributions of the expected SM yields with the signal yields overlaid. The lower panels show the significance of the signal-plus-background model as described in Section 4.4 with 40% uncertainty on the background events assumed. All yields are scaled to the 139fb^{-1} integrated luminosity.

The combined $E_{\mathrm{T}}^{\mathrm{miss}}$ and b-jet triggers are seeded by the `L12J50_XE40` L1 trigger. That means the cuts have to include at least 2 jets in addition to the $E_{\mathrm{T}}^{\mathrm{miss}}$ and a b-

tagged jet p_T requirements. The optimal jet p_T cuts were found to be > 140 GeV p_T for the leading jet and > 100 GeV p_T for the sub-leading jet. Such a configuration selects slightly boosted systems that helps lowering the E_T^{miss} cuts. Pure E_T^{miss} triggers are mostly seeded by the `L1_XE50` L1 trigger so in principle only E_T^{miss} cuts are ne eded to reach the trigger plateau. However it was found that requiring p_T cuts on the two leading jets helps with lowering the E_T^{miss} trigger plateau, similar to what was found in the "tau+X" analysis [4]. This allows to keep a common plateau definition for b-jet + E_T^{miss} and E_T^{miss} triggers with the only difference being the E_T^{miss} cut.

The E_T^{miss} triggers only use the inner detector and calorimeter information which means muons do not participate in the online E_T^{miss} computation. To account for that the offline E_T^{miss} is recomputed with muons treated as invisible particles. The analysis makes use of control and validation regions with and without muons. For regions with muon veto the E_T^{miss} with invisible muons is used for trigger efficiency calculations, see Figure 6.4. For regions where muons are already present normal E_T^{miss} is used to determine the plateau cut, see Figure 6.5. Since the two approaches agree to a large degree a single offline E_T^{miss} cut is derived from the two values, $E_T^{miss} > 160$ GeV. It should be noted that the trigger efficiency is still in the last stage of the turn-on at $E_T^{miss} = 160$ GeV, but the agreement between the data and the MC is good.

The efficiency of the E_T^{miss} trigger is measured in a similar way, see Figures 6.6-6.7 for trigger efficiencies measured with and without treating muons as invisible. The plateau cut is determined to be at $E_T^{miss} \geq 200$ GeV. Similarly to the b-jet + E_T^{miss} case the efficiency is still in the last stage of the turn-on, but the data and the MC agree well so the lower E_T^{miss} cut is justified. To make it clear, the E_T^{miss} with muons treated as invisible is only used for trigger efficiency calculations and nowhere else.

The trigger efficiency is measured using SUSY3 and SUSY5 derivations (since they are used in the analysis). The SUSY3 derivation requires the presence of a loose tau while the SUSY5 derivation requires a presence of a muon or an electron. As the result the SUSY3 selection is more restrictive, but still probes $t\bar{t}$ well which is the principal background. As an additional check MC events are selected using the looser `HLT_xe70_mht` trigger as the baseline that only requires $/geq70$ GeV E_T^{miss} at the HLT level (it is heavily prescaled in data, hence why it is only used for MC). It is meant to be a realistic approximation of how the trigger efficiency is in Monte Carlo without an additional muon being selected. The event selection used to derive trigger efficiency as a function of E_T^{miss} is summarised in Table 6.3. The trigger plateau requirements are summarised in Table 6.4.

6.6 Trigger Scale Factors

In the case of E_T^{miss} triggers the efficiency plateau is at $\approx 100\%$ for both data and MC and the agreement in the turn-on region is reasonable so no additional corrections are needed. The b-jet + E_T^{miss} triggers require a per-b-jet scale factor (SF) for each offline b-jet matched to a trigger-level b-jet to improve the data/MC agreement. The SFs are dependant on the jet p_T and on the efficiency of the offline and online b-tagging working points (WPs, see Section 5.5) used. For this analysis the online WPs are 60% efficiency in 2016 and 50% efficiency in 2017-2018 while the offline WP is always 77% efficiency. The per-b-jet SFs are provided by the b-jet trigger signature group and are

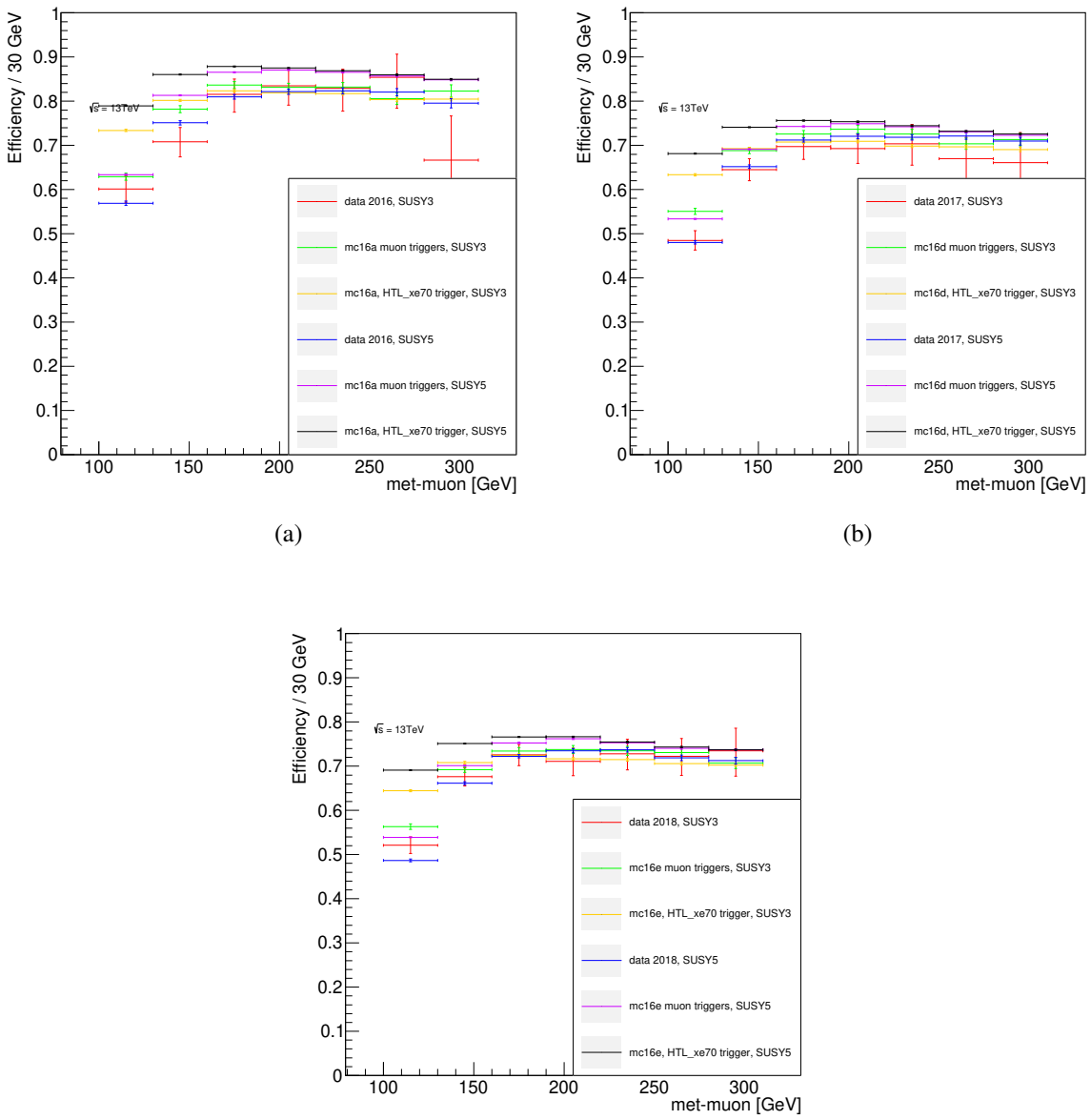

(a) (b)

(c)

Figure 6.4: Trigger turn on curves with respect to the single-muon triggers baseline as a function of offline $E_{\mathrm{T}}^{\mathrm{miss}}$ with invisible muons. All other cuts including jet p_{T} are applied. An offline $E_{\mathrm{T}}^{\mathrm{miss}} \geq 160$ GeV is required for triggers to reach the plateau. Trigger SFs are applied. (a) `HLT_j80_bmv2c2060_split_xe60_L12J50_XE40` trigger, 2016 dataset, $E_{\mathrm{T}}^{\mathrm{miss}}$ with invisible muons. (b) `HLT_j80_bmv2c1050_split_xe60_L12J50_XE40` trigger, 2017 dataset, $E_{\mathrm{T}}^{\mathrm{miss}}$ with invisible muons. (c) `HLT_j80_bmv2c1050_split_xe60_L12J50_XE40` trigger, 2018 dataset, $E_{\mathrm{T}}^{\mathrm{miss}}$ with invisible muons.

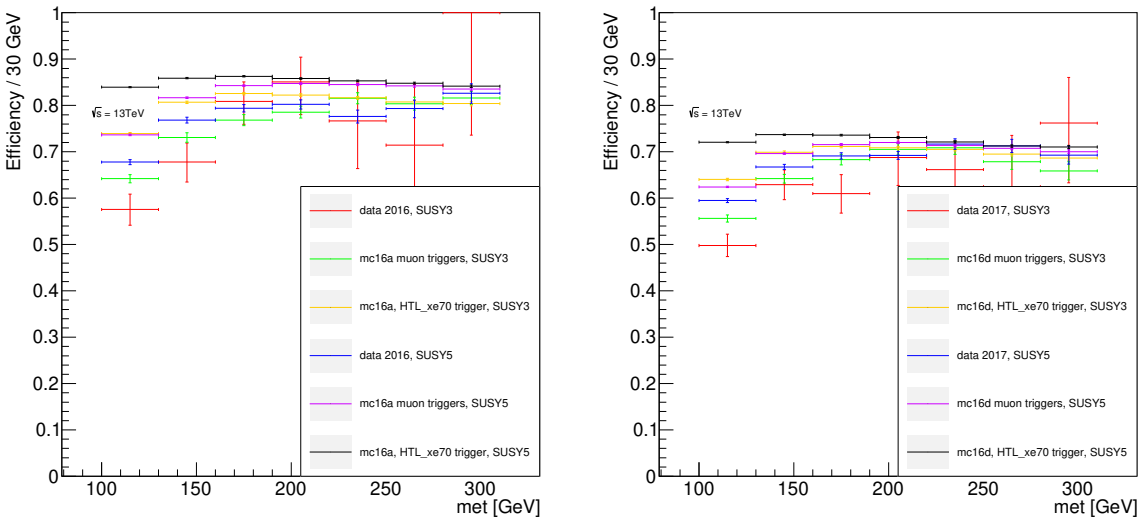

(a) (b)

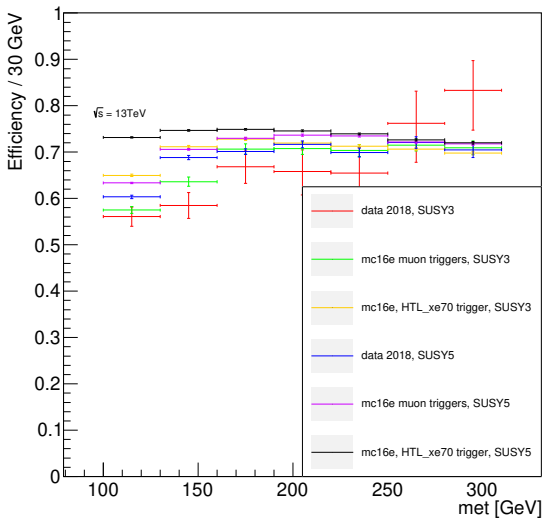

(c)

Figure 6.5: Trigger turn on curves with respect to the single-muon triggers baseline as a function of offline $E_{\mathrm{T}}^{\mathrm{miss}}$. All other cuts including jet p_{T} are applied. An offline $E_{\mathrm{T}}^{\mathrm{miss}} \geq 160$ GeV is required for triggers to reach the plateau. Trigger SFs are applied. (a) `HLT_j80_bmv2c2060_split_xe60_L12J50_XE40` trigger, 2016 dataset, $E_{\mathrm{T}}^{\mathrm{miss}}$. (b) `HLT_j80_bmv2c1050_split_xe60_L12J50_XE40` trigger, 2017 dataset, $E_{\mathrm{T}}^{\mathrm{miss}}$. (c) `HLT_j80_bmv2c1050_split_xe60_L12J50_XE40` trigger, 2018 dataset, $E_{\mathrm{T}}^{\mathrm{miss}}$.

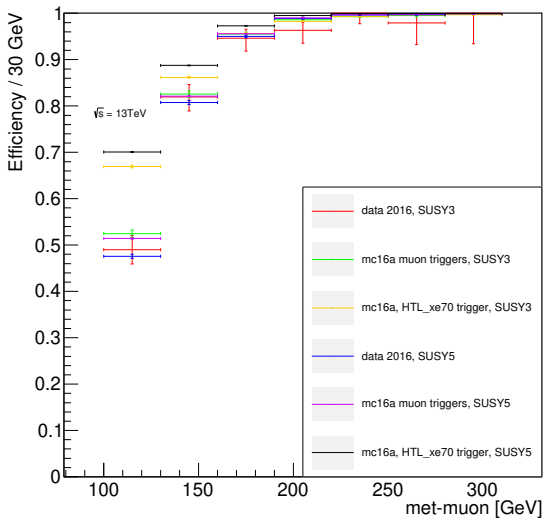

(a)

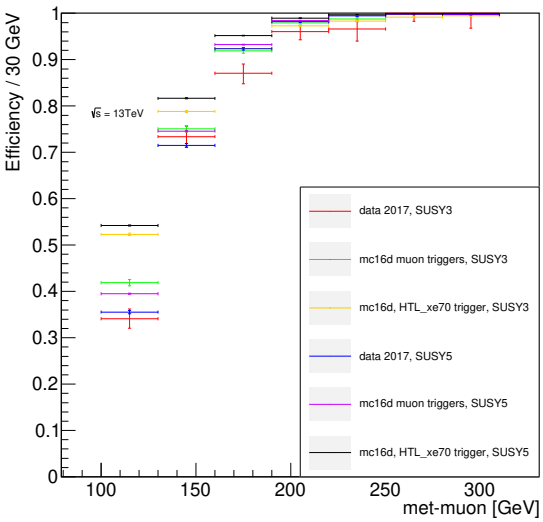

(b)

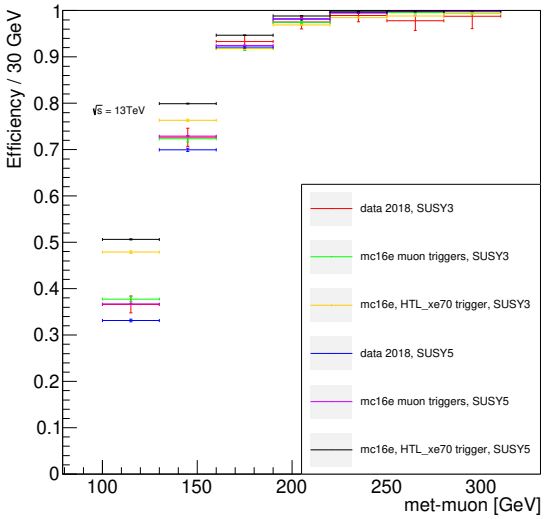

(c)

Figure 6.6: Trigger turn on curves with respect to single-muon triggers as a function of offline $E_{\mathrm{T}}^{\mathrm{miss}}$ with invisible muons. All other cuts including jet p_{T} are applied. An offline $E_{\mathrm{T}}^{\mathrm{miss}} \geq$ 200 GeV is required for triggers to reach the plateau. Lowest unprescaled $E_{\mathrm{T}}^{\mathrm{miss}}$ trigger for the (a) 2015-2016, (b) 2017 and (c) 2018 datasets.

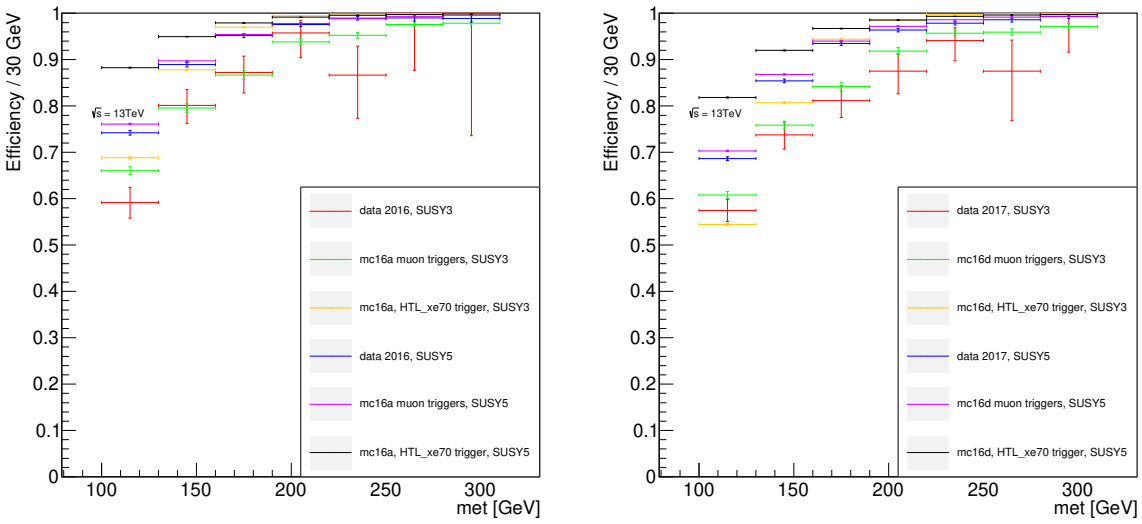

(a) (b)

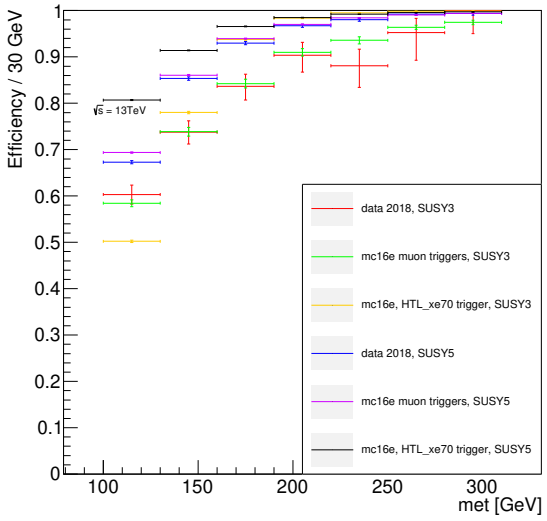

(c)

Figure 6.7: Trigger turn on curves with respect to single-muon triggers as a function of offline $E_{\mathrm{T}}^{\mathrm{miss}}$. All other cuts including jet p_{T} are applied. An offline $E_{\mathrm{T}}^{\mathrm{miss}} \geq 200$ GeV is required for triggers to reach the plateau. Lowest unprescaled $E_{\mathrm{T}}^{\mathrm{miss}}$ trigger for the (a) 2015-2016, (b) 2017 and (c) 2018 datasets.

Table 6.3: Summary of the cuts applied to study the turn-on of b-jet + $E_{\mathrm{T}}^{\mathrm{miss}}$ and $E_{\mathrm{T}}^{\mathrm{miss}}$ triggers.

Derivation	SUSY3	SUSY5	SUSY3
Lowest unprescaled trigger	`HLT_mu`	`HLT_mu`	`HLT_xe`
Anti-QCD cut	$\Delta\phi(\mathrm{jet}_{1,2}, E_{\mathrm{T}}^{\mathrm{miss}}) > 0.5$		
Number of signal muons	≥ 1	≥ 1	0
p_{T}(muon)	≥ 30 GeV	≥ 30 GeV	0
Number of loose taus	1	0	1
p_{T}(tau)	≥ 20 GeV	0	≥ 20 GeV
Number of signal jets	≥ 3	≥ 3	≥ 3
Number of signal b-jets (77% WP)	2	2	2
p_{T}(leading b-jet)	$\geq$100 GeV	$\geq$100 GeV	$\geq$100 GeV
p_{T}(leading jet)	$\geq$140 GeV	$\geq$140 GeV	$\geq$140 GeV
p_{T}(sub-leading jet)	$\geq$100 GeV	$\geq$100 GeV	$\geq$100 GeV

Table 6.4: Summary of the plateau cuts applied to b-jet + $E_{\mathrm{T}}^{\mathrm{miss}}$ and $E_{\mathrm{T}}^{\mathrm{miss}}$ triggers.

	b-jet + $E_{\mathrm{T}}^{\mathrm{miss}}$	$E_{\mathrm{T}}^{\mathrm{miss}}$
N_{jet}	≥ 3	
$\Delta\phi(\mathrm{jet}_{1,2}, E_{\mathrm{T}}^{\mathrm{miss}})$	> 0.5	
$N_{b-\mathrm{jet}}$	≥ 2	
$N_\tau + N_\mu$	≥ 1	
p_{T}(leading b-jet)	≥ 100 GeV	
p_{T}(leading jet)	≥ 140 GeV	
p_{T}(second jet)	≥ 100 GeV	
$E_{\mathrm{T}}^{\mathrm{miss}}$($b$-jet + $E_{\mathrm{T}}^{\mathrm{miss}}$trigger)	≥ 160 GeV	≥ 200 GeV

combined to total per-event efficiencies based on the number of offline b-jets that are matched to the online b-jets. These weights are applied to all the events in the analysis that fire a b-jet + $E_{\mathrm{T}}^{\mathrm{miss}}$ trigger and have an offline b-jet that is matched to the jet that fired the trigger.

When more than one object per event can fire a trigger (as is the case with b-jet + $E_{\mathrm{T}}^{\mathrm{miss}}$ triggers since event selection requires at least 2 b-jets) additional care must be taken when applying the SFs. The scale factors however are computed per b-jet. It is possible to compute the correction per-event by taking all possible combinations of b-jets that can fire the trigger, applying the corrections to them and summing everything up, but it is much easier to compute the probability $\overline{P(event)}$ that exactly 0 b-jets fire the trigger (with the SFs applied) and to use $1-\overline{P(event)}$:

$$\begin{aligned}\overline{P(event)} &= \overline{P(obj1|obj2|obj3)} \\ &= \overline{P(obj1)P(obj2)P(obj3)} \\ &= (1-P(obj1))(1-P(obj2))(1-P(obj3))\end{aligned} \tag{6.1}$$

In this form it is straightforward to apply per-object SFs and to compute the total trigger efficiency $P(event) = 1-\overline{P(event)}$.

Important to note is that the SUSY5 MC samples lack the data needed to perform matching with the online b-jet. A simplified approach is used where a b-jet is consid-

ered as matched to the online b-jet if it has $p_{\mathrm{T}} > 100$ GeV. This approach has been found to lead to 3-4% overestimation of the number of events that pass the trigger plateau selection compared to the properly matched b-jets (and, consequently, data). B-jet + $E_{\mathrm{T}}^{\mathrm{miss}}$ triggers are only used in one auxiliary region with SUSY5 and only contribute around 30% of the events in that region so this is not an issue for the overall analysis, but it causes the efficiency plots to have some disagreement between SUSY5 data and MC.

6.7 Alternative Triggers

In this section a quick overview of alternative triggers that were considered for the analysis, but ultimately were not used is given.

Tau-based triggers have been considered, but signal taus have rather low p_{T} so that the trigger selection actively hurts sensitivity. Lowest unprescaled single tau trigger in 2018 fires on tau-leptons with $p_{\mathrm{T}} > 160$ GeV at the HLT level. Di-tau trigger requires the leading tau to have $p_{\mathrm{T}} > 80$ GeV and second leading tau to have $p_{\mathrm{T}} > 35$ GeV. Similar argument applies to pure b-jet triggers and mixed jets + b-jets triggers. The expected p_{T} of leading tau and b-jet in the unoptimised signal region are shown in Figure 6.8. Combined tau and $E_{\mathrm{T}}^{\mathrm{miss}}$ triggers have been considered for the analysis too, but the signal can accommodate b-jet p_{T} cuts better than tau p_{T} cuts required by the trigger so b-jet + $E_{\mathrm{T}}^{\mathrm{miss}}$ triggers are more advantageous, see Figure 6.8.

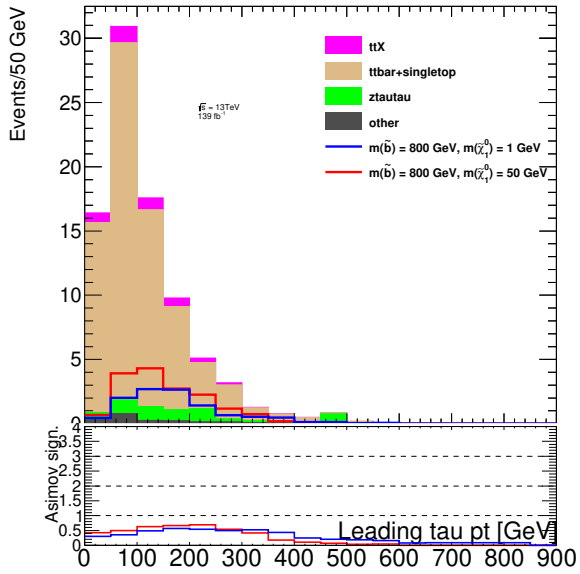

(a) Leading tau p_{T} in the unoptimised signal region.

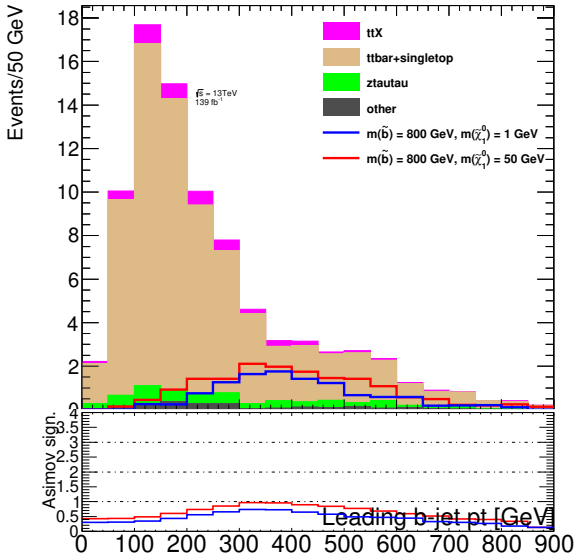

(b) Leading b-jet p_{T} in the unoptimised signal region.

Figure 6.8: p_{T} of (a) the leading tau and (b) the leading b-jet in the unoptimised signal region for background and signal estimations. The upper panels show distributions of the expected SM yields with the signal yields overlaid. The lower panels show the significance of the signal-plus-background model as described in Section 4.4 with 40% uncertainty on the background events assumed. All yields are scaled to the 139fb^{-1} integrated luminosity. Leading tau p_{T} is generally lower than the leading b-jet p_{T}, making b-jet based triggers more desirable.

Chapter 7

Signal Regions Design

In this section the design of the signal regions that are sensitive to the potential signal contribution is described. Everything discussed in this chapter is based on Monte-Carlo estimations only and no fitting strategies are employed at this point.

7.1 Basic Considerations

The signature of interest for the signal is at least two taus with opposite charge and at least two b-jets. If more than two taus or b-jets are present in an event only the two leading ones are considered. The taus are expected to be coming from the SM Higgs boson decay while the b-jets could be coming from the $\tilde{b}$ decay or from the second Higgs boson decay. Requiring at least 2 b-jets and 2 taus serves not only to suppress the background directly, but also allows for definition of more effective discriminating variables. This claim will be motivated later in the section after the criteria for what is considered an "effective selection" are defined.

The region of the phase space on which the initial selection is performed is referred to as the "unoptimised" signal region in the following. It is defined by requiring that an event fires a trigger, satisfies the trigger plateau requirements and has at least two hadronically decaying taus with opposite signs. The definitions are summarised in Table 7.2. Note that the $H_{\mathrm{T}} > 1000$ GeV cut is included in the selection, this is done to increase the purity of the signal and to make the plots more clear, the validity of this selection will be argued further in this section.

The contributions to the background from various processes in the unoptimised signal region are summarised in Table 7.3. Based on the background composition the overall strategy for the signal regions is to primarily suppress semi-leptonic and fully leptonic $t\bar{t}$ production. After the plateau cuts, $t\bar{t}$ production is by far the largest background, but as the selection gets tighter subdominant backgrounds like $Z(\tau\tau) + b\bar{b}$, single top production and $t\bar{t}X$ ($t\bar{t}Z$ and $t\bar{t}H$) can become non-negligible. $t\bar{t}$ and single top production result in a mix of 2 true taus and 1 true + 1 fake tau signatures while $Z(\tau\tau)$ and $t\bar{t}X$ contributions are dominated by 2 true taus. This is further discussed in Section 8. Other SM backgrounds are negligible. The multijet background is efficiently suppressed by a $\Delta\phi(\mathrm{jet}_{1,2}, E_{\mathrm{T}}^{\mathrm{miss}}) > 0.5$ requirement as discussed in Section 8.

A signal region, by definition, is a combination of requirements (or cuts) on kinematic variables that enhance the expected signal yield compared to the background. Estimated Asimov significance Z_A [59] is used to evaluate the signal to background

ratio, see also Section 4.4.

$$Z_A = \left[2\left((s+b)\ln[\frac{(s+b)(b+\sigma_b^2)}{b^2+(s+b)\sigma_b^2}] - \frac{b^2}{\sigma_b^2}\ln[1+\frac{s\sigma_b^2}{b^2+b\sigma_b^2}]\right)\right]^{\frac{1}{2}} \tag{7.1}$$

In this case the background uncertainty σ_b is assumed to be 40%, based on typical uncertainties seen in similar analyses (e.g. [87]). Also important to note is that the estimation Z_A starts to break down when the number of events is lower than 1-2. While no hard lower bounds are placed an effort is made to keep the number of expected background events in the SR higher than 2.

Generally speaking any kinematic variable can be used as a discriminator to separate the signal from the background, but some are more efficient than the others. Estimated significance Z_A is used to compare the effectiveness of the variables as well as to determine the cuts themselves. The study is performed on all available signal samples, but for the sake of clarity, only the performances of two benchmark samples are shown in the plots. Both points are high sbottom mass points (see Table 7.1) on the edge of sensitivity of the analysis.

Table 7.1: Benchmark signal points.

Point	$m_{\tilde{b}}$	$m_{\tilde{\chi}_2^0}$	$m_{\tilde{\chi}_1^0}$
Point 1	800 GeV	131 GeV	1 GeV
Point 2	800 GeV	180 GeV	50 GeV

7.2 Signal Region Optimisation

The "baseline" signal region selection includes the requirements of at least 2 hadronically decaying taus, at least 2 b-jets, one of the triggers has to be fired and the event satisfies the corresponding trigger plateau selection. The taus are required to have opposite charges. Muon veto is applied to ensure orthogonality with the events used for the trigger efficiency estimation (and the signal is not expected to produce a muon either). The multijet-suppressing cuts are also applied, as described in Section 5.6. These selections are summarised in Table 7.2. The $H_{\mathrm{T}} > 1000$ GeV is included in the definition of the baseline signal region. This inclusion is based on the fact that the H_{T} is used in the final selection of the signal regions (with a tighter cut applied) and that the control regions are defined to have $H_{\mathrm{T}} < 1000$ GeV for orthogonality, also see Figure 7.3a.

The optimisation is performed on top of the baseline selection. The general procedure is the following – for each variable considered the Asimov significance Z_A is calculated as a function of the cut on the variable, a scan in significance is performed. This process is repeated for each signal model. The goal is to select one common value that improves the significance for all signal points (or to discard the variable if it isn't helpful). Different signal models respond differently to various cuts, it is not always straightforward to select one common cut. The following criteria are used:

Table 7.2: Summary of the "unoptimised" or "baseline" signal region, the basic selection on which further optimisation is performed.

N_{jet}	≥ 3
$\Delta\phi(\text{jet}_{1,2}, E_{\text{T}}^{\text{miss}})$	> 0.5
$N_{b-\text{jet}}$	≥ 2
N_{τ}	≥ 2
N_{μ}	0
p_{T}(leading b-jet)	≥ 100 GeV
p_{T}(leading jet)	≥ 140 GeV
p_{T}(second jet)	≥ 100 GeV
$E_{\text{T}}^{\text{miss}}$ (b-jet + $E_{\text{T}}^{\text{miss}}$ trigger)	≥ 160 GeV
$E_{\text{T}}^{\text{miss}}$ ($E_{\text{T}}^{\text{miss}}$ trigger)	≥ 200 GeV
Tau opposite charge	$\text{OC}(\tau_1, \tau_2)$
Scalar p_{T} sum	$H_{\text{T}} \geq 1000$ GeV

Table 7.3: Expected background yields before any optimisation cuts in the SR (see Table 7.2), pre-fit, showing statistical uncertainty only.

Background	Weighted yield (pre-fit)
$Z(\mu\mu)$	0 ± 0
$Z(ee)$	0 ± 0
$W(e\nu)$	0.0205 ± 0.016
$Z(\nu\nu)$	0.0394 ± 0.0287
$W(\mu\nu)$	0.0487 ± 0.0249
Di- and triboson	0.361 ± 0.0818
$W(\tau\nu)$	1.18 ± 0.323
$t\bar{t}X$	3.47 ± 0.218
$Z(\tau\tau)$	4.36 ± 0.826
Single top	8.16 ± 0.722
$t\bar{t}$	50.9 ± 0.961
$m_{\tilde{b}} = 800, m_{\tilde{\chi}_2^0} = 131$	6.56 ± 0.48
$m_{\tilde{b}} = 800, m_{\tilde{\chi}_2^0} = 180$	12.10 ± 0.65

- Significance improvement for high sbottom mass models. If low sbottom mass points are hurt too much a separate signal region for them could be considered. This didn't turn out to be a problem for the analysis.

- Physical motivation should be well understood. Many kinematic variables are correlated to some degree, understanding what causes the difference between signal and background is crucial in selecting the most powerful discriminators.

- Significance should have similar shapes for all signal models considered. This is required to ensure that the discriminating power is due to the properties of the signal models and not because of statistical fluctuations in some of the samples.

- Finally, an attempt is made to keep the background "reasonably large". This is

useful for both applying further cuts and for keeping the background modelling reliable and not completely dominated by statistical uncertainties.

After a cut on a variable is fixed it is applied to the selection on which the optimisation is performed. After the final selection has been established the order of the cuts is varied to ensure that there are no issues with the possible correlations.

First the discrete variables were scanned in significance - number of jets, b-jets and hadronically decaying taus. Minimum number of jets is set to 3 due to mismodelling issues in vector boson samples for low jet multiplicity. For N_τ and $N_{b-\text{jet}}$ the minimum is set at 1 each since the SUSY3 derivation already requires at least 1 tau and the b-jet + $E_{\text{T}}^{\text{miss}}$triggers require at least 1 b-jet.

Parallel to the scan on the number of b-jets and taus the working points have been varied. For b-jets the nominal 77% efficiency has been compared to tighter 70% and 60% working points and for taus the nominal "loose" selection was compared to "medium" and "tight". Changing the tau definitions didn't lead to noticeable improvements. Changing the b-tagging requirements to tighter working points leads to slightly better significance, but reduces number of events available for further optimisation and, after full selection, results in similar significance to the nominal working point. The 77% efficiency b-jets and "loose" taus are therefore used.

As the next step various continuous variables that are typical for SUSY searches are scanned. The variables considered include $E_{\text{T}}^{\text{miss}}$, H_{T}, m_{T2}, p_{T} of jets, b-jets and taus, $E_{\text{T}}^{\text{miss}}$ significance, m_{T}^{τ} and variables based on angles and ΔR between objects. In the end four variables were selected as the most effective. They are summarised in Table 7.4 and presented in N-1 plots (i.e. all other cuts except the plotted one have been applied).

Some of the variables that were considered for the SR optimisation, but were not effective enough are gathered in Figures 7.1. The (N-1) plots wouldn't make much sense when the variable itself isn't part of the final cuts so yields in the unoptimised SR are used instead. For comparison $\min_{\Theta}$ (one of the variables used for the SR cuts) is also plotted in the unoptimised SR, see Figure 7.3b. As the final remark, the subleading b-jet p_{T} (Figure 7.1a) has good discriminating power, but unfortunately cuts away too much signal and background to be useful for further optimisation.

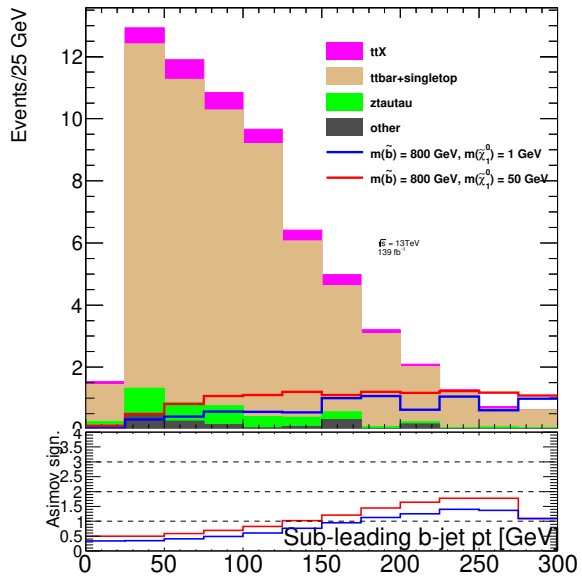

(a) Second b-jet p_{T} in the unoptimised signal region.

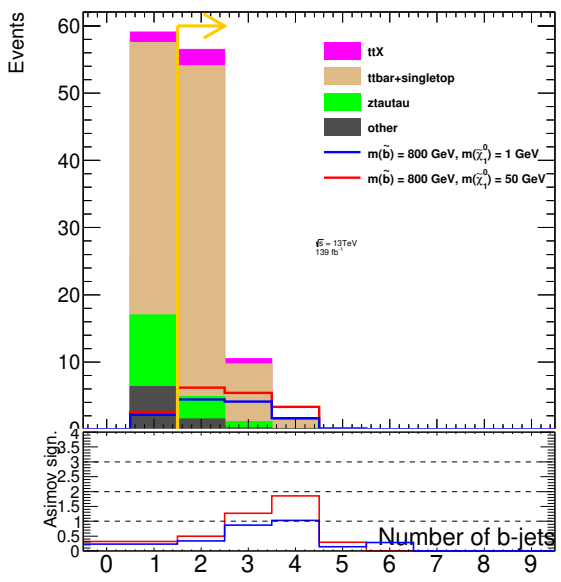

(b) Number of b-jets in the unoptimised signal region.

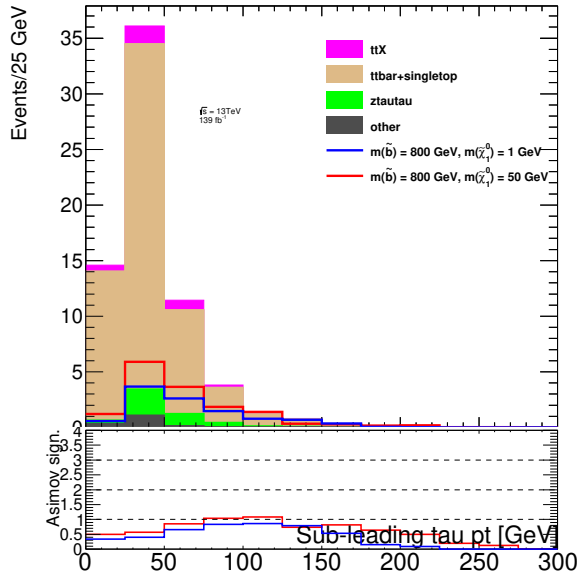

(c) Second tau p_{T} in the unoptimised signal region.

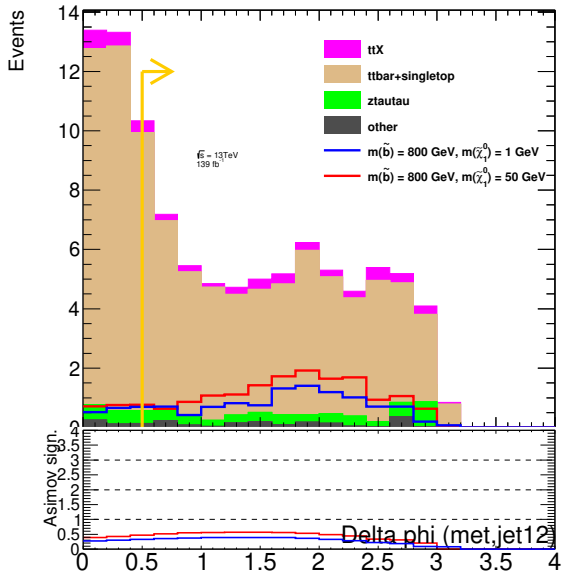

(d) $\Delta\phi(\mathrm{jet}_{1,2}, E_{\mathrm{T}}^{\mathrm{miss}})$ in the unoptimised signal region.

Figure 7.1: Kinematic variables considered for the signal region definition in the unoptimised signal region. Signal is normalised to the expected cross section. The upper panels show distributions of the expected SM yields with the signal yields overlaid. The lower panels show the significance of the signal-plus-background model as described in Section 4.4 with 40% uncertainty on the background events assumed. All yields are scaled to the 139 fb^{-1} integrated luminosity. Arrows show the cuts that are part of the trigger plateau requirements.

7.3 Discriminating Variables

The invariant mass of the ditau system is used as one of the discriminating variables. Since $t\bar{t}$ production is the dominant background most of the taus in the background are not expected to come from the decay of one massive particle. The invariant mass of

background taus has a much wider distribution than that of signal taus as demonstrated in Figure 7.5a. A requirement of $55 \leq m(\tau_1 + \tau_2) \leq 120$ GeV cuts away background tails while leaving the signal events mostly untouched.

Table 7.4: Summary of the single-bin signal region optimisation cuts. These are applied on top of the basic selection summarised in Table 7.2.

Invariant mass of ditau	$55 \leq m(\tau_1 + \tau_2) \leq 120$ GeV
Scalar p_{T} sum	$H_{\mathrm{T}} \geq 1100$ GeV
Stransverse mass	$m_{\mathrm{T2}} \geq 140$ GeV
Minimal angle tau/b-jet	$\min_{\Theta} \geq 0.6$

For signal events, the scalar sum of the transverse momenta H_{T} is expected to be large outside of the compressed low sbottom mass region. The model considered includes production of two b-jets in addition to the decay products of two Higgs bosons. While the background distribution is falling off sharply, the signal exhibits a harder spectrum, see Figure 7.5b. The cut is selected to be $H_{\mathrm{T}} \geq 1100$GeV.

The Higgs bosons produced in signal events are expected to be slightly boosted. The taus resulting from the Higgs decay are thus expected to be somewhat collinear and mostly independent of the b-jet directions. On the other hand, the taus and b-jets from $t\bar{t}$ decays are expected to be more collinear (pairwise) as they are coming from the decays of the same particle. Different functions of angles between the two taus and the two b-jets have been considered and the minimum of the four angles between tau and b-jet was chosen, $\min_{\Theta}$. Background distributions (mostly $t\bar{t}$) are expected to peak closer to 0 than the signal as can be seen in Figure 7.5c. The cut is set at $\min_{\Theta} \geq 0.6$.

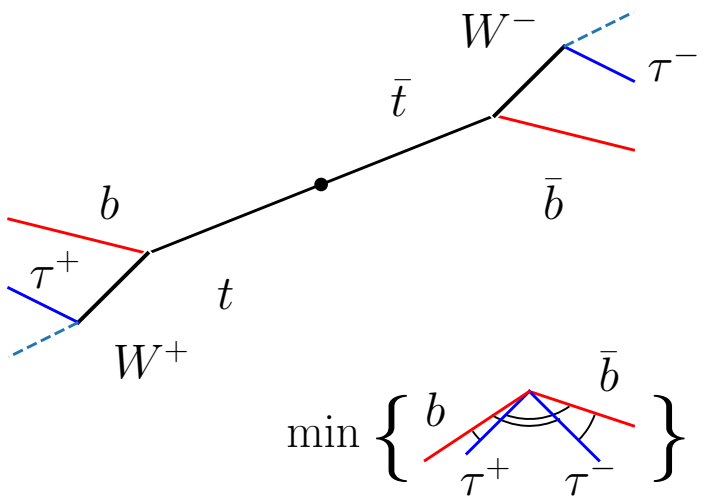

(a)

Figure 7.2: Schematic illustration of the $\min_{\Theta}$ variable for a $t\bar{t}$event.

The last variable used is the stransverse mass m_{T2}. It is yet another variable that re-

lies on the fact that the signal taus come from the decay of the same massive particle while the background ($t\bar{t}$ and singletop) taus in general don't. This difference is well captured by the m_{T2} even if the interpretation of the stransverse mass of two taus from a resonance isn't quite trivial. In combination with the minimal angle $\min_\Theta$ it suppresses most of the expected background contribution as evidenced by Figure 7.5d. The current analysis setup assumes that the two τ leptons are coming from the decay of two invisible particles with masses of 120 GeV. This is further discussed in Appendix A.

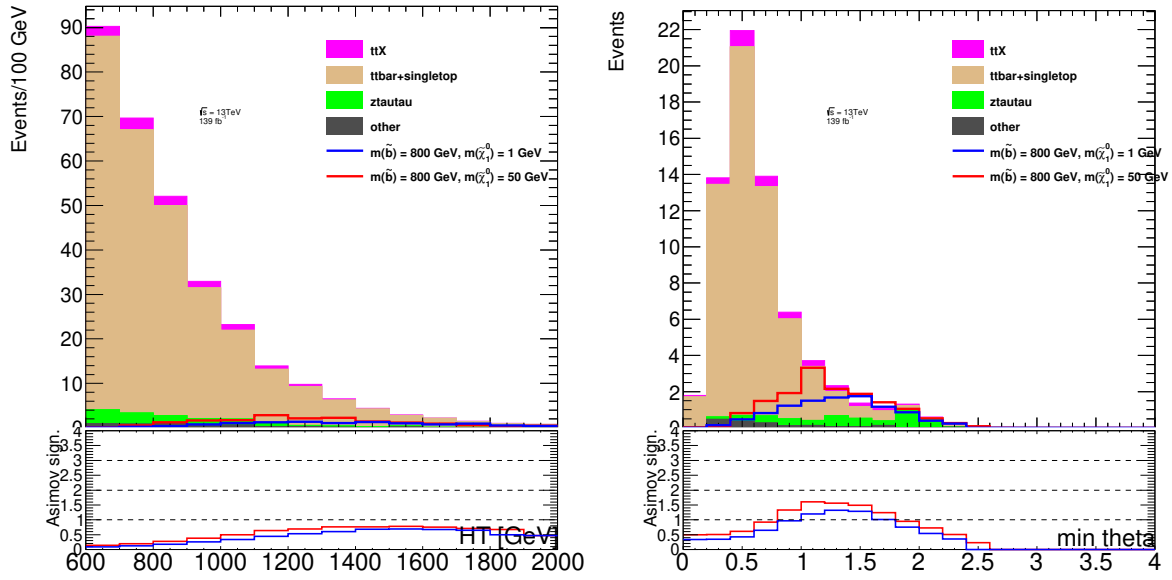

(a) H_T in the unoptimised SR.

(b) $\min_\Theta$ in the unoptimised SR.

Figure 7.3: (a) Extended H_T range (covering CR and SR ranges). (b) $\min_\Theta$ in the unoptimised SR. Signal is normalised to the expected cross section. The lower panels show the significance of the signal-plus-background model as described in Section 4.4 with 40% uncertainty on the background events assumed. All yields are scaled to the 139 fb^{-1} integrated luminosity.

The expected significance for various signal points is summarised in Figure 7.6a and the expected signal yields in Figure 7.6b. The expected contribution of various SM backgrounds and the corresponding raw number of MC events are summarised in Table 7.5.

7.4 Multi-bin Fit

An improvement over the single-bin SR (as described in the previous section) is to relax one of the SR variables and perform a multi-bin fit on it, i.e. an exclusion fit (see section 4.5) that is aware of the shape of the variable. $\min_\Theta$ variable is used to define bins used for the multi-bin fit. H_T bins have been considered as an alternative, but $\min_\Theta$ was selected over it since the modelling of the variable is more robust and more events are available for the fit. The modelling of the $\min_\Theta$ variable is further discussed in Section 8.7.

The multi-bin SR is defined by relaxing the $\min_\Theta > 0.6$ cut of the single-bin discovery SR. The multi-bin SR is divided in 3 bins, 2 bins of size 0.5 starting from 0 and

Table 7.5: Expected background yields after all cuts, pre-fit, statistical uncertainty only.

Background	Weighted yield (pre-fit)	Raw number of MC events
$Z(\nu\nu)$	0	0
$W(\mu\nu)$	0	0
$W(e\nu)$	0	0
$Z(\mu\mu)$	0	0
$Z(ee)$	0	0
Di- and triboson	0.05 ± 0.02	16
$W(\tau\nu)$	0.02 ± 0.02	2
$Z(\tau\tau)$	0.58 ± 0.10	70
Single top	0.56 ± 0.18	22
$t\bar{t}$	2.39 ± 0.18	238
$t\bar{t}X$	0.52 ± 0.07	428
$m_{\tilde{b}} = 800, m_{\tilde{\chi}_2^0} = 131$	5.64 ± 0.44	116
$m_{\tilde{b}} = 800, m_{\tilde{\chi}_2^0} = 180$	9.28 ± 0.57	308

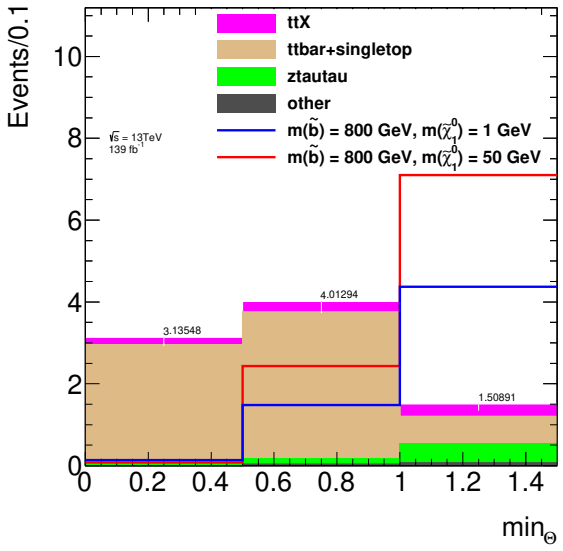

(a) $\min_\Theta$ cut relaxed

Figure 7.4: Background composition in the SRs binned in $\min_\Theta$. SM background yields per bin are included in the plot.

the final inclusive bin gathering everything above $\min_\Theta = 1.0$. Relaxing the $\min_\Theta$ requirements results in 8.6 background events expected, see Figure 7.4a. The background composition changes significantly from bin to bin with last bin dominated by $Z(\tau\tau)$, see also Figure 7.4a. The multi-bin approach doesn't make much sense without the fit itself being performed so the further discussion of it is gathered in the results section. The post-fit yields in the $\min_\Theta$ bins are summarised in Table 10.10 and the expected exclusion can be seen in Figure 10.8.

The strategy is to use the $\min_\Theta$ multi-bin SRs for the exclusion fit and the single-bin Discovery SR (with $\min_\Theta > 0.6$) for the discovery fit.

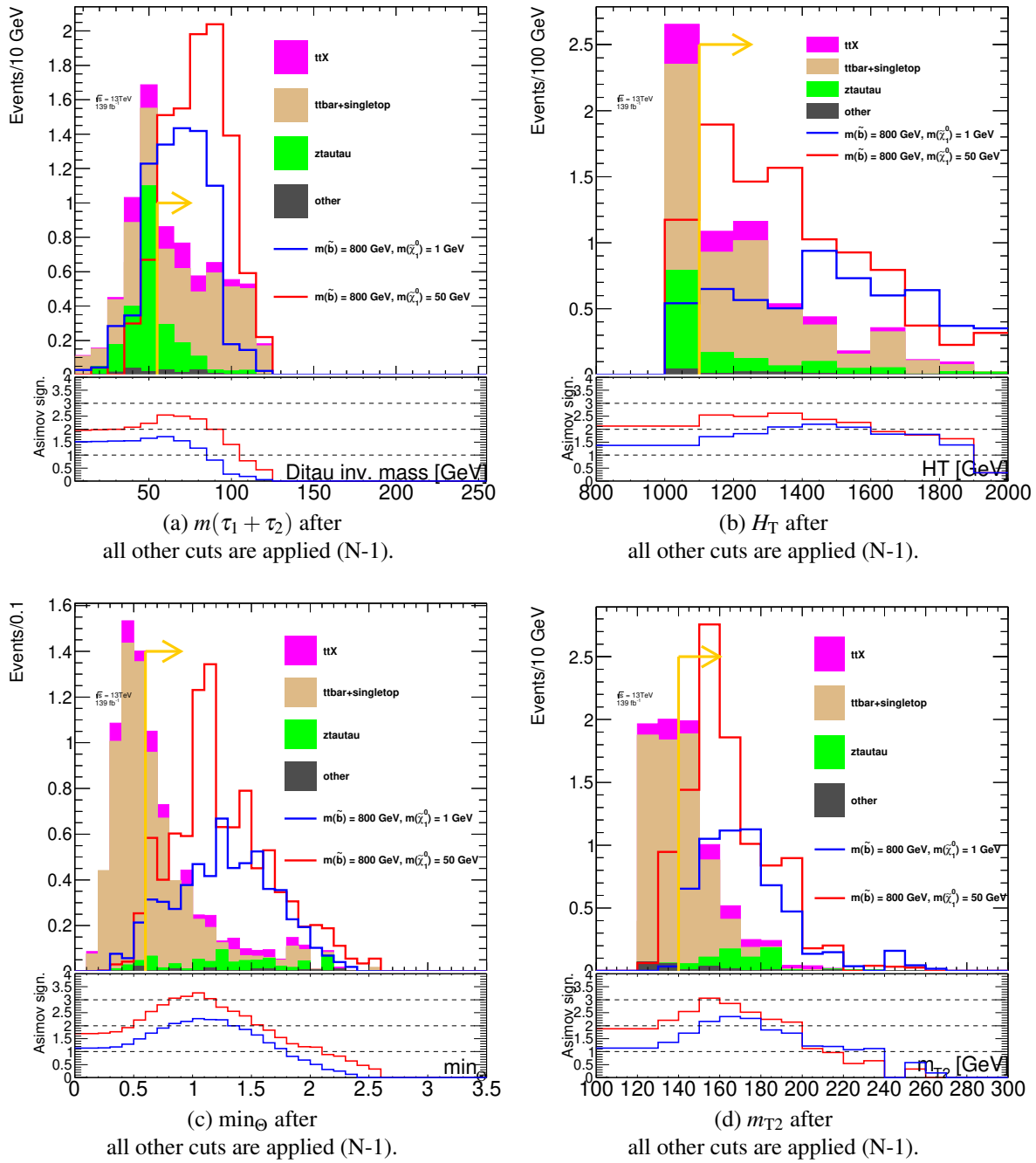

(a) $m(\tau_1 + \tau_2)$ after all other cuts are applied (N-1).

(b) H_{T} after all other cuts are applied (N-1).

(c) $\min_{\Theta}$ after all other cuts are applied (N-1).

(d) m_{T2} after all other cuts are applied (N-1).

Figure 7.5: Kinematic variables used for the signal region, N-1 plots. Signal is normalised to the expected cross section. The lower panels show the significance of the signal-plus-background model as described in Section 4.4 with 40% uncertainty on the background events assumed. Arrows show the cuts selected to optimise the single-bin SR.

7.5 Correlation of Variables

The kinematic variables used to define signal regions (both single-bin and multi-bin) can be correlated to some degree. That is not an issue as long as the Monte-Carlo models the correlation well. This suggests that the comparison should be done after the control regions are defined and the fit-related corrections are applied to the MC. The correlation of variables checks are described in Section 8.7.

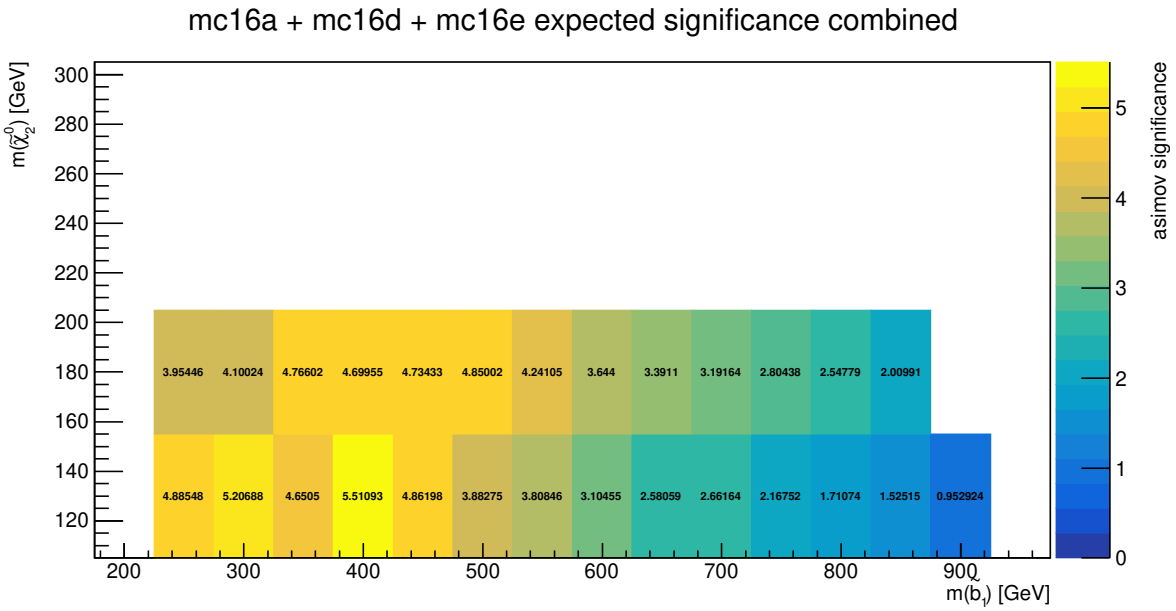

(a) Expected Asimov significance in SR, pre-fit.

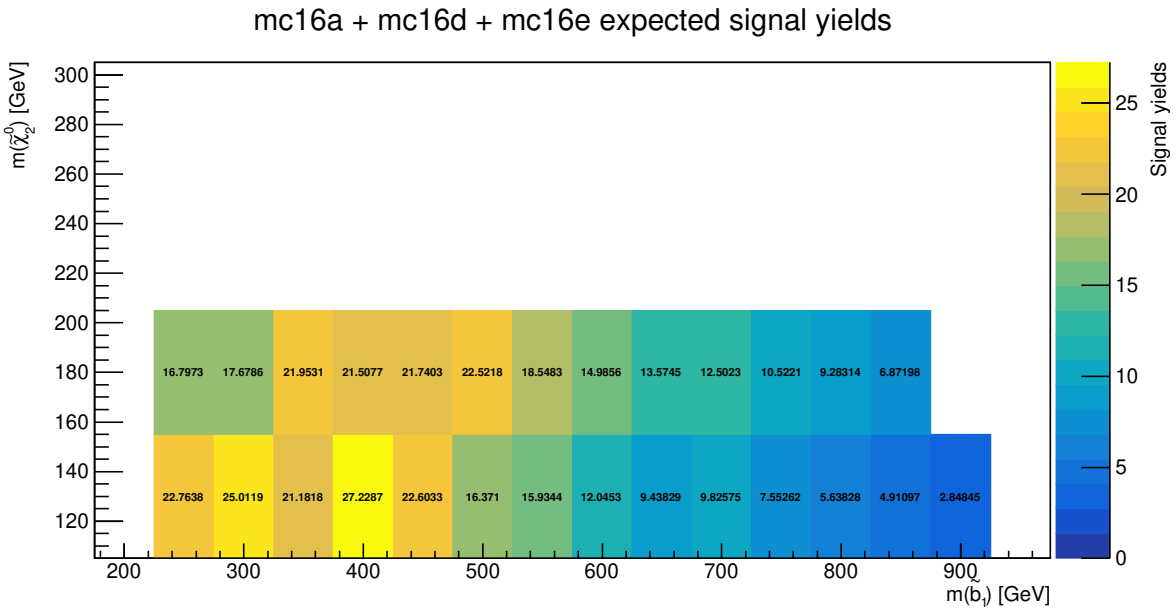

(b) Expected signal yields in SR, pre-fit.

Figure 7.6: Expected signal yields and Asimov significance in the single-bin SR with all cuts applied.

Table 7.6: Binning for SRs based on multi-bin fits.

Bin	$\min_\Theta$ SR
1	$\min_\Theta \leq 0.5$
2	$0.5 < \min_\Theta < 1.0$
3	$\min_\Theta \geq 1.0$

Chapter 8

Control Regions Design

Control regions (CRs, see Section 4.5) are defined for the dominant backgrounds in the signal regions (SRs), namely $t\bar{t}$, single top, and $Z(\tau\tau)$. The normalisation of these backgrounds is fitted to the data in the CRs to improve the modelling. Subdominant backgrounds such as $t\bar{t}X$ (predominantly $t\bar{t}Z$ and $t\bar{t}H$ with taus coming from Z/h decay) are predicted from simulation only as their contributions are too small to define dedicated control regions. The overall aim is to derive a set of weights that improve the data/MC agreement in the SRs.

Validation regions are defined in the vicinity of the SRs to validate the background extrapolation from the CRs to the SRs. One of the main discriminating variables H_{T} is used to separate the control regions from validation and signal regions. The general setup is $H_{\mathrm{T}} \in [600, 1000]$ GeV for control regions, $H_{\mathrm{T}} \in [1000, 1500]$ GeV for validation regions (VRs) and $H_{\mathrm{T}} > 1100$ GeV for the signal region. One validation region is additionally defined in the $H_{\mathrm{T}} \in [600, 1000]$ GeV range as will be discussed in the following.

Whenever a fit is mentioned in this chapter it is referring specifically to the background-only fit (as described in Section 4.5) that only uses control regions to improve modelling of the dominant backgrounds and makes no assumptions about the signal model.

8.1 Top Control Regions

The control regions are built on top of the trigger plateau requirements. The expected yields from various backgrounds are summarised in Table 8.1. The dominant background is $t\bar{t}$ pair production accounting for more than 80% of total background with around 25000 events expected. Other significant backgrounds are single top production and $W(\tau\nu)$ + jets with 3000 and 1000 expected correspondingly. The expected yields of other processes are much lower comparatively and unless dominating in a specific selection like $Z(\tau\tau)$ in the SR they are considered constant for the purposes of the fit.

$t\bar{t}$ and single top production events produce similar signatures with taus coming from top decays, but $t\bar{t}$ dominates single top by a factor of 5-10 depending on the selection. This heavily limits the possibility of a specific single top control region as it would be impossible to separate it from the $t\bar{t}$ background. Instead the $t\bar{t}$ and single top productions are treated as one "top" background for the purpose of the fit. In practice

it just means that the same normalisation factors are applied to the $t\bar{t}$ and single top samples. Everything else like scale factors and uncertainties treatment are separated.

Table 8.1: Expected background yields on the trigger plateau, pre-fit, showing statistical uncertainty only.

Background	Weighted yield (pre-fit)
$Z(\mu\mu)$	1.2 ± 0.2
$Z(ee)$	0.09 ± 0.04
$W(e\nu)$	39.9 ± 3.41
$Z(\nu\nu)$	75.9 ± 2.69
$W(\mu\nu)$	17.9 ± 1.41
Di- and triboson	$112. \pm 3.44$
$W(\tau\nu)$	$1130. \pm 14.8$
$t\bar{t}$X	$407. \pm 2.64$
$Z(\tau\tau)$	$143. \pm 3.07$
Single top	$3060. \pm 20.1$
$t\bar{t}$	$25300. \pm 45.6$
$m_{\tilde{b}} = 800, m_{\tilde{\chi}_2^0} = 131$	63.4 ± 1.5
$m_{\tilde{b}} = 800, m_{\tilde{\chi}_2^0} = 180$	102 ± 1.86

The signal region requires at least 2 hadronically decaying tau leptons. These taus can either be correctly identified "true" taus or other physical objects that are misidentified as "fake" taus. True and fake taus will generally have different properties and need to be treated separately. Taus coming from resonance decays ($Z(\tau\tau)$, $t\bar{t}X$, signal) are dominated by the true-true tau combination ($\approx$ 90-95% purity) as one could expect. The situation is different for $t\bar{t}$ and single top backgrounds where the taus are coming from two separate top decays. Semileptonic $t\bar{t}$ can produce one true tau and an abundance of jets to be misidentified as the second one. Depending on the rate at which jets are misidentified the true-fake tau combination can be comparable to (or even dominating) the true-true taus coming from fully leptonic $t\bar{t}$.

A preliminary pre-fit analysis of the MC predictions suggests that in the signal region the true-true and true-fake tau contributions are comparable while fake-fake is heavily suppressed, see Table 8.2. The true-true and true-fake combinations need to be controlled separately meaning two control regions. The fake-fake tau contribution is taken to be constant in the fit as it's contribution is much lower.

Table 8.2: Number of true and fake taus in the unoptimised signal region

Tau combination	$t\bar{t}$	Single Top
True-True	28.6	4.7
Fake-Fake	1.34	0.39
True-Fake	21.0	3.1

The main problem with defining true-true and true-fake tau control regions is that it is hard to separate fake from true taus (otherwise fake taus would just be rejected to

begin with). The standard approach is to define a same-sign taus selection where the two taus are required to have the same charge. Such a region would be orthogonal to the signal regions as the SRs explicitly require taus to have opposite signs and have high purity fake taus. Another approach would be to define a "mixed" control region with both true-true and true-fake taus contributions and to rely on the fit to provide reasonable normalisation factors (NFs) for both.

The control regions require exactly 2 b-jets so that extrapolation over number of b-jets doesn't become a problem and to keep the fake b-jet rates similar across the whole CR-VR-SR setup. This requirement can be relaxed to 1 b-jet to validate the control regions designs and to make sure the results are consistent. When comparing the same-sign fake tau CR with 1 and 2 b-jets a curious result was obtained - the 2 b-jets CR suggests that the MC slightly underestimates the fake tau contribution while the 1 b-jet selection shows heavy overestimation ($\approx 30\%$). The "mixed" fake tau CRs with both 1 and 2 b-jets also overestimate fake taus. Further investigation shows that in case of having 2 b-jets in the event the same-sign fake taus are predominantly originating from gluon jets. Fake taus in opposite-sign selections (and 1 b-jet same-sign selection) are coming from light flavour jets and b-jets. Since the fake taus in the signal region are similarly originating from light flavour jets and b-jets the idea of same-sign fake tau control region is rejected and the "mixed" approach is adopted. The whole comparison of fake tau CRs procedure is described in greater detail in Appendix B and is only mentioned here to motivate the final design of CRs.

The ideal solution to the top control region would be to define two two-tau control regions – one for true-true and one for true-fake combination – and two validation regions. However requiring 2 taus + 2 b-jets limits the number of events available significantly. Signal contamination becomes an issue too – tails of distributions can be sensitive to the potential signal and have to be blinded further limiting the phase space. The analysis instead adopts a strategy where one of the true taus is replaced by a muon. The true taus in top events are coming from the decays of the W bosons so the branching ratio for taus and muons is similar. Requiring 1 muon + 1 tau (true or fake) wins the (tau hadronic branching ratio) $\times$ (tau reconstruction and identification efficiency) $\times$ (combinatorial factor of 2) since 2 W bosons can decay in 1 tau + 1 muon in 2 different ways as opposed to 1 tau + 1 tau.

Another advantage of using muons in control regions is improved signal rejection. The main source of muon+tau signature in the signal events under consideration would be Higgs decaying to a tau pair one of which further decays to a muon. Back-of-the-envelope calculation suggests that the number of such events in signal is comparable to 2 hadronically decaying taus, but the background is 3-4 times larger than with the 2 tau selection.

It should be stressed that the approach chosen for the control regions is not an "embedding" procedure where the muon would be "promoted" to be a tau by some algorithm. The muons are treated as muons and the method relies on the fact that the W boson has similar branching ratios for taus and muons. However replacing a tau with a muon has some effect on acceptance and efficiency of the selection (e.g. hadronically decaying taus produce neutrinos that result in a $E_{\mathrm{T}}^{\mathrm{miss}}$contribution that muons would lack). A priori there is no reason to believe that the predictions from tau+muon regions actually hold for two tau selections. To quantify and correct for the tau/muon differences two additional auxiliary top control regions are defined.

What we ultimately want is a correction factor such that it improves the data/MC agreement when applied to the MC prediction. From the point of view of a particle generator a $t\bar{t}$ event can be described as the production of a top pair and subsequent decay and then the decay of the W bosons (and b-jets). The two steps are completely separable. The normalisation factor ((NF, the data/MC ratio in some region) for a hypothetical event in the SR with one fake and one true tau should look something like:

$$NF(\tau_{fake} + \tau_{true}\ \text{SR}) \propto NF\left[A\varepsilon(W \to \tau_{\text{true}}\nu) \cdot A\varepsilon(W \to \tau_{\text{fake}}\nu) \cdot A\varepsilon(b\bar{b})\right] \tag{8.1}$$

The normalisation factor that is derived in the 1 tau + 1 muon CR is:

$$NF(\tau_{fake} + \mu\ \text{CR}) \propto NF\left[A\varepsilon(W \to \mu\nu) \cdot A\varepsilon(W \to \tau_{\text{fake}}\nu) \cdot A\varepsilon(b\bar{b})\right] \tag{8.2}$$

Assuming that the acceptance is the same (it is not, this will be discussed later in the chapter) the $NF(\tau_{fake} + \mu\ \text{CR})$ needs to be multiplied by a factor of $\omega_{\text{scale}} = \frac{NF[A\varepsilon(W \to \tau_{\text{true}}\nu)]}{NF[A\varepsilon(W \to \mu\nu)]}$ to get the proper correction term for the events in the SR.

The two auxiliary top control regions mentioned before are used to compute the ω_{scale} term. OneTau CR is defined as a 2 b-jet 1 tau region with a veto on muons. Additional cuts are applied to improve the purity of true taus. OneMu CR is similarly defined as a 2 b-jet 1 muon region with a veto on taus. After the fit the two regions produce the following NFs:

$$NF(\text{OneTau CR}) \propto NF\left[A\varepsilon(W \to \tau_{\text{true}}\nu) \cdot A\varepsilon(W \to qq) \cdot A\varepsilon(b\bar{b})\right] \tag{8.3}$$

and

$$NF(\text{OneMu CR}) \propto NF\left[A\varepsilon(W \to \mu\nu) \cdot A\varepsilon(W \to qq) \cdot A\varepsilon(b\bar{b})\right] \tag{8.4}$$

Taking the ratio of the two factors leads to:

$$\begin{aligned} \frac{NF(\text{OneTau CR})}{NF(\text{OneMu CR})} &= \frac{NF\left[A\varepsilon(W \to \tau_{\text{true}}\nu) \cdot A\varepsilon(W \to qq) \cdot A\varepsilon(b\bar{b})\right]}{NF\left[A\varepsilon(W \to \mu\nu) \cdot A\varepsilon(W \to qq) \cdot A\varepsilon(b\bar{b})\right]} \\ &\approx \frac{NF\left[A\varepsilon(W \to \tau_{\text{true}}\nu)\right]}{NF\left[A\varepsilon(W \to \mu\nu)\right]} = \omega_{\text{scale}} \end{aligned} \tag{8.5}$$

To summarise – the correction factor for a two-tau event can be derived from a one tau + one muon CR corrected for the difference between a muon and a tau under the assumption of the acceptance being the same. Schematically this can be written as:

$$\begin{aligned} &NF(1\tau_{\text{true}} + 1\tau_{\text{fake}}) = NF\left[A\varepsilon(W \to \tau_{\text{true}}\nu) \cdot A\varepsilon(\tau_{\text{fake}}) \cdot A\varepsilon(b\bar{b})\right] \\ &\simeq NF\left[A\varepsilon(W \to \mu\nu) \cdot A\varepsilon(\tau_{\text{fake}}) \cdot A\varepsilon(b\bar{b})\right] \times \frac{NF\left[A\varepsilon(W \to \tau_{\text{true}}\nu)\right]}{NF\left[A\varepsilon(W \to \mu\nu)\right]} \\ &= NF(\text{FakeTau CR}) \times \omega_{\text{scale}} = NF(\text{FakeTau CR}) \times \frac{NF(\text{OneTau CR})}{NF(\text{OneMu CR})} \end{aligned} \tag{8.6}$$

Similar reasoning applies to true-true taus combinations with $NF(\text{TrueTau CR})$ used instead of the FakeTau CR. In both cases the muon is taking the place of a true tau. This

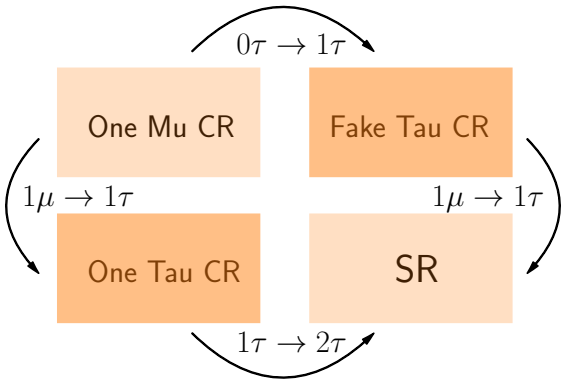

(a)

Figure 8.1: Schematic representation of the control regions for the true+fake tau top background in the SR.

way the corrections for fake taus are derived directly, without relying on muon-fake tau extrapolation.

The setup described above relies on the assumption of the acceptance being the same across all regions. This is obviously not the case - the analysis relies on $E_{\mathrm{T}}^{\mathrm{miss}}$ triggers and hadronically decaying true taus provide some extra $E_{\mathrm{T}}^{\mathrm{miss}}$ as opposed to muons. However, since the method relies only on NFs (essentially ratios of data/MC yields) and not on the yields themselves it can be shown that it holds under certain assumptions even if the acceptance differs across the regions.

Let us consider the 4 regions setup again like in Figure 8.1. The regions have the same kinematic selections and only differ by the particle content - 2 taus, 1 tau+1 muon, 1 tau, 1 muon. Technically the SR has a different H_{T} selection so what is being modelled is a two-tau VR from which the extrapolation over H_{T} to SRs occurs. The yields in the regions can be arranged as:

$$\frac{MC(1\mu+1\tau)}{MC(1\mu+jets)} = \lambda(\tau,\mu) \times \frac{MC(1\tau+1\tau)}{MC(1\tau+jets)}$$

where the $\lambda(\tau,\mu)$ term captures the difference in the acceptance due to substituting a tau with a muon. Similar relation also applies for the data yields. As long as the $\lambda(\tau,\mu)$ is the same for MC and data – that is as long as the Monte-Carlo simulations model the acceptance adequately – dividing the equation for data yields by the equation for MC yields leads to the normalisation factors ratio:

$$\frac{NF(1\mu+1\tau)}{NF(1\mu+jets)} = \frac{NF(1\tau+1\tau)}{NF(1\tau+jets)}$$

with the acceptance correction cancelled out. Notice how the initial requirement of the acceptance being the same in all regions has been replaced by a much looser condition of MC describing the effects of acceptance correctly in the regions. Finally it is worth noting that the

$$\omega_{\mathrm{scale}} = \frac{NF(\mathrm{OneTau\,CR})}{NF(\mathrm{OneMu\,CR})}$$

term is a priori not equal to 1 and there is no reason to expect it to be. It captures the data/MC differences in OneTau and OneMu CRs and the resulting value can be almost arbitrarily large or small. However if the control regions are designed well and the Monte-Carlo describes the data well a value close to 1 wouldn't be unexpected.

A small note is in order here. The tau ID SFs provided by the tau combined performance group are derived using $Z(\tau_\mu \tau_h)$ tag-and-probe method with Z bosons at rest, i.e. for tau p_{T}up to 50-60 GeV. POWHEG MC samples are used. Some ambiguity remains when using taus with $p_{\mathrm{T}} > 60$ GeV or when non-POWHEG generators are used (as is the case for V+jets samples for the presented analysis). The additional regions OneTau CR and OneMu CR give the fit extra freedom to account for this. Similar remark applies for the $Z(\tau\tau)$ control regions.

Table 8.3: Definitions of various control regions.

	OneMu CR	OneTau CR	TrueTau CR	FakeTau CR
Derivation	SUSY5	SUSY3	SUSY3	SUSY3
H_{T}		$[600, 1000]$ GeV		
Number of signal muons	1	0	1	1
Number of taus	0	1	1	1
OS(μ, τ)	–	–	yes	yes
Number of signal jets	≥ 3	≥ 3	≥ 3	≥ 3
Number of signal b-jets	2	2	2	2
Leading tau m_{T}^{τ}	–	≤ 80 GeV	≤ 80 GeV	≥ 100 GeV
p_{T}(leading b-jet)		≥ 100 GeV		
p_{T}(leading jet)		≥ 140 GeV		
p_{T}(sub-leading jet)		≥ 100 GeV		
$E_{\mathrm{T}}^{\mathrm{miss}}$		≥ 160 GeV		

With all of the above in mind we can finally construct the top control regions. Two control regions requiring 1 tau + 1 muon with opposite charges are defined – TrueTau CR and FakeTau CR. They are kept orthogonal by a cut on the leading tau m_{T}^{τ}. The TrueTau CR is defined at $m_{\mathrm{T}}^{\tau} \leq 80$ GeV which results in a region with high purity true taus. The FakeTau CR is required to have events with $m_{\mathrm{T}}^{\tau} \geq 100$ GeV resulting in a "mixed" region with evenly mixed fake and true taus. The auxiliary OneTau CR is defined to have 1 tau and a muon veto. The $m_{\mathrm{T}}^{\tau} \leq 80$ GeV cut is applied to improve the purity of true taus as OneTau CR is supposed to measure the difference between muons and true taus. The OneMu CR is defined with 1 muon and a veto on taus. Technically this means that the SUSY3 derivation (requiring at least 1 tau) is not suitable and SUSY5 is used for it instead. The true muon purity is naturally high in the phase space the analysis is interested in so no additional purity cuts are needed for the OneMu CR. All the CRs are required to have 2 b-jets, at least 3 jets and $H_{\mathrm{T}} \in [600, 1000]$ GeV, to fire one of the triggers used for the analysis and to be on the trigger plateau. The full definitions of 4 top CRs are gathered in Table 8.3.

As a closing remark – it is not necessary to use muons to define the control regions, electrons would work as well. However unlike muons electrons can easily fake taus. Therefore muons are used.

Some plots of kinematic variables before and after the fit in various top control regions are gathered in Figures 8.2 - 8.3 to demonstrate the agreement of data and Monte-Carlo predictions and the improvements with the fit.

8.2 Top Validation Regions

To study the "goodness" of the fitted background-only model several validation regions are designed. These are the regions of phase space that are kinematically closer to the signal region than the CRs and are not used in the fit. Various distributions scaled with the normalisation factors obtained in the CRs can be used to check the data/MC agreement in the VRs.

For each of the four top CRs, a validation region is defined with similar cuts except for the H_{T} range which is set to $H_{\mathrm{T}} \in [1000, 1500]$ GeV. The purpose is to check whether extrapolating over H_{T} is safe. In addition, a Ditau VR requiring 2τ is defined. Since the 2τ phase space is not used for the CRs it can be used for validation instead, $H_{\mathrm{T}} \in [600, 1000]$ GeV. At higher H_{T} values the signal contamination becomes significant in the DitauVR. A cut is also placed on the ditau mass to suppress potential signal contamination. This region is particularly important for the validation of the top background model as it tests the validity of the $\mu \to \tau$ extrapolation on which the whole setup is based.

The definition of the validation regions are summarised in Table 8.4. A further discussion on the data/MC agreement in the VRs can be found in Section 8.6 after all other CRs and VRs used in the analysis are defined.

Table 8.4: Definitions of various validation regions.

	OneMu VR	OneTau VR	TrueTau VR	FakeTau VR	Ditau VR
Derivation	SUSY5	SUSY3	SUSY3	SUSY3	SUSY3
H_{T}		$[1000, 1500]$ GeV			$[600, 1000]$ GeV
Number of signal muons	1	0	1	1	0
Number of loose taus	0	1	1	1	2
Opposite charge	–	–	yes	yes	yes
p_{T}(tau)	–			≥ 20 GeV	
Number of signal jets	≥ 3	≥ 3	≥ 3	≥ 3	≥ 3
Number of signal b-jets	2	2	2	2	2
Leading tau m_{T}^{τ}	–	≤ 80 GeV	≤ 80 GeV	≥ 100 GeV	–
Ditau mass	–	–	–	–	≤ 40 GeV or ≥ 90 GeV
p_{T}(leading b-jet)			≥ 100 GeV		
p_{T}(leading jet)			≥ 140 GeV		
p_{T}(sub-leading jet)			≥ 100 GeV		
$E_{\mathrm{T}}^{\mathrm{miss}}$			≥ 160 GeV		

Plots of $E_{\mathrm{T}}^{\mathrm{miss}}$ distributions before and after the fit in various top validation regions are gathered in Figures 8.4 - 8.5.

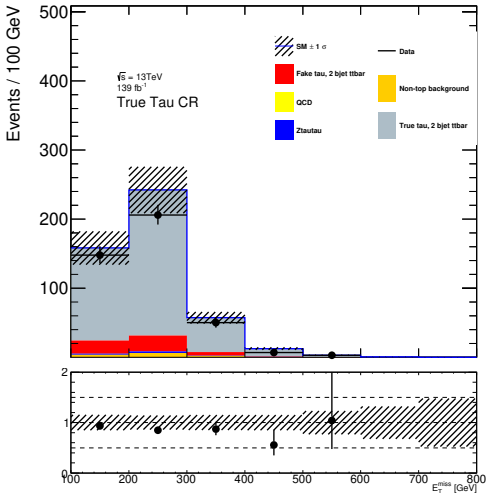

(a) TrueTau CR $E_{\mathrm{T}}^{\mathrm{miss}}$ before the fit.

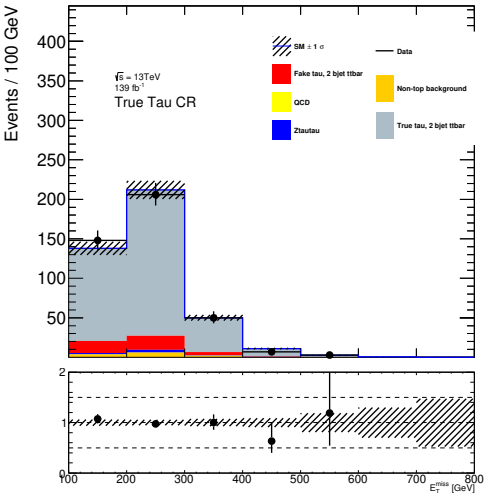

(b) TrueTau CR $E_{\mathrm{T}}^{\mathrm{miss}}$ after the fit.

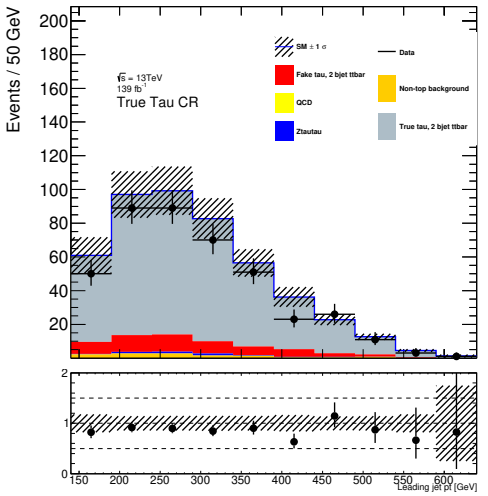

(c) TrueTau CR leading jet p_{T} before the fit.

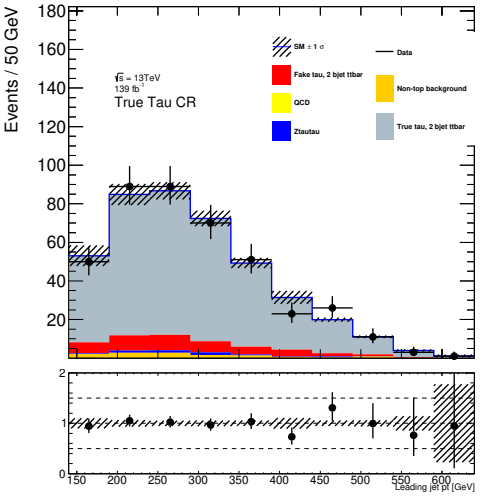

(d) TrueTau CR leading jet p_{T} after the fit.

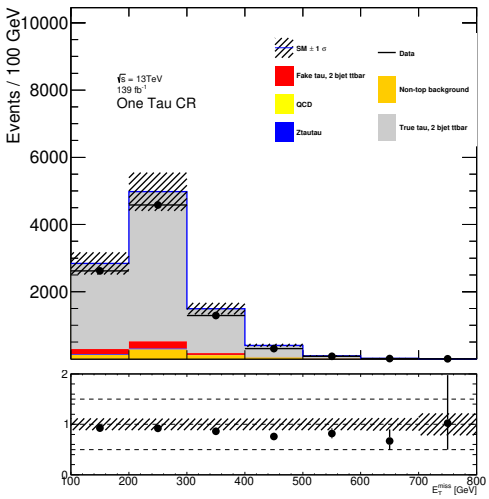

(e) OneTau CR $E_{\mathrm{T}}^{\mathrm{miss}}$ before the fit.

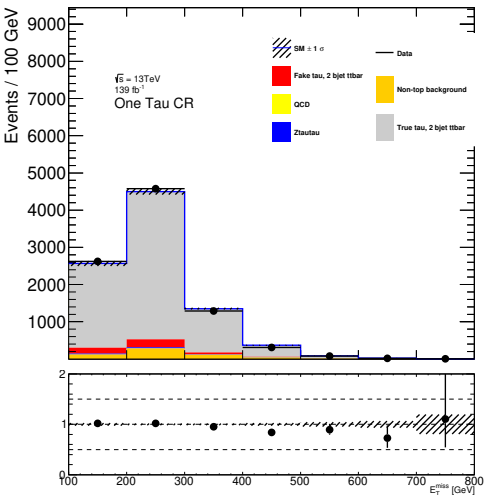

(f) OneTau CR $E_{\mathrm{T}}^{\mathrm{miss}}$ after the fit.

Figure 8.2: Distributions of various variables in the TrueTau CR and OneTau CR. All uncertainties are included and shown as the hatched band. The upper panels show distributions of the expected SM backgrounds with data overlaid. The lower panels show data/MC ratios. In the plots marked "after the fit" the SM backgrounds are scaled with the weights obtained in the background-only fit.

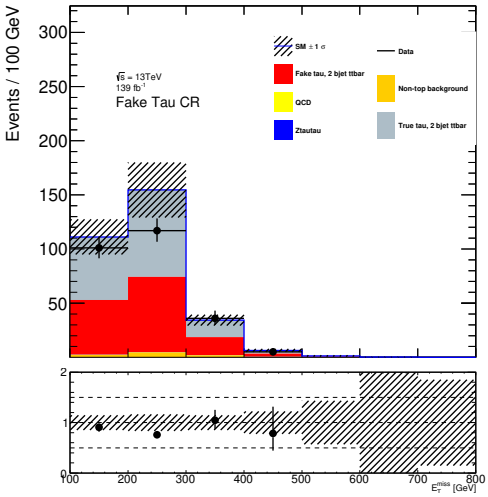

(a) FakeTau CR $E_{\mathrm{T}}^{\mathrm{miss}}$ before the fit.

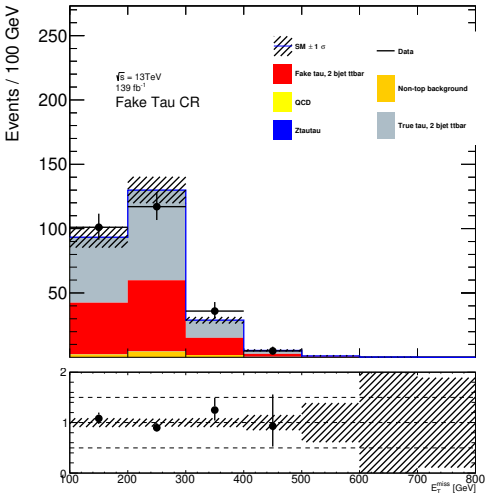

(b) FakeTau CR $E_{\mathrm{T}}^{\mathrm{miss}}$ after the fit.

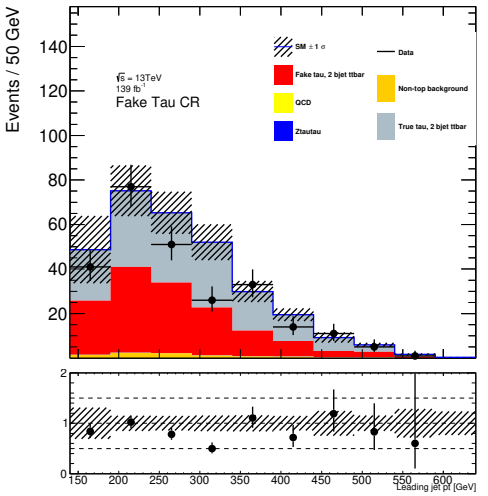

(c) FakeTau CR leading jet p_{T} before the fit.

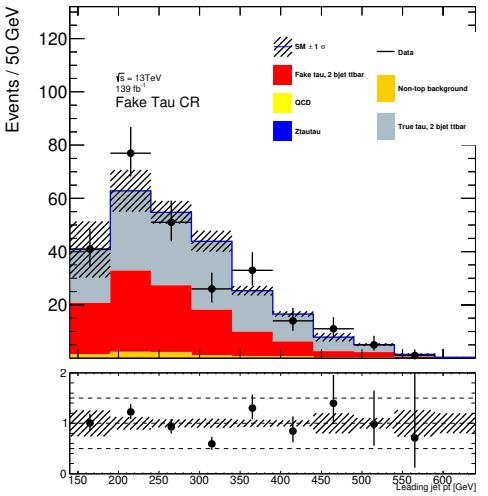

(d) FakeTau CR leading jet p_{T} after the fit.

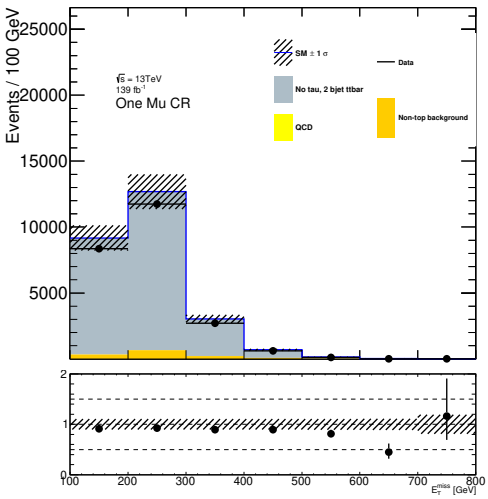

(e) OneMu CR $E_{\mathrm{T}}^{\mathrm{miss}}$ before the fit.

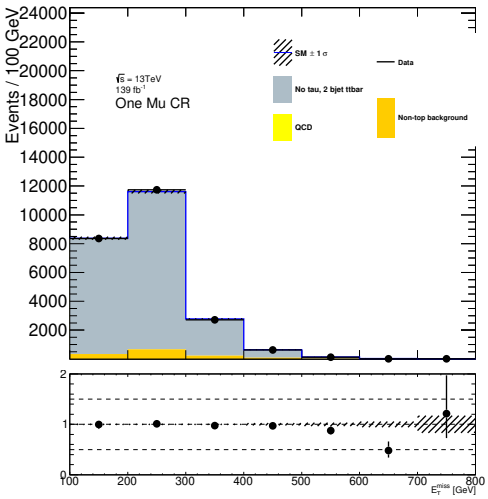

(f) OneMu CR $E_{\mathrm{T}}^{\mathrm{miss}}$ after the fit.

Figure 8.3: Distributions of various variables in the FakeTau CR and OneMu CR. All uncertainties are included and shown as the hatched band. The upper panels show distributions of the expected SM backgrounds with data overlaid. The lower panels show data/MC ratios. In the plots marked "after the fit" the SM backgrounds are scaled with the weights obtained in the background-only fit.

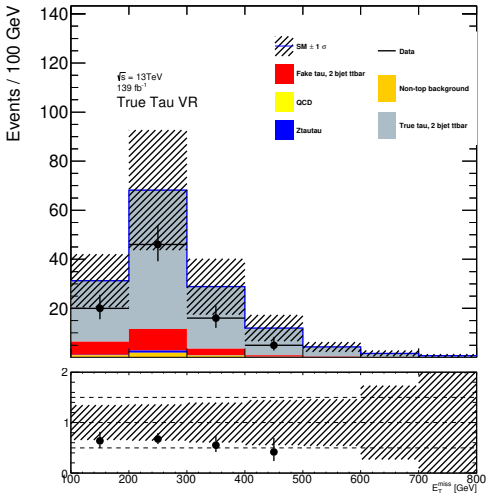

(a) TrueTau VR $E_{\mathrm{T}}^{\mathrm{miss}}$ before the fit.

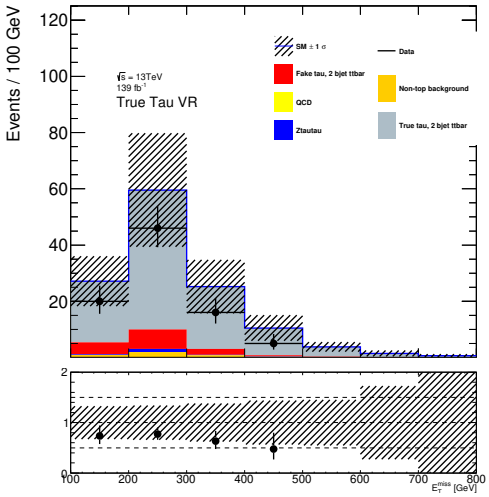

(b) TrueTau VR $E_{\mathrm{T}}^{\mathrm{miss}}$ after the fit.

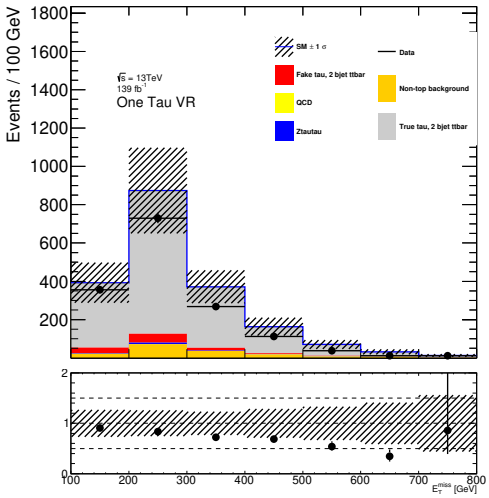

(c) OneTau VR $E_{\mathrm{T}}^{\mathrm{miss}}$ before the fit.

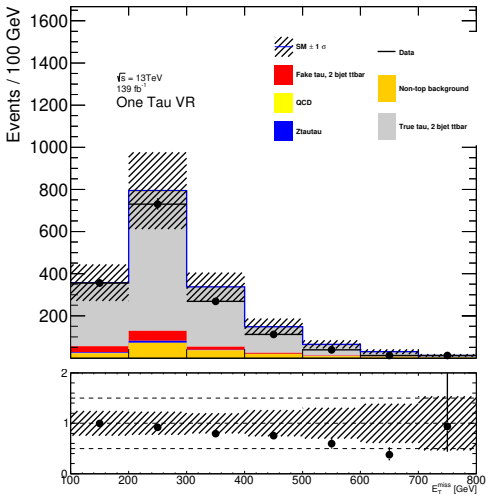

(d) OneTau VR $E_{\mathrm{T}}^{\mathrm{miss}}$ after the fit.

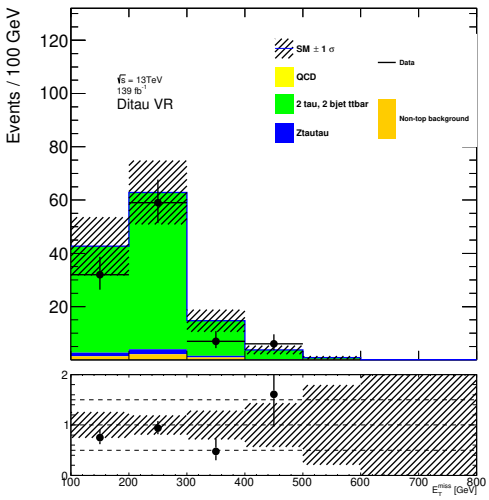

(e) Ditau VR $E_{\mathrm{T}}^{\mathrm{miss}}$ before the fit.

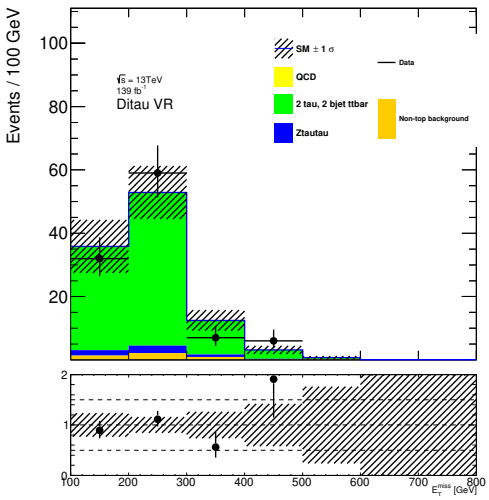

(f) Ditau VR $E_{\mathrm{T}}^{\mathrm{miss}}$ after the fit.

Figure 8.4: Distributions of $E_{\mathrm{T}}^{\mathrm{miss}}$ in the TrueTau VR, OneTau VR and Ditau VR. All uncertainties are included and shown as the hatched band. The upper panels show distributions of the expected SM backgrounds with data overlaid. The lower panels show data/MC ratios. In the plots marked "after the fit" the SM backgrounds are scaled with the weights obtained in the background-only fit.

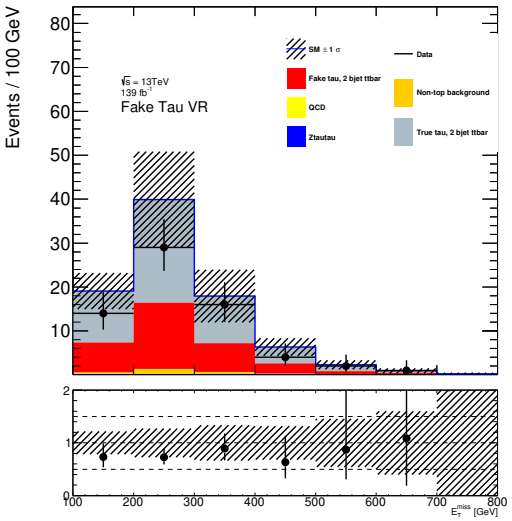

(a) FakeTau VR $E_{\mathrm{T}}^{\mathrm{miss}}$ before the fit.

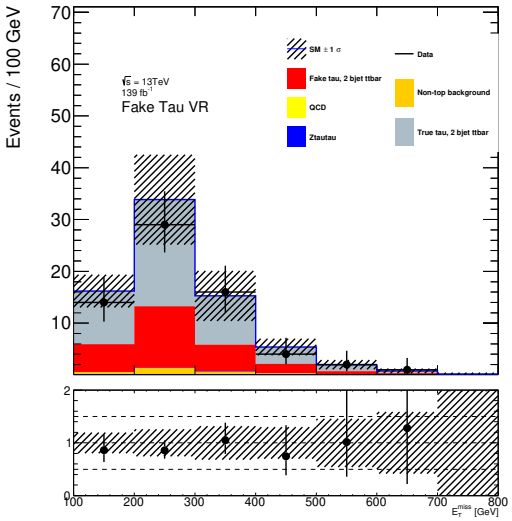

(b) FakeTau VR $E_{\mathrm{T}}^{\mathrm{miss}}$ after the fit.

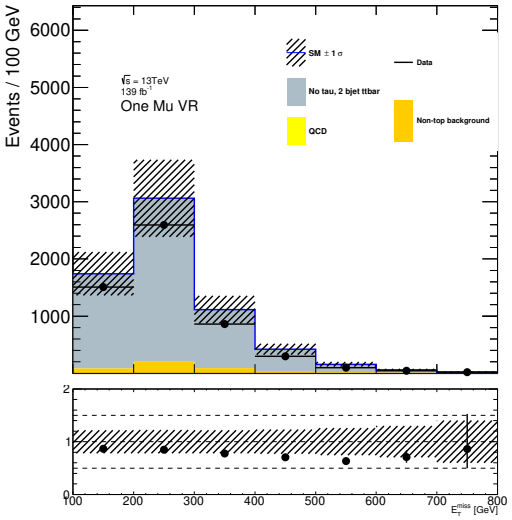

(c) OneMu VR $E_{\mathrm{T}}^{\mathrm{miss}}$ before the fit.

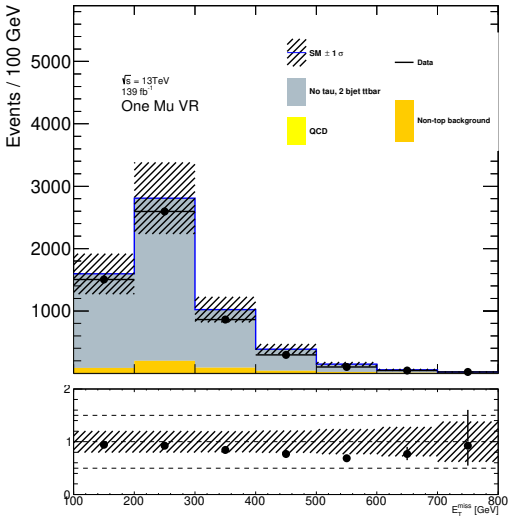

(d) OneMu VR $E_{\mathrm{T}}^{\mathrm{miss}}$ after the fit.

Figure 8.5: Distributions of $E_{\mathrm{T}}^{\mathrm{miss}}$ in the FakeTau VR and OneMu VR. All uncertainties are included and shown as the hatched band. The upper panels show distributions of the expected SM backgrounds with data overlaid. The lower panels show data/MC ratios. In the plots marked "after the fit" the SM backgrounds are scaled with the weights obtained in the background-only fit.

8.3 Z Control Regions

The $Z(\tau\tau)$ background is insignificant compared to the $t\bar{t}$ production at the baseline SR level as it is heavily suppressed by the b-jet p_{T}cut. Yet when all the signal region cuts that are primarily focused on suppressing top backgrounds are applied the $Z(\tau\tau)$ background becomes the second largest contribution, see Table 7.5. Furthermore in the multi-bin setup one of the bins is dominated by the $Z(\tau\tau)$ background. Defining a control region that would target $Z(\tau\tau)+2$ b-jets directly is difficult in terms of available number of events. Around 10 $Z(\tau\tau)$ events are expected on top of 200 $t\bar{t}$ events when trying to construct a region similar to the TrueTau CR and it would be even worse for a validation region. Relaxing the b-jet selection doesn't particularly help and would introduce complications related to extrapolation over the number of b-jets.

Instead a CR based on $Z(\mu\mu)+2$ b-jets (Zmumu2b CR) is used with significantly higher number of events due to the (had tau branching ratio $\times$ reco $\times$ ID)^2 factor that applies to $Z(\tau\tau)$. A $Z(\mu\mu)$ event typically has very low natural $E_{\mathrm{T}}^{\mathrm{miss}}$ so the $E_{\mathrm{T}}^{\mathrm{miss}}$ based triggers used for other regions are less than optimal. The events in Zmumu2b CR are instead required to fire a single muon trigger. Two additional CRs are used to extrapolate from muons to taus targeting $Z(\mu\mu)+0$ b-jet (Zmumu0b CR) and $Z(\tau\tau)+0$ b-jet (Ztautau0b CR) processes. All three CRs require at least 3 jets and $H_{\mathrm{T}} \in [600, 1000]$ GeV.

The fit strategy is similar to that used for the top background. A $Z(\tau\tau)$ + 2 b-jets event is scaled according to the normalisation factors derived in the 3 CRs:

$$\begin{aligned} NF(A\varepsilon(Z(\tau\tau)+2b)) &\simeq \frac{NF(A\varepsilon(Z+0b)\cdot A\varepsilon(Z(\tau\tau)))}{NF(A\varepsilon(Z+0b)\cdot A\varepsilon(Z(\mu\mu)))} NF(A\varepsilon(Z+2b)\cdot A\varepsilon(Z(\mu\mu))) \\ &:= \frac{NF(\text{Ztautau0b CR})}{NF(\text{Zmumu0b CR})}\cdot NF(\text{Zmumu2b CR}) \end{aligned} \tag{8.7}$$

In this case 0 b-jets regions are used to derive a $Z\to\mu\mu$ to $Z\to\tau\tau$ correction. The setup is illustrated in Figure 8.6. The definitions of the 3 CRs are summarised in Table 8.5. The Zmumu0b and Ztautau0b CRs are designed to have comparable acceptance in terms of Z p_{T}, such that the terms $A\varepsilon(Z+0b)$ should mostly cancel out. Similarly, as the Zmumu2b and Zmumu0b CRs only differ by the b-tagging requirement (they both have at least 3 jets), the muons should have similar kinematics in the two CRs and the muon terms $A\varepsilon(Z(\mu\mu))$ mostly cancel out. The argument is the same as for the top control regions, while the acceptance itself is different in the tau and muon regions we are only interested in data/MC ratios and the requirement for them is that acceptance descriptions match for the MC and data.

There are obvious kinematic differences between $Z(\tau\tau)$ and $Z(\mu\mu)$ processes, mainly the presence of $E_{\mathrm{T}}^{\mathrm{miss}}$ in the former. To ensure that the Zmumu2b CR is in a phase space similar to that of the analysis phase space additional requirements are placed on the p_{T} of the dimuon system. Using Monte-Carlo simulations typical p_{T} values of the Z boson in the $Z(\tau\tau)$ events in the analysis phase space are found to be larger than 200 GeV. This requirement is then also applied to the dimuon system.

Using single muon triggers (instead of the b-jet + $E_{\mathrm{T}}^{\mathrm{miss}}$ and $E_{\mathrm{T}}^{\mathrm{miss}}$ triggers used for $\tau\tau$ selection) and requiring $p_{\mathrm{T}}(\mu\mu) > 200$ GeV instead of the $E_{\mathrm{T}}^{\mathrm{miss}}$ plateau cuts brings

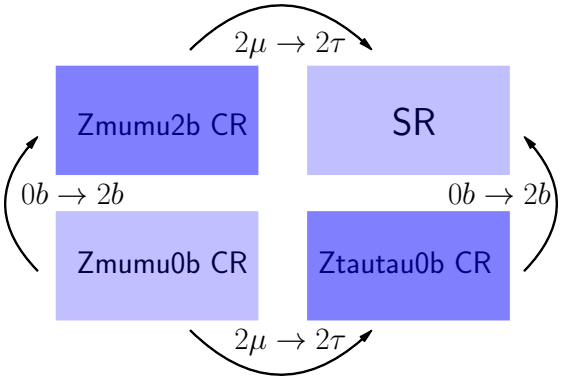

(a)

Figure 8.6: Schematic representation of the control regions for the Ztautau background in the SR.

the $\tau\tau$ and $\mu\mu$ kinematically closer. The leading muon p_{T} is required to be larger than 30 GeV to be on the single-muon trigger efficiency plateau. The invariant mass of the ditau system is required to be within 10 GeV of the Z boson mass to improve the purity. The $E_{\mathrm{T}}^{\mathrm{miss}}$ is required to be lower than 100 GeV to reject non-Z backgrounds and to ensure orthogonality with other regions used by the analysis. These requirements are applied both to Zmumu2b and Zmumu0b CRs.

For the Ztautau0b CR the lowest unprescaled $E_{\mathrm{T}}^{\mathrm{miss}}$ triggers are used. Since the b-jets are vetoed the 2 b-jets requirement for the trigger plateau is relaxed. The sum of tau transverse momenta $m_{\mathrm{T}}^{\tau_1} + m_{\mathrm{T}}^{\tau_2}$ is required to be lower than 100 GeV to increase the purity of the $Z(\tau\tau)$ events. The $Z(\tau\tau)$ events predominantly contain 2 true taus (98% purity in CRs, 99.5% in SRs), so no special treatment for fake tau modelling is needed. The definitions of the Z CRs are summarised in Table 8.5.

The fitted Zmumu2b NF is around 1.3, which is rather large, but comparable to what have been seen in the Z + 2 b-jets cross section measurement [88] in regions with similar kinematic properties.

Zmumu2b and Zmumu0b CRs have a tau veto and use SUSY5 samples. Ztautau0b uses SUSY3 similar to top regions. Some plots showing distributions of kinematic variables in the Z CRs before and after the background-only fit are gathered in Figure 8.7.

8.4 Z Validation Regions

A $Z(\mu\mu)$ + 2 b-jets VR is defined to check the extrapolation from $H_{\mathrm{T}} \in [600, 1000]$ GeV to $H_{\mathrm{T}} \in [1000, 1500]$ GeV similar to how top VRs were defined, see Table 8.5. The agreement of the kinematic variables seems adequate, see Figure 8.8.

In principle similar validation regions can be defined for Ztautau0b and Zmumu0b regions. They are however less interesting for the analysis as they contain 0 b-jets. Nevertheless some plots and figures are gatherer in Appendix C related to these validation regions. The data/MC seems to reasonable.

Due to the low number of events available it is not possible to construct a "$\mu\mu \to$

$\tau\tau$" validation region similar to the Ditau VR. An additional complication is signal contamination – any region with high purity $Z(\tau\tau)$ with two b-jets background based on the triggers available would also be sensitive to the signal. Similarly the SRs are sensitive to the otherwise insignificant $Z(\tau\tau)$ background. Reducing the number of b-jets to exactly 1 has been tried to increases the number of events, but the purity is still severely lacking and the change in number of b-jets would need additional corrections. The conclusion is that no such validation region is possible with the analysis setup.

Table 8.5: Definitions of various regions used to control $Z(\tau\tau)$.

	Zmumu2b CR	Zmumu2b VR	Zmumu0b CR	Ztautau0b CR
Triggers		`HLT_mu50` `HLT_mu26_ivarmedium`		Lowest $E_{\mathrm{T}}^{\mathrm{miss}}$ unprescaled
Jets		≥ 3		
Muons	2	2	2	0
Taus	0	0	0	2
B-jets	2	2	0	0
1st jet p_{T}	> 140 GeV	> 140 GeV	> 140 GeV	> 140 GeV
2nd jet p_{T}	> 100 GeV	> 100 GeV	> 100 GeV	> 100 GeV
μ p_{T}	> 30 GeV	> 30 GeV	> 30 GeV	–
τ p_{T}	–	–	–	> 20 GeV
$E_{\mathrm{T}}^{\mathrm{miss}}$	< 100 GeV	< 100 GeV	< 100 GeV	> 200 GeV
H_{T}	$[600, 1000]$ GeV	$[1000, 1500]$ GeV	$[600, 1000]$ GeV	
Z p_{T}	> 200 GeV	> 200 GeV	> 200 GeV	–
m_Z		$81 < m_Z < 101$ GeV		–
$m_{\mathrm{T}}^{\tau_1} + m_{\mathrm{T}}^{\tau_2}$	–	–	–	< 100 GeV

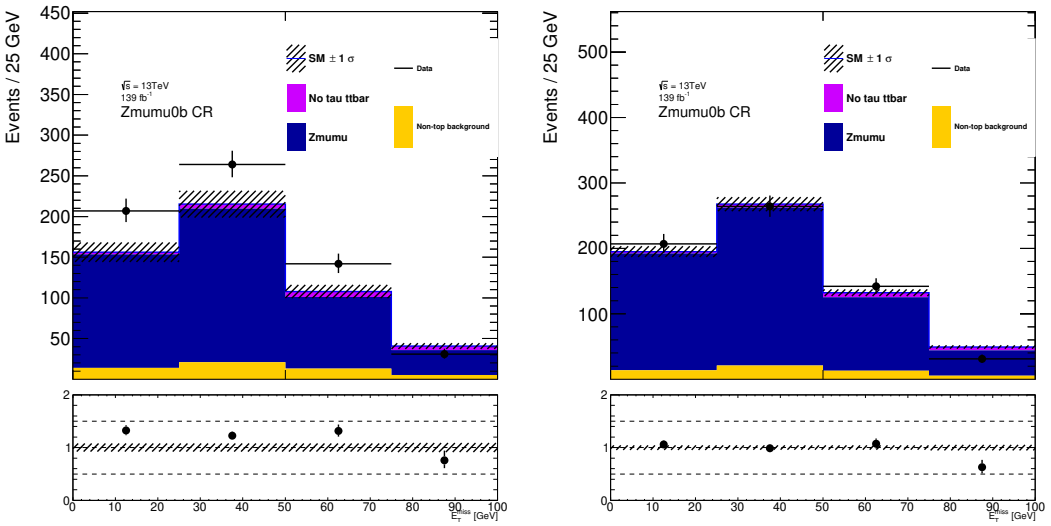

(a) Zmumu2b CR $E_{\mathrm{T}}^{\mathrm{miss}}$ before the fit.

(b) Zmumu2b CR $E_{\mathrm{T}}^{\mathrm{miss}}$ after the fit.

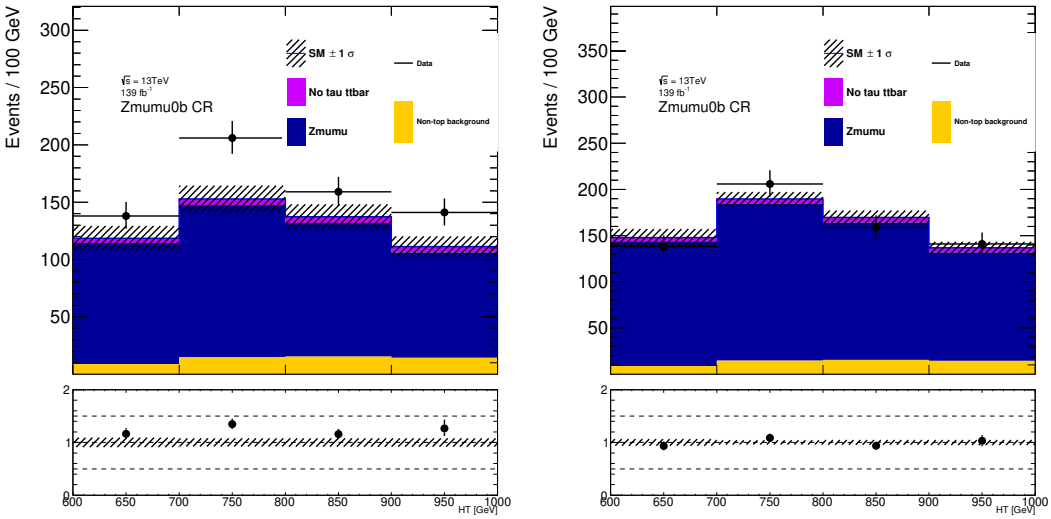

(c) Zmumu2b CR H_{T} before the fit.

(d) Zmumu2b CR H_{T} after the fit.

Figure 8.7: Distributions of various variables in the Zmumu2b CR. All uncertainties are included and shown as the hatched band. The upper panels show distributions of the expected SM backgrounds with data overlaid. The lower panels show data/MC ratios. In the plots marked "after the fit" the SM backgrounds are scaled with the weights obtained in the background-only fit.

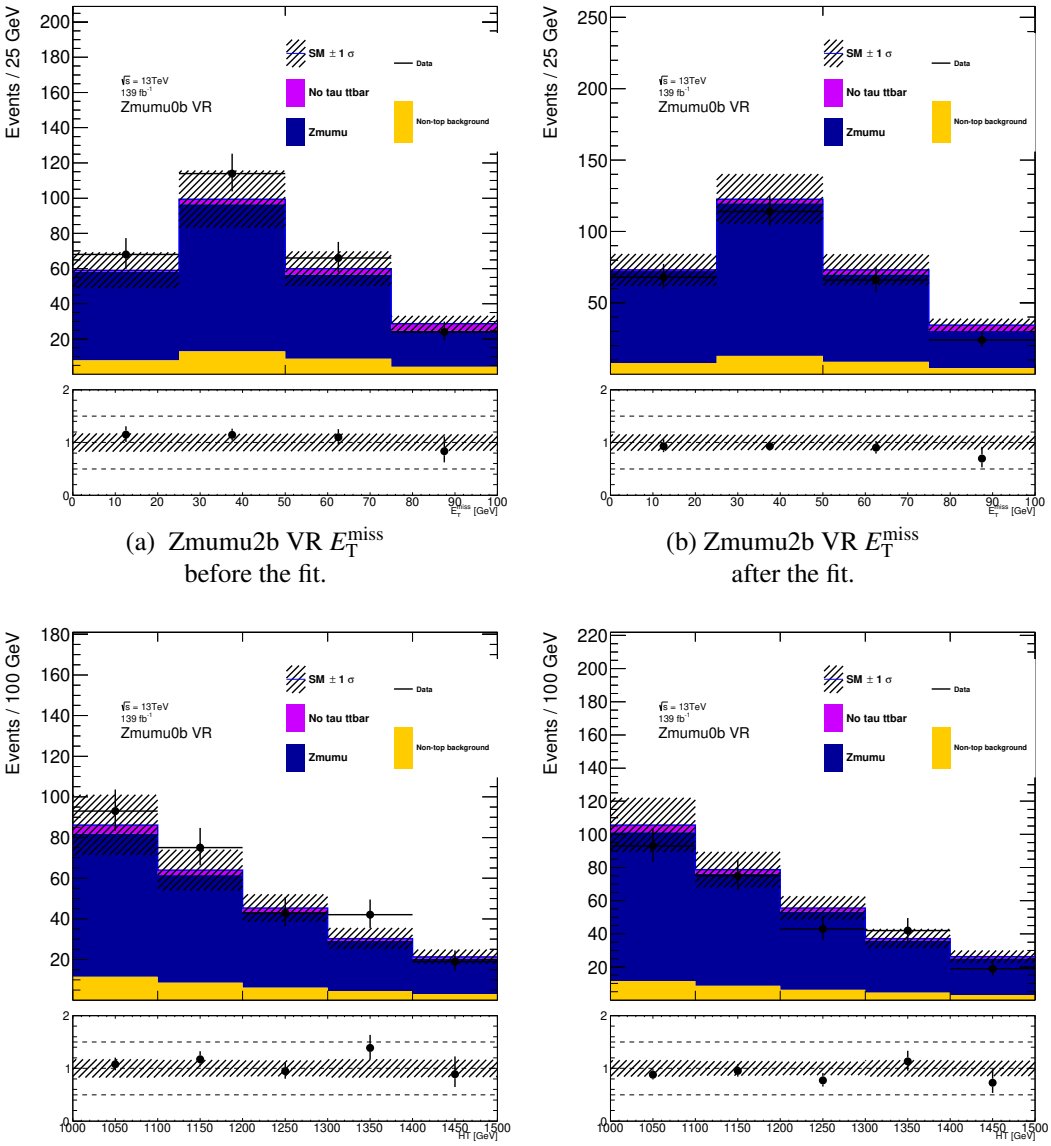

(a) Zmumu2b VR $E_{\mathrm{T}}^{\mathrm{miss}}$ before the fit.

(b) Zmumu2b VR $E_{\mathrm{T}}^{\mathrm{miss}}$ after the fit.

(c) Zmumu2b VR H_{T} before the fit.

(d) Zmumu2b VR H_{T} after the fit.

Figure 8.8: Distributions of various variables in the Zmumu2b VR. All uncertainties are included and shown as the hatched band. The upper panels show distributions of the expected SM backgrounds with data overlaid. The lower panels show data/MC ratios. In the plots marked "after the fit" the SM backgrounds are scaled with the weights obtained in the background-only fit.

8.5 Multijet Background

In the context of this analysis multijet (or QCD) background refers to all-hadronic backgrounds. Some of such backgrounds are modelled (e.g. all-hadronic $t\bar{t}$ samples), but do not necessarily model jets misidentified as taus properly. Other typical sources of multijet backgrounds include hadronically decaying vector bosons and pure QCD events.

Multijet production from pure QCD events has a large cross section at the LHC and is expected to be present in the phase space of the analysis. However, the multijet back-

ground contains neither prompt taus nor true $E_{\mathrm{T}}^{\mathrm{miss}}$ (except for semi-leptonic decays of heavy-flavour jets) that are characteristic for the analysis. Both would have to come from mismeasurements for a multijet event to pass the analysis selection. The mismeasurements of jets can lead to large values of $E_{\mathrm{T}}^{\mathrm{miss}}$ in all-hadronic events, especially if the jets have large p_{T}. The mismeasured $E_{\mathrm{T}}^{\mathrm{miss}}$ is therefore expected to be aligned with one of the jets. The $\Delta\phi(\mathrm{jet}_{1,2}, E_{\mathrm{T}}^{\mathrm{miss}}) > 0.5$ cut is used to suppress the majority of such events as described in Section 5.6. This cut doesn't affect the signal efficiency, see Figure 7.1d.

Jets misidentified as taus need to be controlled too. Such misidentifications are difficult to model properly so using simulation is not preferred. Instead a data-driven technique is used - the jet smearing technique [89]. It is used to produce "multijet pseudo-data" that estimates the real multijet contribution in all relevant regions. Since the method is based on data the jets misidentified as taus (called fake taus) are produced similar to what is expected in real multijet events. This way the fake tau modelling is "built in" and doesn't require a separate correction.

The general idea is to define a QCD CR with high purity and fit the jet smeared events to the data. The resulting normalisation factor is applied to all pseudo-data events that pass the cuts of various CRs/VRs/SRs. The result is treated as the expected multijet contribution. Additional care is taken to ensure that the extrapolation from the QCD CR to other regions is valid. The QCD CR doesn't enter the final fit by itself, the additional freedom it would provide to the fit could lead to instabilities. Instead a separate fit is performed with the QCD CR as the only region to derive the proper normalisation that is kept constant for the main analysis fit. Such an approach is justified since the QCD CR is a high purity region that is isolated from the phase space the analysis is interested in and can be considered fully independent.

8.5.1 Jet Smearing

What does it mean for a jet to be mismeasured and how to quantify it? One can compare the "true" energy of a jet as computed from the MC generators information (MC truth) to the "observed" energy that the jet obtains after the reconstruction and that is used by the analysis. Resolution R of a jet is defined here as $R = \frac{p_{\mathrm{T}}^{reco}}{p_{\mathrm{T}}^{MC}}$ and serves as a measure of how well an object is reconstructed. In a perfect world R would be always equal to 1, in reality the expectation is a gaussian distribution centred at 1 with non-gaussian tails. The resolutions of the leading and sub-leading jets in the phase-space relevant for the analysis is shown in Figure 8.9.

The main reasons for jet energy mismeasurements are:

- Granularity of hadronic calorimeters introduces some smearing of the jet energies. This is the primary reason of the gaussian shape of the resolution.

- Jets are constructed from clusters by various algorithms, some particles belonging to the jet may not be captured and some particles not originating from the jet might be grouped with it. Overlap removal and various cleaning cuts are used to suppress these sources of mis-measurements. Similar comment applies to "dead" tiles in the detector or non-detector material (like the supporting structure or cables), particles that hit them are lost to the detector resulting in smearing of the

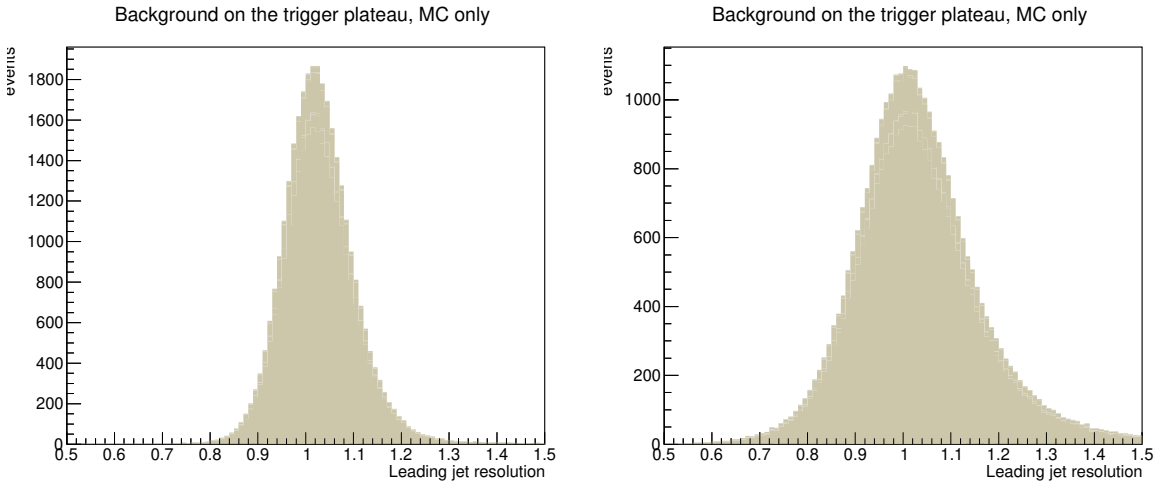

(a) Resolution of the leading jet.

(b) Resolution of the sub-leading jet.

Figure 8.9: Resolution ($p_{\mathrm{T}}^{reco}/p_{\mathrm{T}}^{MC}$) of jets on the trigger plateau.

resolution.

- If a jet is energetic enough it can go through the calorimeter system without depositing it's full energy. This leads to an overall non-gaussian tail.
- If a b-quark decays to a muon or an electron it also emits a neutrino which is invisible to the detector. The neutrino carries some of the jet's energy and resulting in true $E_{\mathrm{T}}^{\mathrm{miss}}$. Since the analysis requires at least 2 b-jets as part of the initial selection it is a rather common occurrence.

The jet smearing technique is based on the idea that $E_{\mathrm{T}}^{\mathrm{miss}}$ in multijet events is coming from mismeasurements of the energy of the jets. One takes well-measured jets in data and smears them within their calorimeter resolution distributions repeatedly. This way some of the events gain $E_{\mathrm{T}}^{\mathrm{miss}}$. The initial, well measured events are referred to as "seed" events. The resolution by which a given jet is smeared is taken randomly from a template (based on the jet's p_{T}) provided by the SUSY working group.

As the input for the jet smearing procedure the full Run2 SUSY11 data events are used, i.e. events that fired a single jet trigger. SUSY11 uses a combination of many single jet triggers, many of them prescaled, so the events have to be weighted to undo the effects of prescaling. This can introduce spikes in the final distributions.

The number of jet smearing iterations is set to 400. The events used for smearing are selected by a cut on $E_{\mathrm{T}}^{\mathrm{miss}}$ significance, defined as:

$$E_{\mathrm{T}}^{\mathrm{miss}}\ \mathrm{sig} = \frac{E_{\mathrm{T}}^{\mathrm{miss}} - M}{\sqrt{\sum E_{\mathrm{T}}}}$$

where M is a parameter that accounts for the $E_{\mathrm{T}}^{\mathrm{miss}}$ soft term. The recommended value of $M = 8$ GeV has been used. The $E_{\mathrm{T}}^{\mathrm{miss}}$ significance cut used for the analysis is $0.5 + 0.1 \times N_{b-\mathrm{jet}}$ based on the recommendations and data/MC agreement studies. The output is a dataset of smeared "pseudo-data" that behaves like the multijet backgrounds, but is statistically independent from it and has much larger number of events available as the number of multijet events falls sharply with $E_{\mathrm{T}}^{\mathrm{miss}}$ increasing.

8.5.2 Multijet Control Region

The aim is to define a control region with a high purity of multijet events to derive the normalisation factor for the QCD background. To define a region of the phase space that is enriched in multijet events the $\Delta\phi(\text{jet}_{1,2}, E_{\text{T}}^{\text{miss}}) > 0.5$ cuts are inverted. An alternative would be to define a low $E_{\text{T}}^{\text{miss}}$region, but that would require a separate correction to account for the $E_{\text{T}}^{\text{miss}}$dependence.

The QCD CR is required to have exactly 1 tau and 1 b-jet and to fire one of the $E_{\text{T}}^{\text{miss}}$or b-jet + $E_{\text{T}}^{\text{miss}}$triggers. The plateau cuts are applied, but the requirements of at least 2 b-jets and on the $\Delta\phi(\text{jet}_{1,2}, E_{\text{T}}^{\text{miss}})$ are relaxed. In addition, events should have $H_{\text{T}} \in [600, 1000]$ GeV to be consistent with the definitions of other control regions. Figure 8.10 shows the distribution of $\min\Delta\phi(\text{jet}_{1,2}, E_{\text{T}}^{\text{miss}})$ in this selection. The smeared pseudo-data used to model multijet background is normalised to the data−MC yields in the $\min\Delta\phi(\text{jet}_{1,2}, E_{\text{T}}^{\text{miss}}) \in [0, 0.5]$ region first before being fitted. This is needed since the pseudo-data is produced from a much larger dataset of well-measured events. The initial ad hoc normalisation (by a factor of approximately 0.005) is needed to make the fit stable and just to make plots readable.

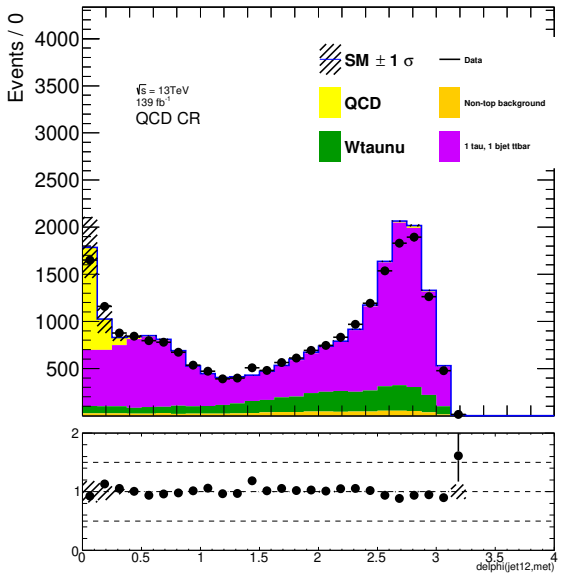

(a)

Figure 8.10: Distribution of $\min\Delta\phi(\text{jet}_{1,2}, E_{\text{T}}^{\text{miss}})$ in the preliminary QCD CR. The analysis uses > 0.5 selection to suppress multijet events for other regions. All uncertainties are included and shown as the hatched band. The upper panels show distributions of the expected SM backgrounds with data overlaid. The lower panels show data/MC ratios.

To increase the purity of the multijet selection additional requirements are placed on angular variables involving $E_{\text{T}}^{\text{miss}}$ and jets, b-jets and taus. The events are required to pass the $\Delta\phi(\text{jet}_{1,2}, E_{\text{T}}^{\text{miss}}) < 0.2$, $\Delta\phi(b\text{−jet}, E_{\text{T}}^{\text{miss}}) > 1.0$ and $\Delta\phi(\tau, E_{\text{T}}^{\text{miss}}) < 1.0$ selections. These choices are motivated in Figures 8.10-8.11. The full definition of the QCD CR is summarised in Table 8.6.

It should be noted that the concept of a trigger firing is ambiguous for a pseudo-data event. The seed event itself will most likely not fire one of the $E_{\text{T}}^{\text{miss}}$ based triggers used for the analysis. The jet smearing procedure is performed on the "offline" jets for

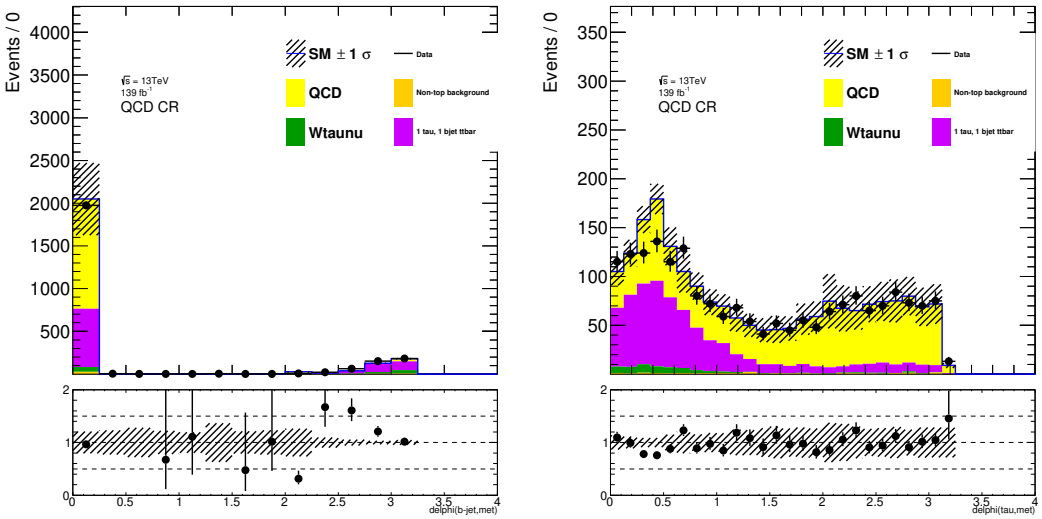

(a) $\Delta\phi(b\text{−jet}_1, E_{\mathrm{T}}^{\mathrm{miss}})$ in QCD CR (b) $\Delta\phi(\tau, E_{\mathrm{T}}^{\mathrm{miss}})$ in QCD CR

Figure 8.11: Angular variables distributions used to define QCD CR. The distribution of $\Delta\phi(b\text{−jet}_1, E_{\mathrm{T}}^{\mathrm{miss}})$ is shown after the $\Delta\phi(\text{jet}_{1,2}, E_{\mathrm{T}}^{\mathrm{miss}}) < 0.2$ cut has been applied. The distribution of $\Delta\phi(\tau, E_{\mathrm{T}}^{\mathrm{miss}})$ is shown after all other angular cuts have been applied. All uncertainties are included and shown as the hatched band. The upper panels show distributions of the expected SM backgrounds with data overlaid. The lower panels show data/MC ratios.

Table 8.6: QCD control region definition.

	QCD CR
$E_{\mathrm{T}}^{\mathrm{miss}}$	> 160 GeV
H_{T}	$600 < H_{\mathrm{T}} < 1000$ GeV
p_{T}(leading b-jet)	≥ 100 GeV
p_{T}(leading jet)	≥ 140 GeV
p_{T}(sub-leading jet)	≥ 100 GeV
Number of signal muons	0
Number of loose taus	1
p_{T}(tau)	≥ 20 GeV
Number of signal jets	≥ 3
Number of signal b-jets	1
$\Delta\phi(\text{jet}_1, E_{\mathrm{T}}^{\mathrm{miss}})$	< 0.2
or $\Delta\phi(\text{jet}_2, E_{\mathrm{T}}^{\mathrm{miss}})$	< 0.2
$\Delta\phi(b\text{−jet}, E_{\mathrm{T}}^{\mathrm{miss}})$	< 1.0
$\Delta\phi(\tau, E_{\mathrm{T}}^{\mathrm{miss}})$	> 1.0

which the response maps (i.e. jet p_{T} resolution distributions binned in p_{T} used to select the amount by which a given jet is smeared) are well measured and available. The trigger decisions on the other hand are made using "online" information that is available to the trigger system during the data-taking. To propagate the changes that the jet smearing procedure inflicts on the event back to the trigger decision would require smearing online and offline jets simultaneously. The necessary machinery and the online response maps do not exist. Instead the smeared events are just required to pass

the trigger plateau cuts.

As has been shown in Section 6.4 the $E_{\mathrm{T}}^{\mathrm{miss}}$ triggers have efficiency of $\approx 100\%$ at the trigger plateau meaning that only events that would have fired the trigger pass the selection. The b-jet trigger efficiency is lower than 1 on the plateau so pseudo-data events in the range $160 < E_{\mathrm{T}}^{\mathrm{miss}} < 200$ GeV need to be scaled down by the corresponding b-jet trigger efficiency. Additionally the effects of the b-jet aware GoodRunList need to be taken into account. Overall the events that pass the b-jet + $E_{\mathrm{T}}^{\mathrm{miss}}$ trigger plateau, but not the $E_{\mathrm{T}}^{\mathrm{miss}}$ trigger plateau are scaled by the factor of ≈ 0.6. Figure 8.12 shows the effects of the correction.

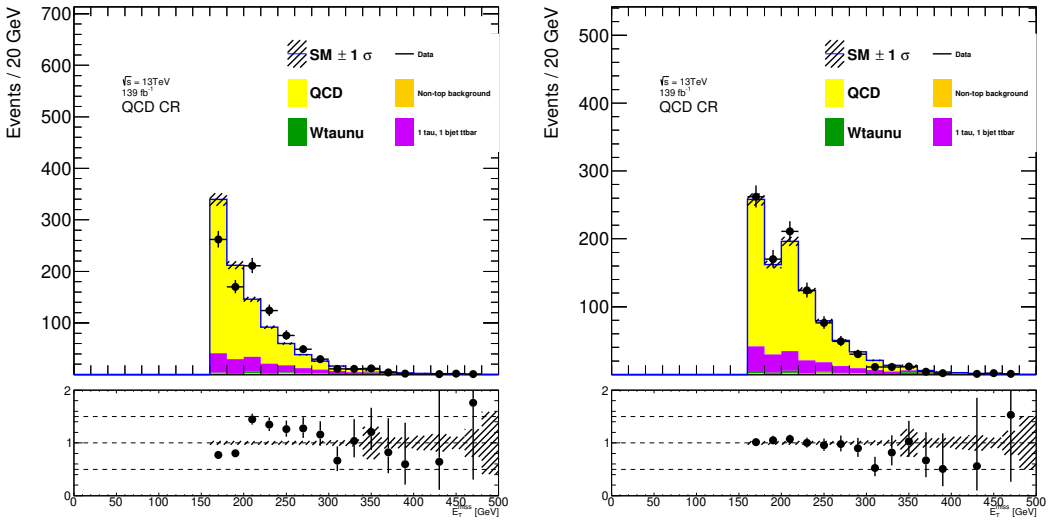

(a) $E_{\mathrm{T}}^{\mathrm{miss}}$in QCD CR before correction

(b) $E_{\mathrm{T}}^{\mathrm{miss}}$in QCD CR after correction

Figure 8.12: Comparison of $E_{\mathrm{T}}^{\mathrm{miss}}$in QCD CR before and after the b-jet trigger efficiency is applied. The multijet background is overestimated in the first two bins ($E_{\mathrm{T}}^{\mathrm{miss}} < 200$ GeV) and underestimated in the other bins without the correction.

8.5.3 Multijet Validation Regions

After the QCD CR is defined there are two things to check:

- Do the important kinematic variables (used to define this and other regions) describe the data well?
- Is the extrapolation from the region to other regions valid?

A selection of plots comparing the MC+smeared pseudo-data prediction (in the future referred to just as MC) against the data is presented in Figure 8.14. Overall the agreement looks reasonable.

The analysis is based on a selection requiring 2 b-jets and at least one mu/tau which in combination with the $\Delta\phi(\mathrm{jet}_{1,2}, E_{\mathrm{T}}^{\mathrm{miss}}) > 0.5$ cuts is fairly effective at rejecting the multijet background. The signal regions additionally require at least 2 taus which is an even stronger constraint. To validate the extrapolation from the QCD CR several validation regions are used. The first check is to relax the $\Delta\phi$ cuts. The $\Delta\phi(b\text{−jet}, E_{\mathrm{T}}^{\mathrm{miss}})$ and $\Delta\phi(\tau, E_{\mathrm{T}}^{\mathrm{miss}})$ are dropped completely and the $\Delta\phi(\mathrm{jet}_{1,2}, E_{\mathrm{T}}^{\mathrm{miss}})$ is relaxed to < 0.5.

The events used in QCD CR are also vetoed. The resulting yields are summarised in Figure 8.13a.

Keeping the $\Delta\phi$ selection relaxed extrapolation over other kinematic variables is checked. The selection on number of objects is changed to 2 b-jets and 2 taus. The resulting yields are summarised in Figure 8.13b. There is no conclusion to make here unfortunately, the contribution is heavily suppressed. As will be shown in the following sections the 2 tau 2 b-jets $t\bar{t}$ is supposed to slightly overestimate the data without any corrections so overall the plot looks reasonable. The second check is to shift the H_{T} selection to $\in [1000, 1500]$GeV, see Figure 8.13c. The extrapolation over H_{T} seems to be reasonable. The conclusion is that the variables used to define the high purity QCD CR can be extrapolated over and the multijet background estimation is kept reasonable. In particular extrapolating over number of taus leads to a strong suppression of the multijet background so that while the CRs and VRs are expected to have some contribution from it, the SRs are mostly QCD-free.

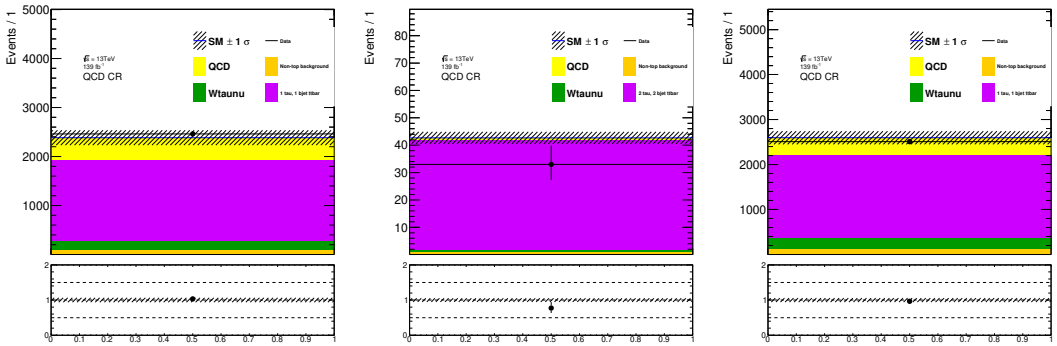

(a) (b) (c)

Figure 8.13: Three QCD VRs that check extrapolation over (a) $\Delta\phi$ cuts, (b) number of b-jets and taus and (c) H_{T}. All uncertainties are included and shown as the hatched band. The upper panels show yields of the expected SM backgrounds with data overlaid. The lower panels show data/MC ratios.

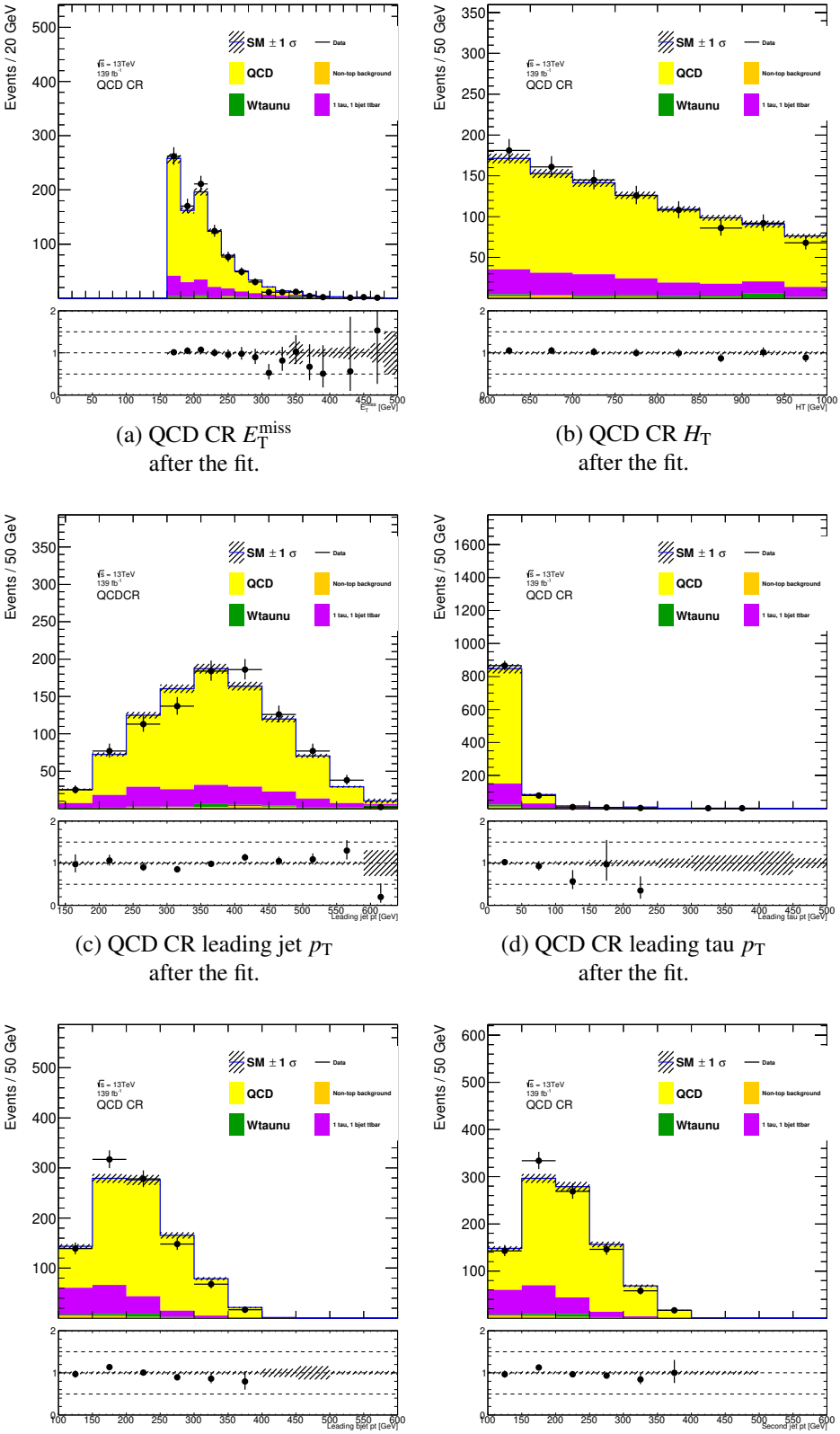

(a) QCD CR $E_{\mathrm{T}}^{\mathrm{miss}}$ after the fit.

(b) QCD CR H_{T} after the fit.

(c) QCD CR leading jet p_{T} after the fit.

(d) QCD CR leading tau p_{T} after the fit.

(e) QCD CR leading b-jet p_{T} after the fit.

(f) QCD CR second jet p_{T} after the fit.

Figure 8.14: Distributions of various variables in the QCD CR. All uncertainties are included and shown as the hatched band. The upper panels show yields of the expected SM backgrounds with data overlaid. The lower panels show data/MC ratios. In the plots marked "after the fit" the "pseudo-data" multijet backgrounds are scaled with the weights obtained in the background-only fit.

8.6 Full Fit Setup

The fit is based on 7 the orthogonal CRs described earlier in this chapter that are used to fit 7 normalisation factors, 4 to control $t\bar{t}$ + single top production and 3 to control $Z(\tau\tau)$. The other backgrounds are small in all relevant regions and are not fitted to the data. The values of fitted NFs, the CRs that are used to fit them and the purity of the corresponding samples are summarised in Table 8.8. The QCD CR as mentioned before is not used directly in the fit.

For technical convinience and to match with the ω_{scale} of Section 8.1 the 7 parameters used are:

- $\omega_{\text{true tau}}$ - normalisation factor of true taus in tau+muon top backgrounds.
- $\omega_{\text{fake tau}}$ - normalisation factor of fake taus in tau+muon top backgrounds.
- ω_{1mu} - normalisation factor of muons in top backgrounds.
- $\omega_{\text{scale top}}$ - ratio of normalisation factors ω_{1mu} and ω_{1tau} (that corresponds to the OneTau CR, but isn't used directly). This is the ω_{scale} for the top backgrounds.
- ω_{zmumu2b} - normalisation factor for $Z \rightarrow \mu\mu$ with associated b-jets production.
- ω_{zmumu0b} - normalisation factor for $Z \rightarrow \mu\mu$ with b-jet veto
- $\omega_{\text{scale Z}}$ = ratio of normalisation factors ω_{zmumu0b} and omega $\omega_{\text{ztautau0b}}$ (that corresponds to the Ztautau0b CR, but isn't used directly). This is the ω_{scale} for the Z backgrounds.

The definitions of all the control and validation regions used are summarised in Table 8.7. Figures 8.15-8.16 show the effect of the fit on the validation regions in terms of significance Z_A. Overall conclusion is that the fit improves the data/MC agreement in all regions.

Table 8.7: Definitions of all CRs and VRs. Red entries ensure orthogonality between CRs. Blue entries separate CRs from VRs.

	OneMu CR/VR	OneTau CR/VR	TrueTau CR/VR	FakeTau CR/VR	Zmumu2b CR/VR	Ditau VR	Zmumu0b CR	Ztautau0b CR
Derivation	SUSY5	SUSY3	SUSY3	SUSY3	SUSY5	SUSY3	SUSY5	SUSY3
H_T		$600 \leq H_T \leq 1000/1000 \leq H_T \leq 1500$ GeV				$600 < H_T < 1000$ GeV	$600 \leq H_T \leq 1000$	$600 \leq H_T \leq 1000$
Number of signal muons	1	0	1	1	2	0	2	0
Number of loose taus	0	1	1	1	0	2	0	2
Opposite charge	–	–	yes	yes	yes	yes	yes	yes
p_T(tau)	–	≥ 20 GeV			–	≥ 20 GeV	–	≥ 20 GeV
p_T(mu)	≥ 25 GeV				≥ 30 GeV		≥ 30 GeV	–
Number of signal jets	≥ 3	≥ 3	≥ 3	≥ 3	≥ 3	≥ 3	≥ 3	≥ 3
Number of signal b-jets	2	2	2	2	2	2	0	0
Leading tau m_T^τ	–	≤ 80 GeV	≤ 80 GeV	≥ 100 GeV	–	–	–	–
Ditau mass	–	–	–	–	–	≤ 40 GeVor ≥ 90 GeV	–	–
p_T(leading b-jet)					≥ 100 GeV			
p_T(leading jet)					≥ 140 GeV			
p_T(sub-leading jet)					≥ 100 GeV			
E_T^{miss}		≥ 160 GeV			≤ 100 GeV	≥ 160 GeV	≤ 100 GeV	≥ 200 GeV
Z p_T	–	–	–	–	≥ 200 GeV	–	≥ 200 GeV	–
m_Z	–	–	–	–	$81 \leq m_Z \leq 101$ GeV	–	$81 \leq m_Z \leq 101$ GeV	–
$m_T^{\tau_1} + m_T^{\tau_2}$	–	–	–	–	–	–	–	≤ 100 GeV

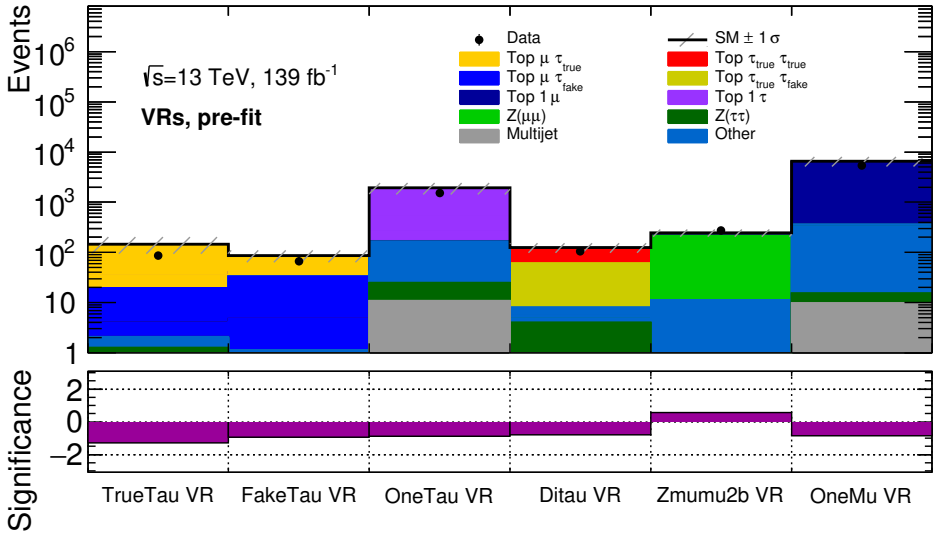

Figure 8.15: Comparison of fitted background yields and data yields in the validation regions before the background-only fit weights are applied. All uncertainties are included and shown as the hatched band. The upper panels show distributions of the expected SM backgrounds with data overlaid. The lower panels show the significance of the deviation of observed data from expected yields.

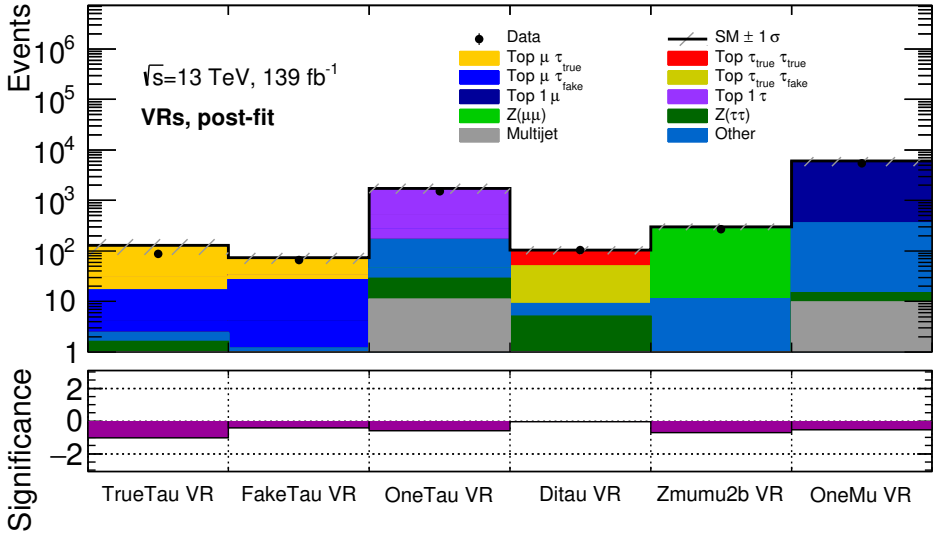

Figure 8.16: Comparison of fitted background yields and data yields in the validation regions. All uncertainties are included and shown as the hatched band. The upper panels show distributions of the expected SM backgrounds with data overlaid. The lower panels show the significance of the deviation of observed data from expected yields. The SM backgrounds are scaled with the weights obtained in the background-only fit.

Table 8.8: Values of normalisation factors after the background-only fit. The control regions that are primarily affecting the normalisation factors are listed together with the purity of the corresponding backgrounds. E.g. $\omega_{\text{true tau}}$ has the value of 0.88 ± 0.16 and is primarily fitted in TrueTau CR (where 86% of all events are top + true tau) and in FakeTau CR (where top + true tau events have 53% purity).

Normalisation Factor	Value	Corresponding CR	Background Purity
$\omega_{\text{true tau}}$	0.88 ± 0.16	TrueTau CR	86%
$\omega_{\text{true tau}}$	0.88 ± 0.16	FakeTau CR	53%
$\omega_{\text{fake tau}}$	0.79 ± 0.30	TrueTau CR	9%
$\omega_{\text{fake tau}}$	0.79 ± 0.30	FakeTau CR	43%
ω_{1mu}	0.91 ± 0.10	OneMu CR	94%
$\omega_{\text{scale top}}$	0.98 ± 0.04	OneTau CR	88%
ω_{zmumu2b}	1.28 ± 0.12	Zmumu2b CR	89%
ω_{zmumu0b}	1.00 ± 0.05	Zmumu0b CR	96%
$\omega_{\text{scale Z}}$	0.99 ± 0.17	Ztautau0b CR	79%

8.7 Diagnostics and Other Sanity Checks

In this section various checks applied to the data and MC are described. These are a part of designing control and signal regions, validating the assumptions and claims made earlier.

Signal Contamination As discussed previously in Chapter 4 the control and validation regions should have low expected signal yields. This is particularly important for the control regions as they are used to model the SM background. If the signal contamination in the control regions is large it can affect the fit and reduce the sensitivity of the signal regions. The potential signal contamination is evaluated for every control and validation region for every signal point as $\frac{N_{signal}}{N_{signal}+N_{bkg}}$. The overall purpose is to fine-tune the CRs and VRs such that the maximum signal contamination is lower than 10%. Some of the signal points considered have already been excluded by other analysis (lower sbottom mass). For these points the leakage requirements can be a bit more lenient.

Another complication is that the signal samples are produced with a tau filter on the generator level with some samples having a two-tau filter. In regions that do not have sufficient tau content (i.e. all regions with a tau veto) the signal contamination is evaluated using non-reconstructed MC truth signal samples, see Appendix E for justifications of using MC truth. The expected signal yields in the muon regions are minimal so that it isn't an issue. The same approach is used for the two-tau filtered samples in one-tau regions, they are evaluated using truth samples. In this case the MC truth estimations are made for all signal points so that it can be compared to the predictions from reconstructed samples where available.

As an example the signal contamination in the TrueTau CR, both measured and extrapolated from MC truth, is summarised in Figure 8.17. The full collection of signal contamination estimations are gathered in Appendix D. The regions used by the

analysis are designed such that the contamination doesn't go above $5-10\%$ in the non-excluded parts of the grid. Only regions with at least one tau are considered - the regions with tau vetoes are expected to have lower signal contamination than the corresponding regions with taus included due to the Higgs boson branching ratios.

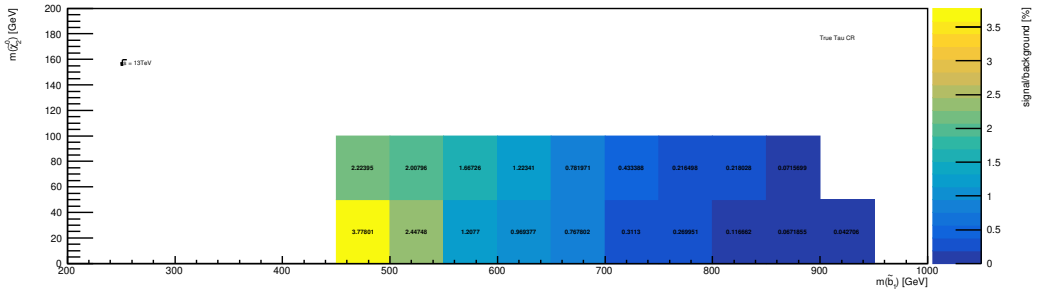

(a) True Tau CR signal contamination

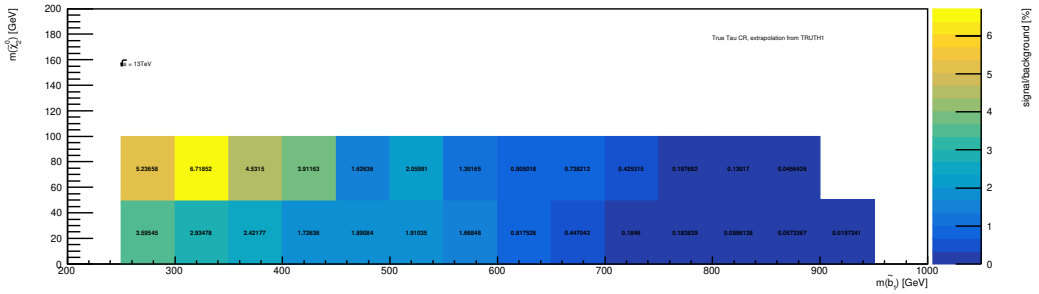

(b) True Tau CR signal contamination extrapolated

Figure 8.17: Signal contamination in the TrueTau control region, measured where possible and extrapolated from MC truth otherwise. The contamination is measured as $\frac{N_{signal}}{N_{signal}+N_{bkg}}$ for each signal point.

Signal Selection Variables The four main kinematic variables used to define the signal region are H_{T}, ditau invariant mass, $\min_{\Theta}$ and m_{T2} as described in Section 7.3. The data/MC agreement for these variables needs to be checked. Another thing to consider is correlation of variables. While the ditau mass and H_{T} are fairly independent, $\min_{\Theta}$ and m_{T2} are both reliant on the angular positions of taus. It is not a problem by itself, but it should be checked whether the MC models the correlation well.

What is a good region to check the data/MC agreement between the variables defining the signal region? The variables are chosen based on their discriminating power meaning the tails of the distributions can be sensitive to the signal even if the overall sum of events in a region isn't. Additional cuts to suppress the signal contamination need to be applied. Lack of events to test on can also be a problem, $\min_{\Theta}$ and m_{T2} are only defined for events with (at least) two taus and two b-jets.

The extrapolation over H_{T} is a main component of the analysis used not only to define SRs, but also to separate CRs from SRs and VRs. The data/MC agreement for H_{T} distributions is discussed separately later in this section. The ditau invariant mass can be studied in Ztautau0b CR (for taus produced from a resonance) and in Ditau VR. Nominally Ditau VR has ditau mass cuts that serve to compress signal contamination,

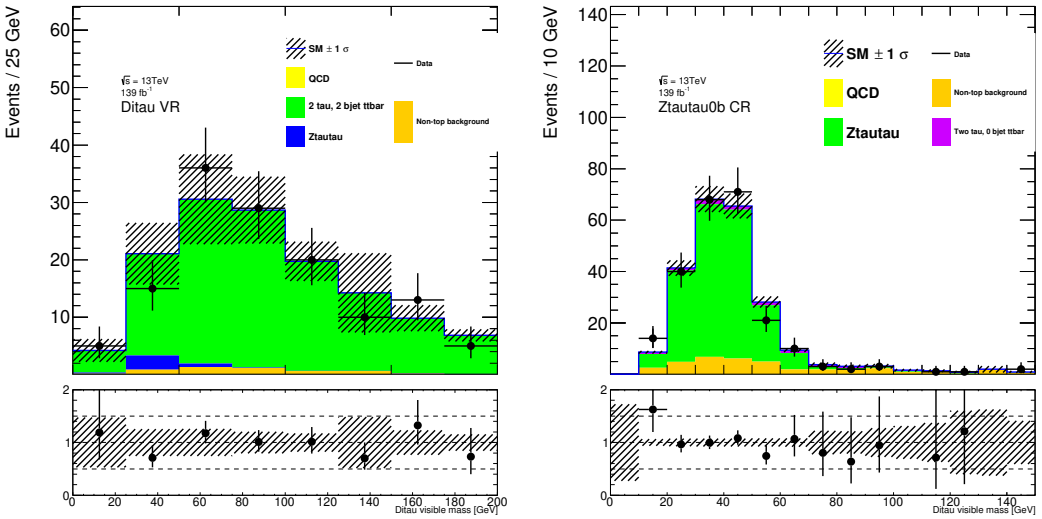

(a) (b)

Figure 8.18: (a) Visible ditau mass in Ditau VR. The cuts on ditau mass have been relaxed and replaced by $\min_\Theta < 1.0$. The majority of taus are coming from top decay chain. (b) Visible ditau mass in Ztautau0b CR. The majority of taus are coming from Z-boson decay. All uncertainties are included and shown as the hatched band. The upper panels show distributions of the expected SM backgrounds with data overlaid. The lower panels show data/MC ratios. The SM backgrounds are scaled with the weights obtained in the background-only fit.

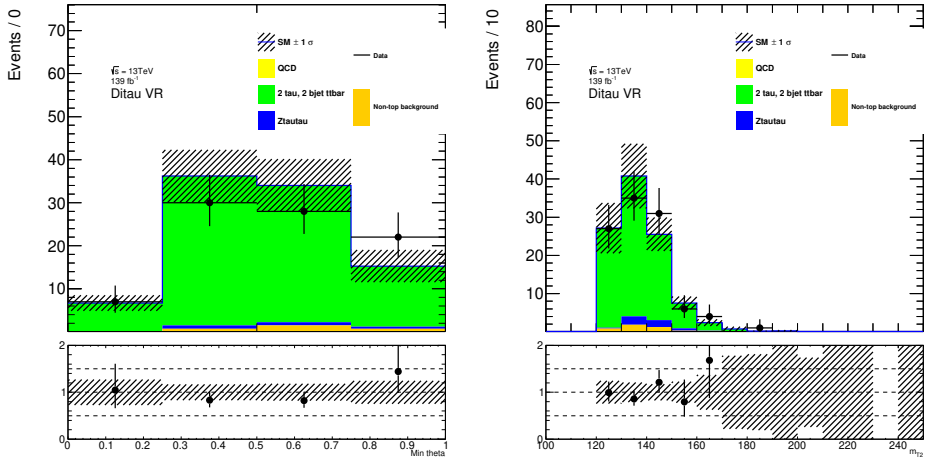

(a) $\min_\Theta$ in the Ditau VR. Blinded at $\min_\Theta > 1$ as the signal contamination is particularly large in those bins.

(b) m_{T2} in the Ditau VR.

Figure 8.19: $\min_\Theta$ and m_{T2} distributions in the Ditau VR. The region naturally contains 2 b-jets and 2 hadronically decaying taus so that the behaviour of the variables are similar to that in the signal regions. All uncertainties are included and shown as the hatched band. The upper panels show distributions of the expected SM backgrounds with data overlaid. The lower panels show data/MC ratios. The SM backgrounds are scaled with the weights obtained in the background-only fit.

but these can be substituted by, e.g. $\min_\Theta$ cuts. This results in proper ditau mass distributions with taus coming from top decays. The visible ditau mass distributions

are shown in Figure 8.18, the MC seems to describe the data well.

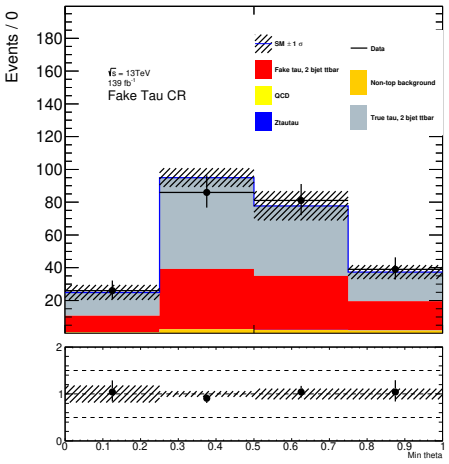

(a) $\min_\Theta$ in the FakeTau CR, one of the taus replaced with a muon.

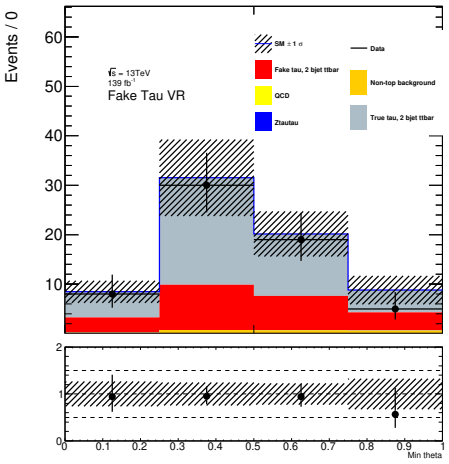

(b) $\min_\Theta$ in the FakeTau VR, one of the taus replaced with a muon.

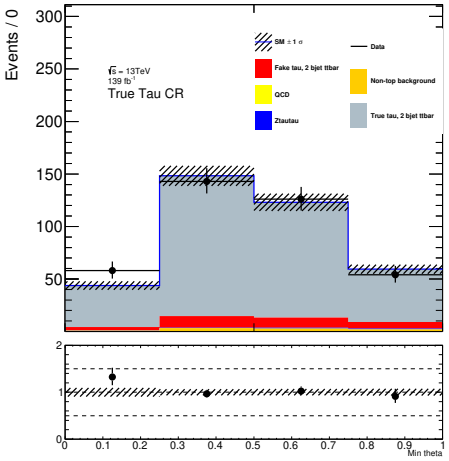

(c) $\min_\Theta$ in the TrueTau CR, one of the taus replaced with a muon.

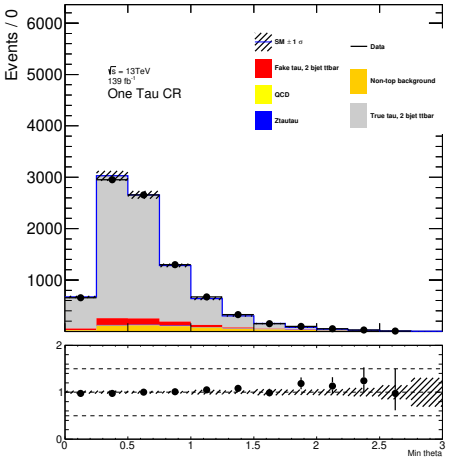

(d) $\min_\Theta$ in the OneTau CR, one of the taus replaced with a jet.

Figure 8.20: Plots of $\min_\Theta$ in various regions. All uncertainties are included and shown as the hatched band. The upper panels show distributions of the expected SM backgrounds with data overlaid. The lower panels show data/MC ratios. The SM backgrounds are scaled with the weights obtained in the background-only fit.

The $\min_\Theta$ variable can be studied by replacing one of the taus with a muon. As discussed previously the signal contamination of a muon+tau selection is generally lower than that of a two-tau selection while having more events and granting access to relevant backgrounds. TrueTau CR and FakeTau CR (and the corresponding VRs) can be used to study the data/MC agreement of the $\min_\Theta$ as well as the two-tau Ditau VR, but they have to be partially blinded. In principle a two-muon region could be used to study the variable too, but it is not utilised by the analysis.

Another approach to estimating the $\min_\Theta$ data/MC agreement is to replace one of the taus with a jet. This leads to loss of interpretation of the variable, but offers a higher number of events to work with and much lower signal contamination (essentially OneTau CR and VR). The discriminating power of $\min_\Theta$ falls off when one of the taus is

replaced by a jet, but the goal here is to evaluate how robust the modelling of the angles between various objects is. Plots of $\min_{\Theta}$ modelling with one of the taus replaced by a muon or a jet are gathered in Figure 8.20, the data/MC agreement seems to be good. The data/MC comparison in Ditau VR is also fine, see Figure 8.19a.

Similar comments apply to the stransverse mass m_{T2}, there are not enough 2 tau events to validate the modelling so one of the taus in the definition is replaced by either a muon or the leading jet. Some plots are gathered in Figure 8.21, the modelling of m_{T2} is acceptable with one bin being off in TrueTau CR. The Ditau VR plot is presented in Figure 8.19b.

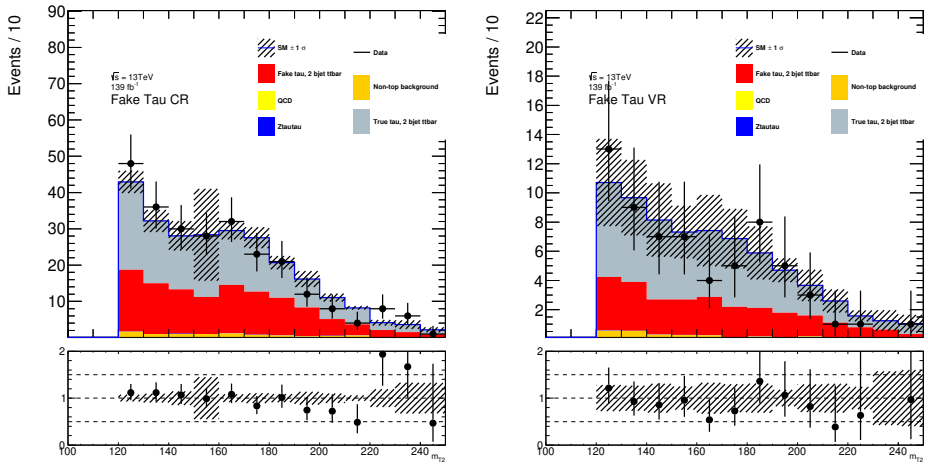

(a) m_{T2} in the FakeTau CR, one of the taus replaced with a muon.

(b) m_{T2} in the FakeTau VR, one of the taus replaced with a muon.

(c) m_{T2} in the TrueTau CR, one of the taus replaced with a muon.

(d) m_{T2} in the OneTau CR, one of the taus replaced with a jet.

Figure 8.21: Plots of m_{T2} in various regions. All uncertainties are included and shown as the hatched band. The upper panels show distributions of the expected SM backgrounds with data overlaid. The lower panels show data/MC ratios. The SM backgrounds are scaled with the weights obtained in the background-only fit.

Signal Variables Correlation Some degree of correlation between the variables used to define the SRs (Section 7.3) is unavoidable. As long as the data/MC agreement is fine

and the order in which the optimal cuts are determined doesn't change the final result the correlation itself is not a problem. The ditau invariant mass is rather decoupled from the other three variables and is not expected to be correlated with them. The correlation H_{T} with other variables is checked naturally due to the design of CRs and SRs. The m_{T2} and $\min_{\Theta}$ variables, on the other hand, are expected to be somewhat correlated as they both depend on the angular positions of taus. Due to low number of two tau events available the check is performed in the OneTau CR (1 tau + muon veto) instead with one of the taus replaced by the leading jet that is not *b*-tagged.

The idea is to apply a cut in one of the variables and to see whether it affects the modelling of the other one. The $\min_{\Theta}$ requirements are set as < 0.6 and > 0.6 while the m_{T2} is required to be > 150 GeV and < 150 GeV to roughly emulate the signal region cuts. The corresponding plots are presented in Figure 8.22. To repeat once again - the goal is not to get rid of correlation somehow, but just to validate that the correlation is well modelled by the Monte-Carlo samples. The plotted distributions suggest that this is indeed the case.

H_{T} Extrapolation and Modelling The overall fit setup has CRs at $H_{\mathrm{T}} \in [600, 1000]$ GeV, VRs at $H_{\mathrm{T}} \in [1000, 1500]$ GeV and SRs at $H_{\mathrm{T}} \geq 1100$ GeV. It is important that the H_{T} is well modelled across the whole range. Looking at Figure 8.24 and at the pull plots in Figure 8.16 the MC seems to be overestimating the data at higher H_{T} values rather consistently in regions dominated by $t\bar{t}$. The issue is most pronounced in the TrueTau VR, but is present to some degree in all top regions as can be seen from the pull plots. The Z+jets modelling seems adequate. The disagreement is mostly contained within systematics and the result is a conservative one, but it would be nice to understand whether the issue comes from a suboptimal fit setup or something outside of the analysis (e.g. MC generators).

A typical reason for $t\bar{t}$ MC to mismodel kinematic variables is mismodeling of the top quark p_{T} at NNLO (this obviously applies to the samples used for the analysis and not to any generic $t\bar{t}$ MC). A reweighting procedure can be applied based on the MC truth top p_{T} to match it with the corrected profile. The $t\bar{t}$ samples have been reweighted and checked in the muon+tau regions, but the results suggest that this is not an issue. An example of H_{T} distribution in $t\bar{t}$ samples before and after the reweighting (and with reweighting in various variables) is presented in Figure 8.23a.

Another option to consider is that the MC prediction is "correct" while a part of data is missing due to, e.g. faulty parts of the detector or some software bug. The analysis has dedicated cuts applied to compensate for the known "dead" tiles in the Tile Hadronic Calorimeter, but they could be insufficient. 2-D angular maps (ϕ vs η) of muons, taus, *b*-jets and jets have been studied in the relevant regions as well as the angular distributions between these objects and each other and $E_{\mathrm{T}}^{\mathrm{miss}}$. Nothing suspicious has been observed. The number of events is fairly low, but the observed discrepancies seem to be consistent with statistical fluctuations and vetoing them doesn't change the shape of the H_{T} distribution, only the overall normalisation.

The alternative generator setups for $t\bar{t}$ (MADGRAPH5_aMC@NLO+PYTHIA8 and POWHEGBOX+HERWIG) produce different shapes of H_{T} in the region of interest. These differences are the main contributions to the systematic uncertainties (see Chapter 9 for more information) and in principle contain the observed data. The comparison

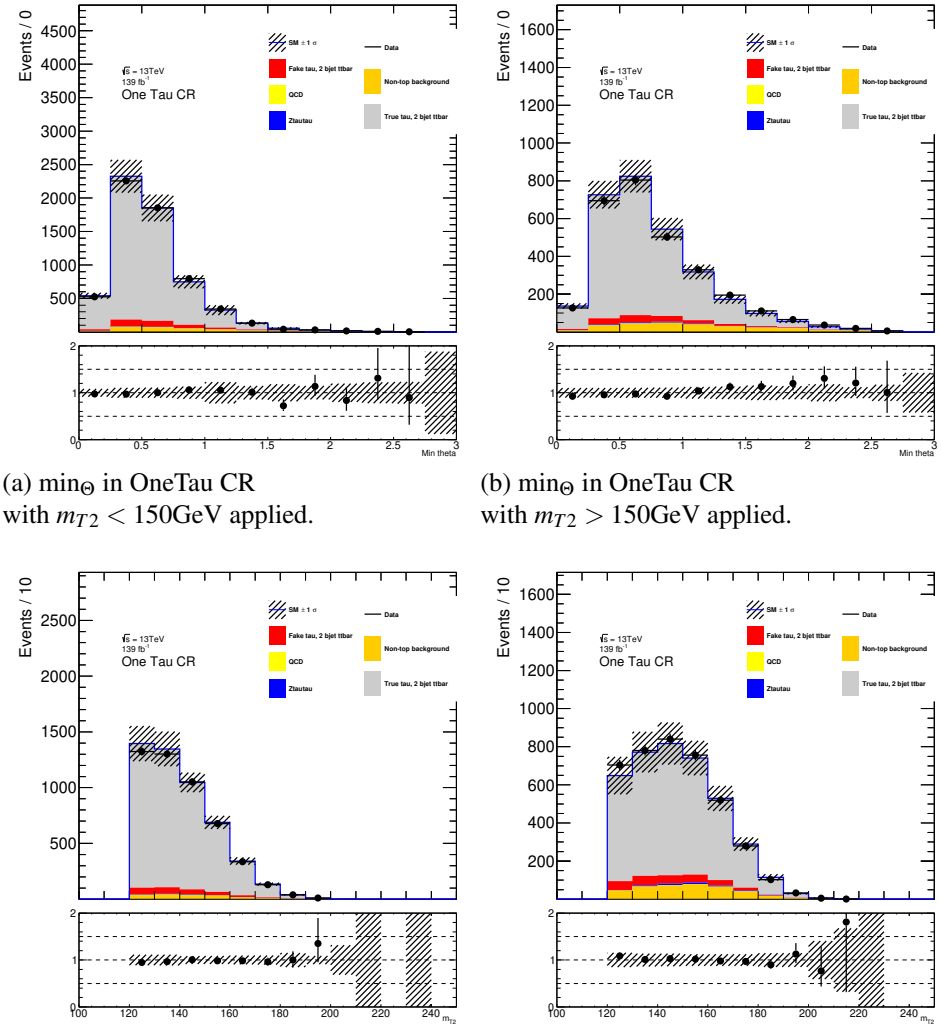

(a) $\min_{\Theta}$ in OneTau CR with $m_{T2} < 150$GeV applied.

(b) $\min_{\Theta}$ in OneTau CR with $m_{T2} > 150$GeV applied.

(c) $m_{T2} > 150$ in OneTau CR with $\min_{\Theta} < 0.6$ applied.

(d) $m_{T2} > 150$ in OneTau CR with $\min_{\Theta} > 0.6$ applied.

Figure 8.22: Distributions validating the data/MC agreement of correlated $\min_{\Theta}$ and m_{T2} variables. All uncertainties are included and shown as the hatched band. The upper panels show distributions of the expected SM backgrounds with data overlaid. The lower panels show data/MC ratios. The SM backgrounds are scaled with the weights obtained in the background-only fit.

of the nominal $t\bar{t}$ samples with the alternatives are shown in Figure 8.23b. The conclusion is that the $t\bar{t}$ MC in the particular phase space tend to overestimate the data somewhat. The discrepancy is contained by the comparison with alternative samples and the current result is conservative.

Additional Validation Regions The current analysis setup doesn't include any validation regions for Zmumu0b CR and Ztautau0b CR. The regions serve to determine the mu/tau extrapolation factor for Z+jets processes and validation regions wouldn't provide any additional information. Instead a simple check of the validity of the H_{T} extrapolation is performed. The claim is that the mu/tau correction developed in these two regions is valid at higher H_{T} (where the SRs are). To test this two additional regions are defined,

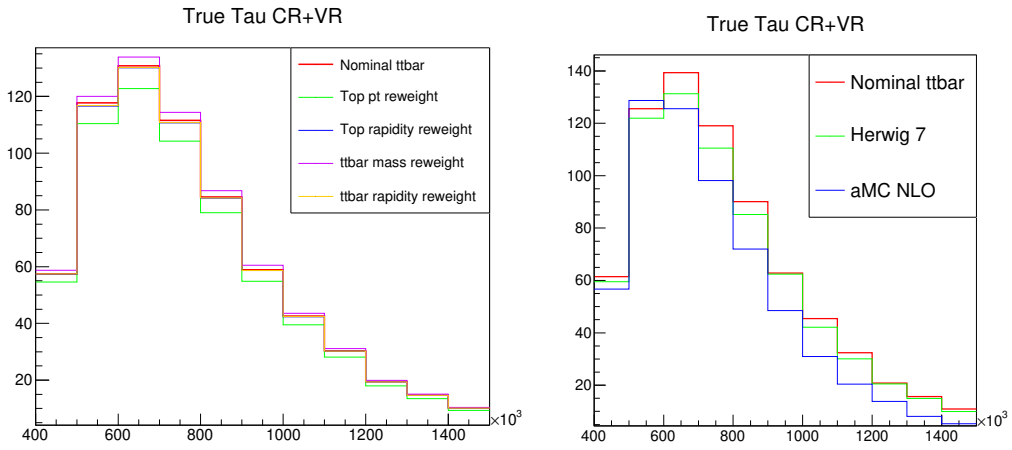

(a) (b)

Figure 8.23: (a) TrueTau CR, H_{T} distribution in $t\bar{t}$ with NNLO top p_{T} reweighting. (b) TrueTau CR, H_{T} distributioni in $t\bar{t}$ with various generators.

Zmumu0b VR and Ztautau0b VR with $H_{\mathrm{T}} \in [1000, 1500]$. Unlike usual validation regions in this case Zmumu0b VR is fitted to the data the Ztautau0b VR is scaled by the Zmumu0b VR NP times the mu/tau correction factor from Zmumu0b and Ztautau0b:

$$NF(\text{Ztautau0bVR} = NF(\text{Zmumu0bVR} \times \frac{NF(\text{Ztautau0bCR}}{NF(\text{Zmumu0bVR}}$$

If the method works properly the overall normalisation in the Ztautau0b VR should be correct. A similar procedure can be performed for OneMu VR and OneTau VR to check the mu/tau extrapolation for leptons coming from top decays. The resulting yields in OneTau VR and Ztautau0b VR are presented in Figure 8.25. The conclusion is that the mu/tau extrapolation used by the analysis is robust against H_{T} extrapolation.

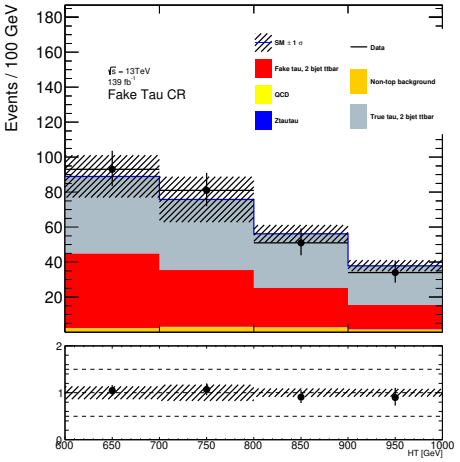

(a) FakeTau CR H_{T} after the fit.

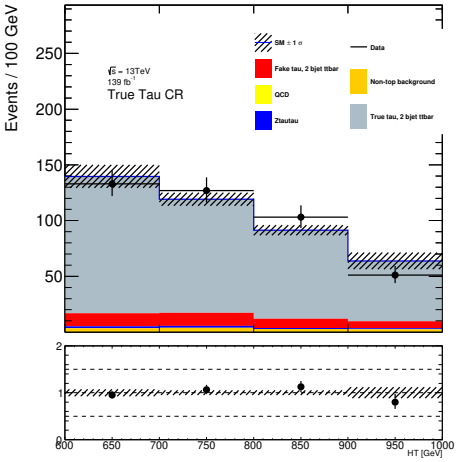

(b) TrueTau CR H_{T} after the fit.

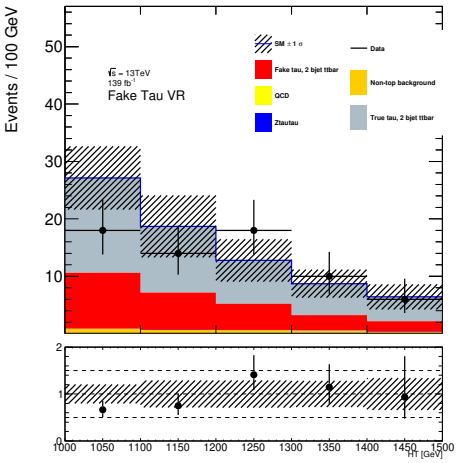

(c) FakeTau VR H_{T} after the fit.

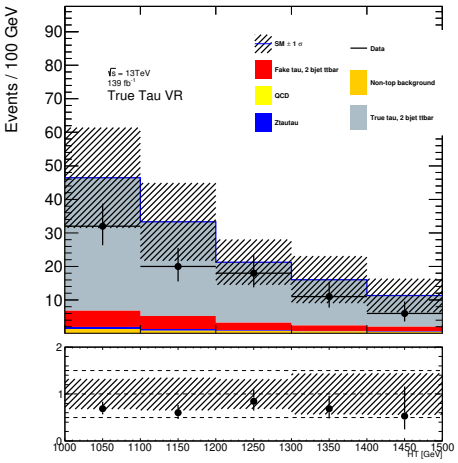

(d) TrueTau VR H_{T} after the fit.

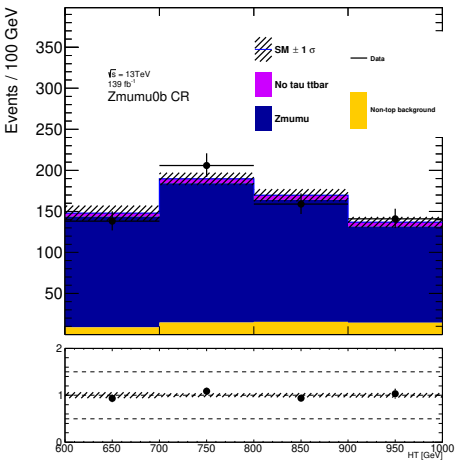

(e) Zmumu2b CR H_{T} after the fit.

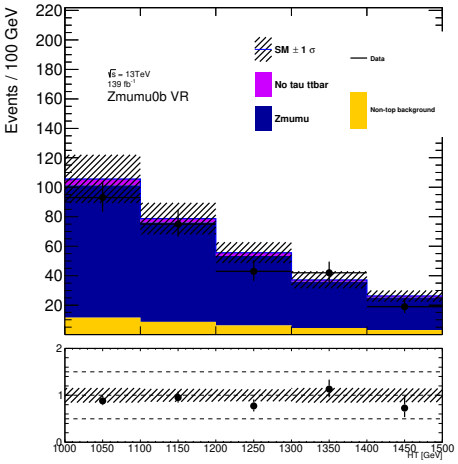

(f) Zmumu2b VR H_{T} after the fit.

Figure 8.24: Distributions of H_{T} in various CRs and VRs. All uncertainties are included and shown as the hatched band. The upper panels show distributions of the expected SM backgrounds with data overlaid. The lower panels show data/MC ratios. In the plots marked "after the fit" the SM backgrounds are scaled with the weights obtained in the background-only fit.

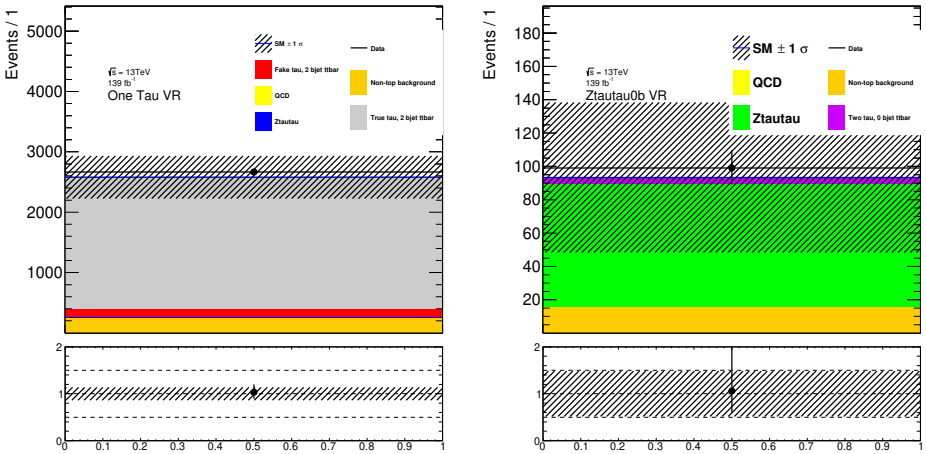

(a) One Tau VR, mu/tau extrapolation check (b) Ztautau0b VR, mu/tau extrapolation check

Figure 8.25: Tau VRs with background expectation estimated from muon VRs × mu/tau extrapolation factor. All uncertainties are included and shown as the hatched band. The upper panels show distributions of the expected SM backgrounds with data overlaid. The lower panels show data/MC ratios. The SM backgrounds are scaled with the weights obtained in the background-only fit.

Chapter 9

Systematic Uncertainties

There is no such thing as a perfectly exact measurement. Any experimental result comes with a certain variability attached. This variability can be represented as the sum of two components - random (or statistical) errors due to random fluctuations that differ from measurement to measurement and systematic errors (or bias) that remain the same when the measurements are repeated. In this section the sources of systematic errors present in the analysis and how they are evaluated is described.

9.1 Modelling Uncertainties

During the production of the Monte-Carlo samples the computation of the matrix element (at the next-to-leading-order) and the subsequent hadron showering are separated. Different software is often used to perform the two tasks, see Section 5.3. There are different ways to match the matrix element to the showers leading to a systematic uncertainty. Similar comments apply to the resummation scale, the upper cutoff of the parton shower. The showering algorithms themselves differ between generators and represent yet another systematic.

Another source of systematic uncertainty comes from the fact that the generators only operate with a limited precision and require Parton Distribution Functions (PDFs, see Section 4.3) that come with their own experimental uncertainties. For processes that are strongly produced an additional thing to worry about is the precision of the strong coupling constant α_s. It is determined experimentally (once again, with it's own uncertainties) at the Z mass peak and propagated using renormalisation group equation that is truncated at a fixed order. The cross sections that are used to normalise MC samples to the expected luminosity have their own uncertainties too.

The analysis considers the following modelling uncertainties:

Parton Density Function uncertainties include experimental uncertainties from the datasets used to determine PDFs, uncertainty on functional form, flavour scheme, nuclear effects. MC samples are generated with the `NNPDF3.0_NNLO` PDF set that contains the nominal set and 100 PDF variations that are used to estimate the uncertainties. The PDF uncertainty is evaluated as the RMS of the variations:

$$\delta^{\mathrm{PDF}} \cdot N_0 = \sqrt{\frac{1}{100}\sum_{i=1}^{100}(N_i - N_0)^2}$$

where N_0 and N_i are the yields for nominal and varied weights, respectively. Additionally, PDF uncertainties due to the uncertainties in the strong coupling constant (both experimental errors and due to truncation of RGE) are evaluated as:

$$\delta^{\alpha_s} \cdot N_0 = \frac{N(\alpha_s^{\text{down}}) - N(\alpha_s^{\text{up}})}{2}.$$

Where $\alpha_s^{\text{up/down}}$ are computed by settining $\alpha_s = 0.119/0.117$ instead of the nominal $\alpha_s = 0.118$ at Z peak mass. This uncertainty is combined with δ^{PDF} quadratically:

$$\delta^{\alpha+\text{PDF}} = \sqrt{(\delta^{\text{PDF}})^2 + (\delta^{\alpha_s})^2}$$

The PDF uncertainties are computed for all samples in the same way (with the α_s variation added when relevant). The overall conclusion is that the analysis is not sensitive to the PDF variations with the largest contributions being of the order of 1%.

Scale uncertainties are evaluated by varying the renormalisation (μ_r) and the factorisation (μ_f) scales. These uncertainties are treated as correlated across regions (e.g. TrueTau CR and FakeTau CR) and uncorrelated across samples (e.g. $t\bar{t}$ and $Z(\tau\tau)$). The nominal μ_r value is scaled by 0.5 and 2.0 to define Down and Up variations correspondingly. The same procedure is applied to μ_f. The two nuisance parameters (NPs) are treated as independent. The coherent-variation combination of scales (that is, the $\{\mu_r, \mu_f\} \times \{0.5, 0.5\}, \{2.0, 2.0\}$ as the down and up variations) is also included as a separate uncertainty to provide more freedom to the fit. Removing the assumption of correlation across the regions leads to exclusion limits that are consistent with or slightly lower than the exclusion limits computed with the correlation assumption.

Radiation (ISR) uncertainty are evaluated for $t\bar{t}$ and single-top backgrounds by varying a combination of parameters. To obtain the Down uncertainty, the renormalisation and factorisation scales are doubled and the Var3c Down shower tune is used [90] (effectively corresponding to the variation of the α_s parameter). For the Up uncertainty, the renormalisation and factorisation scales are halved, the Var3c Up shower tune is used. $t\bar{t}$ specific: for the Up uncertainty the cutoff scale for the first gluon emission h_{damp} is set to 3 m_t (the nominal value being 1.5 m_t). Unlike the other variations that are implemented as generator weights this requires production of alternative MC sample.

Radiation (FSR) uncertainty are evaluated for $t\bar{t}$ and single-top backgrounds by varying the Var2 shower tune [90] (variations related to jet structure effects) to define the Down and Up variations.

Hard Scattering generation and matching uncertainties are evaluated for the $t\bar{t}$ and single-top production backgrounds by comparing nominal samples (produced with POWHEG-BOX+PYTHIA8 generators) with alternative MADGRAPH5_aMC@NLO+PYTHIA8 samples. POWHEG and MADGRAPH5_aMC@NLO use differemt algorithms to match the NLO matrix element to the patron shower. The showering is performed by PYTHIA8 in both cases so that only the variation due to the matching are captured. This is one of the dominating sources of uncertainty for the analysis.

Parton Showering uncertainties are evaluated for the $t\bar{t}$ and single-top production backgrounds by comparing nominal samples (produced with POWHEGBOX+PYTHIA8 generators) with alternative samples (produced with POWHEGBOX+HERWIG). PYTHIA8 and HERWIG7 perform parton showering and hadronisation using different approaches, it is a priori not clear which is the more "correct" one. Both generators are used to shower samples with the matrix element computed by POWHEGBOX, the difference is used as the uncertainty. One of the dominating sources of uncertainty for the analysis (together with the hard scattering uncertainties).

Wt / $t\bar{t}$ interference uncertainty is relevant for single-top samples. It is evaluated by comparing the Wt channel samples generated using DR (nominal) and DS schemes for $t\bar{t}$ subtraction.

V+jets generator modelling: $Z(\mu\mu)$ and $Z(\tau\tau)$ backgrounds are significant in some regions. As an additional systematic uncertainty the nominal samples produced with SHERPAare compared to alternative samples produced with MADGRAPH.

V+jets scale uncertainty parametrisation: to evaluate the matrix element matching scale (CKKW) and resummation scale (QSF) related uncertainties of V+jets SHERPA samples, the parametrisation method [91] is used. In short the effect of these systematics is evaluated at the MC truth level in dedicated SHERPAsamples.

9.2 Experimental Uncertainties

Experimental (or detector) uncertainties are related to the reconstruction of various objects used in the analysis - jets, taus, $E_{\mathrm{T}}^{\mathrm{miss}}$ etc. The recommendations for these uncertainties are provided by the corresponding combined performance groups. Most of the systematics are implemented as up and down variations of the nominal value. The systematics presented in this section are applied to ALL Monte-Carlo samples including the signal samples.

Electron Related Systematics Three nuisance parameters (NP) related to the electron modelling are used, providing variations on the efficiencies of electron reconstruction, isolation and identification.

Muon Related Systematics The muon systematic uncertainties include statistical and systematic errors on the muon scale factor (2 NPs for p_{T} larger or smaller than 15 GeV each). Statistical and systematic errors of the muon isolation, track-to-vertex-association and bad muon veto efficiencies are used as well. Three momentum resolution NPs are due to the resolution of tracks in the Inner Detector and the Muon Spectrometer systems as well as the variations of the momentum scale. Two NPs describe the charge-dependent variations in the momentum scale related to the sagitta bias. Finally two more NPs describe the statistical and systematic errors of the muon trigger scale factors.

Tau Related Systematics Tau systematics include 10 NPs related to the RNN tau ID, based on number of charged tracks and the p_{T} of the tau. Two NPs are related to the tau reconstruction and two more to the electron veto. Finally four NPs describe the uncertainties of the tau energy scale.

$E_{\mathrm{T}}^{\mathrm{miss}}$ Related Systematics $E_{\mathrm{T}}^{\mathrm{miss}}$ is calculated from objects that come with their own systematics defined. The only term this doesn't apply to is the soft term. Three NPs are used describing the variations due to offset along the axis of the hard $E_{\mathrm{T}}^{\mathrm{miss}}$ component and smearing by resolution uncertainty along and perpendicular to the axis of the hard $E_{\mathrm{T}}^{\mathrm{miss}}$ component (with the positive offset applied).

Jet Related Systematics Jet systematics are separated in several subgroups. First two NPs describe uncertainties related to the jet pileup tagging efficiency, one for central and forward jets each. Jet energy resolution (JER) systematics are p_{T} and η dependent and come from several sources - data/MC differences, noise term and dijet p_{T} balance asymmetry. The JER systematics are described by 7 "grouped" NPs in the following way - all possible variations are considered, the six largest are kept while everything else is summed in quadrature as the seventh NP. Additionally one data/MC specific NP is used.

Jet energy scale (JES) uncertainties come from multiple sources and would require $O(100)$ NPs to describe fully. Instead a heavily reduced set of 7 systematics is used. Three of them are related to η inter-calibration, one more to the jet flavour response and the remaining three group everything else. The heavy reduction in the number of systematics can cause the loss of relevant correlation information, This is further discussed in Section 9.3.

Flavour Systematics The uncertainties related to flavour tagging are either the uncertainties of the scale factors used to correct the data/MC flavour tagging differences (3 NPs for b, c and light quarks) or due to extrapolation over p_{T} from the range used in calibration samples to larger values (2 NPs).

9.3 JES Scenarios Variations

As mentioned before, the JES systematics are estimated by using a highly reduced set of NPs. These reductions, among other effects, lead to the loss of information on the correlation between leading and sub-leading jet. This is typically not an issue for exotic or SUSY searches (like this analysis), but needs to be verified nonetheless. There are 3 different reduction scenarios that vary the jet correlations, the nominal scanerio is compared with alternatives to see if it has any effect on the final results (such as limits or p-values). The comparison is described in Appendix F, the conclusion is that the analysis is not sensitive the jet correlations and can use the heavily reduced JES systematics.

9.4 Various Other Uncertainties

There is a group of systematic uncertainties that do not exactly fit in either of the beforementioned categories, but should be mentioned nevertheless. They are summarised in this section.

- Pileup uncertainty is computed by changing the data scale factors up and down from the nominal value.
- Cross-section uncertainty is, in general, provided for each process. However in the analysis the dominant samples are scaled to the data so the cross-section uncertainties do not apply for them. For all samples that are not scaled to data a constant 15% uncertainty is applied as the upper bound. It is in principle possible to apply this uncertainty per sample, but it would require applying $O(900)$ values by hand. Combined with the fact that the dominating backgrounds are not affected this approach is safe if slightly conservative.
- Jet smearing uncertainties are derived by varying the $E_{\mathrm{T}}^{\mathrm{miss}}$ significance cut $(0.5 + 0.1 \times N_{b-\mathrm{jet}})$ by $\pm 30\%$ as the Up and Down variations.

9.5 Signal Uncertainties

The signal samples are produced using the AtlFastII (AFII) simplified approach so in addition to all the experimental systematics described previously the signal samples have 3 additional NPs that describe the JER data/MC agreement for AFII, jets relative non-closure in AFII and the tau specific AFII agreement. The cross sections are calculated to approximate next-to-next-to-leading order in the strong coupling constant, adding the resummation of soft gluon emission at next-to-next-to-leading-logarithmic accuracy (approximate NNLO+NNLL) [92–99]. The nominal cross section and the uncertainty are derived using the PDF4LHC15_mc PDF set, following the recommendations of Ref. [100].

For the detector systematics in signal samples the following variations are considered:

- Factorization and renormalization scale (Scale Up/Down).
- Merging scale xqcut (Xqcut Up/Down).
- Parton shower tuning and radiation (Var1, Var2, Var3a, Var3b, and Var3c Up/-Down PYTHIA8 eigentunes [90])

For this study 7 different signal models evenly spread over the signal grid are selected and all variations (as well as the the nominal job options) are run on them. The differences due to generator variations are determined using MC truth without any reconstruction or digitisation. Some additional weights are applied such as tau reconstruction $\times$ ID efficiencies and generator level weights. The unoptimised SR selection is used for this study to increase the number of events available. The effects of variations are summarised in Table 9.1. The conclusion is to use an overall 20% uncertainty

for all signal points based on average size of the discrepancies. This is a slightly conservative choice for higher sbottom masses, but also robust enough to allow for possible expansions of the grid. The justifications for using MC truth are gathered in Appendix E.

$m_{\tilde{b}}, m_{\tilde{\chi}_2^0}$	250, 180	450, 131	450, 180	700, 131	900, 131	700, 180	850, 180
Var1 Up	0.107717	0.0288867	0.0713142	0.0390725	0.0425806	0.0225189	0.0356681
Var1 Down	0.12786	0.0845837	0.0507875	0.120126	0.0677097	0.151622	0.0469697
Var2 Up	0.181537	0.0766184	0.0585824	0.0588271	0.0375856	0.0534677	0.0269975
Var2 Down	0.0984243	0.034333	0.0296517	0.0926454	0.102172	0.00917675	0.0314725
Var3a Up	0.0219475	0.147467	0.0589198	0.0676276	0.0576551	0.0227046	0.0408336
Var3a Down	0.118363	0.0481287	0.0506902	0.0529077	0.0976902	0.0503399	0.0411962
Var3b Up	0.00733987	0.0332796	0.0801067	0.036283	0.00855128	0.0492464	0.0853271
Var3b Down	0.163585	0.0705848	0.0665704	0.00273273	0.030585	0.0226846	0.045458
Var3c Up	0.0594996	0.0513659	0.17254	0.014504	0.00499475	0.0337029	0.0871849
Var3c Down	0.157304	0.0481784	0.0760004	0.103703	0.0391619	0.0717236	0.00391215
Scale Up	0.010766	0.0221238	0.129477	0.0257872	0.0629988	0.0228133	0.00371411
Scale Down	0.129942	0.044324	0.182302	0.115714	0.0622953	0.0284247	0.0532738
Xqcut Up	0.171048	0.0354804	0.15061	0.113799	0.0269383	0.0466311	0.0569491
Xqcut Down	0.065171	0.0279769	0.0435114	0.101686	0.0624818	0.0254014	0.127668

Table 9.1: Table of systematic variations for select signal samples, (Nominal-Alternative)/Nominal in the unoptimised SR.

9.6 Results and Presentation

All systematic uncertainties related to a region are grouped together in tables. Only entries larger than 1% are presented in the tables, but the total systematic uncertainty is computed using every contribution. The names of the systematics are based on the inner logic and can be somewhat cryptic. The total sum of the systematic uncertainties is not a quadratic sum of all components, the correlations between systematics are considered. An example can be seen in Table 9.2. Prefix alpha indicates that this is a systematic uncertainty while prefix omega is assigned to the uncertainties propagated by the normalisation factors used in the fit.

The Table 9.2 gathers the systematic uncertainties from the three top control regions with taus. Theory systematics are suppressed in these regions as the MC is directly fitted to the data and so the uncertainties propagated by the NPs dominate. This is expected as the normalisation factors are correlated with each other - e.g. the FakeTau CR has an equal mix of true and fake taus. Any change to the normalisation of true taus causes a change to the fake tau normalisation and vice versa. The other significant systematics include JER combined variations, `alpha_jetnp1` and `alpha_jetnp2` and ISR variation in $t\bar{t}$ `alpha_ttbar_syst_radH`. The total uncertainties of these regions are fixed at $\sqrt{N}$ as the overall number of events is normalised to the data.

The next example is Table 9.3 that gathers the systematic uncertainties in the top validation regions with taus. Since there is no normalisation to data in the validation regions the theory systematics become more significant. The leading contributors

(along with what the NPs propagate) are comparison of nominal $t\bar{t}$ with the MADGRAPH5_aMC@NLO+PYTHIA8 alternative samples `alpha_amcnlott` and comparison of DS vs DR schemes for single top samples `alpha_singletopds`. Several other systematic uncertainties are significant for some of the regions, such as JER variations, radiation variations in $t\bar{t}$, FSR variations in $t\bar{t}$ `alpha_fsrsyst`, coherent variation of the factorisation and renormalisation scales in $t\bar{t}$ `alpha_murmufcomb` and comparisons to the alternative POWHEGBOX+HERWIG generators. Note that most of the systematics are related to the $t\bar{t}$ samples since the regions in the example are dominated by $t\bar{t}$.

Uncertainty of channel	Fake Tau CR	True Tau CR	One Tau CR
Observed events	324	483	13793
Total background expectation	258.99	413.99	8891.13
Total statistical ($\sqrt{N_{exp}}$)	±16.09	±20.35	±94.29
Total background systematic	±15.93 [6.15%]	±20.35 [4.92%]	±94.74 [1.07%]
omega_fake_tau	±41.92 [16.2%]	±14.39 [3.5%]	±0.00 [0.00%]
omega_true_tau	±24.46 [9.4%]	±63.39 [15.3%]	±0.00 [0.00%]
alpha_jetnp1	±17.07 [6.6%]	±18.65 [4.5%]	±488.24 [5.5%]
alpha_jetnp2	±16.74 [6.5%]	±18.69 [4.5%]	±504.35 [5.7%]
alpha_amcnlott	±13.84 [5.3%]	±13.83 [3.3%]	±0.00 [0.00%]
alpha_jetflvresp	±13.21 [5.1%]	±13.45 [3.2%]	±383.85 [4.3%]
alpha_ttbar_syst_radH	±11.36 [4.4%]	±32.05 [7.7%]	±440.13 [5.0%]
alpha_fsrsyst	±8.78 [3.4%]	±8.78 [2.1%]	±0.00 [0.00%]
alpha_amcnlost	±6.91 [2.7%]	±6.90 [1.7%]	±0.00 [0.00%]
alpha_bsyst	±6.23 [2.4%]	±10.22 [2.5%]	±192.52 [2.2%]
alpha_singlet_syst_radH	±5.74 [2.2%]	±7.01 [1.7%]	±0.00 [0.00%]
alpha_murmufcomb	±5.20 [2.0%]	±19.31 [4.7%]	±0.00 [0.00%]
alpha_murmufcomb_st	±4.52 [1.7%]	±9.30 [2.2%]	±148.79 [1.7%]
alpha_singletopds	±3.64 [1.4%]	±0.00 [0.00%]	±0.00 [0.00%]
alpha_jeteffnp1	±3.26 [1.3%]	±0.00 [0.00%]	±0.00 [0.00%]
alpha_mursyst	±3.11 [1.2%]	±13.04 [3.2%]	±0.00 [0.00%]
alpha_taurnnidsyst	±3.07 [1.2%]	±7.83 [1.9%]	±173.91 [2.0%]
alpha_metresoperp	±3.00 [1.2%]	±0.00 [0.00%]	±0.00 [0.00%]
alpha_jeteffnp2	±2.77 [1.1%]	±0.00 [0.00%]	±0.00 [0.00%]
alpha_herwig7st	±2.76 [1.1%]	±0.00 [0.00%]	±0.00 [0.00%]
alpha_mursyst_st	±2.75 [1.1%]	±5.81 [1.4%]	±0.00 [0.00%]
alpha_jetdatamc	±2.73 [1.1%]	±0.00 [0.00%]	±0.00 [0.00%]
alpha_taudetector	±0.00 [0.00%]	±6.75 [1.6%]	±161.92 [1.8%]
alpha_mufsyst	±0.00 [0.00%]	±5.79 [1.4%]	±0.00 [0.00%]
omega_1mu	±0.00 [0.00%]	±0.00 [0.00%]	±850.32 [9.6%]
omega_scale_top	±0.00 [0.00%]	±0.00 [0.00%]	±337.13 [3.8%]

Table 9.2: Breakdown of the dominant systematic uncertainties on background estimates in the various signal regions. Note that the individual uncertainties can be correlated, and do not necessarily add up quadratically to the total background uncertainty. The percentages show the size of the uncertainty relative to the total expected background.

Uncertainty of channel	Fake Tau VR	True Tau VR	One Tau VR
Observed events	85	154	2666

Total background expectation	73.76	128.39	1749.46
Total statistical ($\sqrt{N_{exp}}$)	±8.59	±11.33	±41.83
Total background systematic	±17.81 [24.15%]	±44.12 [34.37%]	±390.77 [22.34%]
alpha_amcnlott2	±13.91 [18.9%]	±40.01 [31.2%]	±321.42 [18.4%]
omega_fake_tau	±9.55 [12.9%]	±5.30 [4.1%]	±0.00 [0.00%]
omega_true_tau	±8.03 [10.9%]	±19.25 [15.0%]	±0.00 [0.00%]
alpha_singletopds2	±7.89 [10.7%]	±12.32 [9.6%]	±185.79 [10.6%]
alpha_fsrsyst2	±4.97 [6.7%]	±3.09 [2.4%]	±41.50 [2.4%]
alpha_ttbar_syst_radH	±3.82 [5.2%]	±6.27 [4.9%]	±89.79 [5.1%]
alpha_jetnp1	±3.64 [4.9%]	±5.64 [4.4%]	±93.95 [5.4%]
alpha_jetnp2	±3.34 [4.5%]	±5.19 [4.0%]	±88.08 [5.0%]
alpha_murmufcomb	±2.95 [4.0%]	±8.38 [6.5%]	±42.45 [2.4%]
alpha_murmufcomb_st	±2.87 [3.9%]	±4.43 [3.5%]	±67.62 [3.9%]
alpha_jetflvresp	±2.25 [3.1%]	±3.43 [2.7%]	±62.25 [3.6%]
alpha_bsyst	±1.57 [2.1%]	±3.01 [2.3%]	±36.42 [2.1%]
alpha_mursyst_st	±1.55 [2.1%]	±2.56 [2.0%]	±36.58 [2.1%]
alpha_mursyst	±1.54 [2.1%]	±5.05 [3.9%]	±22.79 [1.3%]
alpha_herwig7tt2	±1.37 [1.9%]	±6.71 [5.2%]	±25.38 [1.5%]
alpha_mufsyst	±1.36 [1.8%]	±3.20 [2.5%]	±18.96 [1.1%]
alpha_mufsyst_st	±1.25 [1.7%]	±1.77 [1.4%]	±29.54 [1.7%]
alpha_amcnlost2	±1.18 [1.6%]	±6.48 [5.0%]	±56.37 [3.2%]
alpha_jetnp3	±1.11 [1.5%]	±0.00 [0.00%]	±25.44 [1.5%]
alpha_taurnnidsyst	±0.99 [1.3%]	±2.39 [1.9%]	±34.13 [2.0%]
alpha_jetdatamc	±0.88 [1.2%]	±0.00 [0.00%]	±0.00 [0.00%]
alpha_fsrsyst2_st	±0.77 [1.0%]	±0.00 [0.00%]	±0.00 [0.00%]
alpha_jeteffnp3	±0.75 [1.0%]	±0.00 [0.00%]	±0.00 [0.00%]
alpha_taudetector	±0.00 [0.00%]	±1.47 [1.1%]	±22.39 [1.3%]
alpha_lsyst	±0.00 [0.00%]	±0.00 [0.00%]	±22.59 [1.3%]
alpha_herwig7st2	±0.00 [0.00%]	±0.00 [0.00%]	±24.84 [1.4%]
alpha_wtaunulumi	±0.00 [0.00%]	±0.00 [0.00%]	±18.54 [1.1%]
omega_1mu	±0.00 [0.00%]	±0.00 [0.00%]	±158.70 [9.1%]
omega_scale_top	±0.00 [0.00%]	±0.00 [0.00%]	±62.92 [3.6%]

Table 9.3: Breakdown of the dominant systematic uncertainties on background estimates in the various signal regions. Note that the individual uncertainties can be correlated, and do not necessarily add up quadratically to the total background uncertainty. The percentages show the size of the uncertainty relative to the total expected background.

Chapter 10

Results

In this section the results of the analysis are presented – yields in various regions, systematics and their correlations, exclusion regions and limits.

10.1 Z Regions Results

The regions used to model $Z \to \tau\tau$ processes include 3 control regions and one validation region. The observed data yields as well as the MC predictions before and after the fit are gathered in Table 10.1. The predictions in the CRs obviously agree with the data since they are normalised to it. Theory systematic uncertainties are suppressed due to the normalisation, the total uncertainties are set to $\sqrt{N}$. Zmumu2b VR on the other hand is not constrained to the data (since it doesn't participate in the fit) so that the systematic uncertainties are much larger there, of the order of 15%. The predicted yields slightly overestimate the observed data, but are well within 1σ uncertainty. The expected signal contribution to the regions is minimal.

The dominating systematics for $Z(\mu\mu)$ regions are summarised in Table 10.2 and for Ztautau0b CR in Table 10.3. For Zmumu2b CR and Zmumu0b CR the dominant systematics are uncertainties of the NPs that are suppressed by normalisation to the data. The same is true for Ztautau0b CR too. For Zmumu2b VR the largest systematic is comparison of the nominal samples to the alternative samples produced with MADGRAPH. Other noteworthy uncertainties include various jets-related systematics (JER and JES).

	Ztautau0b CR	Zmumu0b CR	Zmumu2b CR	Zmumu2b VR
Observed events	241	16475	644	272
Fitted bkg events	240.98 ± 15.48	16474.99 ± 128.47	644.02 ± 25.35	303.27 ± 43.23
Fitted $t\bar{t}X$ events	0.45 ± 0.20	11.41 ± 1.86	31.29 ± 4.81	22.54 ± 3.72
Fitted $Z(\tau\tau)$ events	189.87 ± 17.19	1.71 ± 0.86	0.04 ± 0.01	0.00 ± 0.00
Fitted $Z(\mu\mu)$ events	0.05 ± 0.01	15852.24 ± 169.98	570.67 ± 27.19	258.38 ± 42.51
Fitted $t\bar{t}$ and single top events	11.28 ± 2.19	5.27 ± 3.50	17.89 ± 6.88	10.32 ± 5.06
Fitted "the rest" events	39.33 ± 6.33	603.78 ± 109.74	21.90 ± 4.27	11.28 ± 2.68
Fitted multijet (QCD) events	0.00 ± 0.00	0.00 ± 0.00	0.00 ± 0.00	0.00 ± 0.00
MC exp. $m_{\tilde{b}} = 800$, $m_{\tilde{\chi}_2^0} = 131$	0	0	0	0.03
MC exp. $m_{\tilde{b}} = 800$, $m_{\tilde{\chi}_2^0} = 180$	0	0	0.06	0.06

Table 10.1: Table of contributions from different processes to the control regions. All available systematics included.

Uncertainty of channel	Zmumu2b CR	Zmumu0b CR	Zmumu2b VR
Observed events	644	16475	272
Total background expectation	644.02	16474.99	303.27
Total statistical ($\sqrt{N_{exp}}$)	±25.38	±128.35	±17.41
Total background systematic	±25.35 [3.94%]	±128.47 [0.78%]	±43.23 [14.25%]
omega_zmumu2b	±54.50 [8.5%]	±0.00 [0.00%]	±24.68 [8.1%]
alpha_lsyst	±28.78 [4.5%]	±0.00 [0.00%]	±20.11 [6.6%]
alpha_jetnp2	±20.47 [3.2%]	±519.99 [3.2%]	±11.79 [3.9%]
alpha_jetnp1	±17.62 [2.7%]	±425.25 [2.6%]	±10.87 [3.6%]
alpha_bsyst	±16.33 [2.5%]	±0.00 [0.00%]	±7.32 [2.4%]
alpha_jetflvresp	±14.01 [2.2%]	±346.24 [2.1%]	±7.96 [2.6%]
alpha_csyst	±10.07 [1.6%]	±0.00 [0.00%]	±4.69 [1.5%]
alpha_murecosys	±6.59 [1.0%]	±171.65 [1.0%]	±3.81 [1.3%]
alpha_ttxlumi	±0.00 [0.00%]	±0.00 [0.00%]	±3.36 [1.1%]
alpha_jeteffnp1	±0.00 [0.00%]	±0.00 [0.00%]	±4.27 [1.4%]
alpha_jeteffnp2	±0.00 [0.00%]	±0.00 [0.00%]	±3.44 [1.1%]
alpha_jetaxtracharm	±0.00 [0.00%]	±0.00 [0.00%]	±7.20 [2.4%]
alpha_amcnlott2	±0.00 [0.00%]	±0.00 [0.00%]	±4.88 [1.6%]
alpha_madgraphmu	±0.00 [0.00%]	±0.00 [0.00%]	±36.95 [12.2%]
alpha_paramckkw_zmumu	±0.00 [0.00%]	±0.00 [0.00%]	±10.89 [3.6%]
omega_zmumu0b	±0.00 [0.00%]	±837.75 [5.1%]	±0.00 [0.00%]
alpha_paramqsf_zmumu	±0.00 [0.00%]	±0.00 [0.00%]	±6.42 [2.1%]

Table 10.2: Breakdown of the dominant systematic uncertainties on background estimates in the various regions. Note that the individual uncertainties can be correlated, and do not necessarily add up quadratically to the total background uncertainty. The percentages show the size of the uncertainty relative to the total expected background.

Uncertainty of channel	Ztautau0b CR
Observed events	272
Total background expectation	240.98
Total statistical ($\sqrt{N_{exp}}$)	±15.52
Total background systematic	±15.48 [6.43%]
omega_scale_Z	±32.13 [13.3%]
alpha_jetnp1	±16.60 [6.9%]
alpha_taudetector	±16.16 [6.7%]
alpha_jetnp2	±15.49 [6.4%]
alpha_jetflvresp	±11.50 [4.8%]
omega_zmumu0b	±10.03 [4.2%]
alpha_taurnnidsyst	±8.97 [3.7%]
alpha_jeteffnp2	±5.03 [2.1%]
alpha_jeteffnp3	±4.63 [1.9%]

alpha_taujetidrecotot	±4.06 [1.7%]
alpha_jeteffnp1	±4.03 [1.7%]
alpha_jeteffnp7	±3.91 [1.6%]
alpha_jeteffnp4	±3.52 [1.5%]
alpha_jetnp3	±3.40 [1.4%]
alpha_wtaunulumi	±3.36 [1.4%]
alpha_murmufcomb_diboson	±2.60 [1.1%]
alpha_lsyst	±2.55 [1.1%]
alpha_mursyst_diboson	±2.53 [1.0%]

Table 10.3: Breakdown of the dominant systematic uncertainties on background estimates in the Ztautau0b CR. Note that the individual uncertainties can be correlated, and do not necessarily add up quadratically to the total background uncertainty. The percentages show the size of the uncertainty relative to the total expected background.

10.2 Top Region Results

Top regions are used to control $t\bar{t}$ and single top production with either true-true or true-fake tau combinations. There are 4 control regions in total and 5 validation regions, one for each of control regions plus a "combined performance" one (Ditau VR). One control and one validation region have a tau veto while all others require at least one tau. The yields of the control regions are summarised in Table 10.4. TrueTau CR is dominated by $t\bar{t}$ events with true taus while FakeTau CR has approximately equal contributions from true tau and fake tau events. The OneTau CR is dominated by true tau events while the OneMu CR is selecting $t\bar{t}$ events with 1 muon that plays the role of true tau. The total uncertainties are relatively small similar to the Z control region case as the same normalisation procedure applies. The expected signal contribution is relatively low for the benchmark models.

The yields of the corresponding top validation regions are gathered in Table 10.5. The systematics are rather large, reaching $\approx 35\%$ in case of TrueTau VR. As has been discussed previously due to the H_{T} mismodelling the predictions in top validation regions tend to overestimate the observed data. The difference is mostly contained by 1σ uncertainties. The important systematic uncertainties for these regions have already been discussed in Section 9.6.

The yields for the last validation region, Ditau VR, are shown in Table 10.6. This region is closest to the SRs in the phase space and should be the most representative of the top modelling there. The expected yields match the observed data nicely and the overall systematics are moderately large ($\approx 20\%$). The systematics breakdown is presented in Table 10.7. The dominant uncertainties are due to the true tau and fake tau transfer factors, comparison to the MADGRAPH5_aMC@NLO+PYTHIA8 alternative samples and FSR variations related systematics for $t\bar{t}$ samples and DS/DR scheme comparison for single top production. ISR variations for $t\bar{t}$ and JES combined systematics are also significant. Overall the largest systematics look similar to those discussed in Section 9.6 for the other top validation regions as is expected

	Fake Tau CR	True Tau CR	One Tau CR	One Mu CR
Observed events	259	414	8891	23565
Fitted bkg events	258.99 ± 15.93	413.99 ± 20.35	8891.13 ± 94.74	23565.79 ± 154.45
Fitted $t\bar{t}X$ events	6.72 ± 1.81	9.18 ± 2.94	97.52 ± 28.33	307.64 ± 76.17
Fitted $Z(\tau\tau)$ events	0.28 ± 0.11	5.45 ± 1.10	61.56 ± 8.64	17.72 ± 8.90
Fitted $t\bar{t}$ events with 1 true tau	125.05 ± 27.86	316.37 ± 28.90	6839.14 ± 209.18	0.00 ± 0.00
Fitted single top events with 1 true tau	13.05 ± 10.43	41.57 ± 13.15	941.31 ± 164.61	0.00 ± 0.00
Fitted $t\bar{t}$ events with 0 taus	0.00 ± 0.00	0.00 ± 0.00	0.00 ± 0.00	20002.63 ± 432.98
Fitted single top events 0 taus	0.00 ± 0.00	0.00 ± 0.00	0.00 ± 0.00	2171.79 ± 370.61
Fitted "the rest" events	2.57 ± 1.17	3.20 ± 1.28	480.55 ± 89.32	1048.88 ± 188.21
Fitted multijet (QCD) events	0.02 ± 0.01	$0.01^{+0.07}_{-0.01}$	26.38 ± 12.89	17.14 ± 8.42
Fitted $t\bar{t}$ events with 1 fake tau	102.43 ± 33.77	34.66 ± 15.34	401.85 ± 46.35	0.00 ± 0.00
Fitted single top events with 1 fake tau	8.88 ± 3.73	$3.53^{+4.82}_{-3.53}$	42.82 ± 9.90	0.00 ± 0.00
MC exp. $m_{\tilde{b}} = 800$, $m_{\tilde{\chi}^0_2} = 131$	0.18	0.55	2.61	0.17
MC exp. $m_{\tilde{b}} = 800$, $m_{\tilde{\chi}^0_2} = 180$	0.43	1.04	4.83	0.39

Table 10.4: Table of contributions from different processes to the control regions. All available systematics included.

	Fake Tau VR	True Tau VR	One Tau VR	One Mu VR
Observed events	66	87	1531	5431
Fitted bkg events	73.76 ± 17.81	128.39 ± 44.12	1749.46 ± 390.77	6046.17 ± 1216.95
Fitted $t\bar{t}X$ events	1.91 ± 0.66	3.22 ± 0.92	28.26 ± 7.78	111.81 ± 27.38
Fitted $Z(\tau\tau)$ events	0.15 ± 0.04	1.58 ± 0.32	17.47 ± 2.86	5.32 ± 1.66
Fitted $t\bar{t}$ events with 1 true tau	38.47 ± 11.60	94.80 ± 37.04	1206.61 ± 301.79	0.00 ± 0.00
Fitted single top events with 1 true tau	6.84 ± 6.55	13.90 ± 13.50	245.50 ± 200.72	0.00 ± 0.00
Fitted "the rest" events	1.02 ± 0.22	0.81 ± 0.26	140.73 ± 29.32	345.05 ± 75.48
Fitted multijet (QCD) events	0.01 ± 0.01	0.01 ± 0.00	10.99 ± 5.15	9.71 ± 2.93
Fitter $t\bar{t}$ events with 1 fake tau	22.43 ± 10.31	12.51 ± 7.41	87.40 ± 37.16	0.00 ± 0.00
Fitted single top events with 1 fake tau	$2.92^{+2.99}_{-2.92}$	$1.55^{+1.76}_{-1.55}$	12.51 ± 10.87	0.00 ± 0.00
Fitted $t\bar{t}$ events with 0 taus	0.00 ± 0.00	0.00 ± 0.00	0.00 ± 0.00	4838.70 ± 1080.37
Fitted single top events with 0 taus	0.00 ± 0.00	0.00 ± 0.00	0.00 ± 0.00	735.57 ± 579.94
MC exp. $m_{\tilde{b}} = 800$, $m_{\tilde{\chi}^0_2} = 131$	0.31	1.3	7.5	1.55
MC exp. $m_{\tilde{b}} = 800$, $m_{\tilde{\chi}^0_2} = 180$	0.67	0.86	9.48	2.85

Table 10.5: Table of contributions from different processes to the validation regions. All available systematics included.

	DitauVR
Observed events	104
Fitted bkg events	105.12 ± 18.93
Fitted $t\bar{t}X$ events	3.14 ± 0.95
Fitted $Z(\tau\tau)$ events	5.01 ± 1.88

Fitted single top events with 2 taus	10.99 ± 9.56
Fitted $t\bar{t}$ events with 2 taus	84.22 ± 16.52
Fitted "the rest" events	1.74 ± 0.39
Fitted multijet (QCD) events	0.02 ± 0.00
MC exp. $m_{\tilde{b}} = 800$, $m_{\tilde{\chi}_2^0} = 131$	0.25
MC exp. $m_{\tilde{b}} = 800$, $m_{\tilde{\chi}_2^0} = 180$	0.51

Table 10.6: Table of contributions from different processes to various VRs.

Uncertainty of channel	Ditau VR
Observed events	168
Total background expectation	105.12
Total statistical ($\sqrt{N_{exp}}$)	$\pm$10.25
Total background systematic	$\pm$18.93 [18.01%]
omega_fake_tau	$\pm$15.45 [14.7%]
alpha_amcnlott2	$\pm$10.67 [10.2%]
omega_true_tau	$\pm$9.19 [8.7%]
alpha_singletopds2	$\pm$8.16 [7.8%]
alpha_fsrsyst2	$\pm$7.38 [7.0%]
alpha_ttbar_syst_radH	$\pm$6.58 [6.3%]
alpha_jetnp2	$\pm$6.11 [5.8%]
alpha_jetnp1	$\pm$6.10 [5.8%]
alpha_jetflvresp	$\pm$4.26 [4.1%]
omega_scale_top	$\pm$4.03 [3.8%]
alpha_murmufcomb	$\pm$3.54 [3.4%]
alpha_taurnnidsyst	$\pm$3.43 [3.3%]
alpha_herwig7st2	$\pm$3.12 [3.0%]
alpha_amcnlost2	$\pm$2.61 [2.5%]
alpha_herwig7tt2	$\pm$2.50 [2.4%]
alpha_bsyst	$\pm$2.48 [2.4%]
alpha_murmufcomb_st	$\pm$2.38 [2.3%]
alpha_taudetector	$\pm$1.89 [1.8%]
alpha_mursyst	$\pm$1.81 [1.7%]
alpha_ztautau_MG	$\pm$1.77 [1.7%]
alpha_jeteffnp2	$\pm$1.70 [1.6%]
alpha_mufsyst	$\pm$1.66 [1.6%]
alpha_taujetidrecotot	$\pm$1.61 [1.5%]
alpha_mursyst_st	$\pm$1.45 [1.4%]
alpha_jeteffnp1	$\pm$1.42 [1.4%]
alpha_jeteffnp5	$\pm$1.12 [1.1%]

Table 10.7: Breakdown of the dominant systematic uncertainties on background estimates in the various signal regions. Note that the individual uncertainties can be correlated, and do not necessarily add up quadratically to the total background uncertainty. The percentages show the size of the uncertainty relative to the total expected background.

10.3 Unblinded Signal Regions

There are effectively 4 signal regions used by the analysis, one overlapping with the other three. For exclusion a multi-bin fit is used with three bins in $\min_{\Theta}$. Each bin is statistically independent and orthogonal so they can be considered as separate signal regions. One more region is used for the discovery fit, it overlaps with two of the exclusion bins.

The yields in the single-bin discovery fit are shown in Table 10.8. Note that these are background-only fit results, i.e. the signal region itself doesn't participate in the fit. The yields are also illustrated in Figure 10.1. The agreement of MC prediction with data is great, the total systematic uncertainty reaches 40%. The main contributions to uncertainty come from $t\bar{t}$ and single top samples. The breakdown of systematic uncertainties for discovery SR is shown in Table 10.9. The dominant contributions are comparisons to MADGRAPH5_aMC@NLO+PYTHIA8 samples for $t\bar{t}$ and single top, ISR and FSR variations for $t\bar{t}$ samples, DS/DR scheme comparison for single top, JER data/MC related uncertainties and uncertainty on the transfer factors of true and fake taus. This is consistent with the dominant systematics seen in top validation regions.

Table 10.8: Expected yields in the single bin SR after the background-only fit, all available systematics included.

Observed events	4
Fitted bkg events	3.77 ± 1.53
Fitted $t\bar{t}X$ events	0.52 ± 0.42
Fitted $Z(\tau\tau)$ events	0.74 ± 0.25
Fitted single top true-true events	$0.37^{+0.60}_{-0.37}$
Fitted single top true-fake events	$0.10^{+0.15}_{-0.10}$
Fitted single top fake-fake events	0.00 ± 0.00
Fitted $t\bar{t}$ true-true events	1.04 ± 0.60
Fitted $t\bar{t}$ true-fake events	0.82 ± 0.61
Fitted $t\bar{t}$ fake-fake events	$0.11^{+0.30}_{-0.11}$
Fitted "the rest" events	0.08 ± 0.03
Fitted QCD events	0.00 ± 0.00
$m_{\tilde{b}} = 800, m_{\tilde{\chi}_2^0} = 131$	5.64 ± 0.44
$m_{\tilde{b}} = 800, m_{\tilde{\chi}_2^0} = 180$	9.28 ± 0.57

Uncertainty of channel	Discovery SR
Total background expectation	3.77
Total statistical ($\sqrt{N_{exp}}$)	± 1.94
Total background systematic	± 1.53 [40.66%]
alpha_amcnlott2	± 0.91 [24.2%]
alpha_ttbar_syst_radH	± 0.87 [23.1%]
alpha_amcnlost2	± 0.47 [12.4%]
alpha_singletopds2	± 0.42 [11.1%]

alpha_jetdatamc	±0.39 [10.2%]
alpha_fsrsyst2	±0.36 [9.6%]
omega_fake_tau	±0.34 [9.1%]
omega_true_tau	±0.25 [6.7%]
alpha_mursyst_ttX	±0.24 [6.3%]
alpha_lsyst	±0.19 [5.1%]

Table 10.9: Breakdown of the dominant systematic uncertainties on background estimates in the discovery signal regions. Note that the individual uncertainties can be correlated, and do not necessarily add up quadratically to the total background uncertainty. The percentages show the size of the uncertainty relative to the total expected background.

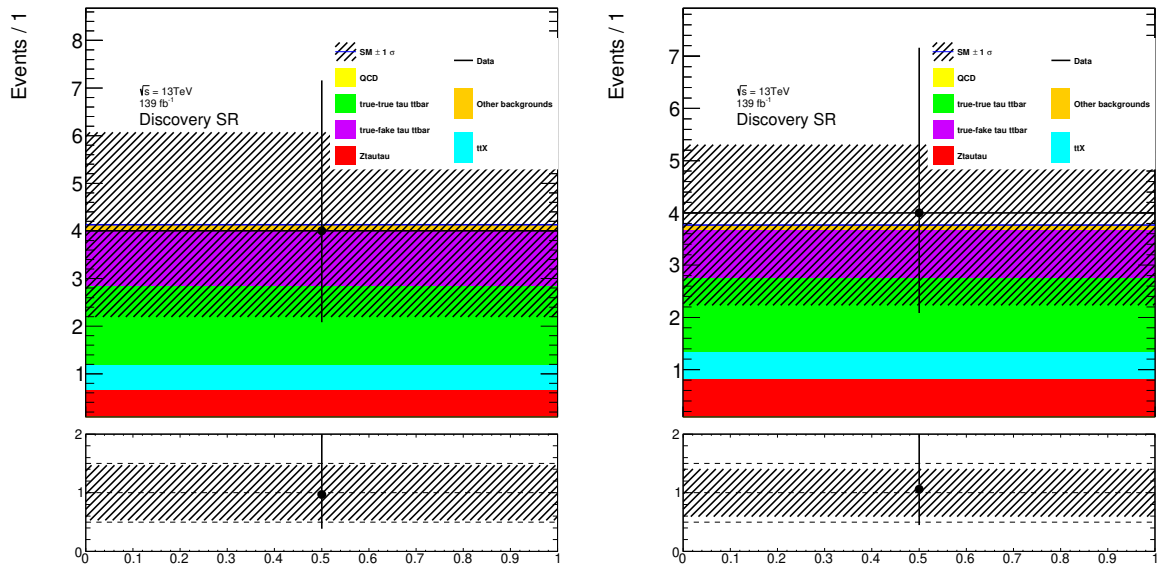

(a) One bin unblinded SR, before the fit

(b) One bin unblinded SR, after the fit

Figure 10.1: One bin yields in the unblinded SR, background-only fit (SR treated as VR). All available systematic uncertainties included.

The yields in the multi-bin signal regions are evaluated in 2 different ways. First one can apply the background-only weights to all three bins and be done with it, essentially treating them as validation regions. This gives an idea of how well the data and the MC predictions agree in the regions and makes them directly comparable to the single-bin SR and validation regions. The results are presented in Table 10.10 and illustrated in Figure 10.2. Alternatively one can consider the yields after the exclusion fit where the signal regions participate in the fit themselves. These yields are gathered in Table 10.11. Additionally Figure 10.3 shows all background-only and exclusion fit yields in one place.

The data yields in the second and third bin differ significantly from the MC prediction. The number of events is extremely low so the statistical uncertainties are large. The systematic uncertainties on the backgrounds predictions are of the order 40%. In the exclusion fit yields the MC predictions are pulled closer to the data. The systematics are once again dominated by the $t\bar{t}$ and single top samples. As a general comment –

for some of the samples the raw number of MC events available is lacking due to heavy constraints placed on the SRs, especially for alternative samples. This leads to large uncertainties ($\pm 100\%$) on some samples.

The systematic uncertainties breakdown for the background-only fit are shown in Table 10.12. Similar to other regions MADGRAPH5_aMC@NLO comparisons, ISR and FSR variations for $t\bar{t}$ samples and uncertainty on transfer factors of true and fake taus are dominating. JER data/MC agreement related uncertainties and DS/DR scheme comparison for single top are significant in the third bin where the $t\bar{t}$ contribution is relatively low.

Table 10.10: Expected yields in the three $\min_\Theta$ bin SR post-fit, all available systematics included. Background-only fit.

	$\min_\Theta < 0.5$	$0.5 < \min_\Theta < 1.0$	$\min_\Theta > 1.0$
Observed events	3	1	3
Fitted bkg events	2.65 ± 1.15	3.45 ± 1.60	1.53 ± 0.64
Fitted $t\bar{t}X$ events	0.18 ± 0.11	$0.26^{+0.32}_{-0.26}$	0.31 ± 0.22
Fitted $Z(\tau\tau)$ events	0.05 ± 0.05	0.17 ± 0.17	0.59 ± 0.23
Fitted single top events	$0.12^{+0.18}_{-0.12}$	$0.45^{+0.67}_{-0.45}$	$0.17^{+0.42}_{-0.17}$
Fitted $t\bar{t}$ events	2.30 ± 1.14	2.53 ± 1.43	0.39 ± 0.30
Fitted "the rest" events	0.00 ± 0.00	0.04 ± 0.01	0.06 ± 0.03
Fitted QCD events	0.00 ± 0.00	0.00 ± 0.00	0.00 ± 0.00
MC exp. $m_{\tilde{b}} = 800$, $m_{\tilde{\chi}^0_2} = 131$	0.143 ± 0.06	1.48 ± 0.23	4.37 ± 0.39
MC exp. $m_{\tilde{b}} = 800$, $m_{\tilde{\chi}^0_2} = 180$	0.08 ± 0.04	2.43 ± 0.30	7.10 ± 0.49

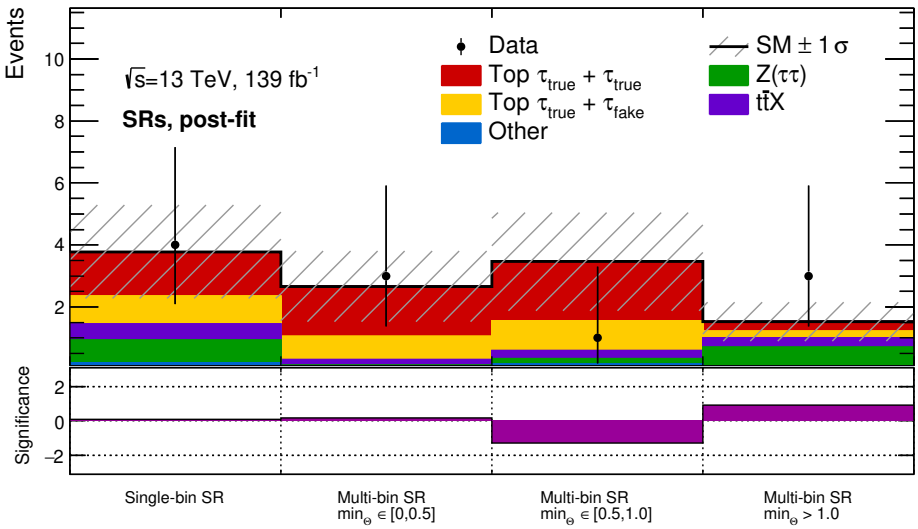

(a) Background-only fit results.

Figure 10.2: Yields in the unblinded SRs, background-only fit (SR treated as VR). All available systematic uncertainties included.

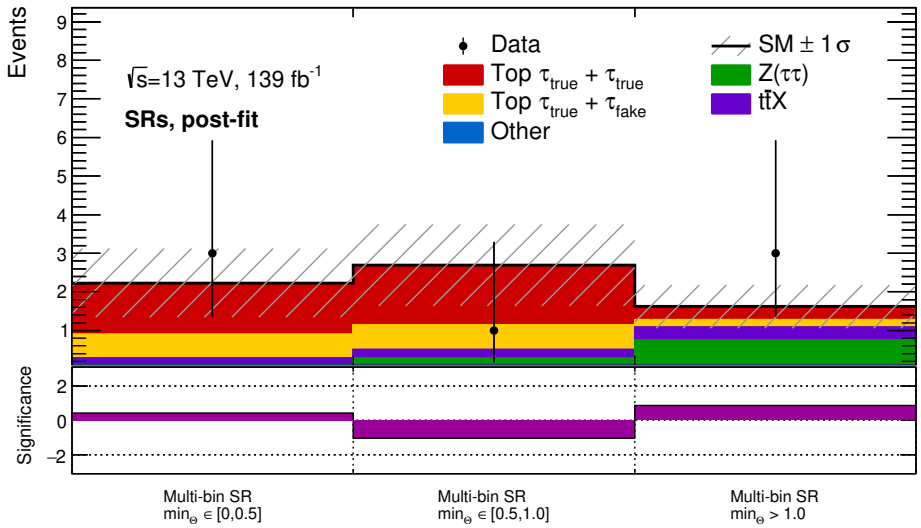

(a) Exclusion fit results.

Figure 10.3: Unblinded SRs, pullplots. All available systematic uncertainties included.

Table 10.11: Expected yields in the three $\min_\Theta$ bin SR post-fit, all available systematics included. Exclusion fit.

	$\min_\Theta < 0.5$	$0.5 < \min_\Theta < 1.0$	$\min_\Theta > 1.0$
Observed events	3	1	3
Fitted bkg events	2.23 ± 0.89	2.68 ± 1.05	1.64 ± 0.58
Fitted $t\bar{t}X$ events	0.20 ± 0.10	$0.23^{+0.26}_{-0.23}$	0.34 ± 0.22
Fitted $Z(\tau\tau)$ events	0.04 ± 0.04	0.16 ± 0.15	0.66 ± 0.25
Fitted single top events	$0.05^{+0.13}_{-0.05}$	$0.34^{+0.52}_{-0.34}$	$0.24^{+0.41}_{-0.24}$
Fitted $t\bar{t}$ events	1.85 ± 0.85	1.92 ± 0.93	0.33 ± 0.23
Fitted "the rest" events	0.00 ± 0.00	0.04 ± 0.01	0.06 ± 0.03
Fitted QCD events	0.00 ± 0.00	0.00 ± 0.00	0.00 ± 0.00
MC exp. $m_{\tilde{b}} = 800$, $m_{\tilde{\chi}_2^0} = 131$	0.143 ± 0.06	1.48 ± 0.23	4.37 ± 0.39
MC exp. $m_{\tilde{b}} = 800$, $m_{\tilde{\chi}_2^0} = 180$	0.08 ± 0.04	2.43 ± 0.30	7.10 ± 0.49

Uncertainty of channel	$\min_\Theta < 0.5$	$0.5 < \min_\Theta < 1.0$	$\min_\Theta > 1.0$
Total background expectation	2.23	2.68	1.64
Total statistical ($\sqrt{N_{exp}}$)	± 1.49	± 1.64	± 1.28
Total background systematic	± 0.89 [39.69%]	± 1.05 [39.26%]	± 0.58 [35.16%]
alpha_amcnlott2	± 0.77 [34.4%]	± 0.85 [31.7%]	± 0.10 [6.2%]
alpha_ttbar_syst_radH	± 0.52 [23.2%]	± 0.60 [22.3%]	± 0.17 [10.6%]
omega_fake_tau	± 0.49 [21.9%]	± 0.51 [18.9%]	± 0.15 [9.2%]
omega_true_tau	± 0.48 [21.5%]	± 0.55 [20.7%]	± 0.13 [7.6%]
alpha_fsrsyst2	± 0.36 [16.2%]	± 0.53 [19.8%]	± 0.06 [3.6%]
gamma_stat_SR_A1_cuts_bin_0	± 0.15 [6.7%]	± 0.00 [0.00%]	± 0.00 [0.00%]

alpha_murmufcomb	±0.15 [6.6%]	±0.16 [6.1%]	±0.03 [1.7%]
alpha_amcnlost2	±0.11 [4.9%]	±0.36 [13.6%]	±0.21 [12.6%]
alpha_herwig7st2	±0.10 [4.6%]	±0.07 [2.7%]	±0.19 [11.8%]
alpha_fsrsyst2_st	±0.04 [1.6%]	±0.07 [2.5%]	±0.14 [8.3%]
alpha_jetdatamc	±0.04 [1.6%]	±0.11 [4.0%]	±0.27 [16.6%]
alpha_singletopds2	±0.03 [1.3%]	±0.36 [13.2%]	±0.21 [12.9%]
alpha_lsyst	±0.03 [1.3%]	±0.08 [3.0%]	±0.10 [6.4%]
alpha_murmufcomb_ttX	±0.02 [1.0%]	±0.14 [5.1%]	±0.00 [0.00%]
alpha_herwig7tt2	±0.00 [0.00%]	±0.16 [6.0%]	±0.09 [5.5%]
omega_scale_Z	±0.00 [0.00%]	±0.00 [0.00%]	±0.11 [6.6%]
alpha_mursyst_ttX	±0.00 [0.00%]	±0.21 [7.7%]	±0.00 [0.00%]
alpha_ztautau_MG	±0.00 [0.00%]	±0.00 [0.00%]	±0.09 [5.6%]
gamma_stat_SR_A2_cuts_bin_0	±0.00 [0.00%]	±0.19 [7.2%]	±0.00 [0.00%]
gamma_stat_SR_A3_cuts_bin_0	±0.00 [0.00%]	±0.00 [0.00%]	±0.17 [10.4%]

Table 10.12: Breakdown of the dominant systematic uncertainties on background estimates in the various signal regions. Note that the individual uncertainties can be correlated, and do not necessarily add up quadratically to the total background uncertainty. The percentages show the size of the uncertainty relative to the total expected background.

10.4 Fit Results and Interpretations

The full systematic set used by the analysis includes more than 80 different entries. Most of them are quite low and do not affect the final result significantly. To discuss the correlation of the systematics easier a "reduced" set is developed by selecting ≈ 20 most significant systematics. All the results are still produced using the full systematics set, the reduced set is only used for demonstration of some properties of the systematic uncertainties.

Background-only fit In the background fit the fit parameters are constrained by the data. No assumptions on the model are made and only control regions are used. After the fit parameters are fixed the extrapolation to validation regions can happen. The signal regions are treated as validation regions in the background-only fit.

The analysis specific implementation includes 7 control regions described in Chapter 8. By construction some of the fit parameters are correlated. The correlation matrix of just the 7 NPs without any systematics applied is shown in Figure 10.5a. $\omega_{\text{fake tau}}$ and $\omega_{\text{true tau}}$ are heavily anti-correlated as the Fake Tau CR has a large true tau contamination so that the increase of one of the parameters causes the decrease of the other. The $\omega_{\text{scale top}}$ and ω_{1mu} are anti-correlated too as $\omega_{\text{scale top}}$ is, in principle, just the ratio of the normalisation factor from OneTau CR and ω_{1mu}. Similarly $\omega_{\text{scale Z}}$ is anti-correlated with ω_{zmumu0b}, but the correlation is much weaker in this case.

The correlation matrix of the background-only fit parameters with all systematics is shown in Figure 10.5b (only correlations larger that 20% are included to improve readability). Interesting to note is that some of the top systematics are correlated to the $\omega_{\text{fake tau}}$ and $\omega_{\text{true tau}}$. Another source of correlation are JES-related systematics such as `alpha_jetnp1`, `alpha_jetnp2` and `alpha_jetflvresp` that effectively vary jets p_{T}.

Control regions definitions are based on leading and sub-leading jet p_{T} and are sensitive to such variations.

The background-only pulls of nuisance parameters are shown in Figure 10.4. Overall the pulls look reasonable, but some are slightly off. These include JER-related `alpha_jeteffnp2` that, as can be seen in Figure 10.5b, is correlated to several fit parameters likely causing the issue. Additionally theory variations of $W(\mu\nu)$ samples are affected, `alpha_mufsyst_wmunu`, `alpha_murmufcomb_wmunu`, `alpha_paramckkw_wmunu` and `alpha_paramqsf_wmunu`. $W(\mu\nu)$ contribution is only somewhat noticeably large in the OneMu CR so there is some correlation with $\omega_{1\mathrm{mu}}$ that results in pulls being slightly off.

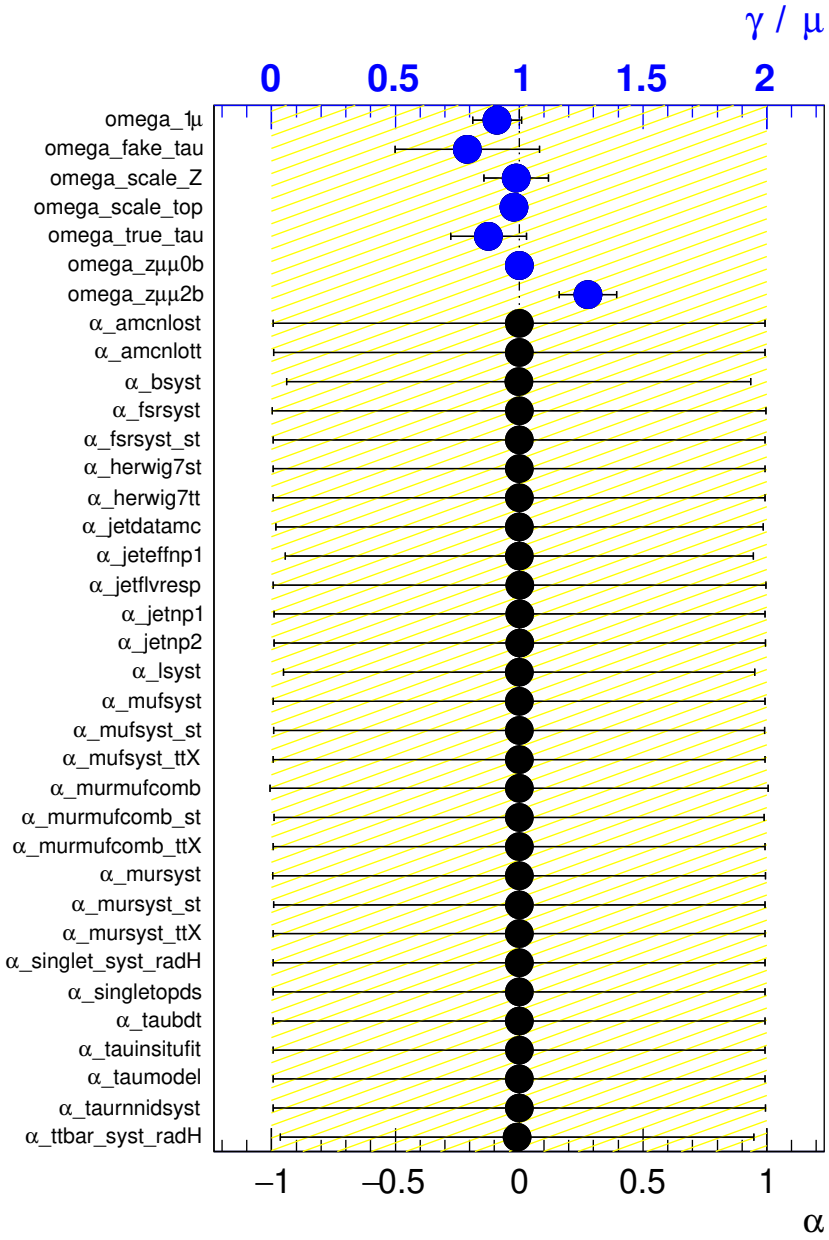

(a) NP pulls, background-only fit, reduced systematics set.

Figure 10.4

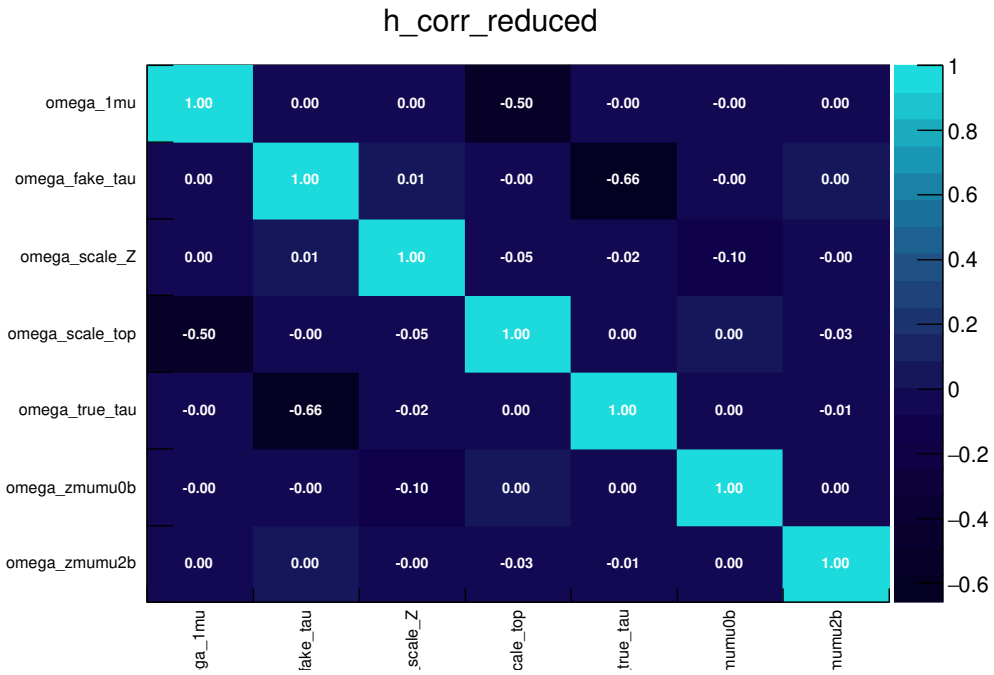

(a) Correlation matrix of the background-only fit. Only fit parameters included

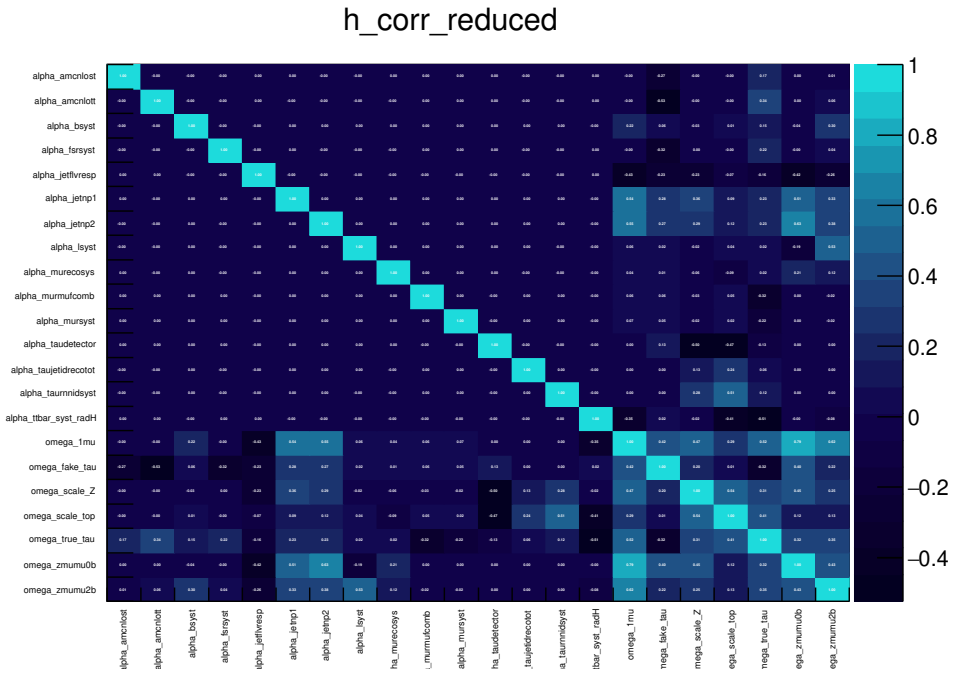

(b) Correlation matrix of the background-only fit. Only correlations larger than 20% included.

Figure 10.5

Exclusion fit The exclusion fit is a model-specific fit that takes the (potential) signal contribution into account. Signal regions contribute to the fit in this setup together with the control regions. The validations regions are not included in the exclusion fit.

The analysis specific implementation of the exclusion fit is using the same 7 control regions used in the background-only fit and, additionally, three multi-bin signal regions that are binned in $\min_{\Theta}$, as defined in Table 10.11. The same correlation considerations as for the background-only fit applies. Correlation matrix for the reduced

systematics set is presented in Figure 10.7a. The exclusion fit pulls of nuisance parameters is shown in Figure 10.7b. The exclusion fit effectively overconstrains the NPs, this results in correlation between `alpha_ttbar_syst_radH` and `alpha_amcnlott2`, two $t\bar{t}$ theory systematics.

The exclusion fit is run for each signal point and combined to form an exclusion contour. The three $\min_{\Theta}$ bins are used to create the main exclusion contour plot, see Figure 10.8. The discovery SR can, in principle also be used to set exclusion limits, but the results are slightly weaker than the multibin fit and the two cannot be combined. For comparison the exclusion plot using discovery SR is shown in Figure 10.9. The multi-bin setup wins $\approx$ 75-100 GeV in $(\tilde{b}_1)$ compared to the single-bin SR.

For the two benchmark signal points a simple scan in signal strength is performed, see Figure 10.6. The results look reasonable suggesting that the overall setup is stable.

A combination with the results obtained in the previous analysis targeting the same model [3] is performed. The combination and the contributions from various analyses are summarised in Figure 10.10.

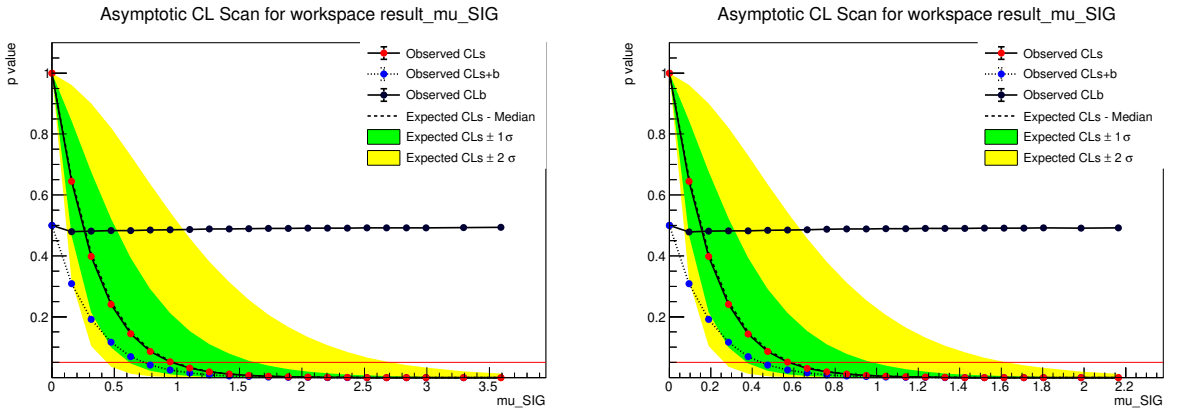

(a) $m_{\tilde{b}} = 800$, $m_{\tilde{\chi}_2^0} = 131$ benchmark point μ scan

(b) $m_{\tilde{b}} = 800$, $m_{\tilde{\chi}_2^0} = 180$ benchmark point μ scan

Figure 10.6: Signal strength μ scan of two benchmark signal points

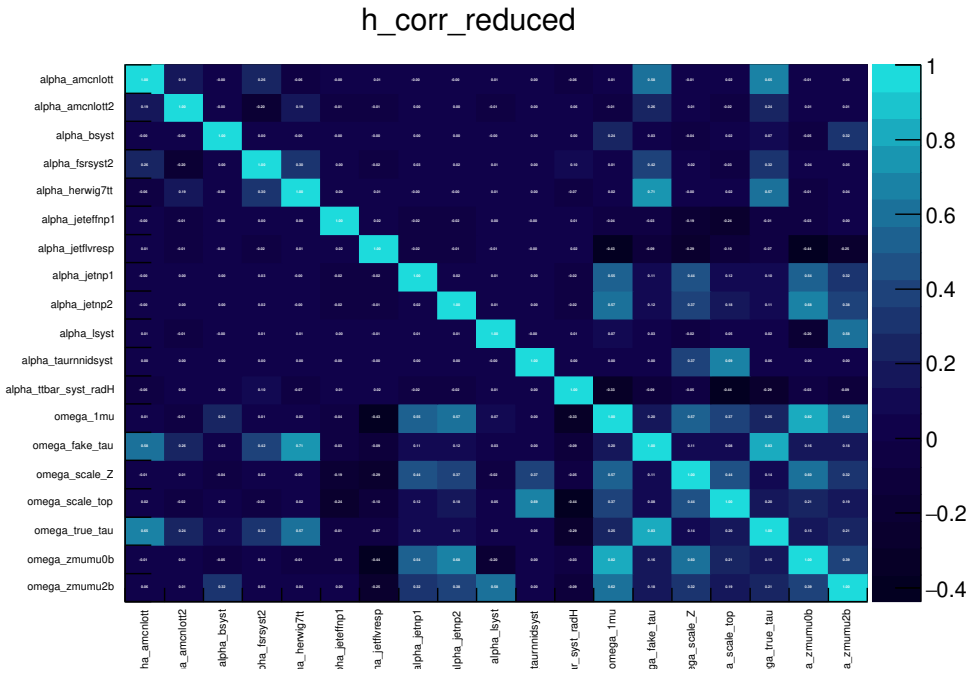

(a) Correlation matrix, exclusion fit (SR used in the fit, SR blinded). Reduced systematics set. Only correlations larger than 20% included.

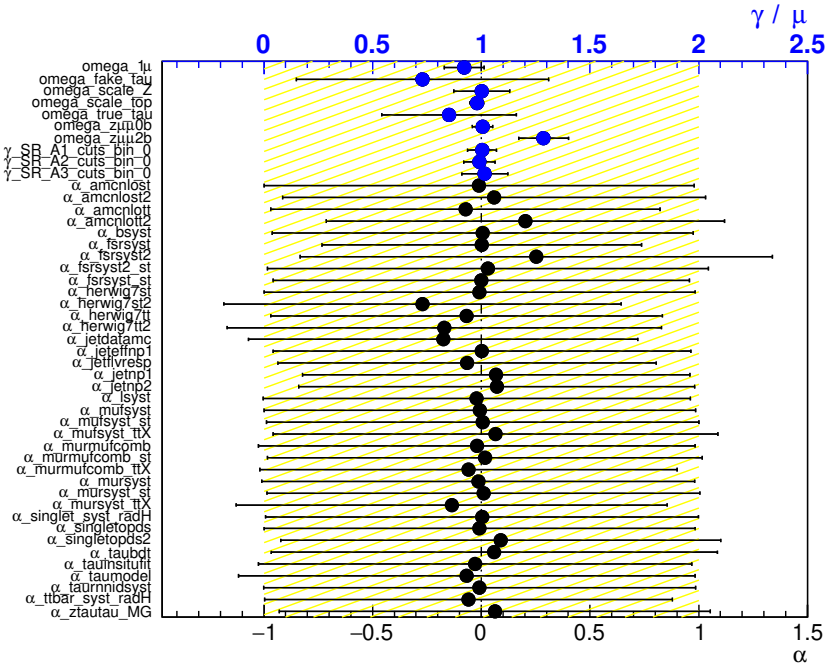

(b) NP pulls, exclusion fit, reduced systematics set.

Figure 10.7

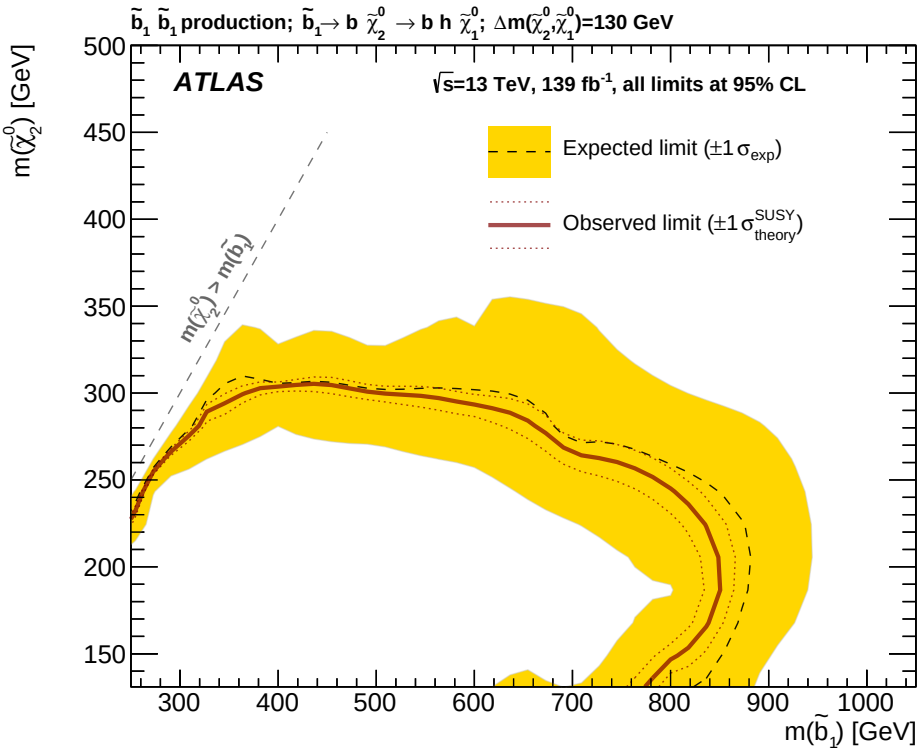

Figure 10.8: Exclusion contours at 95% CL as function for $\Delta m(\tilde{\chi}_2^0, \tilde{\chi}_1^0) = 130$ GeV models as function of $m(\tilde{b})$ and $m_{\tilde{\chi}_2^0}$. Results for the multi-bin exclusion fit based on the shape of $\min_\Theta$ variable are shown. All available systematic uncertainties included.

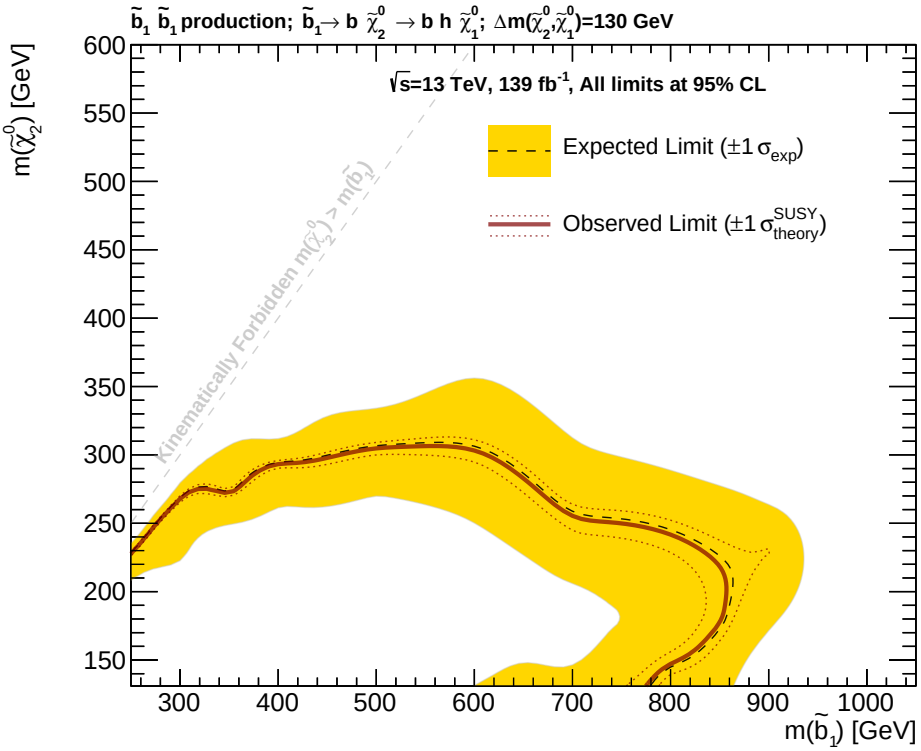

Figure 10.9: Exclusion contours at 95% CL as function for $\Delta m(\tilde{\chi}_2^0, \tilde{\chi}_1^0) = 130$ GeV models as function of $m(\tilde{b})$ and $m_{\tilde{\chi}_2^0}$. Results for the single-bin exclusion fit based on the Discovery SR are shown. All available systematic uncertainties included.

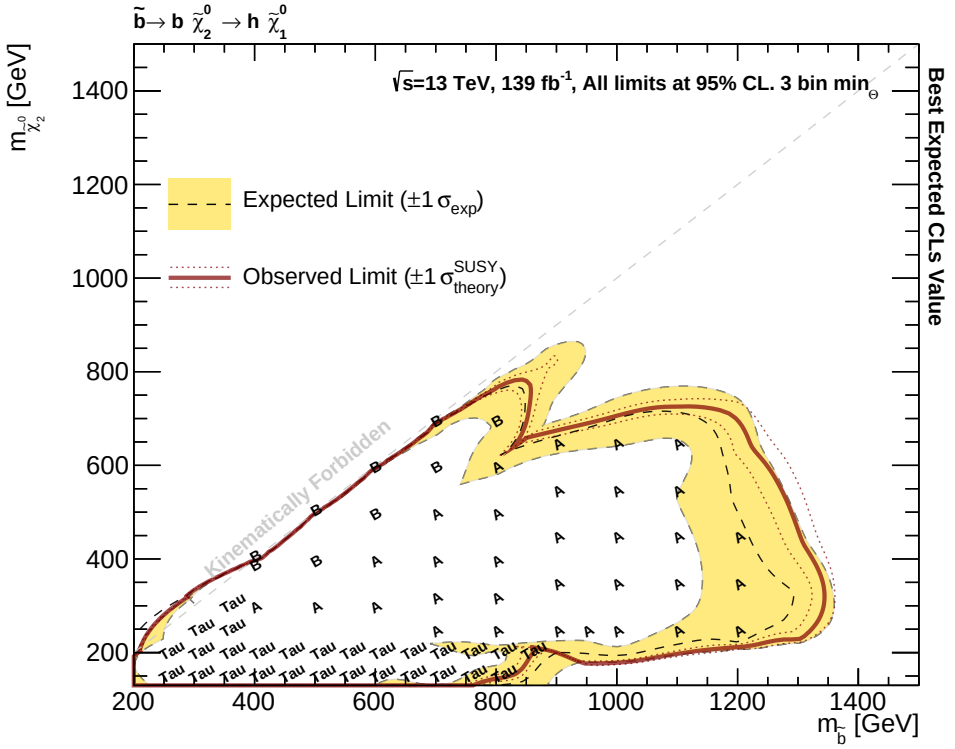

(a) Combined exclusion of sbottom multi-b (SRA and SRB signal regions denoted as "A" and "B") and the presented analysis (denoted "Tau") using the best-CL approach.

Figure 10.10: Exclusion contours at 95% CL as function for $\Delta m(\tilde{\chi}_2^0, \tilde{\chi}_1^0) = 130$ GeV models as function of $m(\tilde{b})$ and $m_{\tilde{\chi}_2^0}$. Results of a combination with the sbottom multi-b analysis [3] using best-CL approach are shown. All available systematic uncertainties included. Labels "A" and "B" indicate the grid points for which "SRA" and "SRB" of the sbottom multi-b analysis have the best sensitivity. The points for which the presented analysis is more sensitive are marked at "Tau".

Discovery fit The model-independent (or discovery) fit is used to set a limit on the number of events in the SR above the background prediction. For this type of fit all control regions and one single-bin signal region are used. No specific signal models are considered. The analysis specific fit is performed using one single-bin SR described in Tables 7.2 and 7.4. The results are summarised in Table 10.13. The following variables are shown:

- $\langle \varepsilon\sigma \rangle^{95}_{obs}$ - 95% CL upper limits on the visible cross section
- S^{95}_{obs} - 95% CL upper limits on the number of signal events
- S^{95}_{exp} - 95% CL upper limits on the number of signal events gives expected number of background events
- CL_B - confidence level for background-only
- $p(s=0)$ (Z) - discovery p-value

Some additional information and checks concerning the stability of the fit and large Up uncertainty variation of S^{95}_{exp} are gathered in Appendix G.

Signal channel	$\langle \varepsilon\sigma \rangle^{95}_{obs}$[fb]	S^{95}_{obs}	S^{95}_{exp}	CL_B	$p(s=0)$ (Z)
Single-bin SR	0.05	6.6	$6.0^{+2.3}_{-1.6}$	0.62	0.34 (0.41)

Table 10.13: Left to right: 95% CL upper limits on the visible cross section ($\langle \varepsilon\sigma \rangle^{95}_{obs}$) and on the number of signal events (S^{95}_{obs}). The third column (S^{95}_{exp}) shows the 95% CL upper limit on the number of signal events, given the expected number (and $\pm 1\sigma$ excursions on the expectation) of background events. The last two columns indicate the CL_B value, i.e. the confidence level observed for the background-only hypothesis, and the discovery p-value ($p(s=0)$).

Chapter 11

Conclusion

A search for pair-production of bottom-squarks at the LHC has been carried out using proton-proton collision data gathered by the ATLAS detecter during 2015-2018 corresponding to the total integrated luminosity of 139 fb^{-1}. The search is interpreted within the simplified model framework focusing on the $\tilde{b}_1 \rightarrow b\tilde{\chi}_2^0 \rightarrow bh\tilde{\chi}_1^0$ decay chain with the $\Delta m(\tilde{\chi}_2^0, \tilde{\chi}_1^0)$ fixed to 130 GeV to ensure that the Higgs boson is produced on-shell. Monte-Carlo is used to model data for all backgrounds other than multijet which is constrained using jet smearing method. No excess is observed the signal regions. Bottom-squarks with masses up to 900 GeV are excluded at 95% confidence level for almost massless $\tilde{\chi}_1^0$. Combination with the sbottom multi-b searches [3] exclusion limits is performed, see Figure 11.1. Model-independent upper limits are set on the cross section of processes beyond the Standard Model.

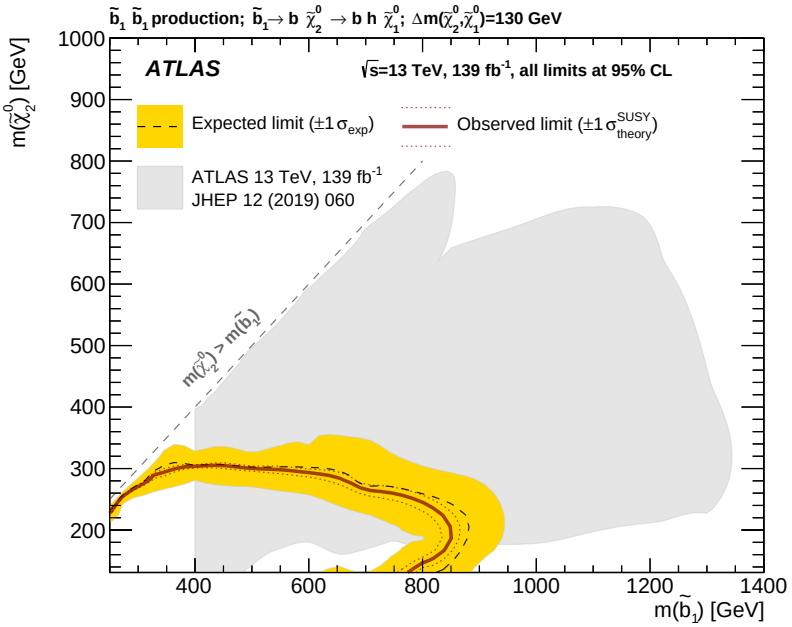

(a)

Figure 11.1: Exclusion contours at 95% CL as function for $\Delta m(\tilde{\chi}_2^0, \tilde{\chi}_1^0) = 130$ GeV models as function of $m(\tilde{b})$ and $m_{\tilde{\chi}_2^0}$. Results for the multi-bin exclusion fit based on the shape of $\min_\Theta$ variable (presented analysis) are overlaid onto results of a previous ATLAS search utilising final states with multiple b-jets and $E_{\mathrm{T}}^{\mathrm{miss}}$ [3]. All available systematic uncertainties included.

Glossary

bosons Particles with integer spin. Bosons obey Bose-Einstein statistics. 3

chiral A chiral theory is a theory that distinguishes between particles transforming under left- and right-handed representation of the Poincare group. For massless particles chirality coincides with helicity, the sign of the projection of spin onto momentum of a particle. 7

fermions Particles with half-integer spin. Fermions obey Fermi-Dirac statistics. 3

fit A fit is a procedure in which a model describing the observed data is chosen. Typically that involves finding a combination of free-floating numerical parameters that describe the data "the best" according to some criteria. 41

jets Cone of particles produced due to the hadronisation process. 2

Lagrangian Lagrangian is a function of generalised coordinates describing dynamics and kinematics of a theory. Action $S = \int Ldt$ is the time integral of the Lagrangian. Lagrangian density $\mathcal{L}$ is defined through $L = \int \mathcal{L} d^3x$. In particle physics it is common to refer to the Lagrangian density $\mathcal{L}$ as just "Lagrangian". 5

leptons Half-integer elementary particles that do not participate in strong interaction. 4

parton A useful approximation for treating composite particles such as protons is to consider them as a collection of point-like objects called partons. 36

PDF There are two related but distinct concepts referred to by the acronym PDF. Probability Density Function describes the relative probability of a continuous random variable taking the given value. The integral of the probability density function over an interval gives the probability that the value of the random variable will be within that interval. The probability density functions are always non-negative and the integral over the whole sample space is normalised to 1. Parton Distribution Functions on the other hand are describing the probability of finding partons of given flavour as a function of the fraction of total momentum x that the parton is carrying and the energy scale of the interaction Q. Parton Distribution Functions are usually obtained from experiments. 36

squarks Partner of an ordinary quark predicted by supersymmetric models. 1

Appendix A

Stransverse Mass Studies

The stransverse mass m_{T2} is used in the analysis as one of the main discriminating variables. It's main purpose is to separate $t\bar{t}$ events in which tau leptons are coming from the decays of two W bosons and signal events with $h \to \tau\tau$. Stransverse mass calculation assumes presence of two particles decaying semi-invisibly into observed particles. In case of $t\bar{t}$ those observed particles are the two tau leptons. Note that calculating stransverse mass for signal (or $Z \to \tau\tau$) events cannot be interpreted in the same way since both observed particles come from the same resonance. So instead the difference in stransverse mass distributions for signal and $t\bar{t}$ events is studied.

The first attempt has been made with the assumption of the masses of the invisible particles being set to 0. The selection is unoptimised SR (2 taus, 2 b-jets, trigger plateau, $H_{\mathrm{T}} >$ 1000 GeV). Two signal points were used, $m_{\tilde{b}} = 350$, $m_{\tilde{\chi}_2^0} = 131$ and $m_{\tilde{b}} = 850$, $m_{\tilde{\chi}_2^0} = 131$, representing the high and low sbottom masses. Due to the large peak at $m_{\mathrm{T2}} = 0$ for both $t\bar{t}$ and signal events this approach is not productive, see Figure A.1.

Increasing the masses of invisible particles leads to distinguishable shapes, see Figures A.2 - A.5. The difference becomes noticeable at $m_{inv} \approx 100$ GeV. The final setup is using $m_{inv} = 120$ GeV and the cut is applied at $m_{\mathrm{T2}} = 140$GeV. Pushing the m_{inv} to higher values doesn't seem to improve the rejection for high sbottom mass points.

An attempt to use b-jet + τ pairs instead of $\tau\tau$ pairs for stransverse mass calculations has been made. One complication is that there are different b-jet + τ pairs as opposed to just 1 $\tau\tau$ pair. In signal b-jets come both from h and sbottom decay, making interpretation harder. As the result the decision to use $\tau\tau$ for stransverse mass calculation as the simplest option was made.

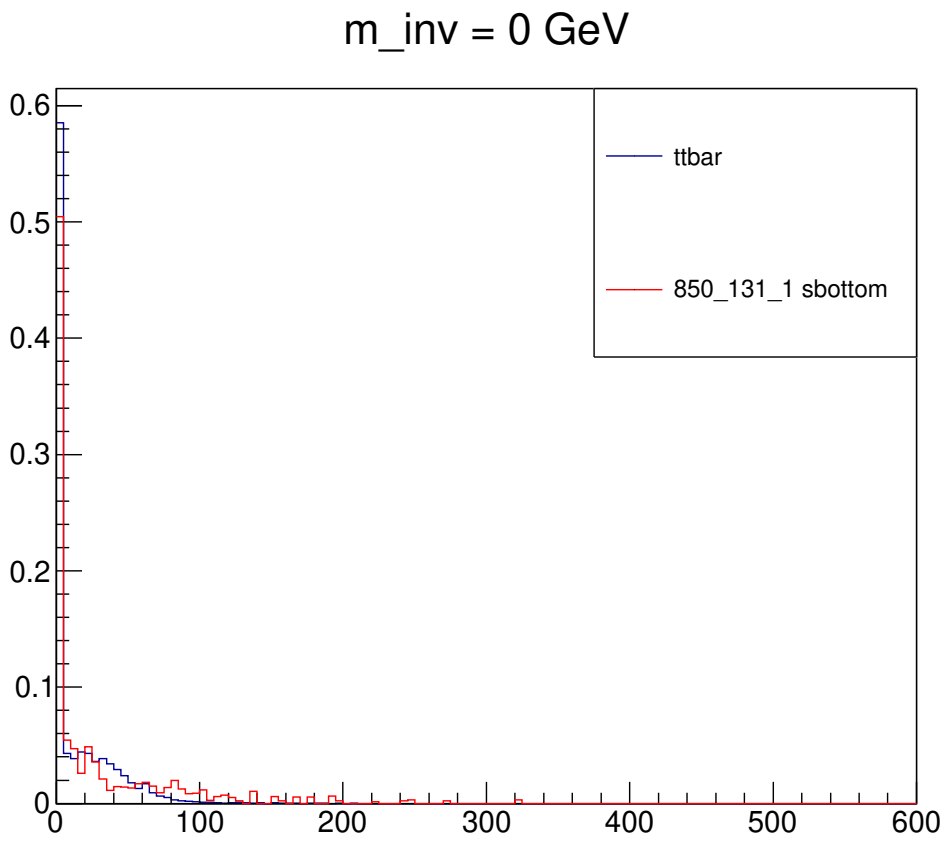

(a) m_{T2} distributions for $t\bar{t}$ and signal events, both scaled to 1.

Figure A.1

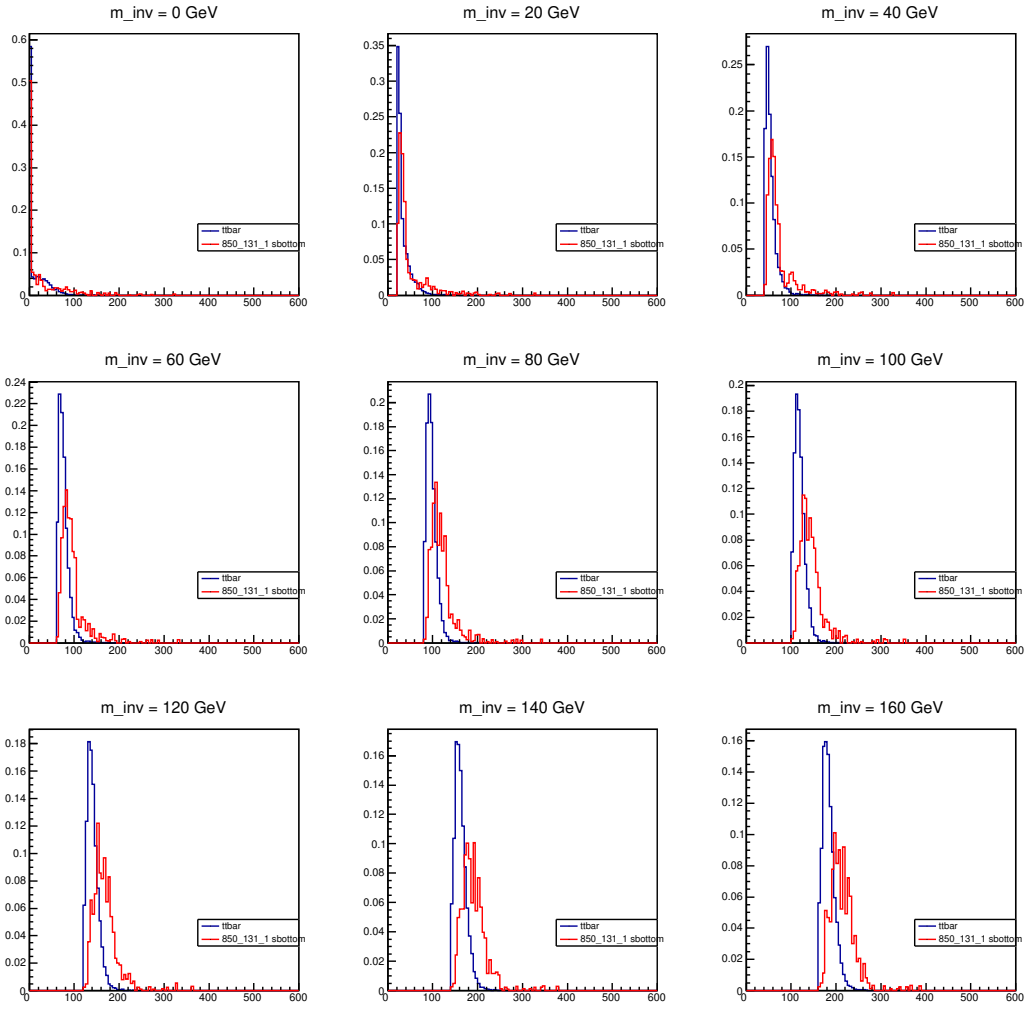

(a) m_{T2} distributions for $t\bar{t}$ and signal events, both scaled to 1.

Figure A.2

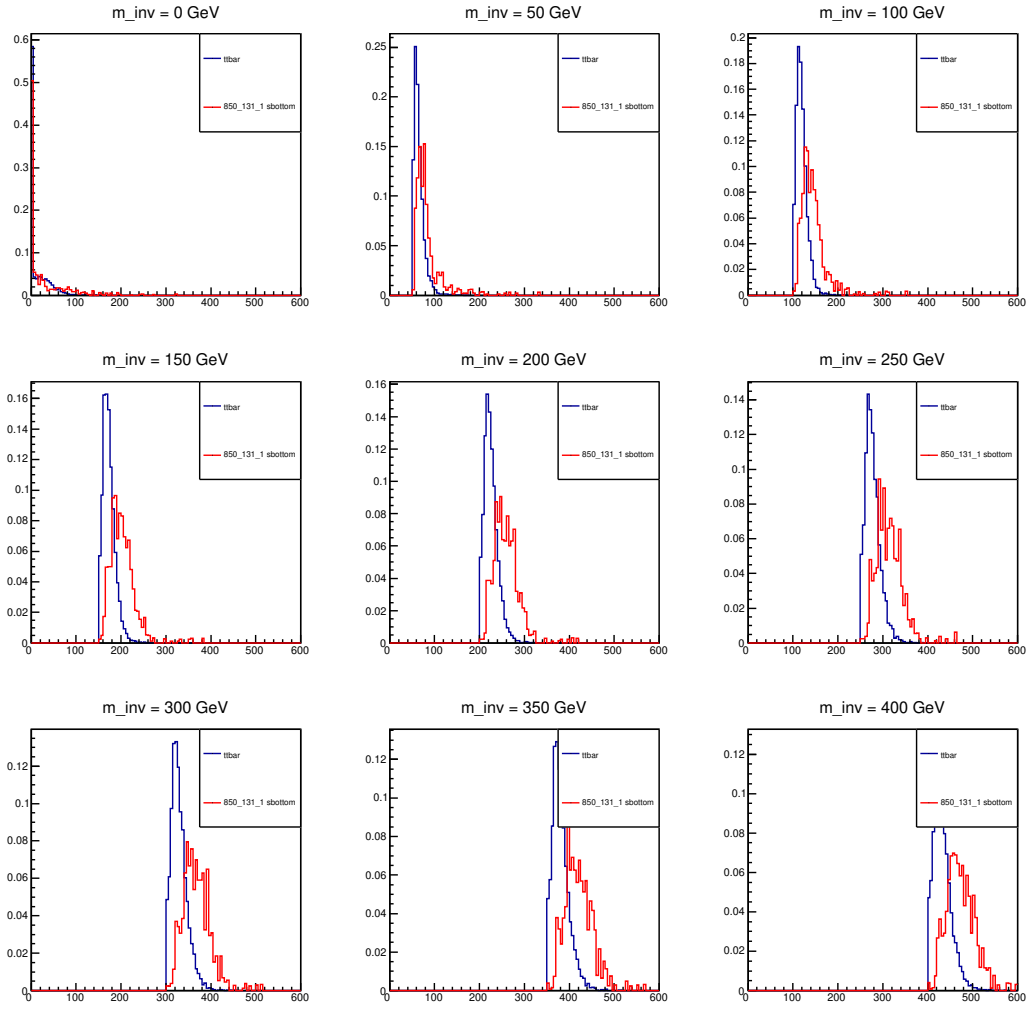

(a) m_{T2} distributions for $t\bar{t}$ and signal events, both scaled to 1.

Figure A.3

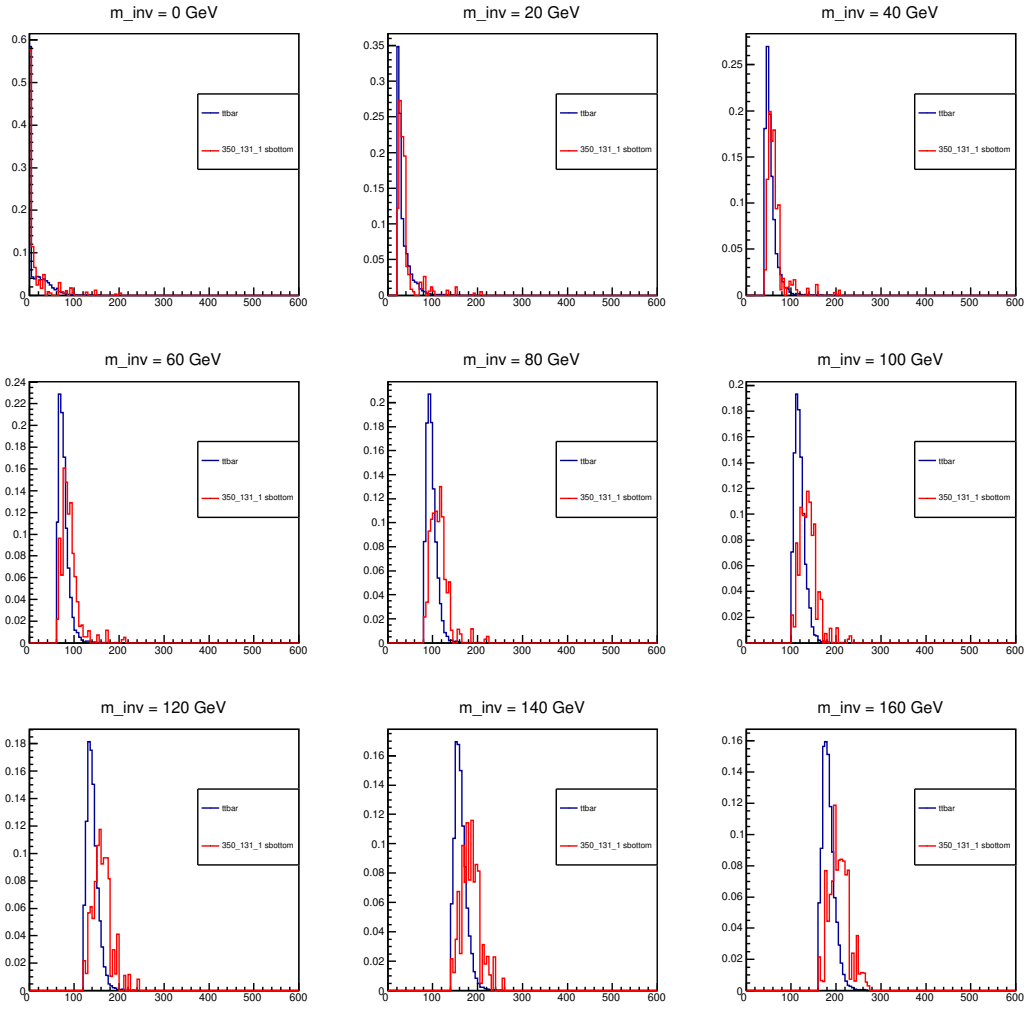

(a) m_{T2} distributions for $t\bar{t}$ and signal events, both scaled to 1.

Figure A.4

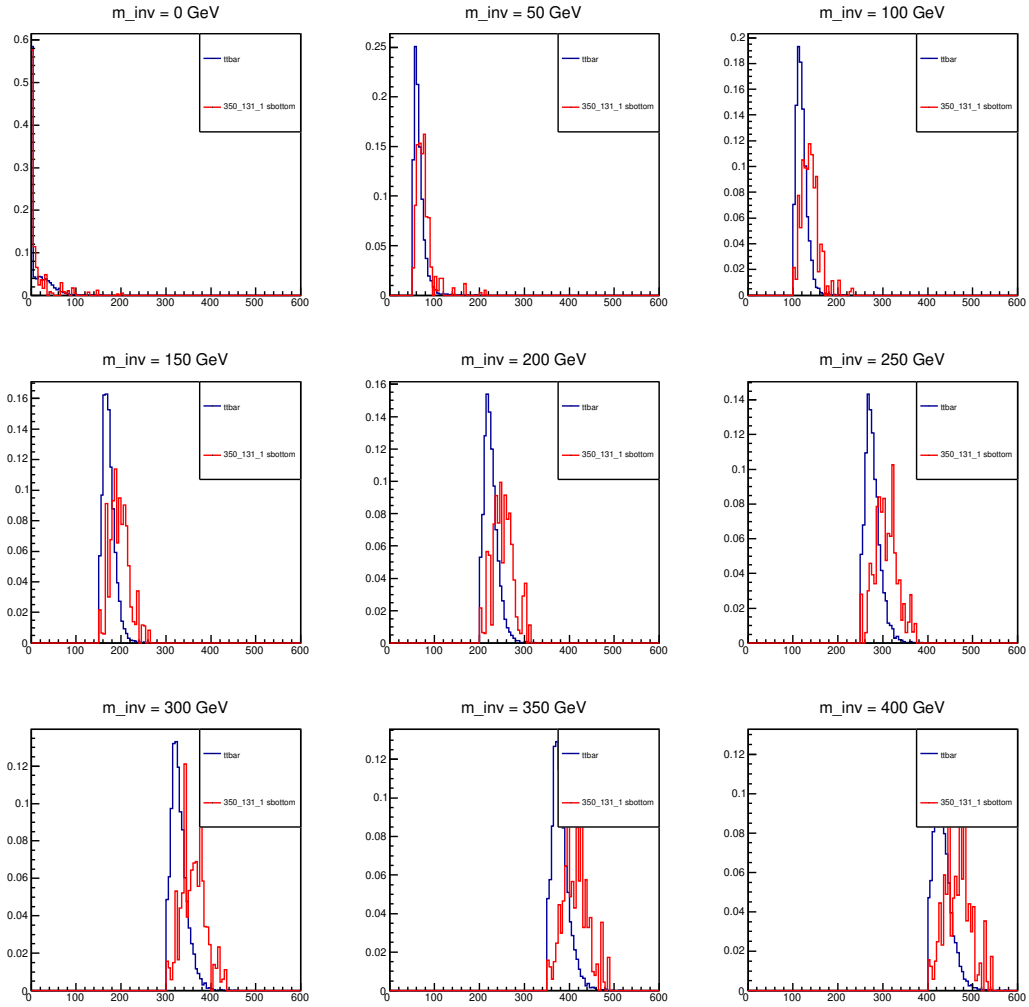

(a) m_{T2} distributions for $t\bar{t}$ and signal events, both scaled to 1.

Figure A.5

Appendix B

Fake Tau CR Selection

The $t\bar{t}$ CRs are constructed using one muon, one tau and 2 b-jets. The TrueTau CR is defined by requiring opposite signed charges of the muon and the tau and applying a cut on the tau transverse mass to increase the purity. To control the fake taus there are two possibilities - using opposite sign muon+tau that are not used for the TrueTau CR or requiring that the muon and the tau have the same sign. Both approaches have been tried and yielded different results, see Table B.1. The same sign approach seems to underestimate the fake taus while the opposite sign tends to overestimate them. There is no indication on which approach is preferable so the same exercise was repeated while requiring exactly 1 b-jet in the regions. The results are in Table B.2.

Table B.1

	Same Sign 2 b-jets	Opposite Sign 2 b-jets
True Tau SF	0.83 ± 0.05	0.89 ± 0.06
Fake Tau SF	1.26 ± 0.13	0.78 ± 0.15

Table B.2

	Same Sign 1 b-jet	Opposite Sign 1 b-jet
True Tau SF	0.98 ± 0.07	1.04 ± 0.08
Fake Tau SF	0.89 ± 0.12	0.53 ± 0.18

The general trend seems to be that 3 out of 4 approaches keep the TrueTau SF close to 1 with FakeTau CR overestimating taus (i.e. FakeTau SF < 1). The 2 b-jets same sign approach tends to underestimate fake taus and pushes the TrueTau SF away from 1. Keeping in mind that the SR will have opposite sign taus the opposite sign approach seems to be more "natural".

A further study into the origin of the fake taus in MC is performed. Using the "PartonTruthLabelID" information the origin of the fake taus is studied, see also Figure B.1. The origin of fake taus in the SR seems to be consistent with the opposite sign FakeTauCR selection while the same sign selection is more heavily dominated by the gluon-produced jets. Since the FakeTauCR is supposed, in the end, to control the SR, the choice to use the opposite-sign design is made.

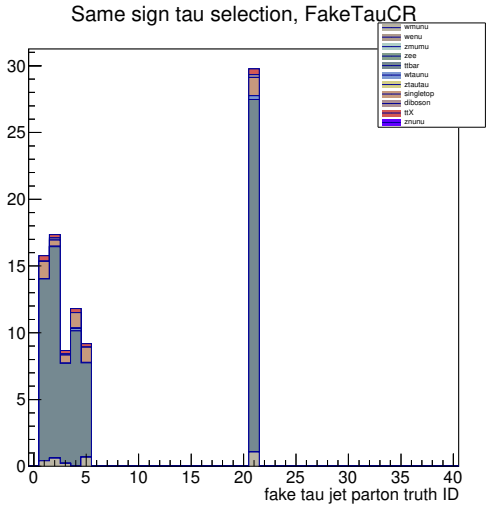

(a) PDG ID of the origin of the jet faking a tau in same sign tau selection, FakeTauCR

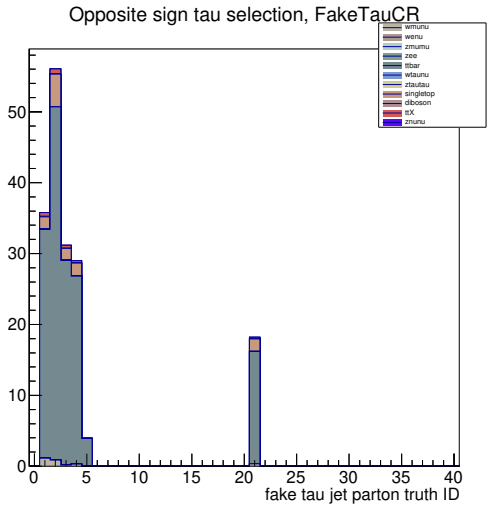

(b) PDG ID of the origin of the jet faking a tau in opposite sign tau selection, FakeTauCR

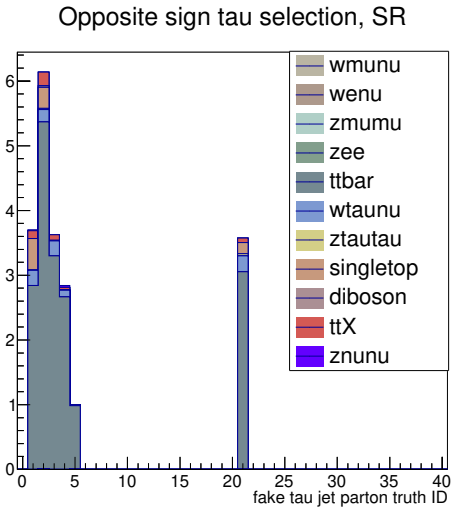

(c) PDG ID of the origin of the jet faking a tau in opposite sign tau selection, SR

Figure B.1: Jet parton truth ID values of 1-5 correspond to the jets originating from quarks (1 for up, 5 for bottom) and 21 corresponding to jets originating from gluons.

Appendix C

Additional Z Validation Regions

In this appendix two additional VRs are defined - Zmumu0b VR and Ztautau0b VR. This is done by the H_{T} extrapolation of the Zmumu0b CR and Ztautau0b CR to the $[1000, 1500]$ GeV range. The two control regions are auxiliary and, in principle, the validation regions do not have much to add. However it is nice to make sure that nothing catastrophic happens when extrapolating over H_{T}.

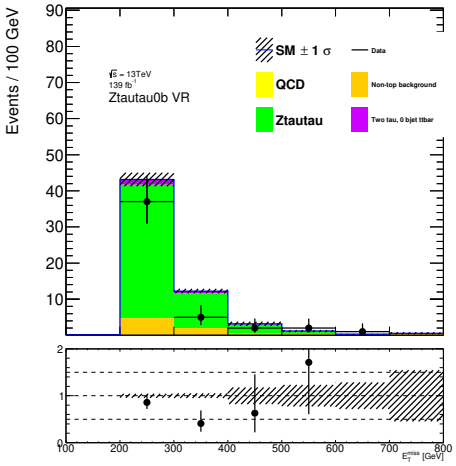

(a) Ztautau0b VR $E_{\mathrm{T}}^{\mathrm{miss}}$ before the fit

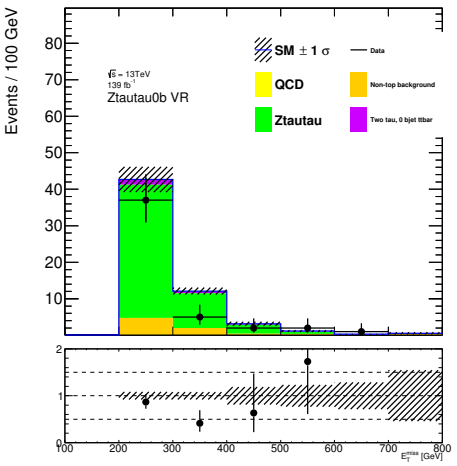

(b) Ztautau0b VR $E_{\mathrm{T}}^{\mathrm{miss}}$ after the fit

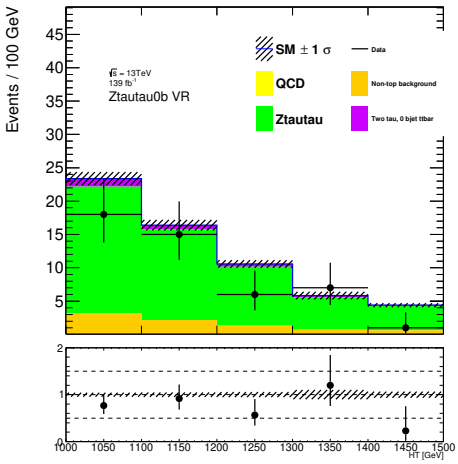

(c) Ztautau0b VR H_{T} before the fit

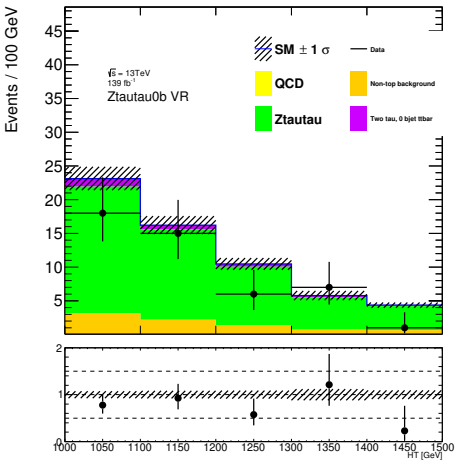

(d) Ztautau0b VR H_{T} after the fit

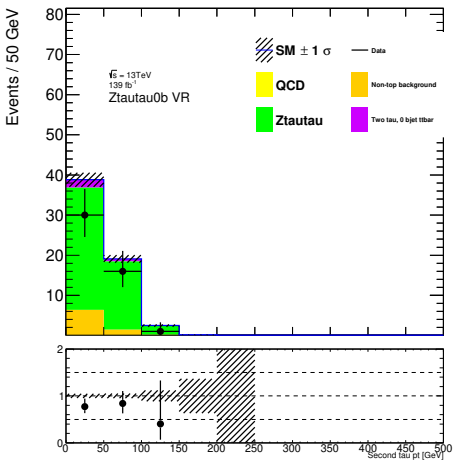

(e) Ztautau0b VR second tau p_{T} before the fit

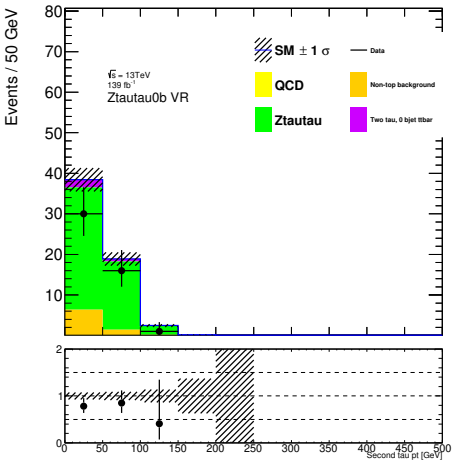

(f) Ztautau0b VR second tau p_{T} after the fit

Figure C.1: Distributions of various variables in the Ztautau0b VR before and after the fit. All uncertainties are included and shown as the hatched band. The upper panels show distributions of the expected SM backgrounds with data overlaid. The lower panels show data/MC ratios. In the plots marked "after the fit" the SM backgrounds are scaled with the weights obtained in the background-only fit.

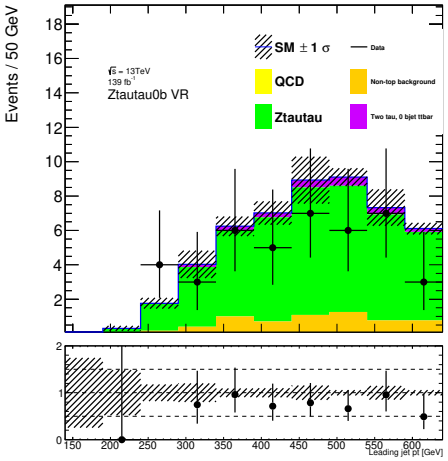

(a) Ztautau0b VR leading jet p_{T} before the fit

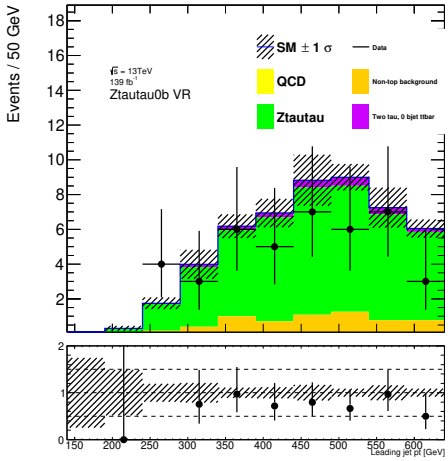

(b) Ztautau0b VR leading jet p_{T} after the fit

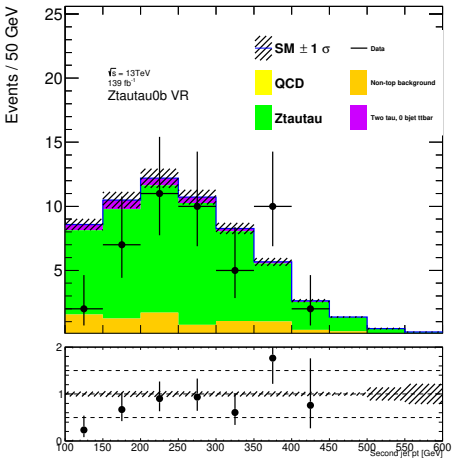

(c) Ztautau0b VR second jet p_{T} before the fit

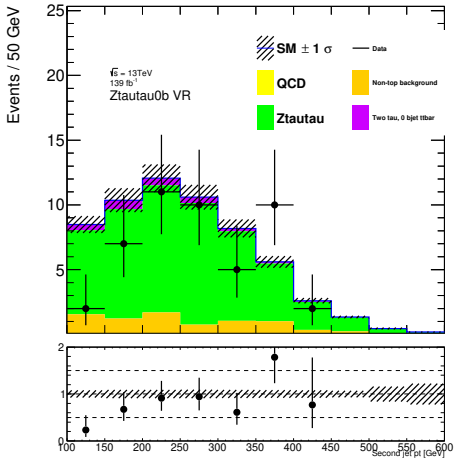

(d) Ztautau0b VR second jet p_{T} after the fit

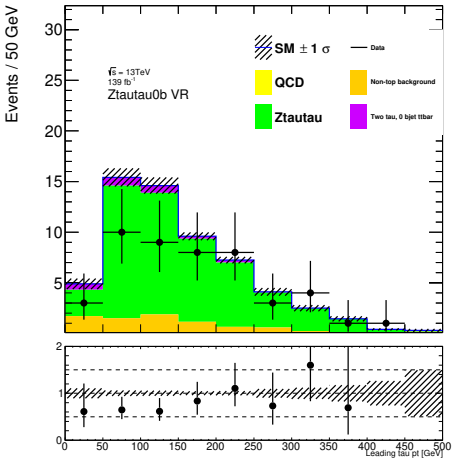

(e) Ztautau0b VR leading tau p_{T} before the fit

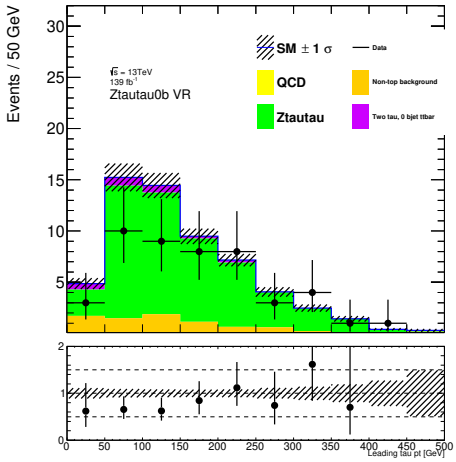

(f) Ztautau0b VR leading tau p_{T} after the fit

Figure C.2: Distributions of various variables in the Ztautau0b VR before and after the fit. All uncertainties are included and shown as the hatched band. The upper panels show distributions of the expected SM backgrounds with data overlaid. The lower panels show data/MC ratios. In the plots marked "after the fit" the SM backgrounds are scaled with the weights obtained in the background-only fit.

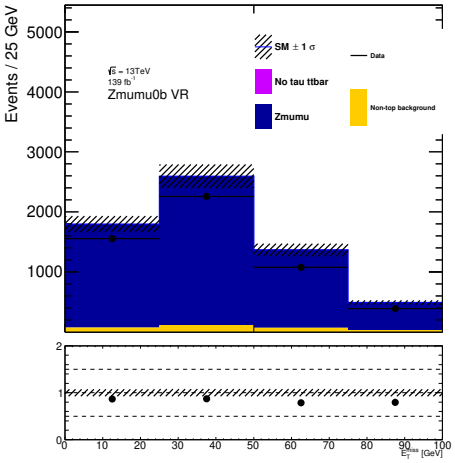

(a) Zmumu0b VR $E_{\mathrm{T}}^{\mathrm{miss}}$ before the fit

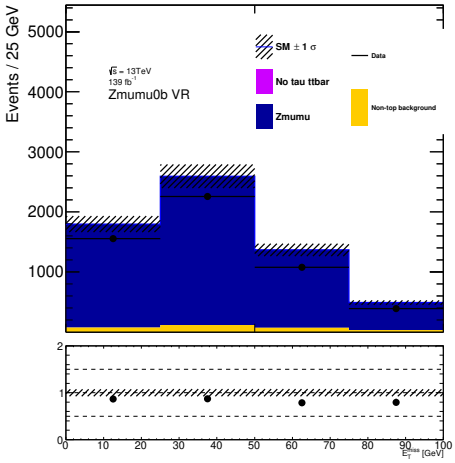

(b) Zmumu0b VR $E_{\mathrm{T}}^{\mathrm{miss}}$ after the fit

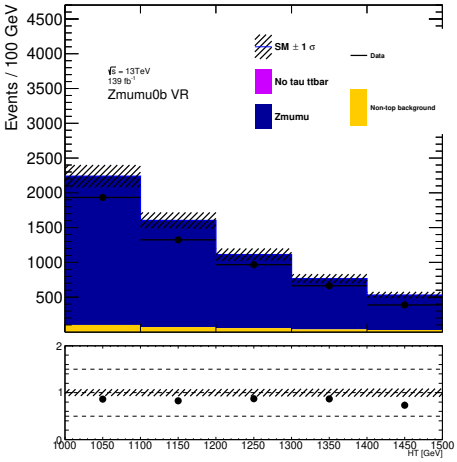

(c) Zmumu0b VR H_{T} before the fit

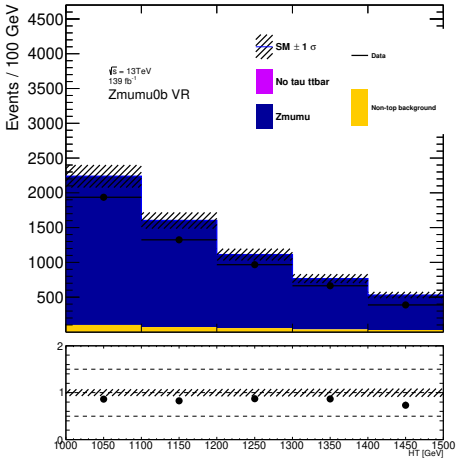

(d) Zmumu0b VR H_{T} after the fit

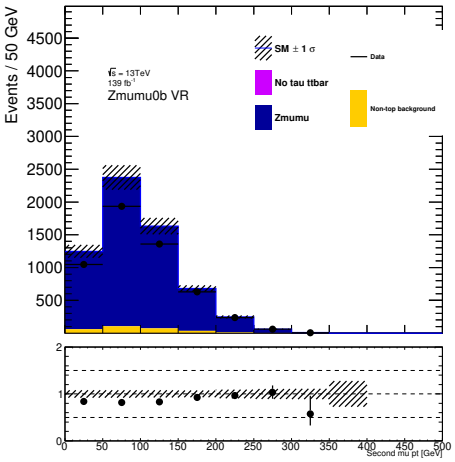

(e) Zmumu0b VR second mu p_{T} before the fit

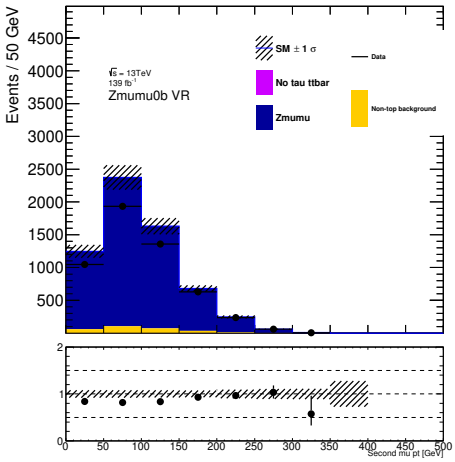

(f) Zmumu0b VR second mu p_{T} after the fit

Figure C.3: Distributions of various variables in the Zmumu0b VR before and after the fit. All uncertainties are included and shown as the hatched band. The upper panels show distributions of the expected SM backgrounds with data overlaid. The lower panels show data/MC ratios. In the plots marked "after the fit" the SM backgrounds are scaled with the weights obtained in the background-only fit.

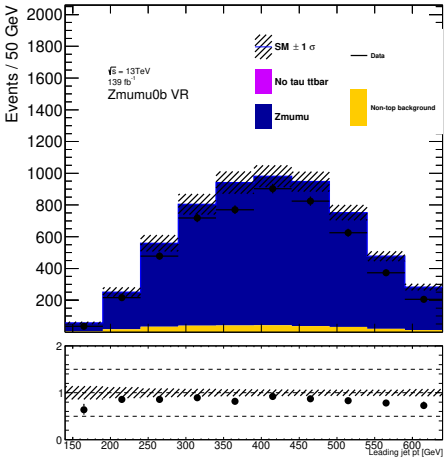

(a) Zmumu0b VR leading jet p_{T} before the fit

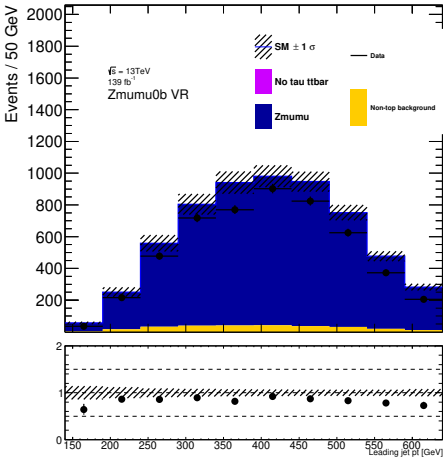

(b) Zmumu0b VR leading jet p_{T} after the fit

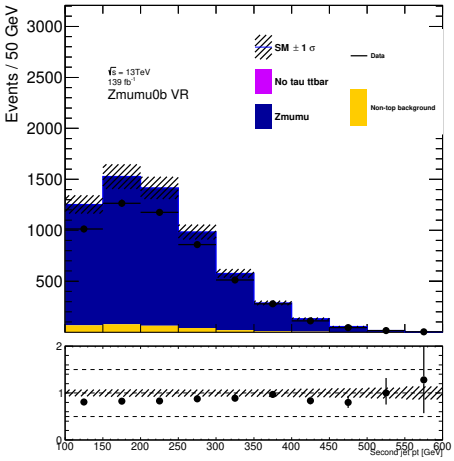

(c) Zmumu0b VR second jet p_{T} before the fit

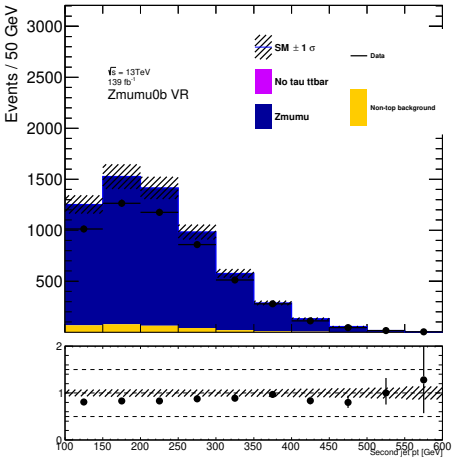

(d) Zmumu0b VR second jet p_{T} after the fit

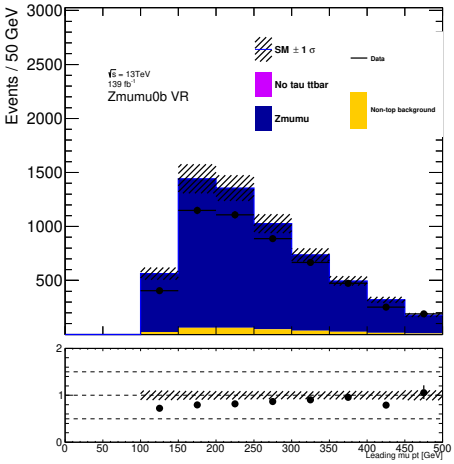

(e) Zmumu0b VR leading mu p_{T} before the fit

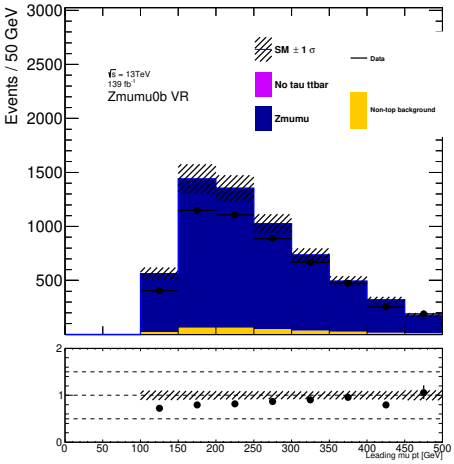

(f) Zmumu0b VR leading mu p_{T} after the fit

Figure C.4: Distributions of various variables in the Zmumu0b VR before and after the fit. All uncertainties are included and shown as the hatched band. The upper panels show distributions of the expected SM backgrounds with data overlaid. The lower panels show data/MC ratios. In the plots marked "after the fit" the SM backgrounds are scaled with the weights obtained in the background-only fit.

Appendix D

Signal Contamination

In this appendix signal leakage in various control and validation regions is evaluated.

Due to the fact that signal samples were partially produced with 2 hadronic tau filter on the generator level it is not always possible to directly estimate the signal contamination. So it is estimated from reconstructed signal samples when possible and from truth studies where it isn't. For regions with 2 taus no extrapolation from MC truth is provided (since it is not needed). Regions without taus (Zmumu0b/Zmumu2b/Ztautau0b) are expected to have a fraction of signal contamination compared to regions with taus. Due to contamination in tau regions being already low the muon regions plots are not included.

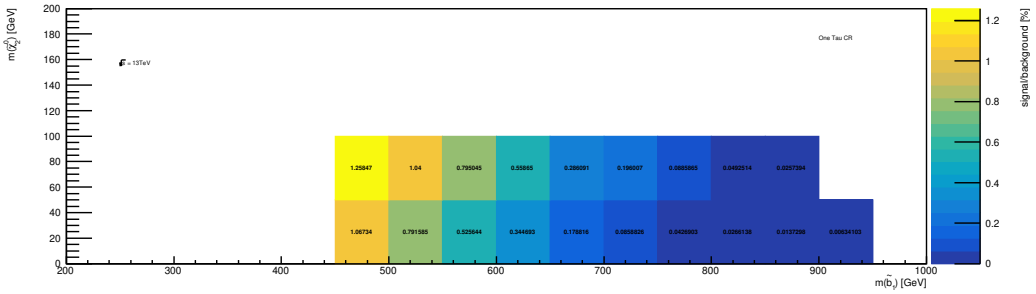

(a) One Tau CR signal contamination

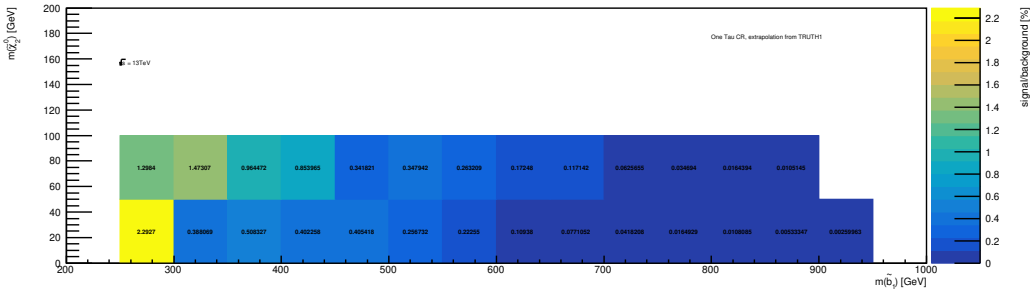

(b) One Tau CR signal contamination extrapolated

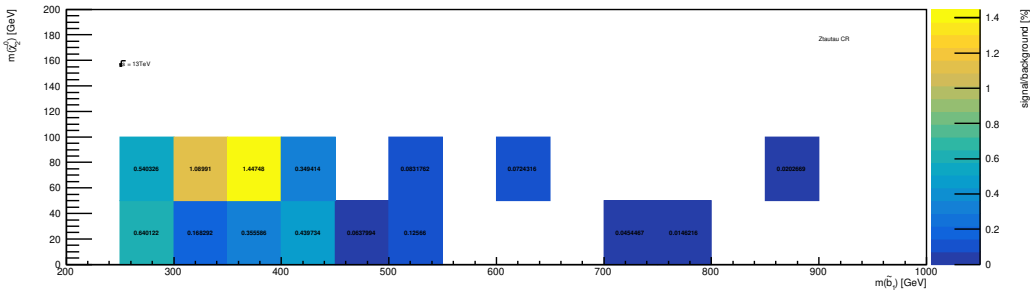

(c) Ztautau CR signal contamination

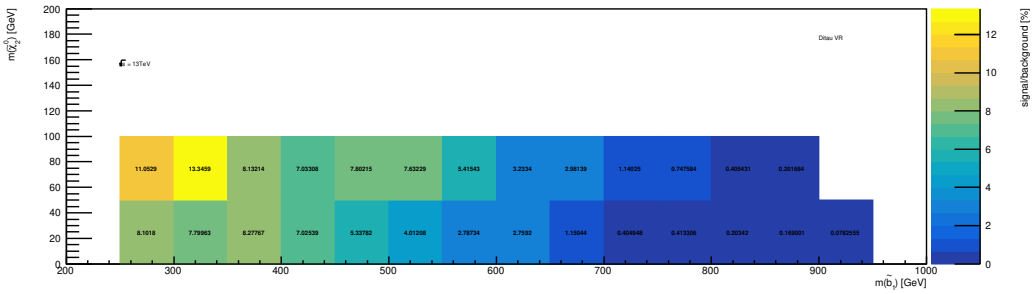

(d) Ditau VR signal contamination

Figure D.1: Signal contamination of various control regions, measured where possible and extrapolated otherwise, combined datasets.

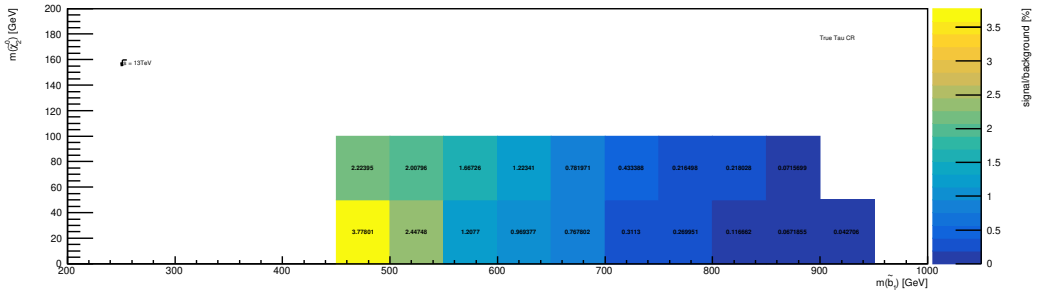

(a) True Tau CR signal contamination

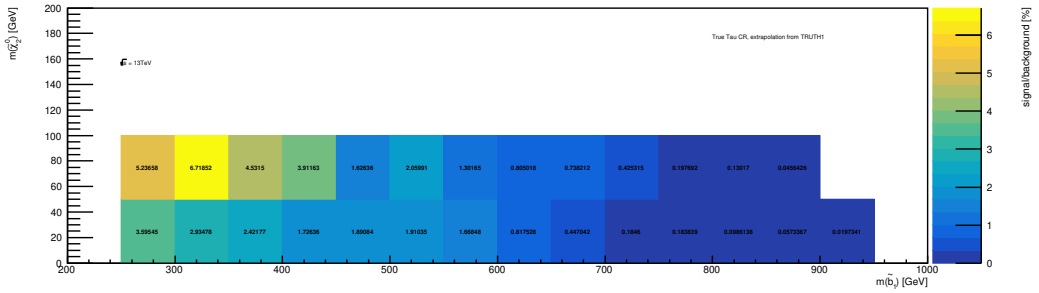

(b) True Tau CR signal contamination extrapolated

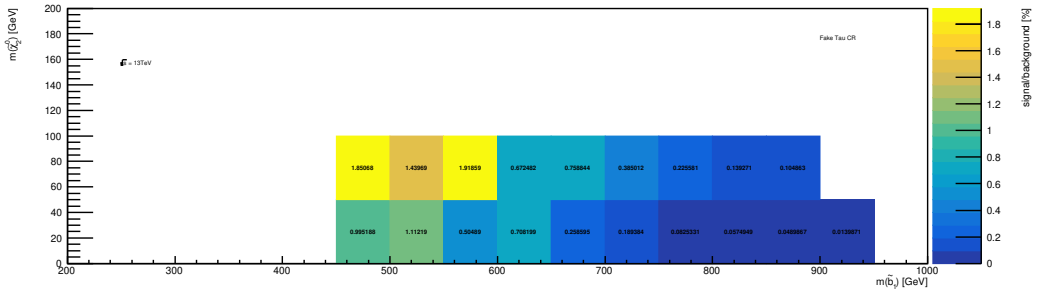

(c) Fake Tau CR signal contamination

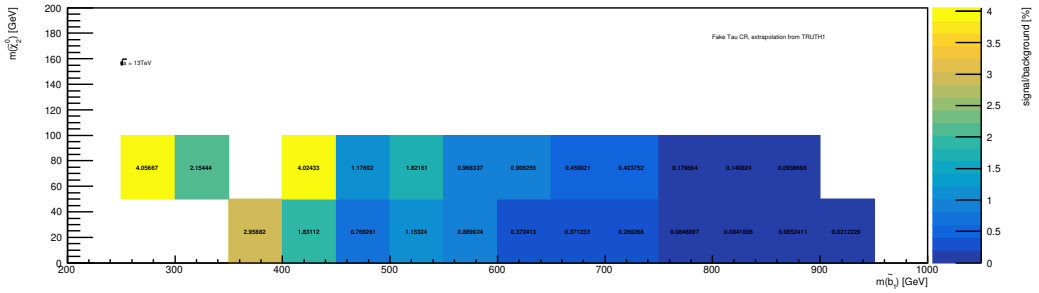

(d) Fake Tau CR signal contamination extrapolated

Figure D.2: Signal contamination of various control regions, measured where possible and extrapolated otherwise, combined datasets.

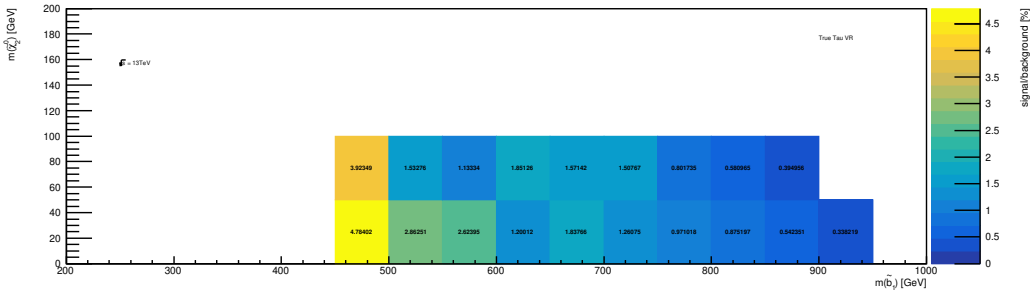

(a) True Tau VR signal contamination

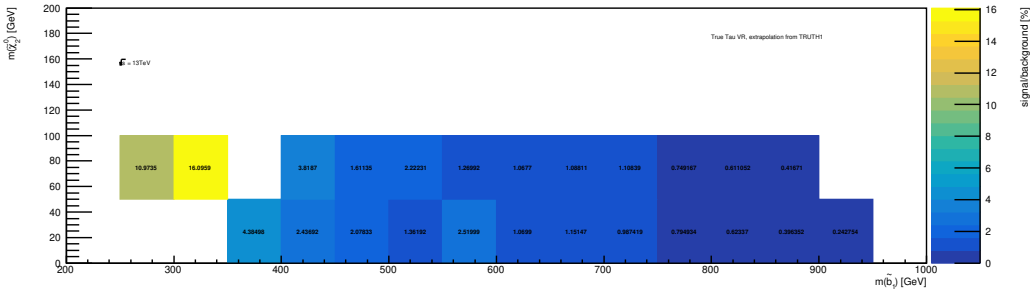

(b) True Tau VR signal contamination extrapolated

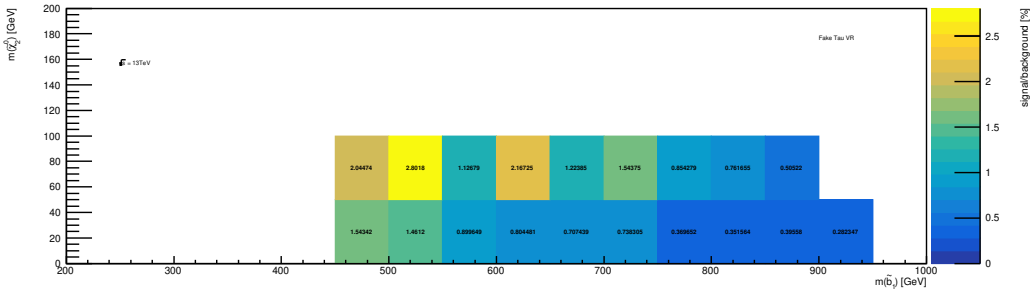

(c) Fake Tau VR signal contamination

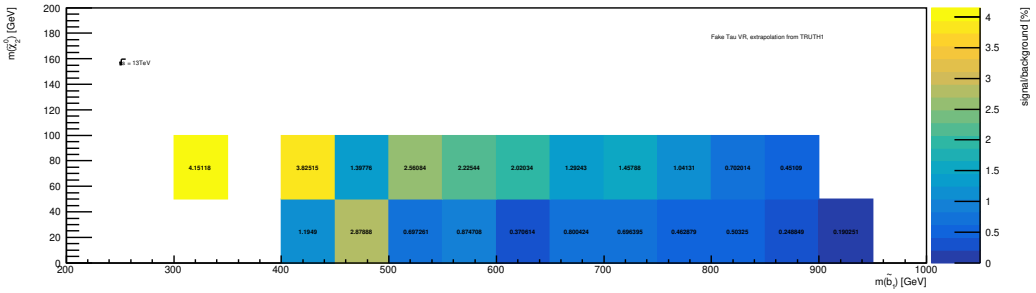

(d) Fake VR signal contamination extrapolated

Figure D.3: Signal contamination of various validation regions, measured where possible and extrapolated otherwise, combined datasets.

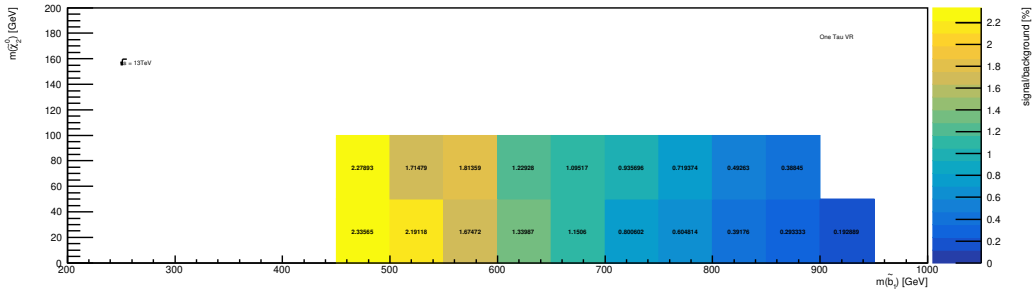

(a) One Tau VR signal contamination

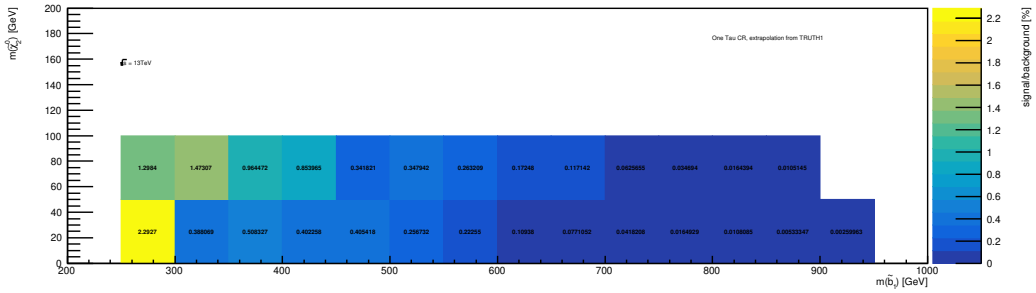

(b) One Tau VR signal contamination extrapolated

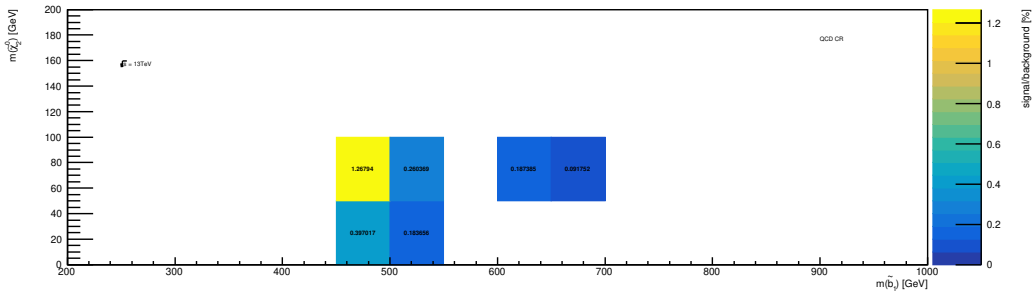

(c) QCD CR signal contamination (QCD itself not included)

Figure D.4: Signal contamination of various validation regions, measured where possible and extrapolated otherwise, combined datasets.

Appendix E

Signal Quality Checks

Truth-reco comparisons Producing Monte-Carlo samples is a rather long and computationally heavy process. The most "expensive" part is reconstruction and digitisation of the events. Computing the matrix element and the consequent parton showers is comparatively much faster. To decide what signal models are worth investigating and how effective the analysis can be one needs access to some sort of signal samples. The approach taken by the analysis is to first perform initial studies on the MC truth samples (called so since they are using true numbers produced by the generators, not the smeared reconstructed and digitised objects) that do not pass the reconstruction and digitisation steps. Based on these studies a range of models is selected and processed centrally.

Samples corresponding to various signal models have been generated and a simplified version of the signal region selection procedure has been run on them. After a first approximation of what it is possible to achieve with the analysis was done a range of signal models were selected. Additional studies were performed on possible filters that would improve the number of events that would eventually pass the selection. This is done to make sure as little "wasted" events as possible go through the reconstruction and digitisation. This procedure was repeated when the extension of the grid was requested to create a closed exclusion contour. Additionally truth-level studies are used for estimation of signal contamination in some regions and for evaluation of generator-related systematic uncertainties for signal samples.

An important question to ask is whether the MC truth studies are accurate enough to trust them. In this section some comparisons of truth and reconstructed samples are gathered. The task of extracting the useful information from the generator output and converting it in a format similar to the one used by the fully processes ATLAS Monte-Carlo is delegated to the SimpleAnalysis framework. Within this framework an analysis-specific selection is implemented that selects objects with similar kinematic properties as those used by the analysis and performing a simple overlap-removal procedure.

The truth-level samples are normalised by the cross section and (eventually) filter efficiency applied to the samples. This number is multiplied by the total integrated luminosity that is being considered. Tile vetoes used in the analysis are also implemented. Since vetoes are period-dependent the events that hit the faulty tiles are not completely rejected, but scaled down according to what fraction of events is expected to be lost in data. The acceptance is roughly emulated by the $|\eta|$ cuts placed on all objects corre-

sponding to what is used for the reconstructed objects. Correcting for efficiency is a bit trickier.

Consider an event that, at the generator level, has 3 b-jets. If the selection for some region is exactly 2 b-jets (as is the case for many regions in the presented analysis) the event would be rejected. However we have to keep in mind that after reconstruction a 77% efficiency b-jets are used meaning there is a $3 \times 0.77 \times 0.77 \times 0.23 = 0.41$ probability that exactly one of the b-jets will not pass the b-tagging and the event with the remaining 2 b-jets will pass the selection. Similar comments apply to hadronically decaying taus. To account for this behaviour all events used are scaled by the tau and b-jet reconstruction and identification efficiencies. Each event gets several different combinations of weights depending on which objects are considered as being identified correctly or not and the sum of these weights is used as the final weight.

Four models have been chosen to check the truth-reco agreement, see Table E.1. Generator-level truth samples are compared to the fully reconstructed and processed samples used for the final analysis in three different regions – preselection corresponding to trigger plateau, TrueTau CR selection and single-bin discovery SR. The results of the comparison are shown in Table E.2. Notice that the uncertainties included are purely statistical. The models used to produce the truth-level and reconstructed samples are the same, but the random is different so the samples are statistically independent. The agreement seems to be reasonable for most points. The conclusion is that the use of truth-level studies is justified.

Table E.1: Grid points used to check truth-reco agreement.

Point	$m_{\tilde{b}}$	$m_{\tilde{\chi}_2^0}$	$m_{\tilde{\chi}_1^0}$
Point 1	850 GeV	180 GeV	50 GeV
Point 2	700 GeV	280 GeV	150 GeV
Point 3	700 GeV	131 GeV	1 GeV
Point 4	450 GeV	180 GeV	50 GeV

Table E.2: Comparison of truth and reco samples. Only statistical uncertainties included.

Region	450,180	700,131	700,280	850,180
Preselection, reco	1110 ± 22.6	149 ± 3.48	27 ± 4.41	76.2 ± 1.3
Preselection, truth	862.30 ± 12.18	139.39 ± 3.41	239.94 ± 2.78	72.41 ± 1.31
TrueTau CR, reco	13 ± 2.16	1.77 ± 0.34	1.6 ± 0.34	0.46 ± 0.10
TrueTau CR, truth	15.08 ± 1.61	2.02 ± 0.40	2.68 ± 0.29	0.51 ± 0.11
Disc SR, reco	21.8 ± 3.31	9.5 ± 0.87	5.38 ± 0.63	6.62 ± 0.381
Disc SR, truth	20.54 ± 1.62	8.92 ± 0.70	6.04 ± 0.37	6.34 ± 0.32

AtlFastII and FullSim Comparison The majority of the background MC samples are reconstructed using the FullSim procedure where the whole ATLAS detector is emulated

using Geant4. The majority of the signal samples are produced using a simplified procedure, AtlFastII (AFII), to save processing time. A couple of signal points are produced using FullSim to be able to compare and justify the use of AFII samples. The comparison is performed on the trigger plateau, both FullSim and AFII samples are normalised to 1. Signal point with $m_{\tilde{b}} = 350$ GeV and $m_{\tilde{\chi}_2^0} = 131$ GeV is used for comparison. The comparison of important kinematic values is shown in Figures E.1 - E.3.

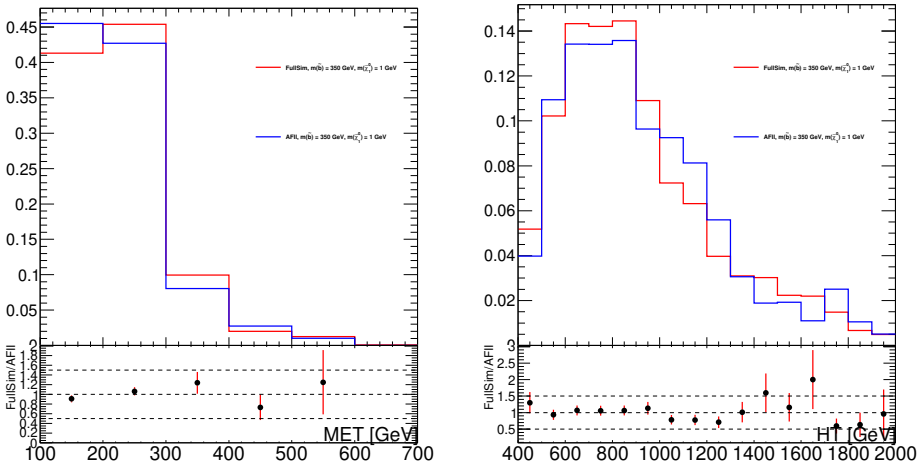

(a) $E_{\mathrm{T}}^{\mathrm{miss}}$ AFII vs FullSim, signal point $m_{\tilde{b}} = 350$ GeV, $m_{\tilde{\chi}_2^0} = 131$ GeV

(b) H_{T} AFII vs FullSim, signal point $m_{\tilde{b}} = 350$ GeV, $m_{\tilde{\chi}_2^0} = 131$ GeV

Figure E.1: Comparison of signal samples produced using AFII and FullSim procedures.

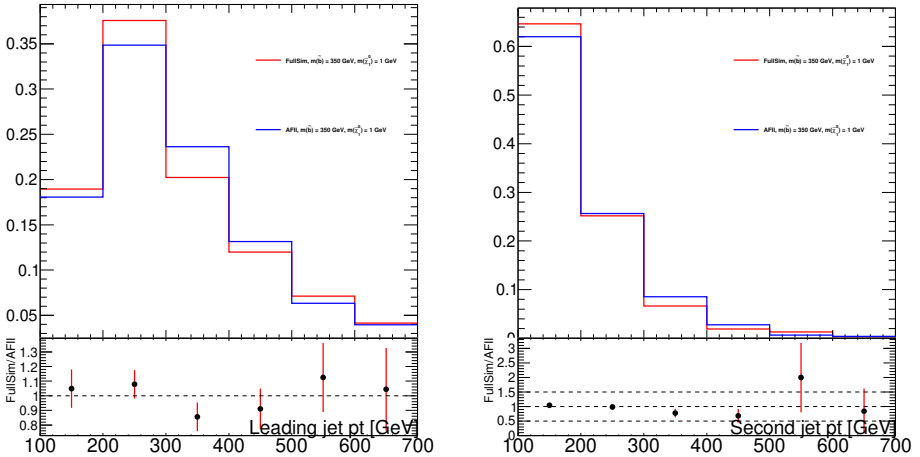

(a) Leading jet p_{T} AFII vs FullSim, signal point $m_{\tilde{b}} = 350$ GeV, $m_{\tilde{\chi}_2^0} = 131$ GeV

(b) Second jet p_{T} AFII vs FullSim, signal point $m_{\tilde{b}} = 350$ GeV, $m_{\tilde{\chi}_2^0} = 131$ GeV

Figure E.2: Comparison of signal samples produced using AFII and FullSim procedures.

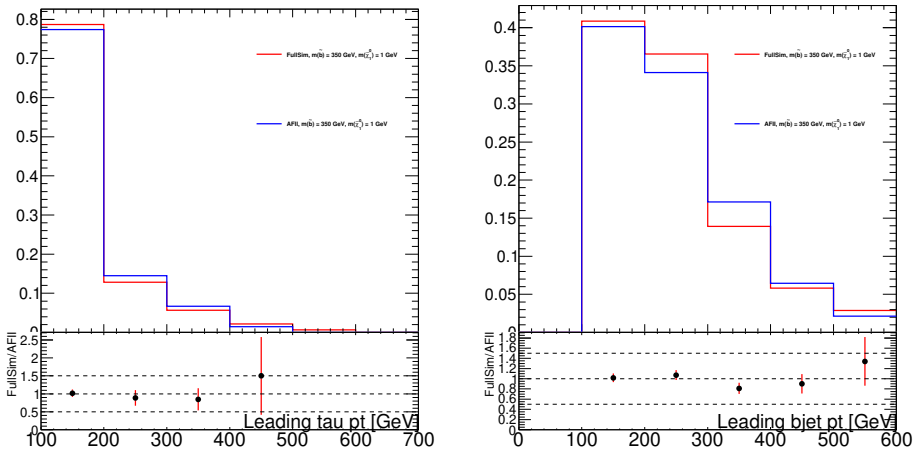

(a) Leading tau p_{T}AFII vs FullSim, signal point $m_{\tilde{b}} = 350$ GeV, $m_{\tilde{\chi}_2^0} = 131$ GeV

(b) Leading b-jet p_{T}AFII vs FullSim, signal point $m_{\tilde{b}} = 350$ GeV, $m_{\tilde{\chi}_2^0} = 131$ GeV

Figure E.3: Comparison of signal samples produced using AFII and FullSim procedures.

Appendix F

JES Scenarios

As part of the systematics evaluation different JES scenarios are compared. All the available background samples are reprocessed with JES scenario 2 (as opposed to scenario 1 used for nominal samples) and the effect of the change on the JES-related systematics and observable results is studied. Comparison of systematic uncertainties in the one-bin SR is summarized in Table F.1. It can be seen that even though the largest JES-related systematic (jetnp1) changes between the scenarios from 0.18 to 0.29 the effect on the overall uncertainty is negligible. Figures F.1 - F.2 show the comparison of expected exclusion using the one bin SR and two different shape fit approaches. Since no differences are observed we conclude that the analysis is not sensitive to the JES scenarios.

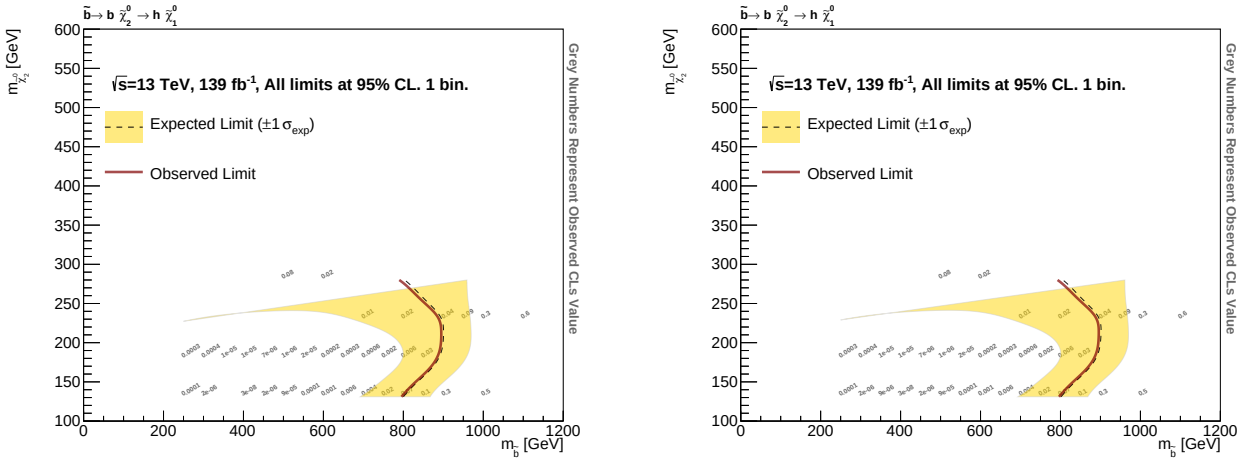

(a) JES sc 1, single bin SR.

(b) JES sc 2, single bin SR.

Figure F.1: Comparison of exclusion plots (blinded) with JES scenario 1 (nominal) and JES scenario 2.

	JES sc. 1	JES sc. 2
Total background expectation	4.01	4.00
Total background systematic	$\pm$1.18 [29.28%]	$\pm$1.17 [29.20%]
alpha_ttbar_syst_radH	$\pm$0.97	$\pm$0.94
alpha_amcnlottbar	$\pm$0.95	$\pm$0.94
alpha_jetdatamc	$\pm$0.39	$\pm$0.39
alpha_fsrsyst	$\pm$0.39	$\pm$0.38
omega_scale_top	$\pm$0.35	$\pm$0.35
omega_true_tau	$\pm$0.34	$\pm$0.34
omega_fake_tau	$\pm$0.33	$\pm$0.33
gamma_stat_SR_cuts_bin_0	$\pm$0.27	$\pm$0.27
alpha_mursyst_ttX	$\pm$0.24	$\pm$0.24
alpha_lsyst	$\pm$0.20	$\pm$0.20
alpha_murmufcomb_ttX	$\pm$0.18	$\pm$0.18
alpha_jetnp1	$\pm$0.18	$\pm$0.29

Table F.1: Comparison of systematic uncertainties in the SR (blinded) with JES scenario 1 (nominal) and JES scenario 2. jetnp1 is the first JES-related systematic.

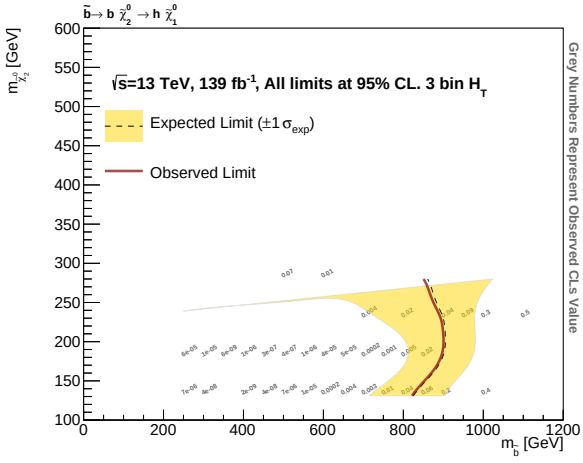

(a) JES sc 1, H_T fit.

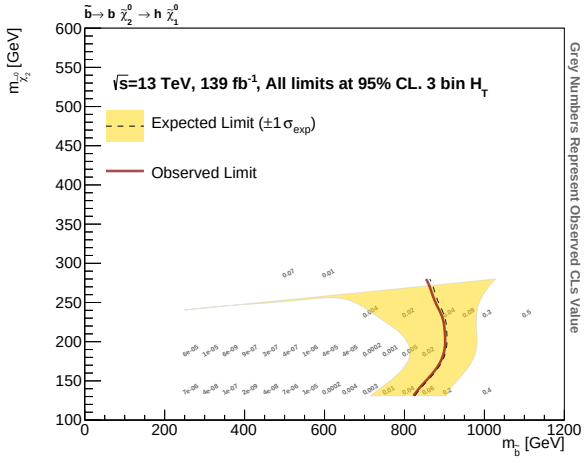

(b) JES sc 2, H_T fit.

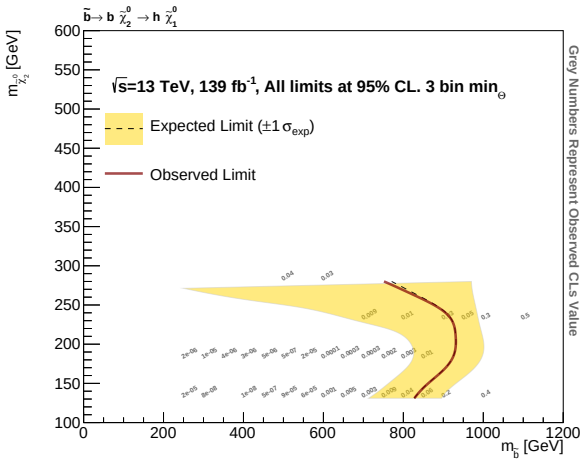

(c) JES sc 1, min_Θ fit.

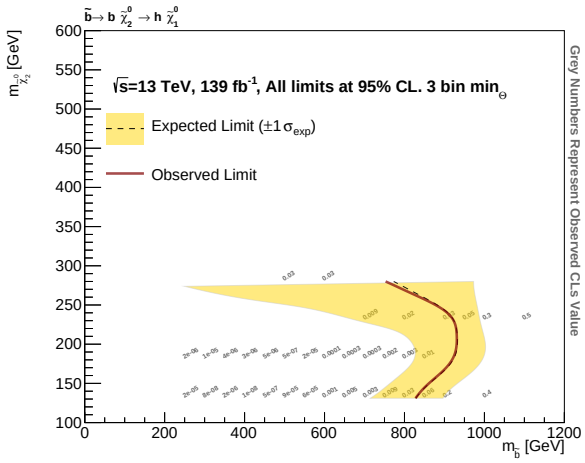

(d) JES sc 2, min_Θ fit.

Figure F.2: Comparison of exclusion plots (blinded) with JES scenario 1 (nominal) and JES scenario 2.

Appendix G

Discovery Fit Checks

Some sanity checks and diagnostics plots for the discovery fit are gathered here.

To begin with the "main" discovery fit results are repeated, see Table G.1. The uncertainty on S^{95}_{exp} seems to be somewhat larger than expected so additional checks are done in an attempt to understand what is going on.

Signal channel	$\langle\varepsilon\sigma\rangle^{95}_{obs}$[fb]	S^{95}_{obs}	S^{95}_{exp}	CL_B	$p(s=0)$ (Z)
100 toys	0.06	8.8	$8.9^{+9.8}_{-3.2}$	0.52	0.47 (0.08)
1000 toys	0.07	9.7	$10.2^{+8.3}_{-2.9}$	0.41	0.44 (0.15)

Table G.1: Left to right: 95% CL upper limits on the visible cross section ($\langle\varepsilon\sigma\rangle^{95}_{obs}$) and on the number of signal events (S^{95}_{obs}). The third column (S^{95}_{exp}) shows the 95% CL upper limit on the number of signal events, given the expected number (and $\pm1\sigma$ excursions on the expectation) of background events. The last two columns indicate the CL_B value, i.e. the confidence level observed for the background-only hypothesis, and the discovery p-value ($p(s=0)$).

The first check was to simply repeat the computation with just the total background + total systematic on background as one number and see if the prediction will vary significantly. This is much more forgiving in terms of processing power so more toys can be run. The results are gathered in Table G.2. The values of S^{95}_{obs} and S^{95}_{exp} differ somewhat, but the overall agreement seems to be ok.

Signal channel	$\langle\varepsilon\sigma\rangle^{95}_{obs}$[fb]	S^{95}_{obs}	S^{95}_{exp}	CL_B	$p(s=0)$ (Z)
100 toys	0.05	6.5	$6.3^{+4.3}_{-0.1}$	0.68	0.38 (0.31)
1000 toys	0.05	6.5	$6.4^{+4.2}_{-0.1}$	0.60	0.44 (0.16)
10000 toys	0.05	6.5	$6.4^{+4.1}_{-0.1}$	0.59	0.45 (0.14)

Table G.2: Left to right: 95% CL upper limits on the visible cross section ($\langle\varepsilon\sigma\rangle^{95}_{obs}$) and on the number of signal events (S^{95}_{obs}). The third column (S^{95}_{exp}) shows the 95% CL upper limit on the number of signal events, given the expected number (and $\pm1\sigma$ excursions on the expectation) of background events. The last two columns indicate the CL_B value, i.e. the confidence level observed for the background-only hypothesis, and the discovery p-value ($p(s=0)$).

Finally the reduced set of systematic is used as the processing speed is still significantly faster than for full systematics setup. The numbers are gathered in Table G.3.

Overall the numbers predicted by the "main" procedure seem reasonable.

Signal channel	$\langle\varepsilon\sigma\rangle^{95}_{obs}$[fb]	S^{95}_{obs}	S^{95}_{exp}	CL_B	$p(s=0)$ (Z)
100 toys	0.06	7.9	$8.7^{+8.0}_{-1.0}$	0.46	0.15 (1.04)
500 toys	0.07	9.5	$9.8^{+5.4}_{-2.6}$	0.39	0.22 (0.77)
1000 toys	0.07	9.4	$9.6^{+6.7}_{-2.7}$	0.42	0.20 (0.83)
2000 toys	0.06	8.9	$9.6^{+6.1}_{-2.1}$	0.41	0.22 (0.79)

Table G.3: Left to right: 95% CL upper limits on the visible cross section ($\langle\varepsilon\sigma\rangle^{95}_{obs}$) and on the number of signal events (S^{95}_{obs}). The third column (S^{95}_{exp}) shows the 95% CL upper limit on the number of signal events, given the expected number (and $\pm1\sigma$ excursions on the expectation) of background events. The last two columns indicate the CL_B value, i.e. the confidence level observed for the background-only hypothesis, and the discovery p-value ($p(s=0)$).

Bibliography

[1] ATLAS Collaboration. A search for Supersymmetry in events containing a leptonically decaying Z boson, jets and missing transverse momentum in $\sqrt{s} =$ 13 TeV pp collisions with the ATLAS detector. Technical Report ATLAS-CONF-2015-082, CERN, Geneva, Dec 2015. 1.1

[2] Morad Aaboud et al. Search for new phenomena using the invariant mass distribution of same-flavour opposite-sign dilepton pairs in events with missing transverse momentum in $\sqrt{s} = 13$ TeV pp collisions with the ATLAS detector. *Eur. Phys. J. C*, 78(8):625, 2018. 1.1

[3] ATLAS Collaboration. Search for bottom-squark pair production with the ATLAS detector in final states containing Higgs bosons, b-jets and missing transverse momentum. 2019. 1.1, 2.4, 2.3, 10.4, 10.10, 11, 11.1

[4] Morad Aaboud et al. Search for squarks and gluinos in final states with hadronically decaying τ-leptons, jets, and missing transverse momentum using pp collisions at $\sqrt{s}$ = 13 TeV with the ATLAS detector. *Phys. Rev. D*, 99(1):012009, 2019. 1.1, 6.5

[5] Alan D. Martin and Francis Halzen. *Quarks and Leptons*. John Wiley and Sons, 1984. 2

[6] Ian Aitchinson Anthony Hey. *Gauge Theories in Particle Physics*. Institute of Physics Publishin, 2004. 2

[7] J. Fuchs and C. Schweigert. *Symmetries, Lie algebras and representations: A graduate course for physicists*. Cambridge University Press, 2003. 2.1

[8] E. Noether. Invariante variationsprobleme. *Nachrichten von der Gesellschaft der Wissenschaften zu Göttingen, Mathematisch-Physikalische Klasse*, 1918:235–257, 1918. 2.1

[9] Steven Weinberg. The Making of the standard model. *Eur. Phys. J.*, C34:5–13, 2004. [,99(2005)]. 2.2

[10] MissMJ and Cush. File:Standard Model of Elementary Particles - Wikimedia Commons. https://commons.wikimedia.org/wiki/File:Standard_Model_of_Elementary_Particles.svg, (accessed 25. June, 2020). 2.1a

[11] D. P. Barber et al. Discovery of Three Jet Events and a Test of Quantum Chromodynamics at PETRA Energies. *Phys. Rev. Lett.*, 43:830, 1979. 2.2

[12] F. Englert and R. Brout. Broken symmetry and the mass of gauge vector mesons. *Phys. Rev. Lett.*, 13:321–323, Aug 1964. 2.2

[13] Peter W. Higgs. Broken symmetries and the masses of gauge bosons. *Phys. Rev. Lett.*, 13:508–509, Oct 1964. 2.2

[14] G. S. Guralnik, C. R. Hagen, and T. W. B. Kibble. Global conservation laws and massless particles. *Phys. Rev. Lett.*, 13:585–587, Nov 1964. 2.2

[15] Serguei Chatrchyan et al. Observation of a New Boson at a Mass of 125 GeV with the CMS Experiment at the LHC. *Phys. Lett. B*, 716:30–61, 2012. 2.2

[16] Georges Aad et al. Observation of a new particle in the search for the Standard Model Higgs boson with the ATLAS detector at the LHC. *Phys. Lett. B*, 716:1–29, 2012. 2.2

[17] John Ellis, Mary K Gaillard, and Dimitri V Nanopoulos. A Historical Profile of the Higgs Boson. An Updated Historical Profile of the Higgs Boson. (arXiv:1504.07217. KCL-PH-TH-2015-20. LCTS-2015-10. CERN-PH-TH-2015-098):22 p, Apr 2015. Comments: 22 pages, 5 figures, update of arXiv:1201.6045, to be published in the volume The Standard Theory of Particle Physics, edited by Luciano Maiani and Gigi Rolandi. 2.2a

[18] Stephen P. Martin. *A Supersymmetry primer*, volume 21, pages 1–153. 2010. 2.3

[19] Fernando Quevedo, Sven Krippendorf, and Oliver Schlotterer. Cambridge Lectures on Supersymmetry and Extra Dimensions. 11 2010. 2.3

[20] Sidney Coleman and Jeffrey Mandula. All possible symmetries of the *s* matrix. *Phys. Rev.*, 159:1251–1256, Jul 1967. 2.3

[21] Rudolf Haag, Jan T. Lopuszanski, and Martin Sohnius. All Possible Generators of Supersymmetries of the s Matrix. *Nucl. Phys.*, B88:257, 1975. [,257(1974)]. 2.3

[22] Johan Alwall, Philip Schuster, and Natalia Toro. Simplified Models for a First Characterization of New Physics at the LHC. *Phys. Rev.*, D79:075020, 2009. 2.3

[23] Johan Alwall, My-Phuong Le, Mariangela Lisanti, and Jay G. Wacker. Searching for Directly Decaying Gluinos at the Tevatron. *Phys. Lett.*, B666:34–37, 2008. 2.3

[24] J. Anders, D. Costanzo, M. D'Onofrio, E. Kourlitis, C. Macdonald, H. Teagle, T. Weston. Search for sbottom pair production with the ATLAS detector in final states containing Higgs bosons, *b*-jets and $E_{\mathrm{T}}^{\mathrm{miss}}$in pp collisions at $\sqrt{s} = 13$ TeV. ATL-COM-PHYS-2018-1361, 2019. 2.4

[25] The ATLAS Collaboration. 3(08):S08003–S08003, aug 2008. Journal of Instrumentation. 3, 3.2

[26] Lyndon Evans and Philip Bryant. LHC Machine. *JINST*, 3:S08001, 2008. 3.2

[27] CERN. Diagram of an LHC dipole magnet. Schéma d'un aimant dipôle du LHC, Jun 1999. 3.1a

[28] L. Rossi. The lhc superconducting magnets. In *Proceedings of the 2003 Particle Accelerator Conference*, volume 1, pages 141–145 Vol.1, May 2003. 3.2

[29] The CMS Collaboration. 3(08):S08004–S08004, aug 2008. Journal of Instrumentation. 3.2

[30] The ALICE Collaboration. 3(08):S08002–S08002, aug 2008. Journal of Instrumentation. 3.2

[31] The LHCb Collaboration. 3(08):S08005–S08005, aug 2008. Journal of Instrumentation. 3.2

[32] Julie Haffner. The CERN accelerator complex. Complexe des accélérateurs du CERN. Oct 2013. General Photo. 3.2a

[33] ATLAS. Luminosity Public Results Run2. https://twiki.cern.ch/twiki/bin/view/AtlasPublic/LuminosityPublicResultsRun2, 2018. 3.3a

[34] Joao Pequenao. Computer generated image of the whole ATLAS detector. Mar 2008. 3.4a

[35] Joao Pequenao. Computer generated image of the ATLAS inner detector. Mar 2008. 3.5a

[36] ATLAS Collaboration. Study of the material of the ATLAS inner detector for Run 2 of the LHC. Study of the material of the ATLAS inner detector for Run 2 of the LHC. *JINST*, 12(CERN-EP-2017-081):P12009. 71 p, Jul 2017. 60 pages in total, author list starting page 44, 21 figures, 7 tables, submitted to JINST, All figures including auxiliary figures are available at https://atlas.web.cern.ch/Atlas/GROUPS/PHYSICS/PAPERS/PERF-2015-07/. 3.6a

[37] M Capeans, G Darbo, K Einsweiller, M Elsing, T Flick, M Garcia-Sciveres, C Gemme, H Pernegger, O Rohne, and R Vuillermet. ATLAS Insertable B-Layer Technical Design Report. Technical Report CERN-LHCC-2010-013. ATLAS-TDR-19, Sep 2010. 3.3.2

[38] IBL Efficiency and Single Point Resolution in Collision Events. Technical Report ATL-INDET-PUB-2016-001, CERN, Geneva, Aug 2016. 3.3.2

[39] ATLAS Collaboration. Operation and performance of the ATLAS semiconductor tracker. Operation and performance of the ATLAS semiconductor tracker. *JINST*, 9(CERN-PH-EP-2014-049. CERN-PH-EP-2014-049):P08009. 80 p, Apr 2014. Comments: 60 pages plus author list (80 pages total), 33 figures, 10 tables, submitted to JINST. All figures are available at http://atlas.web.cern.ch/Atlas/GROUPS/PHYSICS/PAPERS/IDET-2013-01/ v2: replaced unreadable labels in Fig. 2. 3.3.2

[40] Bartosz Mindur. ATLAS Transition Radiation Tracker (TRT): Straw tubes for tracking and particle identification at the Large Hadron Collider. Technical Report ATL-INDET-PROC-2016-001, CERN, Geneva, Mar 2016. 3.3.2

[41] Joao Pequenao. Computer Generated image of the ATLAS calorimeter. Mar 2008. 3.7a

[42] Joao Pequenao. Computer generated image of the ATLAS Muons subsystem. Mar 2008. 3.8a

[43] ATLAS Collaboration. Performance of the ATLAS muon trigger in pp collisions at $\sqrt{s}$ =8 TeV. Performance of the ATLAS muon trigger in pp collisions at $\sqrt{s}$ = 8 TeV. *Eur. Phys. J. C*, C75(CERN-PH-EP-2014-154. CERN-PH-EP-2014-154):120. 19 p, Aug 2014. 19 pages plus author list (34 pages total), 17 figures, 3 tables, submitted to European Physics Journal C, All figures including auxiliary figures are available at http://atlas.web.cern.ch/Atlas/GROUPS/PHYSICS/PAPERS/TRIG-2012-03. 3.9a

[44] ATLAS Collaboration. Commissioning of the ATLAS Muon Spectrometer with Cosmic Rays. Commissioning of the ATLAS Muon Spectrometer with Cosmic Rays. *Eur. Phys. J. C*, 70(arXiv:1006.4384. CERN-PH-EP-2010-045):875–916. 58 p, Aug 2010. 3.10a

[45] ATLAS Collaboration. Magnet System. https://atlas.cern/discover/detector/magnet-system. 3.11a

[46] ATLAS Collaboration. Performance of the ATLAS Trigger System in 2015. Performance of the ATLAS Trigger System in 2015. *Eur. Phys. J. C*, 77(CERN-EP-2016-241. 5):317. 76 p, Nov 2016. 77 pages in total, author list starting page 61, 50 figures, 1 table. Published in Eur. Phys. J. C. All figures including auxiliary figures are available at http://atlas.web.cern.ch/Atlas/GROUPS/PHYSICS/PAPERS/TRIG-2016-01/. 3.3.6

[47] ATLAS Collaboration. https://twiki.cern.ch/twiki/bin/view/AtlasPublic/TriggerOperationPublicResults. 3.12a

[48] S. Agostinelli et al. GEANT4: A Simulation toolkit. *Nucl. Instrum. Meth.*, A506:250–303, 2003. 3.3.7, 5.3

[49] Christopher G. Lester and Benjamin Nachman. Bisection-based asymmetric M_{T2} computation: a higher precision calculator than existing symmetric methods. *JHEP*, 03:100, 2015. 4.1

[50] C. G. Lester and D. J. Summers. Measuring masses of semi-invisibly decaying particles pair produced at hadron colliders. *Phys. Lett.*, B463:99–103, 1999. 4.2

[51] Alan Barr, Christopher Lester, and P. Stephens. m(T2): The Truth behind the glamour. *J. Phys.*, G29:2343–2363, 2003. 4.2

[52] Michael H. Seymour and Marilyn Marx. Monte Carlo Event Generators. In *Proceedings, 69th Scottish Universities Summer School in Physics : LHC Phenomenology (SUSSP69): St.Andrews, Scotland, August 19-September 1, 2012*, pages 287–319, 2013. 4.3

[53] Torbjorn Sjostrand. Monte Carlo Generators. In *High-energy physics. Proceedings, European School, Aronsborg, Sweden, June 18-July 1, 2006*, pages 51–74, 2006. 4.3

[54] V.N. Gribov and L.N. Lipatov. Deep inelastic e p scattering in perturbation theory. *Sov. J. Nucl. Phys.*, 15:438–450, 1972. 4.3.2

[55] Johan Alwall et al. A Standard format for Les Houches event files. *Comput. Phys. Commun.*, 176:300–304, 2007. 4.3.3

[56] Andy Buckley, James Ferrando, Stephen Lloyd, Karl Nordström, Ben Page, Martin Rüfenacht, Marek Schönherr, and Graeme Watt. LHAPDF6: parton density access in the LHC precision era. *Eur. Phys. J.*, C75:132, 2015. 4.3.3

[57] Peter Z. Skands et al. SUSY Les Houches accord: Interfacing SUSY spectrum calculators, decay packages, and event generators. *JHEP*, 07:036, 2004. 4.3.3

[58] M Dobbs and J B Hansen. The HepMC C++ Monte Carlo Event Record for High Energy Physics. Technical Report ATL-SOFT-2000-001, CERN, Geneva, Jun 2000. revised version number 1 submitted on 2001-02-27 09:54:32. 4.3.3

[59] Glen Cowan, Kyle Cranmer, Eilam Gross, and Ofer Vitells. Asymptotic formulae for likelihood-based tests of new physics. *Eur. Phys. J.*, C71:1554, 2011. [Erratum: Eur. Phys. J.C73,2501(2013)]. 4.4, 7.1

[60] S. S. Wilks. The Large-Sample Distribution of the Likelihood Ratio for Testing Composite Hypotheses. *Annals Math. Statist.*, 9(1):60–62, 1938. 4.4

[61] A L Read. Presentation of search results: theCLstechnique. *Journal of Physics G: Nuclear and Particle Physics*, 28(10):2693–2704, sep 2002. 4.4

[62] M. Baak, G. J. Besjes, D. Côte, A. Koutsman, J. Lorenz, and D. Short. HistFitter software framework for statistical data analysis. *Eur. Phys. J.*, C75:153, 2015. 4.5, 4.2a

[63] T. Gleisberg, Stefan. Hoeche, F. Krauss, M. Schonherr, S. Schumann, F. Siegert, and J. Winter. Event generation with SHERPA 1.1. *JHEP*, 02:007, 2009. 5.3

[64] J. Alwall, R. Frederix, S. Frixione, V. Hirschi, F. Maltoni, O. Mattelaer, H. S. Shao, T. Stelzer, P. Torrielli, and M. Zaro. The automated computation of tree-level and next-to-leading order differential cross sections, and their matching to parton shower simulations. *JHEP*, 07:079, 2014. 5.3, 5.4

[65] Paolo Nason. A New method for combining NLO QCD with shower Monte Carlo algorithms. *JHEP*, 11:040, 2004. 5.3

[66] Torbjorn Sjostrand, Stephen Mrenna, and Peter Z. Skands. A Brief Introduction to PYTHIA 8.1. *Comput. Phys. Commun.*, 178:852–867, 2008. 5.3

[67] T Yamanaka. The ATLAS calorimeter simulation FastCaloSim. Technical Report ATL-SOFT-PROC-2011-021, CERN, Geneva, Jan 2011. 5.3

[68] G. Aad et al. The ATLAS Simulation Infrastructure. *Eur. Phys. J. C*, 70:823–874, 2010. 5.3

[69] ATLAS Collaboration. Vertex Reconstruction Performance of the ATLAS Detector at $\sqrt{s} = 13$ TeV. ATL-PHYS-PUB-2015-026, 2015. 5.5

[70] Matteo Cacciari, Gavin P. Salam, and Gregory Soyez. The anti-k_t jet clustering algorithm. *JHEP*, 04:063, 2008. 5.5

[71] Georges Aad et al. Topological cell clustering in the ATLAS calorimeters and its performance in LHC Run 1. *Eur. Phys. J. C*, 77:490, 2017. 5.5

[72] Morad Aaboud et al. Determination of jet calibration and energy resolution in proton-proton collisions at $\sqrt{s} = 8$ TeV using the ATLAS detector. 10 2019. 5.5

[73] M. Aaboud et al. Jet energy scale measurements and their systematic uncertainties in proton-proton collisions at $\sqrt{s} = 13$ TeV with the ATLAS detector. *Phys. Rev. D*, 96(7):072002, 2017. 5.5

[74] Tagging and suppression of pileup jets with the ATLAS detector. Technical Report ATLAS-CONF-2014-018, CERN, Geneva, May 2014. 5.5

[75] Expected performance of the ATLAS b-tagging algorithms in Run-2. Technical Report ATL-PHYS-PUB-2015-022, CERN, Geneva, Jul 2015. 5.5

[76] ATLAS Collaboration. ATLAS b-jet identification performance and efficiency measurement with $t\bar{t}$ events in pp collisions at $\sqrt{s} = 13$ TeV. *Eur. Phys. J. C*, 79:970, 2019. 5.5

[77] $E_{\mathrm{T}}^{\mathrm{miss}}$ performance in the ATLAS detector using 2015-2016 LHC p-p collisions. Technical Report ATLAS-CONF-2018-023, CERN, Geneva, Jun 2018. 5.5

[78] Electron and photon energy calibration with the ATLAS detector using 2015-2016 LHC proton-proton collision data. Technical Report arXiv:1812.03848. 03, Dec 2018. Submitted to JINST. 5.5

[79] Electron identification measurements in ATLAS using $\sqrt{s} = 13$ TeV data with 50 ns bunch spacing. Technical Report ATL-PHYS-PUB-2015-041, CERN, Geneva, Sep 2015. 5.5

[80] Georges Aad et al. Muon reconstruction performance of the ATLAS detector in proton–proton collision data at $\sqrt{s}$ =13 TeV. *Eur. Phys. J. C*, 76(5):292, 2016. 5.5

[81] Reconstruction, Energy Calibration, and Identification of Hadronically Decaying Tau Leptons in the ATLAS Experiment for Run-2 of the LHC. Technical Report ATL-PHYS-PUB-2015-045, CERN, Geneva, Nov 2015. 5.5

[82] T Barillari, E Bergeaas Kuutmann, T Carli, J Erdmann, P Giovannini, K J Grahn, C Issever, A Jantsch, A Kiryunin, K Lohwasser, A Maslennikov, S Menke, H Oberlack, G Pospelov, E Rauter, P Schacht, F Spanó, P Speckmayer, P Stavina, and P Strízenec. Local Hadronic Calibration. Technical Report ATL-LARG-PUB-2009-001-2. ATL-COM-LARG-2008-006. ATL-LARG-PUB-2009-001, CERN, Geneva, Jun 2008. Due to a report-number conflict with another document, the report-number ATL-LARG-PUB-2009-001-2 has been assigned. 5.5

[83] Georges Aad et al. Reconstruction of hadronic decay products of tau leptons with the ATLAS experiment. *Eur. Phys. J. C*, 76(5):295, 2016. 5.5

[84] ATLAS Collaboration. Identification of hadronic tau lepton decays using neural networks in the ATLAS experiment. ATL-PHYS-PUB-2019-033, 2019. 5.5

[85] Selection of jets produced in 13TeV proton-proton collisions with the ATLAS detector. Technical Report ATLAS-CONF-2015-029, CERN, Geneva, Jul 2015. 5.6

[86] Andrea Ventura. ATLAS Muon Trigger Performance. Technical Report ATL-DAQ-PROC-2019-035, CERN, Geneva, Dec 2019. 6.3

[87] Morad Aaboud et al. Search for squarks and gluinos in events with hadronically decaying tau leptons, jets and missing transverse momentum in proton–proton collisions at $\sqrt{s} = 13$ TeV recorded with the ATLAS detector. *Eur. Phys. J.*, C76(12):683, 2016. 7.1

[88] Chiara Debenedetti, Valentina Cairo, Kevin Hildebrand, Jose Luis La Rosa Navarro, Marco Aurelio Lisboa Leite, Evelin Meoni, Jacob Martin Pasner, Douglas Schaefer, Federico Sforza, Semen Turchikhin, Camilla Vittori, Josh Mcfayden, Valerio Dao, Laura Fabbri, Benedetto Giacobbe, Gennadi Lykasov, Vivek Jain, and Stewart Patrick Swift. Measurement of a Z boson produced in association with heavy flavour jets in 36 fb^{-1} collected by the ATLAS experiment at $\sqrt{s} = 13$ TeV. ATL-COM-PHYS-2017-1687, 2017. 8.3

[89] Georges Aad et al. Search for squarks and gluinos with the ATLAS detector in final states with jets and missing transverse momentum using 4.7 fb^{-1} of $\sqrt{s} = 7$ TeV proton-proton collision data. *Phys. Rev. D*, 87(1):012008, 2013. 8.5

[90] ATLAS Pythia 8 tunes to 7 TeV datas. Technical Report ATL-PHYS-PUB-2014-021, CERN, Geneva, Nov 2014. 9.1, 9.1, 9.5

[91] John Kenneth Anders and Monica D'Onofrio. V+Jets theoretical uncertainties estimation via a parameterisation method. Technical Report ATL-COM-PHYS-2016-044, CERN, Geneva, Jan 2016. 9.1

[92] Wim Beenakker, Christoph Borschensky, Michael Krämer, Anna Kulesza, and Eric Laenen. NNLL-fast: predictions for coloured supersymmetric particle production at the LHC with threshold and Coulomb resummation. *JHEP*, 12:133, 2016. 9.5

[93] Wim Beenakker, Christoph Borschensky, Michael Krämer, Anna Kulesza, Eric Laenen, Vincent Theeuwes, and Silja Thewes. NNLL resummation for squark and gluino production at the LHC. *JHEP*, 12:023, 2014. 9.5

[94] Wim Beenakker, Tim Janssen, Susanne Lepoeter, Michael Krämer, Anna Kulesza, Eric Laenen, Irene Niessen, Silja Thewes, and Tom Van Daal. Towards NNLL resummation: hard matching coefficients for squark and gluino hadroproduction. *JHEP*, 10:120, 2013. 9.5

[95] Wim Beenakker, Silja Brensing, Michael Krämer, Anna Kulesza, Eric Laenen, and Irene Niessen. NNLL resummation for squark-antisquark pair production at the LHC. *JHEP*, 01:076, 2012. 9.5

[96] Wim Beenakker, Silja Brensing, Michael Krämer, Anna Kulesza, Eric Laenen, and Irene Niessen. Soft-gluon resummation for squark and gluino hadroproduction. *JHEP*, 12:041, 2009. 9.5

[97] A. Kulesza and L. Motyka. Soft gluon resummation for the production of gluino-gluino and squark-antisquark pairs at the LHC. *Phys. Rev. D*, 80:095004, 2009. 9.5

[98] A. Kulesza and L. Motyka. Threshold resummation for squark-antisquark and gluino-pair production at the LHC. *Phys. Rev. Lett.*, 102:111802, 2009. 9.5

[99] W. Beenakker, R. Hopker, M. Spira, and P.M. Zerwas. Squark and gluino production at hadron colliders. *Nucl. Phys. B*, 492:51, 1997. 9.5

[100] Jon Butterworth et al. PDF4LHC recommendations for LHC Run II. *J. Phys. G*, 43:023001, 2016. 9.5